HAL
open science

Magnetic and structural properties of size-selected FeCo nanoparticle assemblies

Ghassan Khadra

To cite this version:

Ghassan Khadra. Magnetic and structural properties of size-selected FeCo nanoparticle assemblies. Physics [physics]. Université Claude Bernard - Lyon I, 2015. English. NNT : 2015LYO10145 . tel-01262653v2

HAL Id: tel-01262653

https://theses.hal.science/tel-01262653v2

Submitted on 26 May 2016

HAL is a multi-disciplinary open access archive for the deposit and dissemination of scientific research documents, whether they are published or not. The documents may come from teaching and research institutions in France or abroad, or from public or private research centers.

L'archive ouverte pluridisciplinaire **HAL**, est destinée au dépôt et à la diffusion de documents scientifiques de niveau recherche, publiés ou non, émanant des établissements d'enseignement et de recherche français ou étrangers, des laboratoires publics ou privés.

N°d'ordre 145-2015 Année 2015

THESE DE L'UNIVERSITE DE LYON

Délivrée par

L'UNIVERSITE CLAUDE BERNARD LYON 1

ECOLE DOCTORALE MATÉRIAUX

DIPLOME DE DOCTORAT

(arrêté du 7 août 2006)

Présentée et soutenue publiquement le 25 Septembre 2015 par

M. Ghassan KHADRA

Magnetic and structural properties of size-selected FeCo nanoparticle assemblies

Directrice de thèse : Dr. Véronique DUPUIS

Co-encadrant : Dr. Alexandre TAMION

Membres du jury :

Pr. Christophe DUJARDIN	Président du jury
Pr. Marc RESPAUD	Rapporteur
Dr. Véronique PIERRON-BOHNES	Rapporteur
Dr. Armin KLEIBERT	Examinateur
Dr. Olivier PROUX	Examinateur
Dr. Philippe OHRESSER	Examinateur
Dr. Véronique DUPUIS	Directrice de thèse
Dr. Alexandre TAMION	Co-encadrant de thèse

UNIVERSITE CLAUDE BERNARD - LYON 1

Président de l'Université	**M. François-Noël GILLY**
Vice-président du Conseil d'Administration	M. le Professeur Hamda BEN HADID
Vice-président du Conseil des Etudes et de la Vie Universitaire	M. le Professeur Philippe LALLE
Vice-président du Conseil Scientifique	M. le Professeur Germain GILLET
Directeur Général des Services	M. Alain HELLEU

COMPOSANTES SANTE

Faculté de Médecine Lyon Est – Claude Bernard	Directeur : M. le Professeur J. ETIENNE
Faculté de Médecine et de Maïeutique Lyon Sud – Charles Mérieux	Directeur : Mme la Professeure C. BURILLON
Faculté d'Odontologie	Directeur : M. le Professeur D. BOURGEOIS
Institut des Sciences Pharmaceutiques et Biologiques	Directeur : Mme la Professeure C. VINCIGUERRA
Institut des Sciences et Techniques de la Réadaptation	Directeur : M. le Professeur Y. MATILLON
Département de formation et Centre de Recherche en Biologie Humaine	Directeur : Mme. la Professeure A-M. SCHOTT

COMPOSANTES ET DEPARTEMENTS DE SCIENCES ET TECHNOLOGIE

Faculté des Sciences et Technologies	Directeur : M. F. DE MARCHI
Département Biologie	Directeur : M. le Professeur F. FLEURY
Département Chimie Biochimie	Directeur : Mme Caroline FELIX
Département GEP	Directeur : M. Hassan HAMMOURI
Département Informatique	Directeur : M. le Professeur S. AKKOUCHE
Département Mathématiques	Directeur : M. le Professeur Georges TOMANOV
Département Mécanique	Directeur : M. le Professeur H. BEN HADID
Département Physique	Directeur : M. Jean-Claude PLENET
UFR Sciences et Techniques des Activités Physiques et Sportives	Directeur : M. Y.VANPOULLE
Observatoire des Sciences de l'Univers de Lyon	Directeur : M. B. GUIDERDONI
Polytech Lyon	Directeur : M. P. FOURNIER
Ecole Supérieure de Chimie Physique Electronique	Directeur : M. G. PIGNAULT
Institut Universitaire de Technologie de Lyon 1	Directeur : M. le Professeur C. VITON
Ecole Supérieure du Professorat et de l'Education	Directeur : M. le Professeur A. MOUGNIOTTE
Institut de Science Financière et d'Assurances	Directeur : M. N. LEBOISNE

REMERCIEMENT

Je remercie tout d'abord la directrice de l'Institut Lumière Matière (iLM), Marie-France Joubert, pour son accueil au sein du laboratoire. J'adresse mes remerciements aux membres du jury : Christophe Dujardin pour avoir accepté de présider le jury de thèse. Marc Respaud et Véronique Pierron-Bohnes pour avoir rapporté en détail mon manuscrit. Je remercie Armin Kleibert d'avoir participé au jury ainsi que pour son aide précieuse des analyses de l'XPEEMS. Je remercie egalement Olivier Proux pour les mesures d'EXAFS ainsi que d'avoir accepté de participer au jury. Et enfin, je tiens à remercier Philippe Ohresser pour avoir accepté de faire partie du jury ainsi que pour les mesures de XMCD.

Je veux remercier chaleureusement Véronique Dupuis et Alexandre Tamion qui ont dirigé ma thèse. Pour Véronique, merci pour tout le soutien et la gentillesse que tu m'as montrée, pour me pousser au-delà de mes limites, mais surtout, pour tous tes conseils et avis. Merci Alexandre de m'avoir soutenu et aidé jusqu'à la conclusion de cette thèse.

Merci à tous les membres de l'équipe nanoparticules magnétiques pour leur aide et pour les nombreux repas partagés dans la joie et la bonne humeur, Laurent Bardotti, Juliette Tuaillion-Combes, Damien Le Roy, et Estela Bernstein avec une mention particulière pour Florent Tournus pour son aide concernant la microscopie électronique, bonne chance à Anthony et Ophilliam pour leurs thèses. Merci aussi à Olivier Boisron et Clement Albin sans qui la synthèse des échantillons aurait été impossible. Un merci aux anciens doctorants de l'equipe Arnaud Hillion et Simon Oyarzun. Et un grand merci à Nicolas Blanchard pour l'aide et la formation sur le microscope TOPCON.

Je tiens à remercier tous les gens extérieurs au laboratoire pour leurs collaborations essentielles à cette étude. Je remercie, à l'ESRF, Jean-Louis Hazemann pour les mesures d'EXAFS et Nils Blanc pour les mesures d'AXD. Je tiens à remercie Fadi Chouikani de ligne DEIMOS de synchrotron Soleil, pour son aide pour les mesures de XMCD. À Christine Boeglin, Nicolas Bergeard, Spiros Zafeiratos, Frithjof Nolting, Bing Yang et Stefan Vajda un grand merci pour les collaborations. Mes remerciements s'adressent également à Aguilera-Granja Faustino et Yves Joly pour leurs calculs indispensables. Enfin, je tiens à remercier egalement l'équipe du centre lyonnais de microscopie (CLYM) et centre magnétometrie de lyon (CML).

J'ai pu travailler dans un cadre particulièrement agréable, grâce à l'ensemble des Personnels de l'iLM. Je remercie enfin toutes les personnes du l'institut (doctorants, post-doctorants, docteurs et professeurs) pour leur soutien tout au long de ce trois ans ainsi que leur bonne humeur contribuant ainsi à son bon déroulement. Et en particulier je tiens à remercier Guillaume, Julien, encore Binbin, Princesse et Loic. Merci à Christelle Macheboeuf, Delphine Kervella et Audrey Delvart pour tout l'administratif.

Je voudrais montrer ma plus grande gratitude à mes amis qui m'ont soutenu dans l'écriture, et m'ont invité à tendre vers mes objectifs. Je tiens à adresser un merci tout particulier à Alaa, Lina, Mohamed, Hassan, Bilal, Mouhannad, Khodor, Hussein, Mohamad-Mahdi et enfin et surtout à Alissar.

Ces remerciements ne seraient pas complets sans avoir pensé à ma famille dont la présence a permis de poursuivre mes études jusqu'à aujourd'hui. Merci à mon père et ma mère. Je remercie mes frères et mes sœurs. J'espère que la vie nous réunira un jour dans un même pays.

Title : Magnetic and structural properties of size-selected FeCo nanoparticle assemblies.

Abstract : Over the past few decades, use of nanostructures has become widely popular in the different field of science. Nanoparticles, in particular, are situated between the molecular level and bulk matter size. This size range gave rise to a wide variety physical phenomena that are still not quite understood. Magnetic nanoparticles are at their hype due to their applications in medical field, as a catalyst in a wide number of chemical reactions, in addition to their use for information storage devices and spintronics.
In this work, we are interested in studying the intrinsic magnetic properties (magnetic moments and anisotropy) of FeCo nanoparticles. Thus, in order to completely understand their properties, mass-selected FeCo nanoparticles were prepared using the MS-LECBD (Mass Selected Low Energy Cluster Beam Deposition) technique in the sizes range of 2-6 nm and $in-situ$ embedded in a matrix in order to separate them, to avoid coalescence during the annealing and to protect during transfer in air. From a first time, the structural properties (size, morphology, composition, crystallographic structure) of these nanoparticles were investigated in order to directly correlate the modification of the magnetic properties to the structure and chemical ordering of the nanoparticles after high temperature treatment. In addition to the bimetallic FeCo nanoparticles, reference Fe and Co systems were also fabricated and studied using the same techniques. The structural properties were investigated using high resolution transmission electron microscopy (HRTEM), anomalous x-ray diffraction (AXD) and extended x-ray absorption fine structure (EXAFS) where a phase transition from a disordered A2 phase to a chemically ordered CsCl B2 phase was observed and further validated from the magnetic findings using SQUID magnetometry and x-ray magnetic circular dichroism (XMCD).

Keywords : nanoparticle, magnetic anisotropy, ordering, iron-cobalt, HRTEM, AXD, EXAFS, SQUID. XMCD.

Discipline : Physics.

Name and adresse of the laboratory :
Institute Lumière Matière
UMR 5306 Université Lyon 1-CNRS
F-69622 Villeurbanne Cedex

Titre : Propriétés magnétiques et structurales d'assemblées de nanoparticules de FeCo triées en taille.

Résumé : La recherche sur les nanostructures n'a cessé de croître au cours de ces dernières années. En particulier, de grands espoirs sont basés sur l'utilisation possible de nanoparticules, objets situés à la frontière entre les agrégats moléculaires et l'état massif, dans les différents domaines des nanosciences. Mais à cette échelle, les phénomènes physiques ne sont pas encore bien compris. Les nanoparticules magnétiques sont mises en avant pour leurs applications potentielles dans les dispositifs d'enregistrement denses, plus récemment dans le domaine médical, mais aussi comme catalyseur de nombreuses réactions chimiques.
Dans ce travail, nous nous sommes intéressés aux propriétés magnétiques intrinsèques (moments et anisotropie magnétiques) de nanoparticules bimétalliques fer-cobalt. Pour cela, des agrégats FeCo dans la gamme de taille 2-6 nm ont été préparés en utilisant la technique MS-LECBD (Mass Selected Low Energy Cluster Beam Deposition) et enrobés en matrice $in-situ$ afin de les séparer, d'éviter leur coalescence pendant les recuits et de les protéger à leur sortie à l'air. Dans un premier temps, les propriétés structurales (dispersion de taille, morphologie, composition, structure cristallographique) ont été étudiées en vue de corréler directement les modifications des caractéristiques magnétiques des nanoparticules, à leur structure et à l'ordre chimique obtenu après traitement thermique haute température. D'autre part, pour mettre en évidence les effets d'alliages à cette échelle, des références d'agrégats purs de fer et de cobalt ont été fabriquées et étudiées en utilisant les mêmes techniques. Par microscopie électronique en transmission à haute résolution, diffraction anomale et absorption de rayons X (high resolution transmission electron microscopy (HRTEM), anomalous x-ray diffraction (AXD) and extended x-ray absorption fine structure (EXAFS), nous avons mis en évidence un changement structural depuis une phase A2 chimiquement désordonnée vers une phase B2 type CsCl chimiquement ordonnée. Cette transition a été validée par nos résultats obtenus par magnétomètrie SQUID et dichroïsme magnétique circulaire (x-ray magnetic circular dichroism (XMCD)).

Mots-clés : nanoparticules, anisotropie magnétique, ordre chimique, fer-cobalt, METHR, AXD, EXAFS, SQUID, XMCD.

Discipline : Physique.

Intitulé et adresse du laboratoire :
Institute Lumière Matière
UMR 5306 Université Lyon 1-CNRS
F-69622 Villeurbanne Cedex

PUBLICATIONS

1. **Low Temperature Ferromagnetism in Chemically Ordered FeRh Nanocrystals.**
Hillion A., Cavallin A., Vlaic S., Tamion A., Tournus F., Khadra G., Dresier J., *et al*.
Physical Review Letters, **2013** *110, 087207*.

2. **Mixing Patterns and Redox Properties of Iron-based Alloy Nanoparticles under Oxidation and Reduction Conditions.**
Papaefthimiou V., Tournus F., Hillion A., Khadra G., Teschner D., Knop-Gericke A., *et al*.
Chemistry of Materials, **2014** *26, 1553-1560*.

3. **Anisotropy in FeCo nanoparticles , a first step**
Khadra. G., Tamion. A., Tournus F., Canut B., Dupuis V.
Solid State Phenomena, **2015** *233-234, 550-553*.

4. **Magnetic moments in chemically ordered mass-selected CoPt and FePt clusters.**
Dupuis V., Khadra G., Linas S., Hillion A., Gragnaniello L., Tamion A., *et al*.
Journal of Magnetism and Magnetic Materials, **2015** *383, 73-77*.

5. **Intrinsic magnetic properties of bimetallic nanoparticles elaborated by cluster beam deposition.**
Dupuis V., Khadra G., Hillion A., Tamion A. Tuaillon-Combes J., Bardotti L. Tournus F.
Physical Chemistry Chemical Physics, *accepted* **2015**.

6. **Temperature-dependent evolution of the oxidation state of cobalt and platinum in Co1-xPtx bimetallic clusters under H2 and CO + H2 atmosphere.**
Yang B., Khadra G., Tuaillon-Combes J., Tyo E., Seifert S., Chen X., Dupuis V., Vajda S.
Physical Chemistry Chemical Physics, *accepted* **2015**.

TABLE OF CONTENTS

List of figures **xix**

List of tables **xxxi**

Introduction **1**

1 Motivation **3**

1.1 Nanoalloys 3

1.2 State of the art of FeCo system 5

1.2.1 Bulk phase 5

1.2.2 Thin films 8

1.2.3 Nanoparticles 10

2 Synthesis and experimental techniques **13**

2.1 Synthesis technique 13

2.1.1 The nucleation chamber 13

2.1.2 Classic source 14

2.1.3 Mass selected source 15

2.1.4 Clusters deposition 16

2.2 Morphology and composition 17

2.2.1 Transmission Electron Microscopy 18

2.2.2 EDX and RBS 19

2.3 Synchrotron techniques 21

2.3.1 X-ray Absorption Spectra (XAS) 22

2.3.2 Extended X-ray Absorption Fine Structure (EXAFS) 24

2.3.2.1 Basic principle 24

2.3.2.2 Experimental setup 25

2.3.2.3 Data treatment 27

2.3.2.3.1 Pre-edge subtraction 27

2.3.2.3.2 Edge step 28
2.3.2.3.3 Background removal 29
2.3.2.3.4 FEFF calculations 31
2.3.2.3.5 Fitting procedure 33
2.3.2.3.6 Path parameters 33
2.3.3 X-ray Magnetic Circular Dichroism (XMCD) 34
2.3.3.1 Basic Principle 34
2.3.3.2 Experimental setup 36
2.3.3.3 Data treatment 37
2.3.3.3.1 Normalization and XMCD signals 38
2.3.3.3.2 XAS and step function 38
2.3.3.3.3 Integrated signals 39
2.3.3.3.4 Sum rules 40
2.3.4 Anomalous Scattering 40
2.3.4.1 Basic Principle 40
2.3.4.2 Experimental Setup 42
2.3.4.3 Simulation 44
2.4 SQUID magnetometry 44
2.4.1 Basic principle 44
2.4.2 Model 46
2.4.2.1 Notations 46
2.4.2.2 Energy sources 47
2.4.2.3 Stoner-Wohlfarth macrospin model 50
2.4.2.4 Superparamagnetism 54
2.4.2.5 Nanoparticle assembly 55
2.4.3 Data treatment 56
2.4.3.1 Magnetization curves 57
2.4.3.2 Magnetic susceptibility curves 58
2.4.3.2.1 ZFC-FC protocol 59
2.4.3.2.2 Analytical expressions of the ZFC-FC curves . 60
2.4.3.3 Triple-fit procedure 61
2.4.4 Hysteresis loops (low temperature) 62
2.4.4.1 Uniaxial anisotropy of the second order 64
2.4.4.2 Biaxial anisotropy of the second order 67
2.4.4.3 Superparamagnetic contribution 69
2.4.5 Remanence measurements 72

2.4.5.1 IRM-DcD background 72
2.4.5.2 Analytical expressions 75
2.4.5.2.1 Expressions at zero temperature 75
2.4.5.2.2 Temperature integration 77
2.4.5.2.3 Size distribution 78
2.4.5.2.4 Anisotropy constant distribution 80
2.4.5.2.5 Case of biaxial anisotropy 81

3 Structure and morphology of nanoparticle assemblies embedded in a matrix 83
3.1 Structure and morphology of the nanoparticles 83
3.2 Size distribution of clusters 88
3.3 Size and composition 88
3.3.1 Neutral clusters 88
3.3.1.1 Lognormal distribution 88
3.3.1.2 Morphology 90
3.3.1.3 Composition 90
3.3.2 Mass-selected clusters 94
3.3.2.1 Gaussian distribution 94
3.3.2.2 Size histograms 94
3.3.2.2.1 Pure clusters 94
3.3.2.2.2 As-prepared FeCo clusters 96
3.3.2.2.3 Annealed FeCo clusters 98
3.4 High resolution transmission electron microscopy 100
3.4.1 As-prepared nanoparticles 100
3.4.2 Annealed nanoparticles 101
3.5 Anomalous scattering spectroscopy 102
3.5.1 Simulation 102
3.5.2 Experiment 104
3.6 EXAFS spectroscopy 106
3.6.1 Bulk metallic foil references 106
3.6.2 Neutral clusters 108
3.6.3 Iron carbide 115
3.6.4 Mass-selected clusters 118
3.6.4.1 Pure clusters 119
3.6.4.1.1 Fe system 119
3.6.4.1.2 Co system 120
3.6.4.2 Bimetallic FeCo clusters 123

3.6.4.2.1 As-prepared 123
3.6.4.2.2 Annealed 125
3.6.4.2.3 FeCo 3.7 nm / FeCo 4.3 nm 127
3.6.4.2.4 FeCo 6.1 nm 132
3.7 Discussion 136

4 Magnetic properties of nanoparticle assemblies embedded in a matrix 139
4.1 Magnetic properties of neutral clusters 139
4.1.1 10 % - Concentrated clusters 141
4.1.2 1 % - Diluted clusters 144
4.1.2.1 Pure clusters 145
4.1.2.2 Bimetallic clusters 153
4.2 Spin and orbital moments of size-selected clusters 156
4.2.1 Pure clusters 157
4.2.1.1 Co clusters 157
4.2.1.2 Fe clusters 161
4.2.2 Bimetallic clusters 165
4.2.2.1 $FeCo_{3.7}$ 165
4.2.2.2 $FeCo_{4.3}$ 166
4.2.2.3 $FeCo_{5.8}$ 167
4.2.2.4 $FeCo_{6.1}$ 168
4.2.2.5 Magnetization curves 173
4.2.2.6 Saturation magnetization 174
4.3 SQUID magnetometry of size-selected clusters 177
4.3.1 Pure Fe clusters 177
4.3.1.1 $Fe_{4.4}$ clusters 177
4.3.1.2 $Fe_{6.1}$ clusters 179
4.3.2 Bimetallic clusters 181
4.3.2.1 $FeCo_{3.7}$ clusters 182
4.3.2.2 $FeCo_{4.3}$ clusters 184
4.3.2.3 $FeCo_{6.1}$ clusters 186
4.3.3 Copper matrix 188
4.3.3.1 $FeCo^{Cu}{}_{4.3}$ clusters 190
4.3.3.2 $FeCo^{Cu}{}_{6.1}$ clusters 192
4.4 Discussion 195

General conclusion 201

References **205**

LIST OF FIGURES

1.1 Slater-Pauling curve showing the mean atomic moment for a variety of binary nanoalloys as a function of their composition [13]. 5
1.2 FeCo bulk alloy phase diagram. 6
1.3 Schematics of a chemically ordered CsCl-B2 phase FeCo unit cell. 7
1.4 Calculated uniaxial MAE K_u and saturation magnetic moment μ_s of tetragonal $Fe_{1-x}Co_x$ as a function of the c/a ration and the Co concentration x [27]. 8
1.5 Stability contour plot of high K_u materials in open circles, with the maximum uniaxial MAE for FeCo in closed circle. The dotted line is the 40 Gbits/in^2 stability boundary [30], for a write field of 0.5100 Tesla and 12 nm grains. . 9

2.1 Geometry of the laser evaporation nucleation source. 14
2.2 Diagram of the classic source of cluster fabrication by the LECBD technique. 15
2.3 3D representation of the mass selected cluster source made by C. Albin. . . 16
2.4 Two types of 3D samples: (a) Multi-layered samples; (b) co-deposited samples 17
2.5 Schematic representation of the different electron interactions with a sample. 18
2.6 Absorption coefficient versus photon energy; individual absorption thresholds are marked 22
2.7 Emission of a core level electron due to the absorption of an X-ray photon . 23
2.8 X-ray absorption measurement in which the resonance energy coincides with the bonding energy of a core electron. 25
2.9 Sketch of a Monochromator 26
2.10 Analyzed sample and the detector system. 26
2.11 FeRh example of pre-edge subtraction 28
2.12 Example of normalized absorption spectrum obtained on annealed FeRh nanoparticles. 29
2.13 Example of the $\chi(k)$ function obtained on annealed FeRh nanoparticles. . . 30
2.14 Example of the $\chi(k)k^3$ function obtained on annealed FeRh nanoparticles. . 31

2.15 Path of a photoelectron during propagation in a crystal. 32
2.16 The "two step" model of the XMCD at the L_2 edge for transition metals. The absorption of circularly polarized X-rays depends on the relative direction between the propagation vector and the direction of the local magnetization. 35
2.17 Schematic view and modes of operation of an APPLE-II undulator. 37
2.18 Example of a normalized XAS left and right polarized signals, and XMCD difference signal. 38
2.19 Averaged XAS left and right polarized signals and the two-step function. . . 39
2.20 Integrated white line function and XMCD signal. 40
2.21 Dispersion corrections as a function of the atomic number Z of Copper Cu Kα radiation. 42
2.22 Schematics of the Kappa Goniometer used at the D2am beamline at the ESRF. 43
2.23 Schematics of a SQUID magnetometer detection loop. 45
2.24 Reducing the magnetostatic energy by the creation of domain walls. 50
2.25 Schematic representation of (Left) a macrospin in an external magnetic field,(Right) a superparamagnetic potential well at different magnetic fields. 51
2.26 An example of solution for the Stoner-Wolhfarth model for two positions of easy magnetization. The continuous line represents the positions of the energy minimum; the dashed line, the local energy minima. The energy profiles for three different applied magnetic fields are represented. 52
2.27 Magnetization curves for the Stoner-Wohlfarth model for various angles ϕ between the applied field direction and the easy axis. 53
2.28 Diagram of the Stoner-Wohlfarth astroid in two dimensions. 54
2.29 $m(H)$ at 300 K for Cobalt nanoparticles in a gold matrix. The curve can be fitted with several size distributions as is shown in insert. 58
2.30 Example of a sample of FeRh nanoparticles embedded in a carbon matrix. These curves present the schematic transition from a blocked to superparamagnetic state around T_{max}. 59
2.31 ZFC-FC susceptibility curves for a sample of Cobalt in gold matrix. The red curve corresponds to the triple fit. The two other curves correspond to the fitting based on the size distributions of figure 2.29. The insert present the size distributions deduced from the triple fit and TEM observations. 62
2.32 Hysteresis loop at 0 K in the Stoner-Wohlfarth model for an assembly of three dimensional particles having randomly oriented uniaxial anisotropies (left). An example of hysteresis loops at low temperature (2 K) for an assembly of Co nanoparticles embedded in a Cu matrix (right). 63

2.33 System of axes used in the calculations. The easy magnetization axis is along z direction. 64
2.34 Simulation of hysteresis loops at 2, 4, 6, 8, 10 and 12 K in the case of a uniaxial anisotropy without (a) and with a size distribution (b); in the case of a biaxial anisotropy $|K_2/K_1| = 0.5$ without (c) and with a size distribution (d). 66
2.35 Numeric simulation of hysteresis loops at 0 K in the uniaxial case ($K_2 = 0$) (black) and biaxial ($|K_2/K_1| = 0.5$) (red). The corresponding astroids are shown in insert. 68
2.36 Example of a fit for the hysteresis loop at 2 K of an as-prepared non mass-selected Co nanoparticles sample. 71
2.37 Schematic representation of the IRM measurement. 73
2.38 IRM, DcD and Δm curves calculated at $T = 0$ K for an assembly of randomly oriented uniaxial macrospins. 75
2.39 Numerical simulation of an IRM curve at 0 K (right) for a 3D assembly of uniaxial macrospins deduced from the switching field H_{sw} (left). 77
2.40 Simulated IRM curve, at 2 K, for an assembly of particles with a Gaussian size distribution with a mean diameter of 4 nm (left) and 2.5 nm (right) with a dispersion of 8%, as well as for a single size. 78
2.41 Simulated IRM curve at 2 K, normalized with respect to m_r, for an assembly of particles with a Gaussian size distribution. (Left) The effect of changing the mean diameter: D_m takes the values of 2.5, 3, 4, 5 and 8 nm successively while the relative dispersion is fixed to ω = 20 %. (Right) The effect of changing the relative dispersion: ω takes the values 1 %, 8 %, 20 % and 50 % while D_m is fixed to 3 nm. 79
2.42 Comparison of IRM curves for the couples (K_{eff},V) and ($K_{eff}/2$,$2V$). . . . 80
2.43 Simulated IRM curve at 2 K for a particle assembly of a 3 nm diameter with a Gaussian anisotropy constant distribution $\rho(K_{eff})$ centered at 120 kJ.m^{-3} and for different relative dispersions $\omega(K)$. 80
2.44 Simulated IRM curves at 0 K in the case of uniaxial ($K_2 = 0$) (black) and biaxial ($|K_2/K_1| = 0.5$) (red) anisotropies. The corresponding astroids are presented in insert. 81

3.1 Stable shape for a face centered cubic: truncated octahedron (a) and a body centered cubic: rhombic dodecahedron (b). 85
3.2 Schematic representation of N = 65 atoms clusters having different central atoms. 87

3.3 Evolution of the interatomic distances of Fe-Fe, Co-Co and Fe-Co as a function of size from SIESTA calculations. 87
3.4 (Left) TEM image of non mass-selected (neutral) Co (a), Fe (b) and FeCo (c) nanoparticles protected by a thin carbon film. (Right) Size histogram deduced from TEM observations as well as its best fit obtained using a lognormal distribution. 89
3.5 EDX spectrum for a FeCo nanoparticle. 91
3.6 RBS with the corresponding fit for an annealed neutral FeCo sample. 91
3.7 Reflectivity measurements and fit for a sample composed of 5 carbon layers with an evaporator distance of 70 mm. A simple model of 5 carbon layers with the density of carbon of 2.25 g/cm^3 and rugosity of 8 ± 1 Å was used for the fit. 92
3.8 TEM images for mass-selected (a, b) Co and (c, d) Fe nanoclusters and their corresponding size histogram for two voltage deviations, 150 V and 300 V. 95
3.9 TEM images for mass-selected FeCo nanoparticles obtained under deposition conditions for deviation voltages of (a) 75 V, (b) 150 V, (c) 300 V, (d) 450 V, (e) 600 V and (f) 1200 V; (g) and (h) represent nanoparticles for deviation voltages of 300 V and 450 V respectively obtained with a gas mixture of Argon and Helium. 97
3.10 TEM images for annealed mass-selected FeCo nanoparticles at 500°C for 2 hours for deviation voltages of (a) 300 V and (b) 600 V, and their corresponding size histogram as well as that of the size histogram for the as-prepared particles of the same deviation in dotted line. 99
3.11 HRTEM images for as-prepared FeCo nanoparticles for deviation voltages of (a) 300 V and (b) 600 V. 100
3.12 HRTEM images for annealed FeCo nanoparticles for deviation voltages of (a) 150 V, (b) 300 V and (c) 600 V along with their corresponding FFT. . . 101
3.13 Anomalous scattering coefficients $f'(E)$ and $f''(E)$ for Fe, Co and Rh elements as a function of photon energy (and wavelength). 103
3.14 Simulated X-ray scattering curves for CsCl-B2 phase (a) FeRh and (b) FeCo systems for different nanoparticle sizes. 103
3.15 Measured X-ray scattering spectrum for 600 V deviated FeCo annealed at 500°C with the corresponding fits of the peak. 105
3.16 Normalized absorption spectra of (a) bcc Fe and (b) hcp Co bulk reference foils. 107

3.17 Radial distribution of EXAFS oscillations for (a) bcc Fe and (b) hcp Co bulk reference foils. 107
3.18 EXAFS oscillations of (a) bcc Fe and (b) hcp Co bulk reference foils as well as their corresponding fits. 107
3.19 Radial distribution of EXAFS oscillations for (left) Fe:K edge and (right) Co:K edge for as-prepared (blue line) and annealed (red line) neutral FeCo samples. 109
3.20 EXAFS oscillations for as-prepared (left) and annealed (right) neutral FeCo nanoparticles at the Fe:K-edge with their corresponding best fits. 110
3.21 EXAFS oscillations for as-prepared (left) and annealed (right) neutral FeCo nanoparticles at the Co:K-edge with their corresponding best fits. 111
3.22 A chemically ordered B2 phase CsCl unit cell for two different species of atoms. 113
3.23 Phase diagram for Co-C alloy as a function of temperature and atomic composition. 115
3.24 Phase diagram for Fe-C alloy as a function of temperature and atomic composition. 116
3.25 Simulated radial distributions of EXAFS oscillations for the iron carbide systems for a Debye-Waller factor of 0.000 (light solid line) and Debye-Waller factor of 0.010 (thick solid line). 117
3.26 Radial distributions of EXAFS oscillations of the as-prepared and annealed $Fe_{4.4}$ nanoparticles. 119
3.27 EXAFS oscillations for as-prepared (left) and annealed (right) pure $Fe_{4.4}$ nanoparticles at the Fe:K-edge with their corresponding best fits. 120
3.28 Radial distributions of EXAFS oscillations of the as-prepared and annealed $Co_{3.4}$ nanoparticles. 121
3.29 EXAFS oscillations for as-prepared (left) and annealed (right) pure $Co_{3.4}$ nanoparticles at the Co:K-edge with their corresponding best fits. 122
3.30 The simulations of the XANES signal for 1.6 nm Fe and FeCo (B2) nanoparticles (performed by Yves Joly, Institut Néel Grenoble) show the difficulties to distinguish a bcc from a CsCl-B2 phase. 123
3.31 The normalized XAS signal (left) and Radial Distributions of EXAFS oscillations (right) for the as-prepared $FeCo_{3.7}$, $FeCo_{4.3}$ and $FeCo_{6.1}$ samples at the Fe:K-edge. 124

3.32 The normalized XAS signal (left) and Radial Distributions of EXAFS oscillations (right) for the as-prepared $FeCo_{3.7}$, $FeCo_{4.3}$ and $FeCo_{6.1}$ samples at the Co:K-edge. 124
3.33 The normalized XAS signal (left) and Radial Distributions of EXAFS oscillations (right) for the annealed $FeCo_{3.7}$, $FeCo_{4.3}$ and $FeCo_{6.1}$ samples at the Fe:K-edge. 125
3.34 The normalized XAS signal (left) and Radial Distributions of EXAFS oscillations (right) for the annealed $FeCo_{3.7}$, $FeCo_{4.3}$ and $FeCo_{6.1}$ samples at the Co:K-edge. 126
3.35 The radial distributions of EXAFS oscillations for the annealed $FeCo_{6.1}$ nanoparticles sample at both Fe and Co K-edges, and for the Fe metallic foil at the Fe K-edge. 127
3.36 Radial Distributions of EXAFS oscillations for as-prepared (blue) and annealed (red) $FeCo_{3.7}$ nanoparticles at the Fe:K-edge (left) and Co:K-edge (right). 128
3.37 Radial Distributions of EXAFS oscillations for as-prepared (blue) and annealed (red) $FeCo_{4.3}$ nanoparticles at the Fe:K-edge (left) and Co:K-edge (right). 129
3.38 EXAFS oscillations for as-prepared (left) and annealed (right) $FeCo_{4.3}$ nanoparticles at the Fe K-edge with their corresponding best fits. 130
3.39 EXAFS oscillations for as-prepared (left) and annealed (right) $FeCo_{4.3}$ nanoparticles at the Co K-edge with their corresponding best fits. 131
3.40 Radial Distributions of EXAFS oscillations for as-prepared (blue) and annealed (red) $FeCo_{6.1}$ nanoparticles at the Fe:K-edge (left) and Co:K-edge (right). 132
3.41 EXAFS oscillations for as-prepared (left) and annealed (right) $FeCo_{6.1}$ nanoparticles at the Fe K-edge with their corresponding best fits. 134
3.42 EXAFS oscillations for as-prepared (left) and annealed (right) $FeCo_{6.1}$ nanoparticles at the Co K-edge with their corresponding best fits. 135

4.1 ZFC-FC curves at 5 mT for the (left) as-prepared and (right) annealed samples, and the $m(H)$ at $T = 200$ K are presented in insert. 141
4.2 IRM/DcD curves at 2 K for the (left) as-prepared and (right) annealed samples and their corresponding Δm. 142
4.3 Visual representation of a simulation of the sample before (left) and after annealing (right). The top representations are viewed with an oblique angle while the bottom ones are a cross-sectional view. 143

4.4 Visual representation of a simulation of the sample before (left) and after annealing (right) viewed from an oblique angle. 143

4.5 (Left) Size distribution of the as-prepared and coalesced samples. (Right) ZFC of the as-prepared and annealed samples alongside the simulated ZFC curves. 144

4.6 (a) ZFC/FC and $m(H)$ experimental data for neutral as-prepared Co clusters along with their best fits; (b) IRM experimental data with the corresponding biaxial contribution simulation; (c) IRM/DcD curves with the Δm; (d) hysteresis loop at 2 K along with the corresponding simulation. 145

4.7 (a) ZFC/FC and $m(H)$ experimental data for neutral annealed Co clusters along with their best fits; (b) IRM experimental data with the corresponding biaxial contribution simulation; (c) IRM/DcD curves with the Δm; (d) hysteresis loop at 2 K along with the corresponding simulation; the dashed line is the as-prepared experimental data. 146

4.8 Neutral Co nanoparticles size histogram obtained from TEM observations along with the corresponding fit, as well as the two size distributions obtained from the triple-fit of the as-prepared and annealed neutral Co samples. . . . 147

4.9 (a) ZFC/FC and $m(H)$ experimental data for neutral as-prepared Fe clusters along with their best fits; (b) IRM experimental data with the corresponding biaxial contribution simulation; (c) IRM/DcD curves with the Δm; (d) hysteresis loop at 2 K along with the corresponding simulation. 149

4.10 (a) ZFC/FC and $m(H)$ experimental data for neutral annealed Fe clusters along with their best fits; (b) IRM experimental data with the corresponding biaxial contribution simulation; (c) IRM/DcD curves with the Δm; (d) hysteresis loop at 2 K along with the corresponding simulation; the dashed line is the as-prepared experimental data. 150

4.11 (Left) Core-shell nanoparticle model; (Right) homogeneous nanoparticle model; from F. Calvo [210] 152

4.12 (a) ZFC/FC and $m(H)$ experimental data for neutral as-prepared FeCo clusters along with their best fits; (b) IRM experimental data with the corresponding biaxial contribution simulation; (c) IRM/DcD curves with the Δm; (d) hysteresis loop at 2 K along with the corresponding simulation. 153

4.13 (a) ZFC/FC and $m(H)$ experimental data for neutral annealed FeCo clusters along with their best fits; (b) IRM experimental data with the corresponding biaxial contribution simulation; (c) IRM/DcD curves with the Δm; (d) hysteresis loop at 2 K along with the corresponding simulation; the dashed line is the as-prepared experimental data. 154
4.14 XMCD signal at 2 K at the $L_{2,3}$ Co edge for the as-prepared (left) and annealed (right) mass-selected $Co_{2.9}$ nanoparticles. 158
4.15 XMCD signal at 2 K at the $L_{2,3}$ Co edge for the as-prepared (left) and annealed (right) mass-selected $Co_{3.4}$ nanoparticles. 158
4.16 Hysteresis loops of $Co_{2.9}$ (left) and $Co_{3.4}$ (right) nanoparticles measured by XMCD at the Co:L_3-edge at 2 K. 159
4.17 Magnetization curves of $Co_{2.9}$ (left) and $Co_{3.4}$ (right) nanoparticles measured by XMCD at the Co:L_3-edge at 300 K. 160
4.18 XMCD signal at 2 K at the $L_{2,3}$ Fe edge for the as-prepared (left) and annealed (right) mass-selected $Fe_{3.3}$ nanoparticles. 161
4.19 XMCD signal at 2 K at the $L_{2,3}$ Fe edge for the as-prepared (left) and annealed (right) mass-selected $Fe_{4.4}$ nanoparticles. 162
4.20 Hysteresis loops of $Fe_{3.3}$ (left) and $Fe_{4.4}$ (right) nanoparticles measured by XMCD at the Fe:L_3-edge at 2 K. 163
4.21 Magnetization curves of $Fe_{3.3}$ (left) and $Fe_{4.4}$ (right) nanoparticles measured by XMCD at the Fe:L_3-edge at 300 K. 163
4.22 XMCD signal at 2 K at the Co (top) and Fe (bottom) $L_{2,3}$ edges for the as-prepared (left) and annealed (right) mass-selected $FeCo_{3.7}$ nanoparticles. 165
4.23 XMCD signal at 2 K at the Co (top) and Fe (bottom) $L_{2,3}$ edges for the as-prepared (left) and annealed (right) mass-selected $FeCo_{4.3}$ nanoparticles. 166
4.24 XMCD signal at 2 K at the Co (top) and Fe (bottom) $L_{2,3}$edges for the as-prepared (left) and annealed (right) mass-selected $FeCo_{5.8}$ nanoparticles. 167
4.25 XMCD signal at 2 K at the Co (top) and Fe (bottom) $L_{2,3}$edges for the as-prepared (left) and annealed (right) mass-selected $FeCo_{6.1}$ nanoparticles. 168
4.26 Plot for the evolution of the spin magnetic moment at the Co (left) and Fe (right) edges for the FeCo samples before and after annealing along with the results for the pure samples and the bulk values. 169
4.27 Plot for the evolution of the orbital magnetic moment at the Co (left) and Fe (right) edges for the FeCo samples before and after annealing along with the results for the pure samples and the bulk values. 170

4.28 (Left) Surface atom vacancies substituted by impurities (C or O) and (Right) impurities added in interstitial position between surface atoms. 171

4.29 Calculated average moment for Fe and Co atoms with the substitution of three C/O atoms in the vacancy positions for $Co_{15}Fe_{41}$ (Left) and $Co_{41}Fe_{15}$ (right) (in collaboration with Aguilera-Granja *et al*., private comm.). 172

4.30 Calculated average moment for Fe and Co atoms with the addition of three C/O atoms in interstitial position for $Co_{15}Fe_{44}$ (Left) and $Co_{44}Fe_{15}$ (right) (in collaboration with Aguilera-Granja *et al*., private comm.). 172

4.31 Hysteresis loops of $FeCo_{3.7}$, $FeCo_{4.3}$ and $FeCo_{6.1}$ nanoparticles measured by XMCD at the Co (Left) and Fe (right) L_3-edges at 2 K. 173

4.32 Magnetization curves of $FeCo_{3.7}$, $FeCo_{4.3}$, $FeCo_{5.8}$ and $FeCo_{6.1}$ nanoparticles measured by XMCD at the Co (Left) and Fe (right) L_3-edges at 300 K. 173

4.33 (a) ZFC/FC and $m(H)$ experimental data for mass-selected as-prepared $Fe_{4.4}$ clusters along with their best fits; (b) IRM experimental data with the corresponding biaxial contribution simulation; (c) IRM/DcD curves with the Δm; (d) hysteresis loop at 2 K along with the corresponding simulation. . . 177

4.34 (a) ZFC/FC and $m(H)$ experimental data for mass-selected annealed $Fe_{4.4}$ clusters along with their best fits; (b) IRM experimental data with the corresponding biaxial contribution simulation; (c) IRM/DcD curves with the Δm; (d) hysteresis loop at 2 K along with the corresponding simulation; the dashed line is the as-prepared experimental data. 178

4.35 (a) ZFC/FC and $m(H)$ experimental data for mass-selected as-prepared $Fe_{6.1}$ clusters along with their best fits; (b) IRM experimental data with the corresponding biaxial contribution simulation; (c) IRM/DcD curves with the Δm; (d) hysteresis loop at 2 K along with the corresponding simulation. . . 180

4.36 Susceptibility curves for mass-selected $FeCo_{3.7}$, $FeCo_{4.3}$ and $FeCo_{6.1}$ before and after annealing. 181

4.37 (a) ZFC/FC and $m(H)$ experimental data for mass-selected as-prepared $FeCo_{3.7}$ clusters along with their best fits; (b) IRM experimental data with the corresponding biaxial contribution simulation; (c) IRM/DcD curves with the Δm; (d) hysteresis loop at 2 K along with the corresponding simulation. 182

4.38 (a) ZFC/FC and $m(H)$ experimental data for mass-selected annealed $FeCo_{3.7}$ clusters along with their best fits; (b) IRM experimental data with the corresponding biaxial contribution simulation; (c) IRM/DcD curves with the Δm; (d) hysteresis loop at 2 K along with the corresponding simulation; the dashed line is the as-prepared experimental data. 183

4.39 (a) ZFC/FC and $m(H)$ experimental data for mass-selected as-prepared $FeCo_{4.3}$ clusters along with their best fits; (b) IRM experimental data with the corresponding biaxial contribution simulation; (c) IRM/DcD curves with the Δm; (d) hysteresis loop at 2 K along with the corresponding simulation. 184

4.40 (a) ZFC/FC and $m(H)$ experimental data for mass-selected annealed $FeCo_{4.3}$ clusters along with their best fits; (b) IRM experimental data with the corresponding biaxial contribution simulation; (c) IRM/DcD curves with the Δm; (d) hysteresis loop at 2 K along with the corresponding simulation; the dashed line is the as-prepared experimental data. 185

4.41 (a) ZFC/FC and $m(H)$ experimental data for mass-selected as-prepared $FeCo_{6.1}$ clusters along with their best fits; (b) IRM experimental data with the corresponding biaxial contribution simulation; (c) IRM/DcD curves with the Δm; (d) hysteresis loop at 2 K along with the corresponding simulation. 186

4.42 (a) ZFC/FC and $m(H)$ experimental data for mass-selected annealed $FeCo_{6.1}$ clusters along with their best fits; (b) IRM experimental data with the corresponding biaxial contribution simulation; (c) IRM/DcD curves with the Δm; (d) hysteresis loop at 2 K along with the corresponding simulation; the dashed line is the as-prepared experimental data. 187

4.43 Binary phase diagram of Fe-Cu. 189

4.44 Binary phase diagram of Co-Cu. 189

4.45 (a) ZFC/FC and $m(H)$ experimental data for mass-selected as-prepared $FeCo^{Cu}{}_{4.3}$ clusters embedded in Cu matrix along with their best fits; (b) IRM experimental data with the corresponding biaxial contribution simulation; (c) IRM/DcD curves with the Δm; (d) hysteresis loop at 2 K along with the corresponding simulation. 190

4.46 ZFC/FC curves for $FeCo^{Cu}{}_{4.3}$ nanoparticles embedded in copper matrix and annealed at a range of temperatures from 250°C to 500°C. 192

4.47 (a) ZFC/FC and $m(H)$ experimental data for mass-selected as-prepared $FeCo^{Cu}{}_{6.1}$ clusters embedded in Cu matrix along with their best fits; (b) IRM experimental data with the corresponding biaxial contribution simulation; (c) IRM/DcD curves with the Δm; (d) hysteresis loop at 2 K along with the corresponding simulation. 193
4.48 ZFC/FC curves for $FeCo^{Cu}{}_{6.1}$ nanoparticles embedded in copper matrix before and after annealing at 500°C under UHV. 194
4.49 Evolution of the shape anisotropy K_1 as a function of the ellipsoid c/a ratio for the two values of saturation magnetization $M_s = 1100$ kA/m and 1650 kA/m. 200

LIST OF TABLES

2.1 Dispersion corrections values (in electrons) for a few elements for Copper Cu Kα radiation. 42
2.2 Cobalt and iron magnetic parameters at ambient temperature [98]. 51

3.1 Interatomic distances, magnetic moments and number of holes obtain for FeCo CsCl-B2 phase clusters with three different sizes depending on the central atom (see figure 3.2). 86
3.2 Average value and dispersion of the particles' sphericity (major to minor axis ratio). 90
3.3 Thickness of the carbon layer corresponding to the distance of the evaporator from the sample. 92
3.4 Mean diameter and dispersion of mass-selected Co and Fe nanoparticles for two voltage deviations, 150 V and 300 V. 96
3.5 Mean diameter and sphericity and their corresponding dispersion of mass-selected FeCo nanoparticles for voltage deviations between 150 V and 1200 V. 96
3.6 Mean diameter and dispersion of annealed mass-selected FeCo nanoparticles at 500°C for 2 hours for voltage deviations of 300 V and 600 V, as well as their corresponding sphericity values and its dispersion. 99
3.7 Values obtained for the Scherrer diameter ($D_{Scherrer}$) as well as the peak position and width for the X-ray scattering spectrum. 105
3.8 Fitting parameters for the bcc Fe (first and second neighbours) and hcp Co bulk-reference foils. 108
3.9 Values obtained the for best fits of the EXAFS oscillations for as-prepared and annealed neutral FeCo nanoparticles at the Fe:K-edge. 110
3.10 Values obtained for the best fits of the EXAFS oscillations for as-prepared and annealed neutral FeCo nanoparticles at the Co:K-edge. 111
3.11 Fe-C carbides, their composition, space group and lattice parameters. 116

3.12 Fe-C distances expected for the different carbides. 117
3.13 List of mass-selected FeCo, Co and Fe samples. 118
3.14 Values obtained for the best fits of the EXAFS oscillations for as-prepared and annealed pure $Fe_{4.4}$ nanoparticles at the Fe:K-edge. 120
3.15 Values obtained for the best fits of the EXAFS oscillations for as-prepared and annealed pure $Co_{3.4}$ nanoparticles at the Co:K-edge. 122
3.16 Values obtained for the best fits of the EXAFS oscillations for as-prepared and annealed $FeCo_{4.3}$ nanoparticles at the Fe K-edge. 130
3.17 Values obtained for the best fits of the EXAFS oscillations for as-prepared and annealed $FeCo_{4.3}$ nanoparticles at the Co K-edge. 131
3.18 Values obtained for the best fits of the EXAFS oscillations for as-prepared and annealed $FeCo_{6.1}$ nanoparticles at the Fe:K-edge. 134
3.19 Values obtained for the best fits of the EXAFS oscillations for as-prepared and annealed $FeCo_{6.1}$ nanoparticles at the Co:K-edge. 135
3.20 Ratio of the NN distances (R_1/R_2) after annealing for the neutral and mass-selected 6.1 nm FeCo nanoparticles. 137

4.1 List of neutral samples measured in this section. 140
4.2 Maximums of the ZFC (T_{max}), coercive field ($\mu_0 H_C$) and the deduced parameters from the adjustment of the SQUID measurements for neutral Co nanoparticles embedded in C matrix as-prepared and after annealing as well as the percentage of superparamagnetic magnetic signal at saturation for the low temperature hysteresis loop fit. 146
4.3 Maximums of the ZFC (T_{max}), coercive field ($\mu_0 H_C$) and the deduced parameters from the adjustment of the SQUID measurements for neutral Fe nanoparticles embedded in C matrix as-prepared and after annealing in addition to the percentage of SP contribution for the 2 K hysteresis loop. . . 150
4.4 Maximums of the ZFC (T_{max}), coercive field ($\mu_0 H_C$) and the deduced parameters from the adjustment of the SQUID measurements for neutral FeCo nanoparticles embedded in C matrix as-prepared and after annealing in addition to the percentage of SP contribution for the 2 K hysteresis loop. . . 154
4.5 List of mass-selected FeCo, Co and Fe samples. 157
4.6 Orbital and spin moments of the Co atoms before and after annealing for two nanoparticle sizes, $Co_{2.9}$ and $Co_{3.4}$. 159
4.7 Orbital and spin moments of the Fe atoms before and after annealing for two nanoparticle sizes, $Fe_{3.3}$ and $Fe_{4.4}$. 162

4.8 Orbital and spin moments of the FeCo samples before and after annealing for the four nanoparticle sizes, $FeCo_{3.7}$, $FeCo_{4.3}$, $FeCo_{5.8}$ and $FeCo_{6.1}$. . . . 169

4.9 Saturation magnetization of the Co and Fe samples before and after annealing for all the nanoparticle sizes, $Co_{2.9}$, $Co_{3.4}$, $Fe_{3.3}$ and $Fe_{4.4}$. 175

4.10 Saturation magnetization of the FeCo samples before and after annealing for the four nanoparticle sizes, $FeCo_{3.7}$, $FeCo_{4.3}$, $FeCo_{5.8}$ and $FeCo_{6.1}$. 175

4.11 Maximums of the ZFC (T_{max}), coercive field ($\mu_0 H_C$) and the deduced parameters from the adjustment of the SQUID measurements for mass-selected $Fe_{4.4}$ nanoparticles embedded in C matrix as-prepared and after annealing in addition to the percentage of SP contribution for the 2 K hysteresis loop. . . 178

4.12 Maximums of the ZFC (T_{max}), coercive field ($\mu_0 H_C$) and the deduced parameters from the adjustment of the SQUID measurements for as-prepared mass-selected $Fe_{6.1}$ nanoparticles embedded in C matrix in addition to the percentage of SP contribution for the 2 K hysteresis loop. 180

4.13 Maximums of the ZFC (T_{max}), coercive field ($\mu_0 H_C$) and the deduced parameters from the adjustment of the SQUID measurements for mass-selected $FeCo_{3.7}$ nanoparticles embedded in C matrix as-prepared and after annealing in addition to the percentage of SP contribution for the 2 K hysteresis loop. 183

4.14 Maximums of the ZFC (T_{max}), coercive field ($\mu_0 H_C$) and the deduced parameters from the adjustment of the SQUID measurements for mass-selected $FeCo_{4.3}$ nanoparticles embedded in C matrix as-prepared and after annealing in addition to the percentage of SP contribution for the 2 K hysteresis loop. 185

4.15 Maximums of the ZFC (T_{max}), coercive field ($\mu_0 H_C$) and the deduced parameters from the adjustment of the SQUID measurements for mass-selected $FeCo_{6.1}$ nanoparticles embedded in C matrix as-prepared and after annealing in addition to the percentage of SP contribution for the 2 K hysteresis loop. 187

4.16 Maximums of the ZFC (T_{max}), coercive field ($\mu_0 H_C$) and the deduced parameters from the adjustment of the SQUID measurements for as-prepared mass-selected $FeCo^{Cu}{}_{4.3}$ nanoparticles embedded in Cu matrix in addition to the percentage of SP contribution for the 2 K hysteresis loop. 190

4.17 Maximums of the ZFC (T_{max}), coercive field ($\mu_0 H_C$) and the deduced parameters from the adjustment of the SQUID measurements for as-prepared mass-selected $FeCo^{Cu}{}_{6.1}$ nanoparticles embedded in Cu matrix in addition to the percentage of SP contribution for the 2 K hysteresis loop. 193

4.18 Anisotropy constants obtained from the magnetic measurements and simulated values from the shape, with a c/a ratio of 1.65 for the $FeCo_{6.1}$ and 1.47 for the $FeCo_{4.3}$ as-prepared nanoparticles samples (see table 3.5). 199

INTRODUCTION

Over the past few decades, use of nanostructures for the miniaturization of electrical components, creating new tools for medical diagnosis or even in the fields of pharmacology and cosmetics has become quite indispensable and industrially backed. Nanoparticles, in particular, are situated between the molecular level and bulk matter size. This size range gave rise to a wide variety of physical phenomena that are still not quite yet understood. In fact, for nanometric particles, the number of atoms present at the surface of these particles is very high and depending on the size of the particles, the percentage of surface atoms can reach higher quantities than its core ones. In addition, having a finite number of atoms, adding or removing an atom can have a huge impact on the different properties of these nanoparticles. In particular, magnetic nanoparticles are the origin of a great number of studies.

Magnetic nanoparticles are at their hype due to their applications in medical field (MRI application as contrast agents, treating of hyperthermia, as well as their recent incorporation in the targeted treatment of cancerous cells), as a catalyst in a wide number of chemical reactions, in addition to their use for information storage devices and spintronics. Among the current technologies, the domain of spintronics attracts a lot of attention for the promise of fabricating the ultimate storage ”bit”, where a single nanoparticle sees a single atom. The reading and writing of such a system requires the complete understanding of its magnetic properties. Such studies were performed on single nanoparticles using a micro-SQUID magnetometer. The next step is to reproduce the measurements of the intrinsic properties of nanoparticles as part of nanoparticle assemblies in order to advance a next step towards actual applications.

In this PhD work, we are interested in studying the intrinsic magnetic properties of FeCo nanoparticles. Thus, in order to completely understand their properties mass-selected FeCo nanoparticles fabricated using the MS-LECBD (Mass Selected Low Energy Cluster Beam Deposition) technique was used to fabricate FeCo nanoparticles having different sizes in the range of 2-6 nm. From a first time, the structural properties (size, morphology, composition, crystallographic structure) of these nanoparticles were investigated in order to directly correlate the modification of the magnetic properties to the structure of the nanoparticles.

In addition to the bimetallic FeCo nanoparticles, reference Fe and Co systems were also fabricated and studied using the same techniques.

This manuscript is divided into four chapters:

- In the first chapter, the main motivation for magnetic nanoparticles, specifically bimetallic FeCo nanoparticles, are presented and discussed.
- Chapter two is dedicated to introducing the fabrication technique and the different characterization techniques used throughout chapters three and four. In addition, chapter two includes all the used models for the characterization of our nanoparticles.
- In chapter three, the different experimental results for the structural properties are presented and discussed for non mass-selected as well as mass-selected FeCo and reference nanoparticles before and after annealing.
- The fourth chapter is devoted to the magnetic characterization of our bimetallic FeCo and reference nanoparticles before and after annealing.

CHAPTER 1

MOTIVATION

Clusters or nanoparticles are aggregates having between a few to millions of atoms or molecules. These particles are the limit between molecular complexes and the bulk materials. They can consist of identical atoms, molecules, of two or more different species. They can be studied in a number of media, such as molecular beams, the vapor phase, colloidal suspension and isolated in inert matrices or on surfaces.

Interest in magnetic clusters arises, in part, because they constitute a new type of material which may have properties that are distinct from those of individual atoms, molecules or bulk matter. From a fundamental point of view, the effects that emerge from the small size of the system, in particular surface effects, are the reason for a large number of studies. The interest in clusters is the size-dependent evolution of their properties, such as their crystalline structure. In fact, both the geometric shape and energetic stability of clusters may drastically change with size. This enthusiasm is also linked to their enormous application potential in areas such as the transfer and storage of magnetic information, catalysis, energy, biotechnology and medical diagnostics (magnetic resonance imaging, hyperthermia, *etc.*). Indeed, because of their size in the nanometer range, they are now considered as building blocks used in the framework of the bottom-up approach to nanotechnology.

1.1 Nanoalloys

The constant miniaturization of the electronic and biomedical equipment has allowed, over the last few decades, to reach the nanoscale. At the nanoscale, different nanometric object geometries are manifested: thin films (2D), nanofilaments (1D) and nanoparticles (0D). In this work, we are solely interested in the last category. The studied magnetic nanoparticles are made up of assemblies of metallic atoms in the 2 - 6 nm range. Their atomic and electronic properties depend on their size and derive from the fact that these present an

intermediary evolution between the two extreme states of matter, atoms and bulk materials, due to their high surface-to-volume ratios which in turns results in the emergence of new physical (magnetic, optical, *etc.*) and chemical (surface reactivity, catalysis, *etc.*) properties.

From recording media to medical application, there is constant need for the miniaturization of magnetic materials. Whether it is to increase the areal density of hard disk drives to accommodate more information or to have functionalized bio-compatible MRI contrast agents for various medical diagnosis, the race for miniaturizing magnetic materials has witnessed staggering amounts of research and publications. State of the art research on magnetic nanoparticles is constantly on going focusing on data storage [1–3], sensing [3–7], drug delivery [8, 9], MRI [10], hyperthermia [11], ... In order to achieve the different research goals in the different scientific fields that rely on the novel properties of magnetic nanoparticles, it is necessary to understand, control and tune the magnetic properties of such systems [12].

From a physics point of view, simply scaling down the size of magnetic materials from the bulk to nanoparticles has created a wide range of unique properties, and at the same time it has brought up critical limitations. For nanoparticle systems, the superparamagnetic limit, *i.e.* the ratio of magnetic energy per particle grain $\Delta E = KV$, where K is the anisotropy of a particle and V is its volume, equivalent to the thermal energy $k_B T$, has been reached. At this limit, thermal fluctuations rule over the behaviour of these particles. These fluctuations occur in a time frame of a few nanoseconds causing the particles to continually switch magnetization direction thus effectively limiting their magnetic properties. Overcoming the superparamagnetic limit of magnetic nanoparticles is constantly being researched.

The magnetic anisotropy energy of these particles (KV) represents the energy barrier that blocks these particles in one direction of magnetization or another. In order to overcome the superparamagnetic limit, either larger particles need to be used or particles with a higher value of magnetic anisotropy. On the other hand, increasing the anisotropy of nanoparticles would, for magnetic storage applications, require large writing fields (H_{sw}) *i.e.* the magnetic field necessary to switch the magnetization of the particle from one direction to another. The switching field is proportional to the ratio of the anisotropy to the magnetization. Thus, it is possible to minimize the switching field by using materials with a high magnetic anisotropy K value provided they have a large saturation magnetization M_s ($H_{sw} \propto K/M_s$).

From the Slater-Pauling curve [13], presented in figure 1.1, the bimetallic FeCo system has the highest recorded magnetic moment per atom and thus the largest saturation magnetization. Nevertheless, FeCo is well known to be a soft ferromagnet.

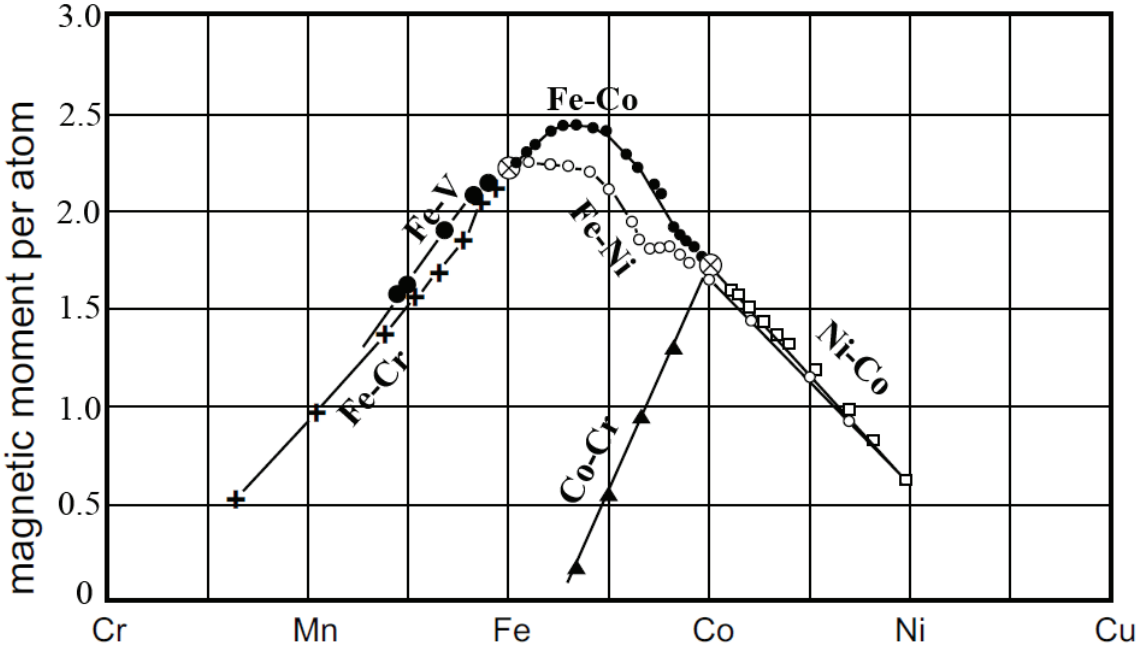

Fig. 1.1 Slater-Pauling curve showing the mean atomic moment for a variety of binary nanoalloys as a function of their composition [13].

1.2 State of the art of FeCo system

1.2.1 Bulk phase

Despite having a large saturation magnetization, FeCo has a cubic structure at ambient temperature [14]. Due to this symmetry FeCo has a low magnetocrystalline anisotropy, and is thus considered as a soft magnet [14]. Nevertheless, soft magnetic materials are important for a wide variety of applications, with applications ranging from power generation and distribution, actuators, magnetic shielding, data storage, microwave communications [15].

The binary FeCo phase diagram is shown in figure 1.2 taken from [16]. From Raynor *et al*. [17], at ambient temperatures, the intermetallic compound FeCo (α) is stable in the range of 29-70 at.-%Co. The B2 (CsCl) structure of FeCo is an ordered bcc structure can be viewed as two interpenetrating simple cubic sub-lattices in which the Fe atom occupies one sub-lattice and the Co atom occupies the other sub-lattice (see figure 1.3). The α phase undergoes an order-disorder transformation when heated to high temperatures. The variation in the degree of long-range order with temperature of FeCo bulk alloys was studied by

specific heat measurements [18], theoretical calculations [19, 20] and by X-ray [21] and neutron diffraction techniques [22]. At 900°C iron transforms into the face-centered cubicγ phase, and at 1400°C into the δ phase which has the same structure as the α phase. At about 400°C cobalt transforms, on heating, from the ε phase (hexagonal structure) into the γ phase. The FeCo binary alloy exhibits a high Curie temperature (T_C) of $T_C = 920 - 985$°C depending on the Co concentration [14]. The slash-dotted line indicates the Curie point, at which the material becomes paramagnetic.

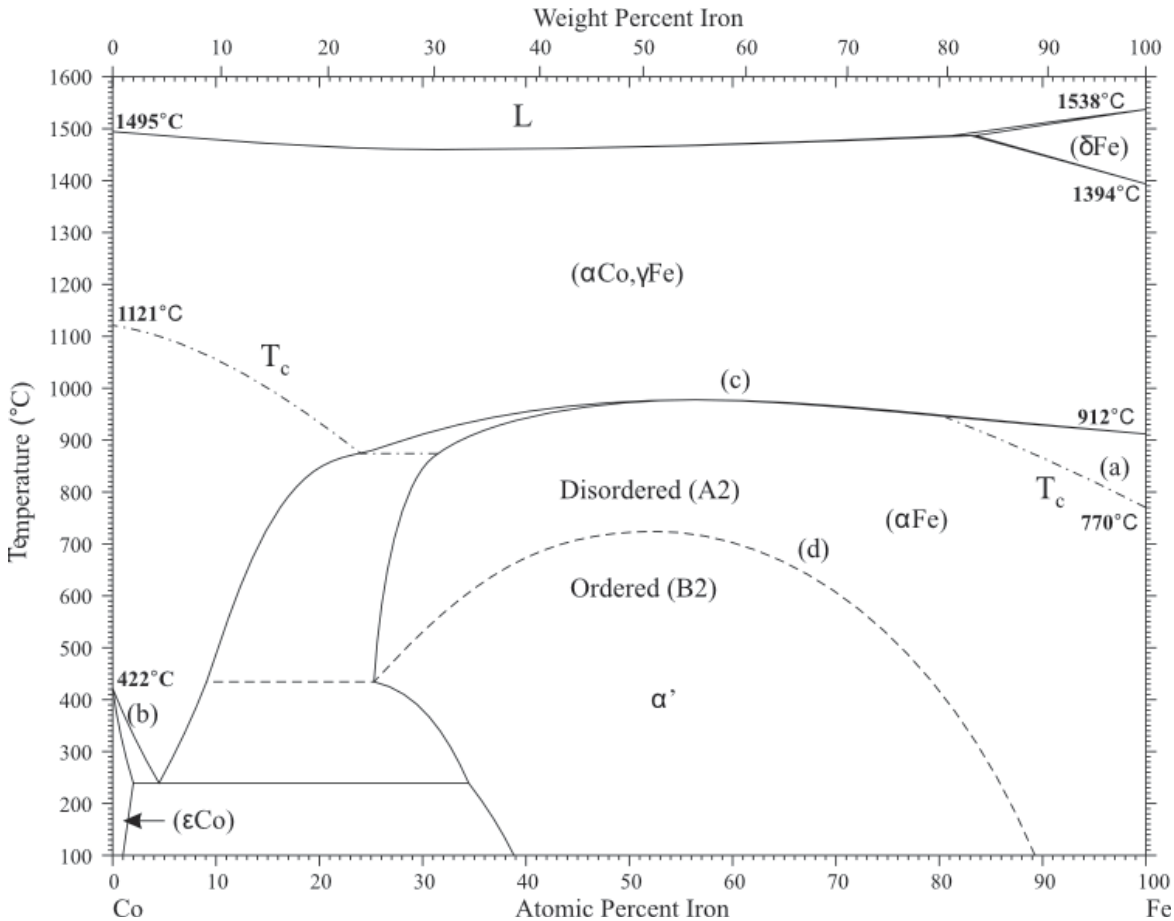

Fig. 1.2 FeCo bulk alloy phase diagram.

In addition, figure 1.2 shows several changes that affect the magnetic properties of FeCo. At (a) the material becomes paramagnetic on heating, without change in phase. At (b) there is a change of phase, with both phases being magnetic. At (c) there is a change from a ferromagnetic to a paramagnetic phase due to by-passing of the Curie temperature (T_C) and the change of phase. The line (d) represents the ordered-disordered phase transformation with both phases being magnetic.

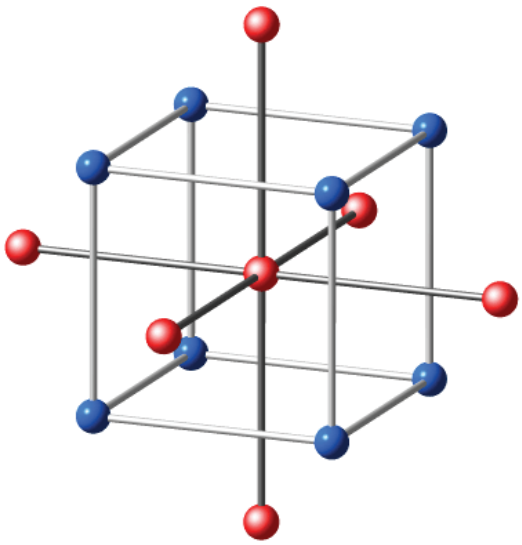

Fig. 1.3 Schematics of a chemically ordered CsCl-B2 phase FeCo unit cell.

The $Fe_{1-x}Co_x$ bulk alloy is ferromagnetic, at ambient temperatures, for all x [23], and its saturation magnetization increases with x in the range of $x \in [0, 0.4]]$ (see figure 1.1) because the magnetic moment of Fe increases whereas that of Co remains almost constant [23, 24]. The maximum saturation magnetization (M_s) of the $Fe_{1-x}Co_x$ bulk alloy occurs at x = 0.28 [25], $M_s = 1982$ kA/m with an average magnetic moment $m_j = 2.457$ μ_B/atom. For an equiatomic $Fe_{1-x}Co_x$ alloy, the average magnetic moment $m_j = 2.425$ μ_B/atom, with $M_s = 1912$ kA/m. The bcc cell length for FeCo bulk alloys is reported to be 2.868 Å [26].

1.2.2 Thin films

A novel generation of soft magnetic materials was made possible by the development of thin film growth and their heteroepitaxy on monocrystalline structures. Burkert *et al.*, as well as Turek *et al.*, predict using first-principles theory that very specific structural distortions of a FeCo alloy leads to not only a large saturation magnetization M_s but also a large uniaxial magnetic anisotropy energy (MAE) K_u [27, 28]; they argue how breaking the cubic symmetry of the FeCo binary alloy increases the MAE by several orders of magnitude. The uniaxial MAE was calculated for a tetragonal $Fe_{1-x}Co_x$ for the whole concentration range. Using virtual crystal approximation (VCA), the MAE of ordered $Fe_{0.5}Co_{0.5}$ in the tetragonally distorted CsCl structure was calculated for different values of c/a ratios. Figure 1.4 shows the plot for the uniaxial MAE and saturation magnetic moment per atom μ_s of tetragonal $Fe_{1-x}Co_x$ as a function of the c/a ratio and the Co concentration x.

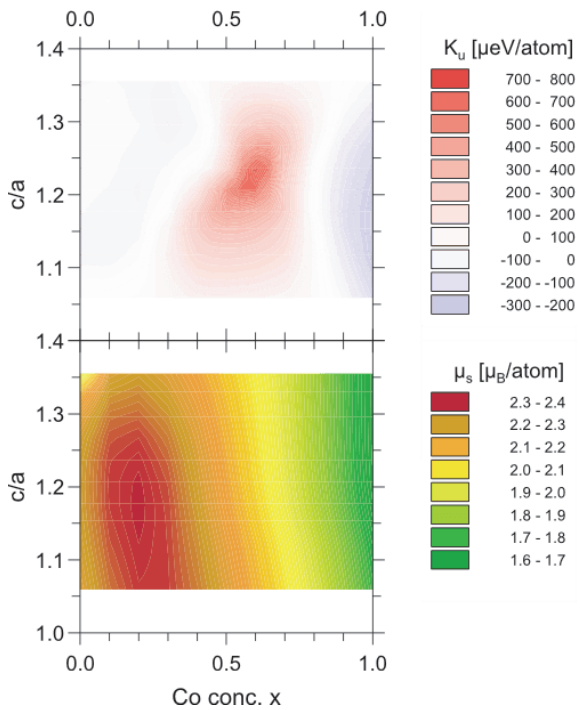

Fig. 1.4 Calculated uniaxial MAE K_u and saturation magnetic moment μ_s of tetragonal $Fe_{1-x}Co_x$ as a function of the c/a ration and the Co concentration x [27].

To compare the calculated MAE and saturation magnetic moment of the FeCo alloys shown in figure 1.4 to other high K_u materials, Burkert *et al.* [27] included their calculated values for $c/a = 1.2$ to that of Weller *et al.* [29] and Charap *et al.* [30] in figure 1.5.

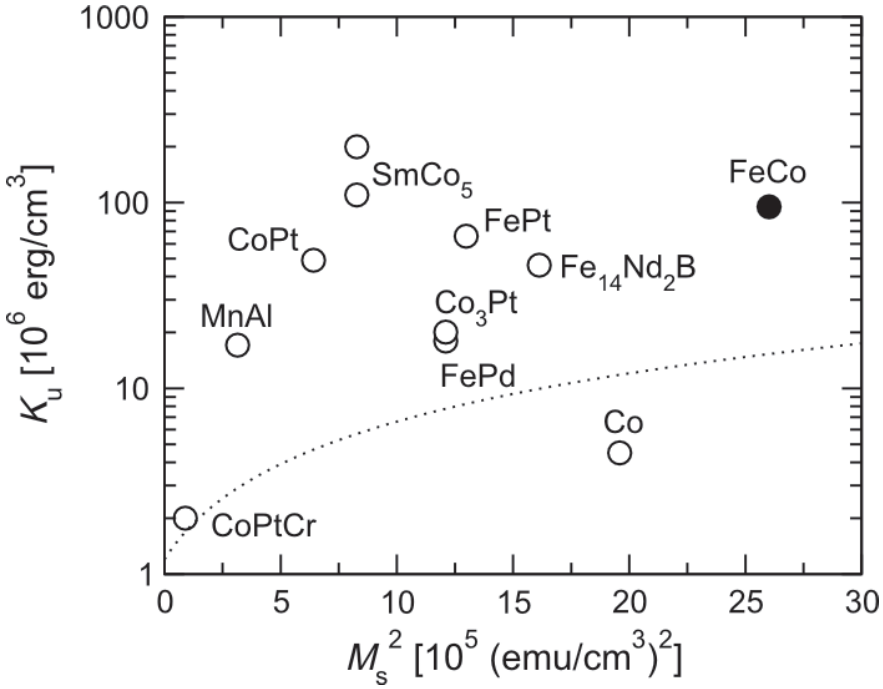

Fig. 1.5 Stability contour plot of high K_u materials in open circles, with the maximum uniaxial MAE for FeCo in closed circle. The dotted line is the 40 Gbits/in^2 stability boundary [30], for a write field of 0.5100 Tesla and 12 nm grains.

For a c/a ratio of 1.20-1.25 and 60% Co, the MAE increases in magnitude to reach a value of the order of 700-800 $\mu eV/atom$. Moreover, Burkert *et al*. suggests growing of tetragonally distorted FeCo alloys by epitaxial growth to achieve the desired c/a ratio. If thin films of Fe [31] and Co [32] are grown on Rh(100), c/a ratios of 1.16 and 1.19, respectively, are obtained. Using Pd(100) as the substrate, the corresponding values are 1.11 for Fe [33] and 1.15 for Co [34].

Sun *et al*. studied the effect of annealing on FeCo alloy films [35]. They report improved soft magnetic properties after annealing in magnetic field; annealing with a field applied along the easy magnetization axis showed a reduced coercivities along both the easy axis and hard axis, whereas annealing along the hard axis caused a switched easy and hard axis in these films for annealing temperatures above 255°C. Furthermore, they report that a reduction of the tensile stress after annealing which in turns facilitates the integration of FeCo films into magnetic recording heads.

On the other hand, density functional theory calculations were performed on the structural and magnetic properties of FeCo alloys doped by carbon [36]. They report a stable tetragonal distortion in a wide range of cobalt concentrations, which translates to an enhancement of the MAE well above that of elemental iron, cubic cobalt or FeCo bulk alloys reaching values of

740 kJ/m^3 and a reduced average moment per atom of $m_j = 1.94$ μ_B/atom for a composition of $(Fe_{0.35}Co_{0.64})_{24}C$ with a c/a ratio of 1.036.

In addition to the previous studies, FeCo-based alloys are also an important subject of research. Among the most studied FeCo-based alloys are FeCoC alloys. FeCoC granular thin films are studied as soft magnetic layer in order to obtain a low noise double-layered perpendicular recording media, as reported by Soo *et al.* [37]. The underlayer was co-sputtered at room temperature and showed very good soft magnetic properties that can be varied by adjusting the C concentration. Edon *et al.* also studied the effects of adding carbon to FeCo alloyed thin films by sputtering [38]. They report a change in the crystalline structure as the carbon content in the film was increased that was accompanied by a large decrease of the saturation magnetization from $M_s = 1974$ kA/m to $M_s = 414$ kA/m.

Gautam *et al.* studied the influence of the controlled addition of Co on the electronic structure and magnetic properties of FeCo-based ribbons [39]. They observe that Co atoms, at ambient temperature, tend to bond with other present elements in the random/amorphous matrix rather than with the Fe atoms, while Fe atoms remain metallic. Moreover, they report an average magnetic moment for the Fe atoms of $m_j{}^{Fe} = 0.94$ μ_B/atom for a $Fe_{80}Co_{20}$ composition.

1.2.3 Nanoparticles

In addition to the large number of publications available for the bulk and thinfilm FeCo alloys, there is also quite a number of publications on FeCo nanoparticle sample. Most of these studies focus on chemically prepared nanoparticles [40–46]. However, there are fewer publications on FeCo nanoparticles prepared using physical means [47–50].

Kim *et al.* synthesized FeCo nanoparticles by co-precipitation chemical method [40]. They obtained 20 nm Fe_7Co_3 nanocrystallite were annealed for 1 hour at 800°C and achieved a high saturation magnetization of $M_s = 1687$ kA/m. Shin *et al.* also used the co-precipitation technique to prepare FeCo nanoparticles under varying reaction times [41]. Their particles had a larger size of around 35 nm and achieved a saturation of $M_s = 1212$ kA/m. Chaubey *et al.* studied FeCo nanoparticles prepared by the reductive decomposition of organometallic precursors in the presence of surfactants [42]. They report a $M_s = 1712$ kA/m for 20 nm particles compared to $M_s = 1057$ kA/m for the 10 nm ones. Lacroix *et al.* examined the magnetic hypothermia properties of 14 nm sized monodisperse FeCo nanoparticles prepared using an organometallic synthesis technique [43]. Self organized 20 nm FeCo monodisperse nanoparticles were synthesized by thermal decomposition by Desvaux *et al.* [44]. Their obtained nanoparticles showed M_s values ranging between $1300 - 1500$ kA/m. Using a hydrothermal process, Lee *et al.* elaborate the synthesis of 7 nm core-shell FeCo particles

[45]. They obtain a large value of $M_s = 1884$ kA/m for nanoparticles with a ratio of 60/40 of Fe/Co. Poudyal *et al*. obtained monodisperse FeCo nanoparticles with sizes of 8, 12 and 20 nm by reductive salt-matrix annealing [46]. They report an increase of the magnetization with the increase of the particle diameter.

Dong *et al*. demonstrates the formation of FeCo and FeCo(C) nanocapsules by an electric arc discharge method [47]. Happy *et al*. used pulsed laser ablation deposition to study the effects of the deposition parameters on the size and morphology of FeCo nanoparticles [48]. They report an increase in the particle size by increasing the gas pressure due to higher collision frequency in the growth stage. Ong *et al*. also studied the synthesis of FeCo particles using pulsed laser deposition [49]. They report a change in the particle's morphology from linear interconnected chains formed by diffusion limited aggregation processes to dense fibrous structures when the number of laser pulses is increased. The magnetic properties of 10 nm mass-filtered Fe and FeCo nanoparticles prepared under ultra-high vacuum conditions by an arc cluster ion source and soft-landed on W(110) surface were investigated by Kleibert *et al*. [50]. Their particles show a uniaxial magnetic anisotropy with the magnetic hard axis being perpendicular to the surface plane.

Interestingly, a number of publications study FeCo nanoparticles as a nanocatalyst in the formation of carbon nanotubes (CNT) [51, 52]. In addition, a few articles discuss the effects of using transition metals (Fe, Co and Ni) and their alloys on the formation of CNT from simulations and calculations [53–55] and from chemically synthesized nanoparticle catalysts [56].

In chapter 2, we describe the synthesis technique as well as the experimental ones used to study our systems. In chapters 3 and 4 we present and discuss the structural and magnetic data, respectively, obtained for the Fe, Co and FeCo non mass-selected and mass-selected followed by a general conclusion and perspectives.

In addition to the work presented in the manuscript, all published and accepted research papers are included as back matter at the end of the manuscript.

CHAPTER 2

SYNTHESIS AND EXPERIMENTAL TECHNIQUES

2.1 Synthesis technique

The nanoparticles studied in this work were synthesized by a bottom-up technique using the "Plateforme LYonnaise de Recherche sur les Agrégats" (PLYRA) by the Low Energy Cluster Beam Deposition (LECBD) technique. Contrary to most nanoparticle studies, this synthesis method is by physical means using laser vaporization source, rather than chemical means. The generators are divided into two parts: the first part is a conventional vacuum nanoparticle nucleation chamber, and the second part is an ultra-high vacuum (UHV) chamber dedicated to the deposition and eventually $in-situ$ sample characterization.

2.1.1 The nucleation chamber

The nucleation chamber used for the synthesis of nanoparticles is presented in figure 2.1. The particle formation is achieved in three steps: [57–59]

- A pulsed Nd:YAG laser hits the considered target rod. The laser has an energy of around 20-50 mJ with a frequency of 10 Hz and a wavelength of 532 nm. The laser, focused with the help of converging lenses, vaporizes a few μm^2 of the target rod resulting in a partially ionized plasma gas of clusters. The target rod is kept moving, using a mechanical system of motors, in a helical motion to avoid rapid deterioration.

- The plasma formed at the target's surface is then subjected to an ultra-fast quenching through the continuous injection of a carrier gas (Helium). The helium gas is at an ambient temperature and a pressure of around 30 mbar. This induces the nucleation of the particles.

- Finally, the mixture of carrier gas and clusters undergoes an adiabatic supersonic expansion as it passes the outlet. Pressure drops rapidly, collisions become rare and the nucleation process of clusters ceases. A skimmer, knife-edged structure, is placed near the outlet to direct the beam of clusters and to limit the presence of helium in the following ultra-high vacuum chamber.

This technique is highly adapted for our study. Indeed it allows the laser evaporation of any material, even the most refractory. In addition, it presents the high advantage of conserving the composition of the target rod, which is particularly interesting for the synthesis of alloys.

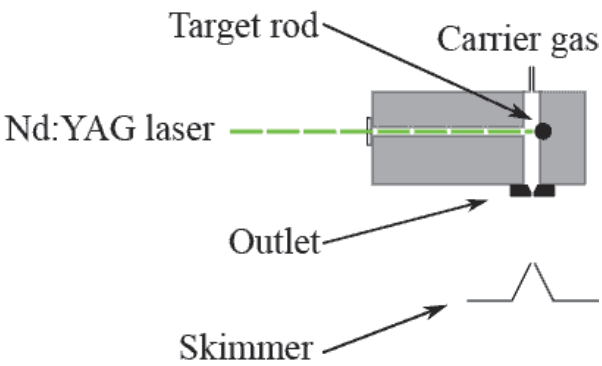

Fig. 2.1 Geometry of the laser evaporation nucleation source.

2.1.2 Classic source

The nucleation chamber is located in a primary vacuum chamber $\sim 10^{-7}$ mbar that raises during deposition, due to the injection of the carrier gas, to $\sim 10^{-4}$ mbar. A second higher vacuum chamber is situated behind the skimmer to create a vacuum gradient until the UHV portion (10^{-9} - 10^{-10} mbar and raises to 10^{-8} during deposition). The deposition chamber has a manipulator allowing to orient the substrate either to face the jet of nanoparticles or at an angle of 45° to co-deposit simultaneously the clusters with a matrix evaporated with an electron gun (see figure 2.2). Several in-situ characterization techniques are attached to the UHV chamber such as an XPS analyzer (and / or Auger), a UHV furnace, a UHV STM, *etc*.

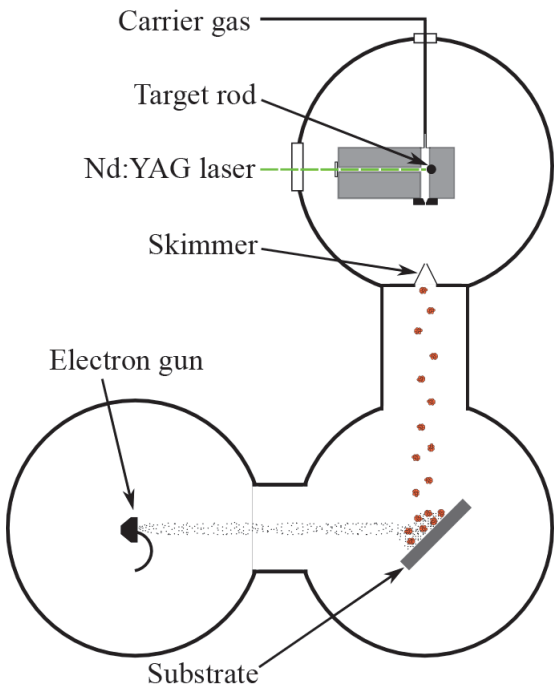

Fig. 2.2 Diagram of the classic source of cluster fabrication by the LECBD technique.

2.1.3 Mass selected source

The study of nanometric objects requires to have the narrowest possible size distribution to shed light on their size effects. For this purpose, a second cluster generator was developed for the PLYRA enabling the selection of charged particles [59–61] (see figure 2.3). Thus, in this generator, the second chamber after the skimmer contains an electrostatic quadrupole deviator. The deviator consists of four electrodes of the same hyperbolic geometry and polarized alternatively $\pm U$, coupled with horizontal and vertical slit lenses for beam shaping. The electrodes arranged vertically select a slice of the ions produced in the cluster beam having an energy:

$$E_{electrostatic} = E_{kinetic} \quad \text{thus} \quad eU = mv^2/2 \tag{2.1}$$

with m the mass of the cluster, v its speed, e the elementary charge of an electron (we consider that the produced ionized clusters possess one charge $\pm\, e$) and U the voltage of the deviator electrodes. Based on the measurements carried out on Platinum clusters [62], the speed can be considered as a constant and equal to around 550 m.s^{-1}. The selection of the kinetic energy is thus equivalent to the mass selection given by:

$$m = 2eU/v^2 \tag{2.2}$$

Contrary to the classic source, the deposition rate with the mass selected source is rather significantly low since the generator only produces 3 to 5% of positively or negatively charged clusters that are then deviated by the quadrupole.

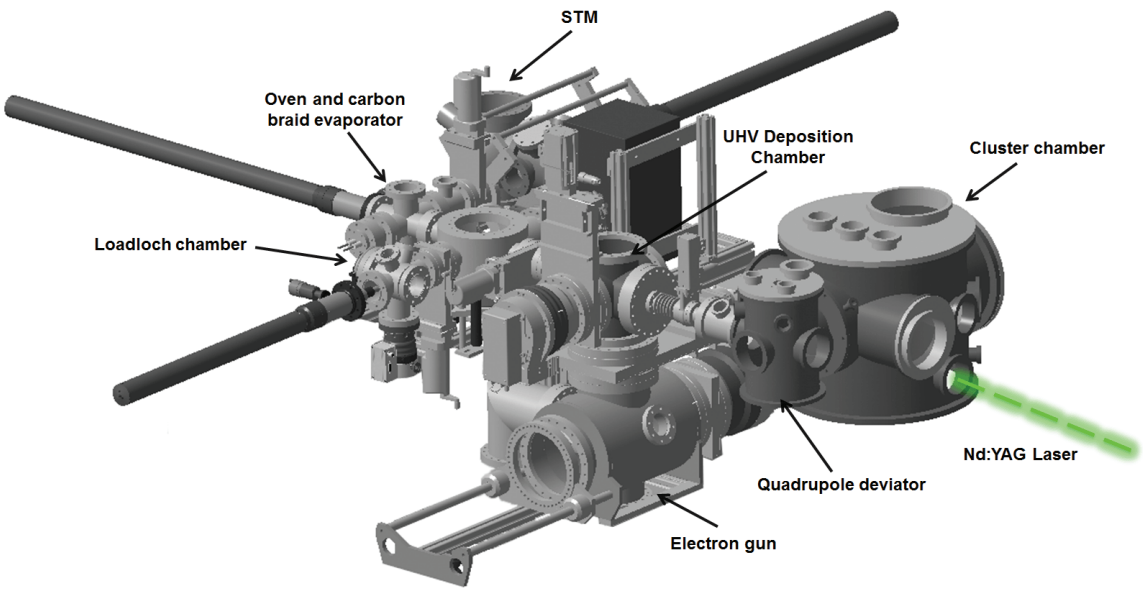

Fig. 2.3 3D representation of the mass selected cluster source made by C. Albin.

The classic source and the mass selected source are both equipped with an electron gun evaporator under UHV with four crucibles to have a large array of matrix choices. Another method to protect the nanoparticles is the evaporation of carbon braids directly in front of the sample.

2.1.4 Clusters deposition

After the skimmer of the deposition chamber, the clusters continue towards a substrate where they are soft landed on the surface with very little energy thus avoiding any fragmentation. The choice of substrate is dictated by the studies we wish to achieve. Clusters are deposited on substrates suitable for the different means of characterization. For transmission electron microscopy (TEM) measurements, thin samples are needed (2D Samples). On the other hand, some experiments require a more important amount of deposited material because of their detection limit (3D Samples). For these samples, a monocrystalline Silicon substrate is used for deposition of the matrix and clusters. It is possible to create two different types of 3D samples (see figure 2.4).

2D Samples Ultra-fine commercial grids are used consisting of a copper grid coated with first a pierced carbon film and then a thin layer of amorphous carbon of about 2 nm thick. On these grids a discontinuous layer of clusters is deposited coated with an amorphous carbon layer to prevent oxidation and pollution by transferring into air.

3D Samples Samples for SQUID magnetometry measurements or some synchrotron radiation experiments require a certain amount of materials. Thus, two types of samples are fabricated to avoid excessive crowding between nanoparticles (to avoid interactions or coalescence during annealing):

- A multi-layered structure or «mille-feuilles». This type of structure achieves a sufficient equivalent thickness with a large enough distance between the different nanoparticles. It is fabricated by first depositing a matrix layer to cover the surface of the Silicon substrate, then by alternatively depositing a discontinuous layer of clusters followed by a thick layer of the matrix used (around 2 nm).
- A co-deposition 3D structure. The matrix deposition is simultaneous with the deposition of clusters (the sample is placed in a 45° position, see figure 2.2). A quartz microbalance allows monitoring the rate of deposition of the matrix continuously. An electron gun is used to evaporate various matrices (C, Cu, Nb . . .). By controlling the rate of deposition of the clusters and adjusting the rate of evaporation of the matrix it is possible to control the concentration of the clusters in the samples and obtain the very diluted desired samples ($\sim$ 1% vol.).

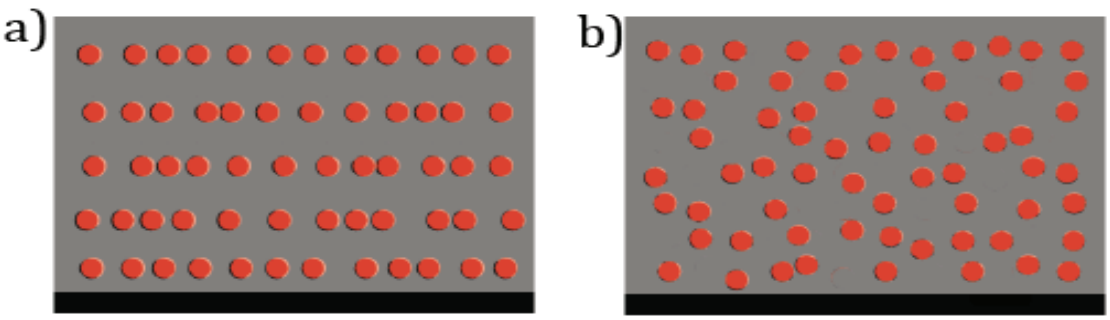

Fig. 2.4 Two types of 3D samples: (a) Multi-layered samples; (b) co-deposited samples

2.2 Morphology and composition

In order to characterize the morphology and composition of our samples, TEM coupled with energy-dispersive x-ray (EDX) spectroscopy as well as Rutherford backscattering (RBS)

spectrometry were employed. TEM allows to determine the shape (morphology) and mean particle diameter as well as the size distribution. In high resolution mode, the crystallographic structure of the particle can also be investigated. Both EDX and RBS are used to quantify the composition of the sample, and thus the concentration and the stoichiometry of the investigated nanoparticles.

2.2.1 Transmission Electron Microscopy

Electron microscopy is an indispensable and complementary technique often used to characterize nanostructures in order to extract structural and chemical information from the studied samples. The wave nature of the electron makes it a good candidate to probe matter at the atomic scale. For an acceleration voltage of 200 kV the wavelength of the electron beam in a microscope is 2.51 pm, smaller than the interatomic distances.

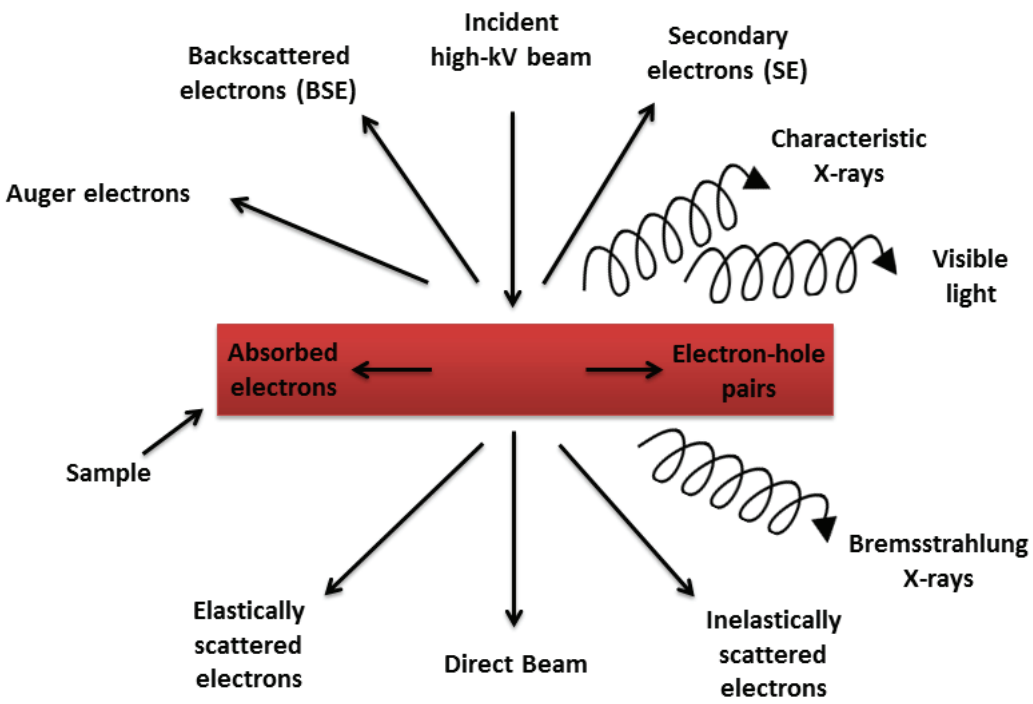

Fig. 2.5 Schematic representation of the different electron interactions with a sample.

The electron-matter interactions (figure 2.5) can be considered as strong interactions compared to that of X-rays and neutrons, which are also used to probe matter. Several measurement techniques can be devised according to the nature of the interaction. An elastic electron interaction, for instance, contains structural information. Electrons that emerge from an inelastic scattering contain chemical information about the sample. The later

allows performing techniques such as electron energy loss spectroscopy (EELS) or EDX spectroscopy.

A transmission electron microscope consists essentially of four parts: An electron gun which produces the necessary high energy electrons (20 to 300 keV); an illumination system with two or three magnetic lenses, known as condensers; an objective lens with a sample holder; and finally, a projection system (or magnification) made up of three magnetic lenses: diffraction lens, intermediary lens (or lenses) and projector lens; An electron beam which is accelerated by a potential difference in the electron gun arrives at the objective lens. A thin sample (in order to maintain a good resolution taking into account energy loss) is placed in the sample holder in a gap inside the objective lens. This lens ensures the first magnification, thus it is what determines the image quality (mainly the resolution). The electrons are then either diffused by the atoms in the sample or scattered by a crystalline planes. They are then collected by a set of lenses forming an enlarged image of the object. The variation of the focal length is used to vary the magnification and the focal point.

The transmission electron microscope has two principal operational modes depending on whether an image is desired or a diffraction pattern:

- Imaging mode: the electron beam traverses the sample. Depending on the thickness, the density and the chemical nature of the sample the electrons are more or less absorbed. It is possible to obtain an image of the radiated zone by placing the detector in the image plane. The image of the object appears darker the larger the atomic number of its constituents (gold will be appear darker than silver).

- Diffraction mode: this mode takes advantage of the wave nature of the electrons. When electrons arrive at a crystalline structure they will be scattered in certain directions depending on the organization of atoms. The beam is scattered in several small bundles and these are recombined to form the image through magnetic lenses.

Microscopy observations give images, that are size calibrated, of the projected surface of the particles. The latter gives, after a simple image treatment, a size histogram of the projected areas. The image processing consists of the binarization of the images followed by the evaluation of the area of each particle using an image processing software, *ImageJ* [63]. The particles' projections are fitted with an ellipse giving a list of particles with their areas and the values of minor and major axis.

2.2.2 EDX and RBS

Knowing the local chemical composition of a sample is an important step when working with nanoparticles. Especially alloyed nanoparticles could present a distribution of compositions

around the desired stoichiometry. As an example, energy dispersive X-ray spectroscopy in a nanoparticle allows to determine locally the abundance of each present species. In addition, it is possible to obtain a mapping of the sample when working in the scanning mode, scanning transmission electron microscopy (STEM). Another method to effectively quantify the composition of a sample is to use the Rutherford backscattering spectroscopy which uses high energy ion scattering to probe the sample, however this technique is considered as a destructive one.

Energy dispersive X-ray For electrons having a high energy, a part of their energy can be transferred to the sample. This energy transfer can cause a core electron to eject from a present atom and thus ionizing it. In this case, the excited atom will emit a characteristic X-rays when it returns to its ground state. The emitted X-ray depends on the excited shell K, L or M and consequently the emission of K_{α_1}, K_{α_2}, K_{β}, *etc*. This process is composed of a cascade of electrons from the valence shell to the core electron levels. X-ray emission is in competition with the emission of Auger electrons and their relative intensity depends on the atomic number of the measured atom. For light elements, the return to the fundamental, or ground state, is principally accompanied by the emission of Auger electrons. For instance, in the case of carbon K_{α} decay, the X-ray fluorescence probability is 0.8%, while for oxygen it is 2%. The detected X-rays are then quantified according to the Cliff-Lorimer equation [64]:

$$\frac{C_A}{C_B} = \left(\frac{\sigma_B \omega_B a_B \varepsilon_B}{\sigma_A \omega_A a_A \varepsilon_A}\right) \frac{I_A}{I_B} \tag{2.3}$$

where C_i is the atomic percentage of the element, I_i is the intensity of the considered X-ray, σ_i is the ionization cross-section for a given shell, ω_i is the X-ray fluorescence yield, ε_i is the efficiency coefficient of the detection system for the considered energy and a_i is the relative weight of the considered x-ray (which takes into account that an excited atom can decay in many ways).

Rutherford backscattering The RBS technique consists of detecting the energy of α backscattered particles (He^{+}, He^{2+}) by the sample. An accelerator of Van de Graaf's type produces particles having 3 - 3.5 MeV of energy. The detector is situated at an angle of 160° with respect to the incidence direction. The energies of the backscattered α particles depend on the nature of the scattering atoms and their depth from the sample's surface. A typical RBS spectrum is composed of several peaks that include the different elements present in the sample as well as a signal coming from the silicon substrate. The surface S_i is directly proportional to the number of atoms of the element i in cm^2 in the sample. RBS data are

quantified using *SimNRA* software [65]. It should be noted that in the case of RBS, due to the size of the bombarding atoms, the technique ejects atoms from the sample's surface. Thus, the longer the sample is bombarded the more damage is done. The information obtained using this technique are more reliable compared to those obtained by EDX, which can cause the evolution of the sample in time with atoms evaporating under the electron beam increasing the uncertainty. However the RBS technique does not allow to study the composition of a single nanocluster.

2.3 Synchrotron techniques

When charged particles (electrons e^-, positrons e^+, *etc*...) moving at speeds close to the speed of light (c), are forced on a curved trajectory, they emit electromagnetic radiation in a direction tangent to the direction of motion. This radiation is known as synchrotron radiation. It was first observed in the General Electric particle accelerator in 1947 and was considered to be a problem as it was associated to a major source of energy loss. Such radiation is extremely intense and extends over a broad energy range, from the infrared through the visible and ultraviolet, into the soft and hard x-ray regions of the electromagnetic spectrum.

A synchrotron is made up of several parts that include a LINAC, a BOOSTER and a storage ring. Generally, the LINAC and the BOOSTER accelerate particles having an electric charge. Once accelerated, these particles are injected into the storage ring. In the ring, these charged particles are confined to their circular trajectories by the use of bending magnets (dipoles, quadrupoles and octopoles). Radiation created in bending magnets is not very intense and thus it is only suitable for some experiments. For experiments that require higher radiation intensity, insertion devices used in 3rd generation synchrotron facilities, such as undulators and wigglers, are laid out in the straight sections of the storage rings. These insertion devices produce very intense synchrotron radiation by imposing multiple periodic bending of the charged particle's trajectory. The electromagnetic radiation emitted by undulators and wigglers covers a broad range of energies [66].

These broad ranges of energies along with the high intensity of synchrotron radiation resulted in quick advances and developments in the different experimental methods associated with condensed matter researches. Increasing the intensity and energy of the synchrotron radiation leads to many possible applications and various experimental methods in the different fields of science (physics, chemistry, biology, *etc*...). At the receiving end of bending magnets and insertion devices are located the experimental hutches, known as beamlines. These experimental hutches contain an assembly of optical elements used to

collect synchrotron radiation, from the bending magnets or insertion devices, on a sample, generally placed in the experimental station.

Experimental techniques that use synchrotron radiation differ in terms of energy, polarization, brilliance of the radiation beam, *etc*... Methods exploiting synchrotron radiation can study phenomena related to the crystalline structure, magnetism, electronic structure and other aspects of matter. In this work, two main synchrotron techniques, Extended X-ray Absorption Fine Structure (EXAFS) and X-ray Magnetic Circular Dichroism (XMCD), were adopted. The experimental details of the methods are presented in this chapter. In both cases, EXAFS and XMCD, synchrotron x-ray radiation is absorbed by the probed atom. This phenomenon is referred to as X-ray Absorption Spectra (XAS).

2.3.1 X-ray Absorption Spectra (XAS)

In the absorption spectroscopy experiments, the absorption of synchrotron radiation by the system under study is measured as a function of energy. This process is described by the Beer-Lambert law:

$$\mu(E) = \ln(\frac{I_1}{I_2}) \tag{2.4}$$

where I_1 is the intensity of the incident beam and I_2 is the intensity of the transmitted beam, $\mu(E)$ is the absorption coefficient. The energy dependence of the absorption coefficient $\mu(E)$ is schematically shown below:

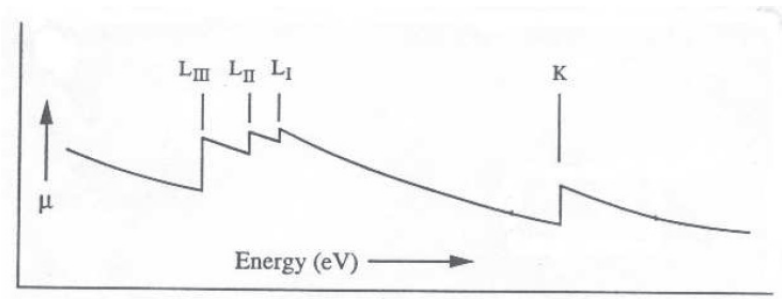

Fig. 2.6 Absorption coefficient versus photon energy; individual absorption thresholds are marked

Two main features can be observed from the photon energy dependence of $\mu(E)$. First, $\mu(E)$ is inversely proportional to the photon energy far from any absorption edge. In addition, in the $\mu(E)$ steep increases (absorption thresholds) occur at certain energies corresponding to the different atomic levels of a given atom. Moreover, at energy values just above the absorption edge, EXAFS oscillations of $\mu(E)$ can be observed with an amplitude of a few percent of the edge step. For a given element, the optical excitation of a core electron requires

a binding energy E_B as a minimum photon energy, the crossing of this energy will coincide with an increased absorption coefficient. This leads to the formation of absorption thresholds, which can be observed in the figure 2.6. The prominent thresholds of the $\mu(E)$ correspond to the different energy levels (K-Shell, L-Shell, M-Shell ...). When the energy of an incident X-ray is larger than the energy difference between the core level and the Fermi level, the incoming X-ray is absorbed; the core electron is excited above the Fermi energy level and gets a non-zero kinetic energy. This electron is called a "Photoelectron". The process is shown in figure 2.7.

In the XMCD technique, the absorption of a circularly polarized x-ray radiation by the probed atom invokes an electron transition between the core electron level and the valence band one. In the case where the orbital and spin magnetic moments are not negligible, the absorption of left circularly polarized light is different than the right circularly polarized one. This difference is directly correlated to the spin and orbital magnetic moments by the sum rules.

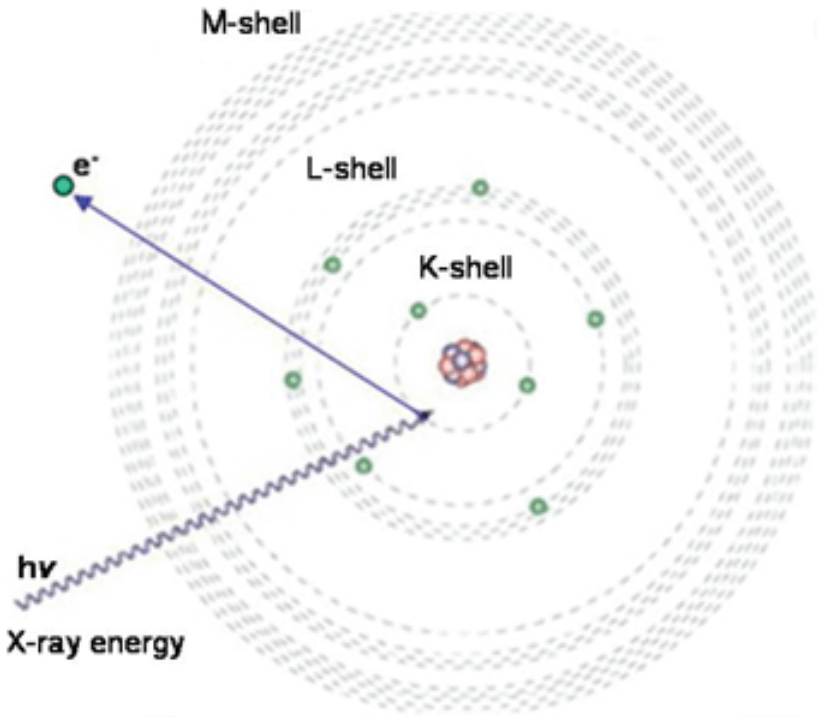

Fig. 2.7 Emission of a core level electron due to the absorption of an X-ray photon

The EXAFS technique is based on the effect of photoelectron emission by absorption of a photon by core electrons. The emitted photoelectron propagates in the material lattice (or molecule) and interacts with the surrounding atoms. The forward propagating wave associated with the photoelectron scatters from surrounding atoms. It interferes with the

back-scattered photoelectron wave resulting in an interference pattern. This interference pattern appears as a modulation of the measured absorption coefficient, thus causing the oscillation of absorption coefficient called EXAFS spectra. These oscillations are analyzed by simulations and best-fit procedures to obtain the structural parameters, *i.e.* the coordination, interatomic distances and Debye-Waller factor of the absorber from its neighbours.

2.3.2 Extended X-ray Absorption Fine Structure (EXAFS)

2.3.2.1 Basic principle

EXAFS is a spectroscopy method providing structural information about a sample through the analysis of its X-ray absorption spectrum [67]. It allows determining the chemical environment of a probe atom in terms of the number and type of its neighbours, inter-atomic distances as well as structural disorder.

In an absorption spectra, two features can be observed: the X-ray Absorption Near Edge Structure (XANES) and the EXAFS (see figure 2.8). For quantitative analysis, only the structural oscillations above the absorption threshold are considered (EXAFS). Therefore, the absorption threshold and background measurement are removed. The EXAFS function describing the structural oscillation is defined by:

$$\chi(E) = \frac{\mu(E) - \mu_i(E)}{\Delta_{\mu_i(E_0)}} \tag{2.5}$$

where μ is the experimental absorption coefficient, E_0 is the absorption threshold energy, Δ_{μ_i} is the threshold step in absorption, and μ_i is a free atomic background which represents the absorption on the free ion in the same state as the studied material but without oscillations coming from diffraction of photoelectrons on the surrounding atoms. We can define the photoelectron wave vector k as:

$$k = \sqrt{\frac{2m_e e}{\hbar^2}(E - E_0)} \tag{2.6}$$

where e is the electric charge of the electron, E_0 is the absorption threshold energy, E and E_0 are in eV and k is in Å^{-1}, the function $\chi(E)$ should be written as a function of $\overrightarrow{k}$ vector *i.e.* $\chi(\overrightarrow{k})$. The symbol k in this notation is the absolute value of the photoelectron wave vector $\overrightarrow{k}$, $k = |\overrightarrow{k}|$. The $\chi(k)$ function is a sum of $\chi_i(k)$ contributions of electron waves back-scattered from each surrounding ion/atom A_i,

$$\chi(k) = \sum \chi_i(k) \tag{2.7}$$

The EXAFS $\chi(k)$ function is Fourier transformed to obtain a radial distribution function, which provides the information on the distances and type (number of electrons) of surrounding atoms or ions.

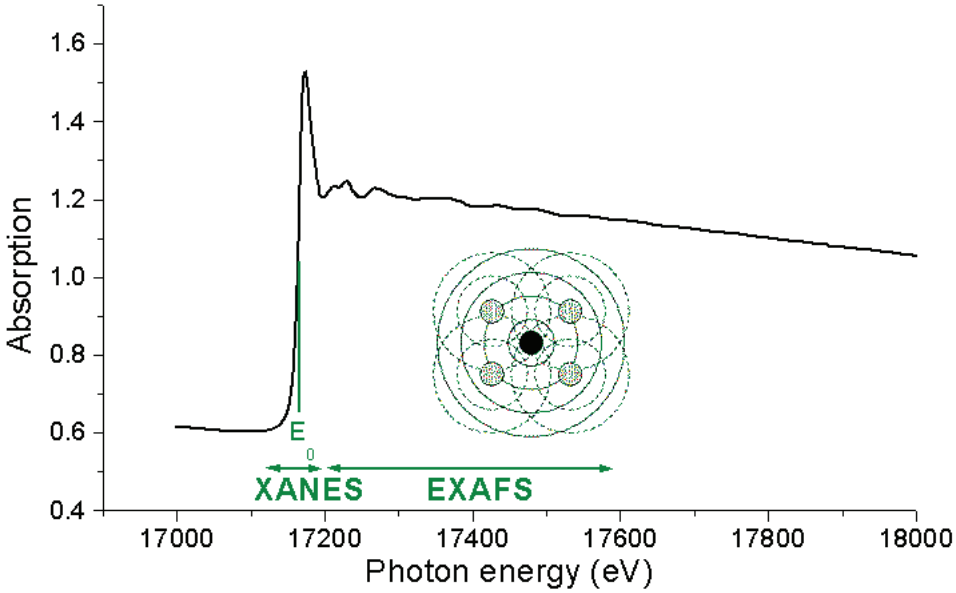

Fig. 2.8 X-ray absorption measurement in which the resonance energy coincides with the bonding energy of a core electron.

2.3.2.2 Experimental setup

The setup for EXAFS measurements can have different configurations depending on the type of sample and the type of measured emitted X-rays (transmitted or scattered). In general, the experimental setup for the EXAFS experiments consists of a system of mirrors and windows used to direct the incoming X-ray beam and define its dimension. A monochromator is used to select a specific energy value; it operates through the X-ray diffraction process according to Bragg's law.

$$2d\sin(\theta) = n\lambda \tag{2.8}$$

The monochromator, at the BM30B beamline, is made up of two Silicon (Si) crystals positioned as shown in the figure 2.9; a motor system is used to control the monochromator's angular difference $\delta\theta$. Thus, allowing a specific wavelength to be diffracted.

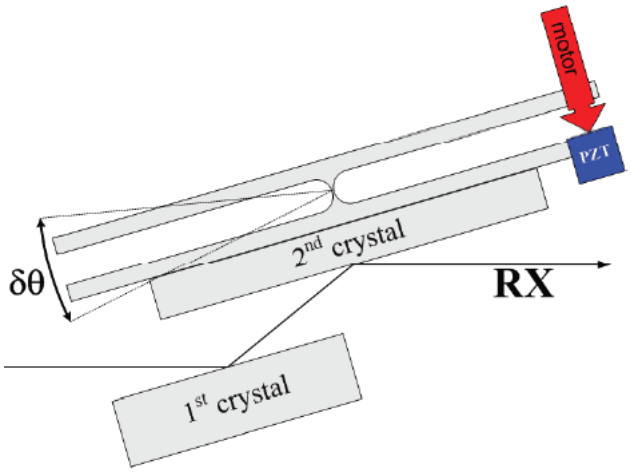

Fig. 2.9 Sketch of a Monochromator

After the monochromator the beam passes through the second part of the experimental setup where we have a system of two different detectors and the sample. A first detector is used to measure the incident X-ray beam intensity I_0. This beam hits the sample and we can have transmitted X-rays and fluorescence. The choice of the detector is sample dependent. For our samples, the nanoparticles are supported on a Silicon substrate. In this case, the thickness of the substrate was enough to absorb all transmitted X-rays thus the only information that can be collected is from fluorescence. For samples that allow for transmission measurements, a second detector is placed behind the sample to measure the transmitted X-ray beam intensity I. A simple illustration of the setup is shown in figure 2.10 below:

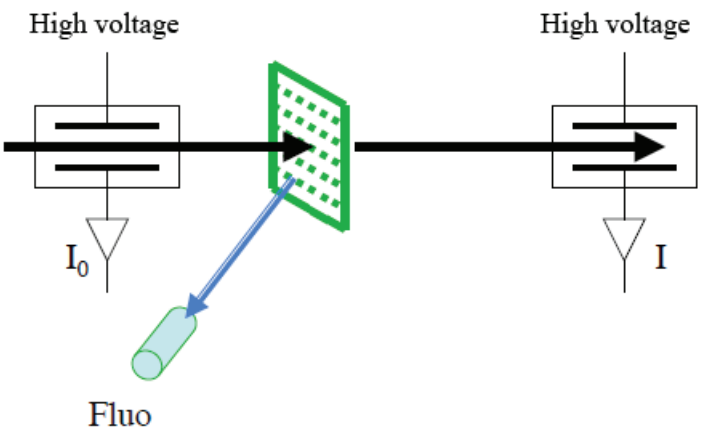

Fig. 2.10 Analyzed sample and the detector system.

It should be noted that the position (vertical and horizontal) of the sample as well as the angle with the incident X-rays can be controlled. This is essential for the case of fluorescence as it allows placing the sample in order to have the incident x-ray beam grazing the surface of the sample. This geometry helps probe a maximum of diluted clusters in a sample and to avoid X-ray diffraction peaks originating from the substrate. Thus, we have more fluorescence than diffraction. In the FAME beamline (BM30B) of the ESRF, the fluorescence detector uses an array of thirty detectors. The measured signal is the sum of all the signals measured by the thirty detectors.

2.3.2.3 Data treatment

X-ray absorption measurements were carried out on the BM30B FAME beamline in ESRF, Grenoble, France (Co:K edge, Fe:K edge measurements) in collaboration with Olivier PROUX. EXAFS spectra on all thresholds were measured in fluorescence mode. The measured nanoalloy samples (FeCo, FeRh, etc...) were all prepared at the PLYRA, Lyon, using the LECBD technique. Two types of samples were measured, the mass-selected samples and non mass-selected samples. All measurements were carried out at room temperature. The obtained EXAFS spectra were analyzed using *IFEFFIT* tools [68–75].

A double Si(111) single crystal monochromator with energy resolution of order of 2 eV was used and the absorption spectra μ were measured in the energy range from 7000 eV to 8000 eV for Fe:K edge measurements and in the energy range from 7600 eV 8600 eV for Co:K edge.

The information about the local environment is in the post edge absorption region where the oscillations occur as described earlier. Detailed analysis has to be performed in order to obtain precise and reliable information from the measurements. The analysis procedure is based on fitting a theoretical function to the experimental data. We use a software package called *IFEFFIT* which is a set of programs for processing the EXAFS data; this package was developed by Bruce Ravel and his colleagues at the Washington University [76].

The first part of the analysis is done using the software *Athena* of the *IFEFFIT* package. In the following, the example graphs used are from a sample of annealed mass selected FeRh nanoparticles at the Fe-K edge [77].

2.3.2.3.1 Pre-edge subtraction The pre-edge part of the absorption spectrum is fitted with a linear function within the range which is chosen by user defined variables *pre1* and *pre2*, see figure 2.11. If these parameters are not set by the user then values of these parameters are set as defaults by the software.

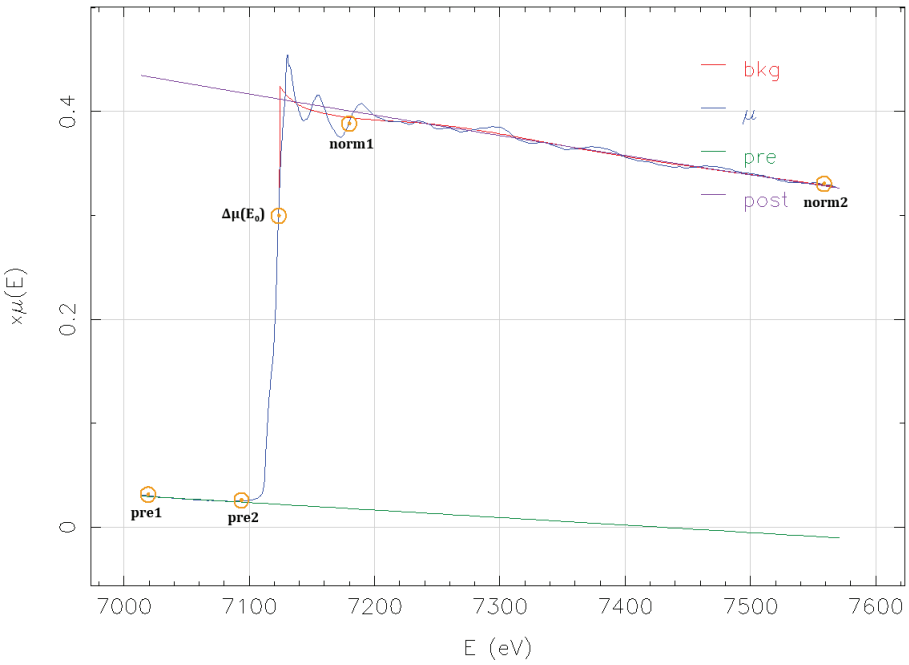

Fig. 2.11 FeRh example of pre-edge subtraction

2.3.2.3.2 Edge step Next step in the analysis is to find the threshold energy E_0 (referred to as $e0$ in the software) which is defined as maximum of the derivative $\partial\mu(E)/\partial E$. An option for manually setting $e0$ is also available in the software. The quadratic function is fitted to the post-edge region which is determined by the parameters *norm1* and *norm2*, default values for these two parameters are set in the software as *norm1 = 150 eV* and *norm2* is calculated for the given spectrum. The difference between the quadratic function (fitted to the post-edge region) and the linear function (fitted to the pre-edge region) at E_0 is taken as the edge step (denoted as $\Delta_{\mu(E_0)}$, see figure 2.11). The spectrum is normalized to the unity edge step according to the formula:

$$\mu_n = \mu - f_l\Psi(E_0) - (1 - f_q\Theta(E_0)) \tag{2.9}$$

where f_l is the pre-edge line, f_q is the post edge quadratic function, $\Psi(E_0)$ is equal to 1 for $E < E_0$ and 0 for $E > E_0$, $\Theta(E_0)$ is equal to 1 for $E > E_0$ and 0 for $E < E_0$. The result of this normalization is stored in an array (user defined). This step is done in order to compare the absorption spectra of different samples. An example of a normalized EXAFS spectrum is shown in figure 2.12.

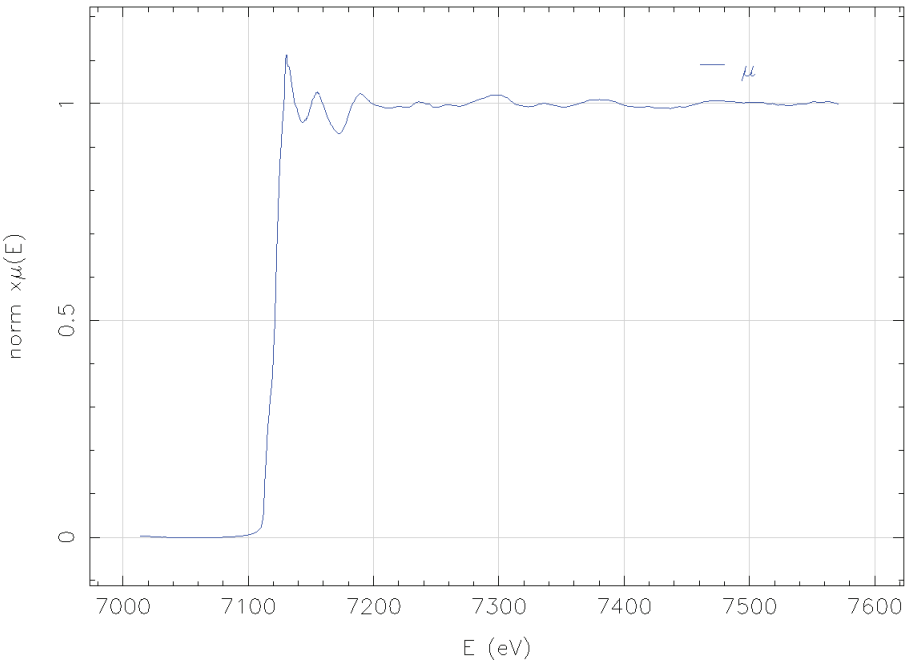

Fig. 2.12 Example of normalized absorption spectrum obtained on annealed FeRh nanoparticles.

2.3.2.3.3 Background removal A correct free atomic background removal is an essential step in the analysis of EXAFS spectra. The *Athena* application contains a procedure called *spline* which finds the optimal free atom absorption $\mu_0(E)$. The procedure *spline* also contains the pre-edge and post-edge background removing. It is based on minimizing of the Fourier Transform $FT(\chi)$ in the range from 0 to *rbkg* which is an input parameter for the spline procedure. There are also other parameters which have to be given by the user in order to remove the free atomic background, they include: Fourier transform window, k range, r range, k-weight and others. Varying these parameters does not have a strong influence on the result if the background is removed properly with the exception of the *rbkg* parameter which has a meaning of the size of the central atom.

The EXAFS function $\chi(k)$ is calculated according to the formula:

$$\chi(E) = \frac{\mu(E) - \mu_0(E)}{\Delta_{\mu(E_0)}} \tag{2.10}$$

where the E is transformed to k domain according to the formula 2.6. This means that χ is always normalized to a unit edge step. The origin of k vector is set to E_0, the electron

kinetic energy E_e is given as $E_e = E - E_0$ where E is the energy of the incoming X-ray. By applying the *spline* function to the experimental data we obtain the EXAFS function $\chi(k)$ in which the information on the structure is encoded. An example of the $\chi(k)$ is shown in figure 2.13.

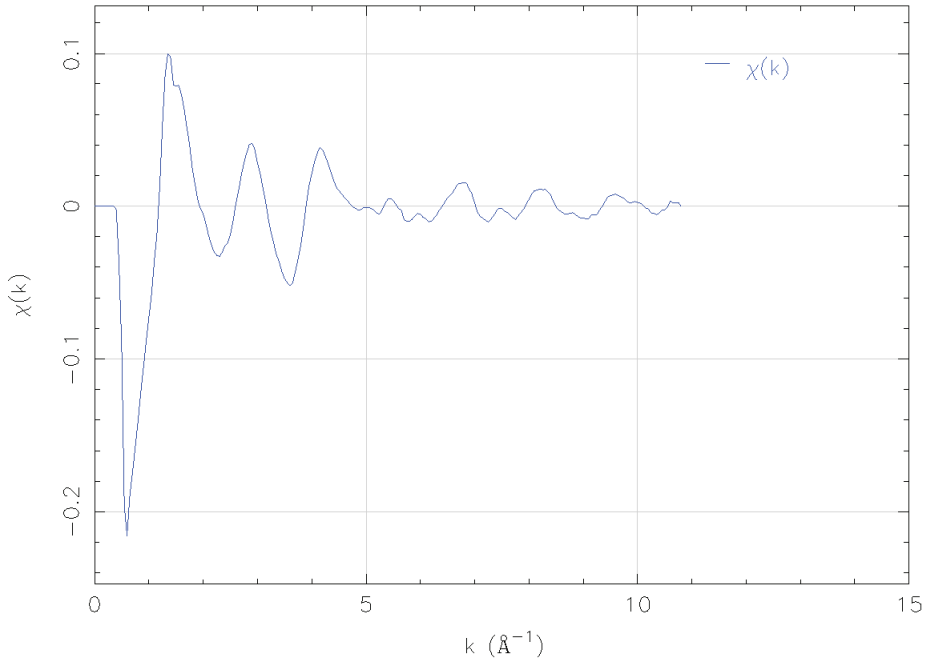

Fig. 2.13 Example of the $\chi(k)$ function obtained on annealed FeRh nanoparticles.

Usually the $\chi(k)$ function is weighted by a factor of k^p, where p is 1, 2 or 3 depending on the measurement. The factor k^p is applied in order to treat the data points at high k values which are strongly damped as compared to those at low k, and in order to obtain a more suitable function for the Fourier transformation (see figure 2.14). A Fourier transform of weighted $\chi(k)$ function leads to the radial distribution function (EXAFS function in R-space) [78].

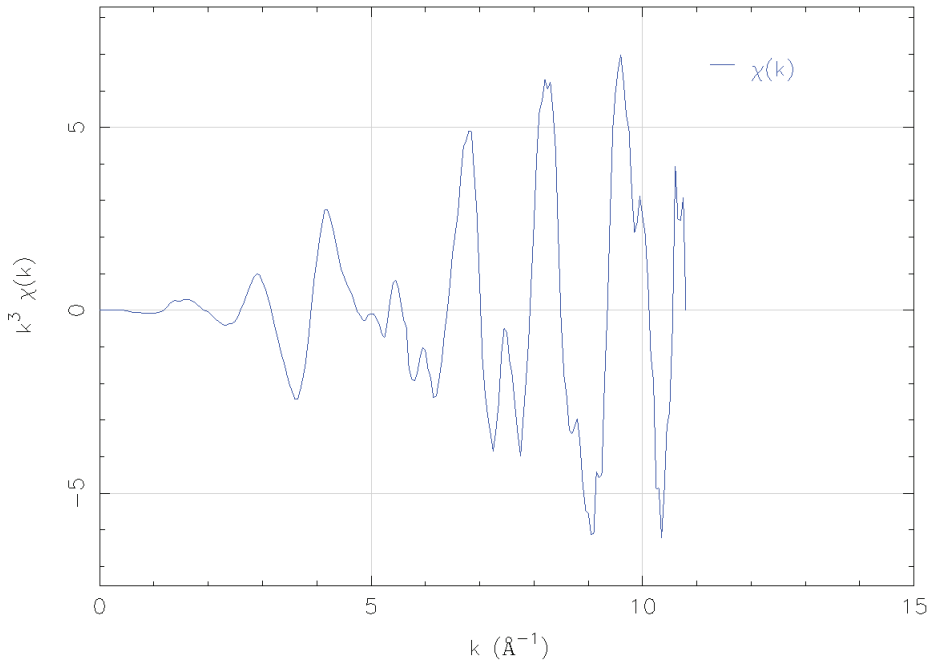

Fig. 2.14 Example of the $\chi(k)k^3$ function obtained on annealed FeRh nanoparticles.

The second part of the analysis is done using the *Artemis* software of the *IFEFFIT* package.

2.3.2.3.4 FEFF calculations The *Artemis* program allows to calculate the functions $\chi(k)$ and $\mu(E)$ for a given crystal structure. The calculation is based on an all-electrons real space relativistic Green's functions formalism with no symmetry requirements. Scattering potentials are calculated by overlapping the free atom densities within the muffin approximation [72].

When the photoelectron is emitted from the central atom it propagates in the matter and the wave associated with this electron is reflected from a neighbouring atom. Then it propagates back and it can be reflected on the original central atom or another atom which is close. Thus, the photoelectron during propagation through the material can be reflected once, twice or more times before it "returns" to the central atom. All possible traces of the photoelectron are called paths. A path can consist of several jumps from one atom to a neighbouring atom. A schematic diagram of the photoelectron propagation can be seen in figure 2.15.

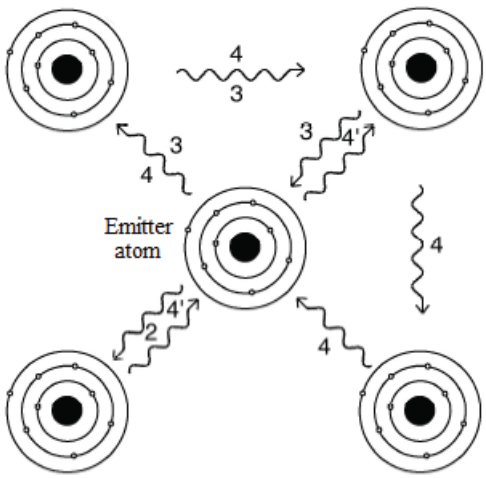

Fig. 2.15 Path of a photoelectron during propagation in a crystal.

For an electron emitted from an atom, the electron can have one of the several scattering paths as shown in figure 2.15. This electron, depending on its energy, can undergo one or more scatterings from the neighbouring atoms before it is reabsorbed by the emitter atom. Each path contributes to the total χ function and the paths are combined to the total χ function according to the formula:

$$\chi(k) = \sum_i \frac{(N_i {S_0}^2 F_i(k))}{k{R_i}^2} \sin(2k{R_i}^2 + \varphi_i(k)) \exp(-2{\sigma_i}^2 k^2) \exp(-2R_i/\lambda(k)) \tag{2.11}$$

$$R_i = R_0 + \Delta R$$
$$k^2 = 2m_e(E - E_0)/\hbar$$

where N is the degeneracy of the path, S_0^2 is the passive electron reduction factor, R is the distance between the central and surrounding atoms, σ is the Debye-Waller factor, $\lambda(k)$ is the mean free path, $F(k)$ is the effective scattering amplitude, $\varphi(k)$ is the effective scattering phase shift.

A path with one reflection is called a single path; a path with more reflections is called a multiple path. Paths do not have the same weight (importance) and the contribution of each path to the χ function depends on the path length, number of reflections and the angle between each jump. For instance, if we consider a photoelectron which moves from the central atom and is reflected back on a neighbouring atom in the direction of the central atom,

we have two jumps and the angle between them is 180°. Paths with an angle between jumps equal to 180° are more important than paths with an angle lower than $180°$.

The input parameters for a *FEFF* calculation is the positions of all the surrounding atoms up to a defined limit. Usually the first 10 neighbouring atoms are chosen for the calculation.

2.3.2.3.5 Fitting procedure The whole fitting procedure is done by *Artemis* of the *IFEFFIT* software package. *Artemis* is an interactive graphical utility used for fitting EXAFS data using theoretical standards. In *Artemis*, the first thing to do is import the experimental treated data from *Athena*. At the first step of the fitting procedure, we have to build a physical model for our measured sample. The model can be a small molecule or a complex crystal. After setting up the local environment of the probed atom, *Artemis* calculates all the possible paths for the electron. Each path has up to five parameters which can be varied during the fitting procedure. Thus, we have to simplify the situation and put some constrains between parameters to reduce the number of fitted parameters. In our case, the number of paths is limited to the first two neighbour shells. The chosen physical model is usually based on known or anticipated physical parameters of the studied material.

2.3.2.3.6 Path parameters For each path generated by the *FEFF* calculation, there are several important parameters for calculating the $\chi(k)$ function.

- The first parameter is called $e0$. This parameter does not have the same meaning as E_0: $e0$ is the difference between the theoretically calculated value for E_0 and the one obtained from the measurement. This parameter couples the theoretical and measured energy absorption threshold. Usually $e0$ is the same for all paths in the fit and is set as variable (*guess*) during the fitting process.

$$k \rightarrow \sqrt{k^2 - e0(2m_e/\hbar^2)} \tag{2.12}$$

- Next, the *amp* parameter which has a meaning of the amplitude of the χ function. This parameter is also often the same for all paths.

- *delR* is also an important parameter, it is given by the following equation:

$$R_{eff} = R_0 + delR \tag{2.13}$$

  R_{eff} is half of the real path length (calculated by *FEFF*) and R_0 is half of the path length calculated from lattice parameters and crystal structure given as input when creating the physical model.

- The Debye-Waller factor usually denoted as σ^2, here as a fitting parameter *sigma*^2, is the mean square deviation from the equilibrium position in the crystal structure. This deviation can be caused by a thermal motion of atoms/ions (time averaging) and also by a static disorder (space averaging).

2.3.3 X-ray Magnetic Circular Dichroism (XMCD)

2.3.3.1 Basic Principle

XMCD is a spectroscopy technique providing quantitative information on the magnetic properties through the analysis of circularly polarized x-ray absorption spectrum. Thanks to its chemical selectivity, its capacity to separate the orbital and spin moments and its sensitivity, the XMCD became a reference technique in the 1990s to study thin films and magnetic multilayers [79–81]. In recent years, use of the XMCD as a source of magnetic contrast lead to the development XMCD-PEEM microscopy (PEEM: PhotoEmission Electron Microscopy), an advanced magnetic imaging technology with spatial resolution, chemical selectivity and, recently, temporal resolution [82, 83].

The concept of the XMCD was first established in 1975 when mathematical calculations predicted the difference in the absorption of a polarized light as a function of the magnetization of Ni [60]. The first experimental realization was obtained twenty years later [84]. The general XMCD theory was only recently developed allowing direct and quantitative measurement of the spin and orbital magnetic moments [85, 86].

It is the difference between the absorption of circularly polarized left (μ_-) and right (μ_+) X-rays, for a magnetic material. It is the equivalent in the range of X-rays to the Faraday effect in the visible range. The visible light absorption causes electronic transitions from one state to an unoccupied state in the valence band, whereas in the field of X-rays a core electron is excited with well-defined energy and symmetry. In the range of soft X-rays, the absorption cross-sections are very large, making it possible to measure very small quantities of material, down to the fraction of a mono-layer.

A simple model to understand the link between the absorption of circularly polarized photons and the magnetism for the $L_{2,3}$ edges is the "two-step" model of Stöhr and Wu [87] shown in figure 2.16. The L_2 and L_3 edges are separated in energy by the spin-orbit coupling (4-20 eV for 3d metals). The polarization of the photons acts on the spin of the excited electron through the spin-orbit coupling. It can be shown that at the L_3 edge, left polarized photons excite 62.5% of spin *up* and 37.5% spin *down* electrons. At the L_2 edge the proportions become 25% (spin *up*) and 75% (spin *down*). For the right circular polarization,

the spin *up* and *down* are inverted at the two edges. Due to the spin-orbit coupling, the emitted photoelectrons are thus spin polarized.

Since the transition probability depends on the empty *d* density of states, in the second step the *d* band becomes a spin detector. In a non-magnetic material where the density of *up* and *down* spins is the same, the absorption of left and right circularly polarized light is the same. However, in a magnetic material where the two densities of spin are not equal due to the exchange coupling, one of the two polarizations is better absorbed and thus a dichroic signal is obtained. It should be noted that the magnetic dipolar moment (m_D), that reflects the asphericity of the distribution of the spin moment around the absorbing atom, is nullified in our case, since the samples are fabricated from randomly oriented nanocrystals.

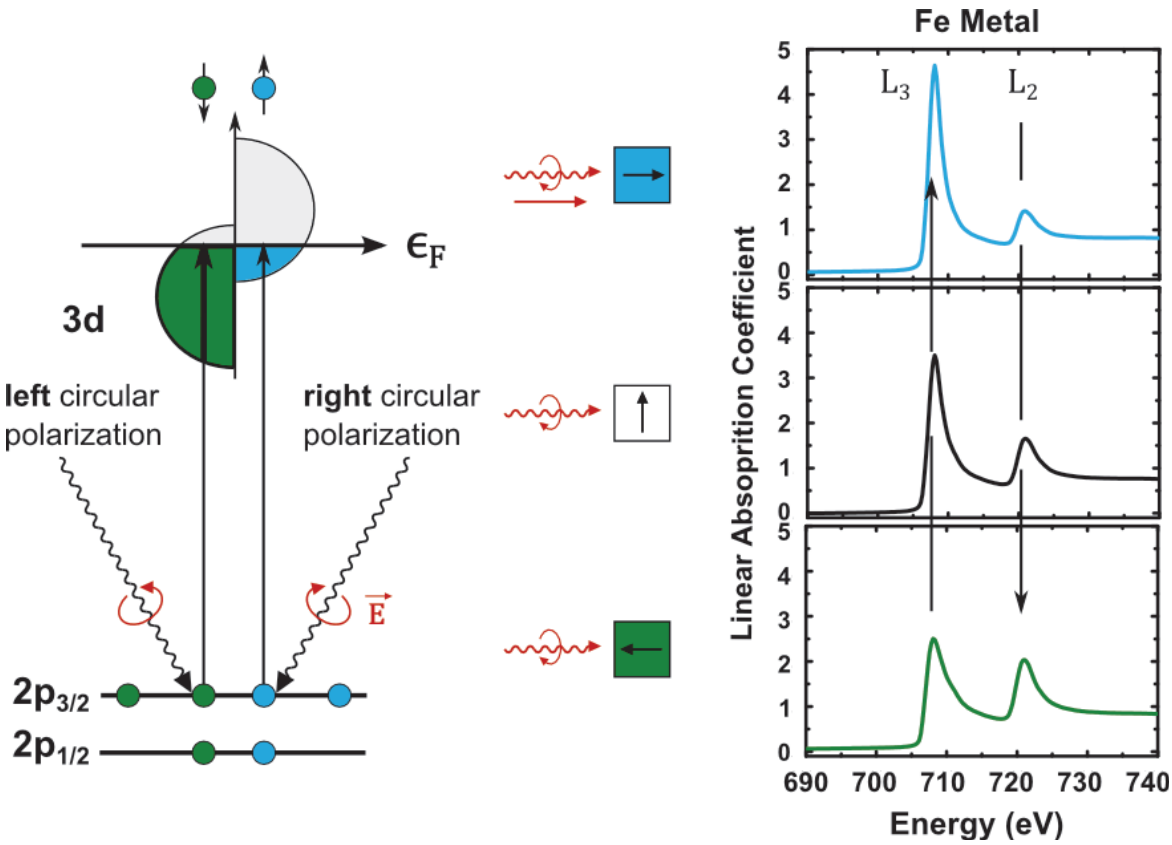

Fig. 2.16 The "two step" model of the XMCD at the L_2 edge for transition metals. The absorption of circularly polarized X-rays depends on the relative direction between the propagation vector and the direction of the local magnetization.

Quantitative data treatment of XMCD signal is achieved using the sum rules. The sum rules were first derived in 1992 for the orbital magnetic moment $\langle L_z \rangle$ (by Thole *et al*. [86]) and for the spin magnetic moment $\langle S_z \rangle$ in 1993 (by Carra *et al*. [85]). The sum rules allow the simultaneous determination of the spin and angular magnetic moments from the

measurements of the left and right circular polarized x-rays (XAS) and their difference (XMCD spectrum). The general formula for the sum rules given by Thole and Carra for $3d$ metals, that is the $L_{2,3}$ edges:

$$\frac{m_L}{N_h} = \frac{\int(\mu_+ - \mu-)}{\int(\mu_+ + \mu- + \mu_0)} \times (-2) \tag{2.14}$$
$$= -\frac{2}{3}q/r$$
$$\frac{m_S}{N_h} = -2.\frac{\int_{L_3}(\mu_+ - \mu-) - \int_{L_2}(\mu_+ - \mu-)}{\int(\mu_+ + \mu- + \mu 0)}(1 + \frac{7}{2}\frac{T_z}{S_z})^{-1} \tag{2.15}$$
$$= -\frac{3p-2q}{r}(1 + \frac{7}{2}\frac{T_z}{S_z})^{-1}$$

where N_h is the number of $3d$ holes, p is the integral of the XMCD signal over the L_3 edge, q is the integral of the XMCD signal over the L_3 and L_2 edges, r is the integral of the white line of the isotropic spectra and T_z the dipolar operator. The dipolar term T_z is often disregarded in the case of cubic symmetry. So the effective spin magnetic moment is expressed as:

$$m_S = m_S{}^{eff} = -\frac{3p-2q}{r}N_h \tag{2.16}$$

2.3.3.2 Experimental setup

A typical XMCD beamline has different configurations to accommodate different experimental needs. It is possible to perform X-ray Magnetic Linear Dichroism (XMLD) and X-ray Linear Dichroism (XLD) as well as XMCD to study magnetic and non-magnetic samples. An XMCD experiment utilizes a plane grating monochromator (PGM) with a Variable Groove Depth (VGM) grating to select specific and precise energy values. In this study, the Deimos beamline at the Soleil synchrotron was used in collaboration with Philippe OHRESSER.

After the monochromator, the beamline is equipped with a cryomagnet that reaches $\pm$ 7 T in the direction of the beam and $\pm$ 2 T perpendicular to the beam with a sample cryostat that works in temperature range of 1.5 K to 350 K. The Deimos experimental setup allows performing measurements in transmission mode as well as in total electron yield (TEY). The nature of our nanoparticle samples necessitates the use of TEY mode as the substrate is made of a thick silicon layer. TEY mode consists of measuring all the electrons leaving the sample, most of which are Auger electrons that cascade up to the surface of the sample. This limits

the probed depth to the escape depth λ_e, which is the distance an electron covers without losing energy. In the case of 3d metals this distance is only a few nanometers.

For Deimos, the x-ray source is a type APPLE II (Advanced Planar Polarized Light Emitter II) undulator. An undulator consists mostly of an array of permanent magnets that modify the trajectory of electrons passing through it into a helix trajectory. The resulting radiation is then emitted in a narrow energy range and can be tuned by adjusting the vertical gap between two magnet arrays. Additionally, the polarization (linear, circular or elliptical) can be tuned by adjusting the horizontal shift between the magnet arrays as shown in figure 2.17. Depending on the geometrical configuration of the magnet arrays in the undulator one can chose to have a specific polarization (linear or circular).

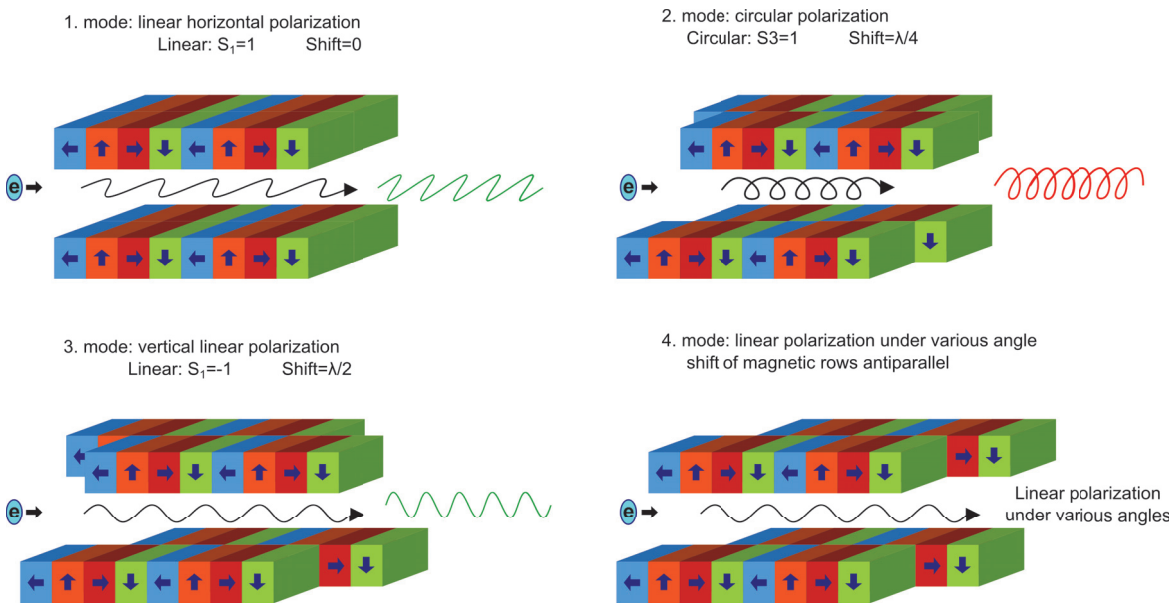

Fig. 2.17 Schematic view and modes of operation of an APPLE-II undulator.

2.3.3.3 Data treatment

X-ray absorption dichroic measurements were performed on the Deimos beamline at Soleil, Saclay, France (Co:$L_{3,2}$ edge and Fe:$L_{3,2}$ edge). XAS spectra on all thresholds were measured in TEY mode. The measured nano-alloy samples were all fabricated at the PLYRA using the LECBD technique. As XMCD is a surface technique, samples were prepared in the «mille-feuilles » configuration (see figure 2.4) having around 3 - 4 layers of nanoparticles separated by amorphous carbon layers, the total equivalent thickness of the layers is close to 10 nm. XAS spectra having two polarizations (left and right) were measured at about 2 K with a magnetic field of 5 T for all samples. In addition, magnetic hysteresis curves were also recorded at ambient temperature as well as 2 K between 5 T and -5 T. The

absorption spectra (μ_+ and μ_-) were obtained in the energy range of 690 eV to 780 eV for Fe:$L_{3,2}$ edge and 760 eV to 850 eV for the Co:$L_{3,2}$ edge. Generally XMCD spectra are obtained with all the experimental magnetic field (H) and right and left polarization ($+\varphi$, $-\varphi$) couples, *i.e.* ($+H$,$+\varphi$), ($+H$,$-\varphi$), ($-H$,$+\varphi$) and ($-H$,$-\varphi$), in order to minimize instrumental errors. Information about the spin and orbital magnetic moments are extrapolated using the sum rules from the measured XAS signals. A careful treatment of the measured data is required in order to obtain precise and reliable information.

2.3.3.3.1 Normalization and XMCD signals The pre-edge part of the absorption spectrum is normalized for all measured XAS signals couples. For each couple, the difference between the two polarizations (XMCD signal) is then calculated (see figure 2.18).

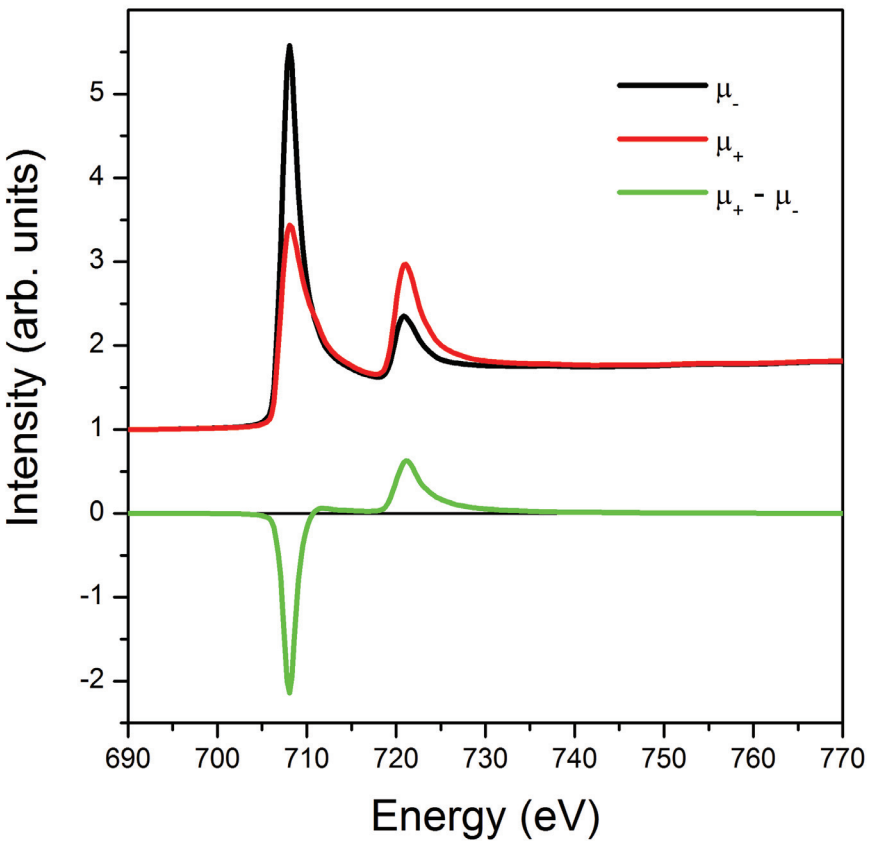

Fig. 2.18 Example of a normalized XAS left and right polarized signals, and XMCD difference signal.

2.3.3.3.2 XAS and step function The next step in the analysis requires the isotropic XAS signal. To build the isotropic spectra one has actually to take into account μ_0, *i.e.* the XAS with linear polarization along the magnetic field. For 3d elements, this is not easy to

measure, thus μ_0 is approximated by the sum of the left and right polarizations (μ_+ and μ_-). So, the isotropic spectra is calculated from the average of the left and right polarized XAS signals. The absorption signal related to transition into empty 3d states shows up as two peaks at the energetic position of the $2p_{1/2}$ and $2p_{3/2}$ states, whereas the unoccupied s, p states give rise to a step-like background. Since the magnetic moment of 3d transition metals is mainly governed by 3d valence electrons, the latter is usually subtracted as a step-function with a relative step heights of 2:1 according to the occupation of the $2p_{3/2}$ and $2p_{1/2}$ core states. The first step is chosen at the center of the L_3 edge, while the second step is chosen at the L_2 edge center as shown in figure 2.19.

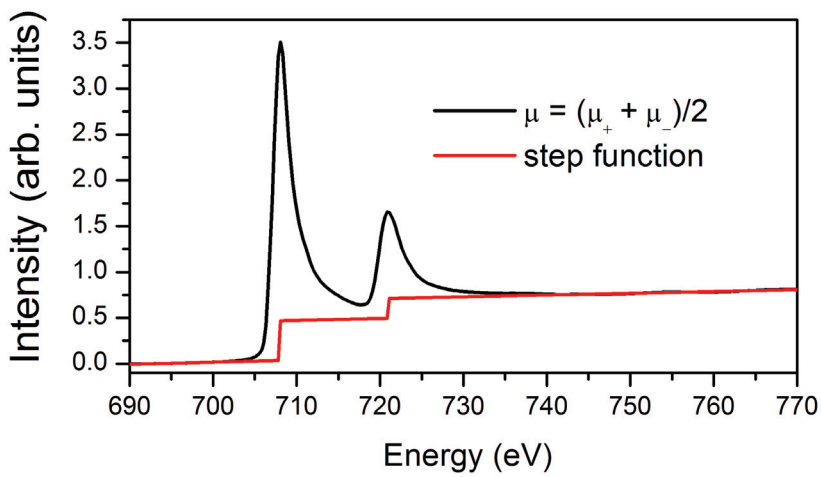

Fig. 2.19 Averaged XAS left and right polarized signals and the two-step function.

2.3.3.3.3 Integrated signals The background removal of the average XAS signal is achieved with the help of the obtained two-step function. The latter give the white line of the isotropic signal. Integrating the white line we obtain the value of r. On the other hand, integrating the XMCD signal, we obtain the values of p and q which are the values of the integral over the L_3 edge and L_2 edge, respectively (as shown in figure 2.20).

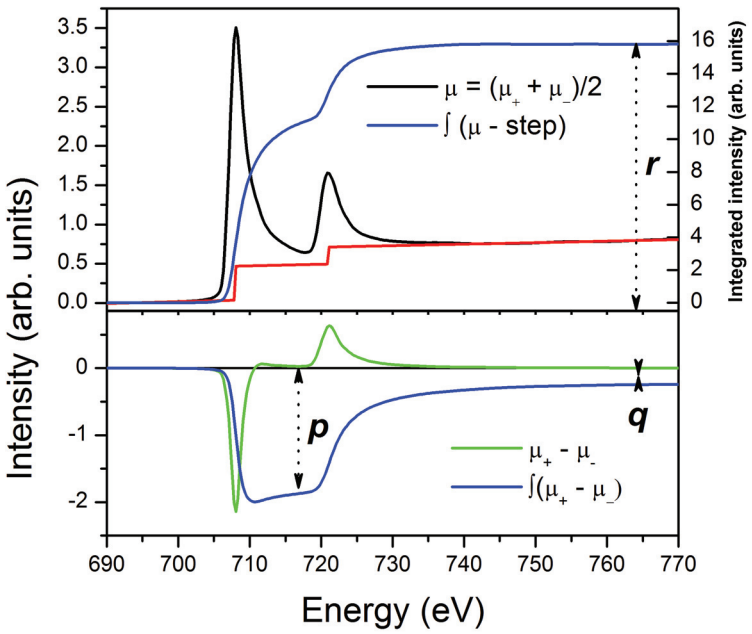

Fig. 2.20 Integrated white line function and XMCD signal.

2.3.3.3.4 Sum rules With the obtained values for p, q and r by applying the previously established sum rules equation, we can easily find the values of the spin and orbital magnetic moments. For iron atoms the number of holes for the bulk is $N_h = 3.39$, and for the bulk cobalt atoms $N_h = 2.49$ as calculated from the values of Chen *et.al*. [88].

2.3.4 Anomalous Scattering

2.3.4.1 Basic Principle

The use of scattering is necessary to understand the crystalline structure of our particles and their phase, as complementary information to electron microscopy and EXAFS spectroscopy. In fact, scattering provides information on the inter-atomic distances, the crystallinity, the phase, *etc*... The samples are made up of nanoparticles embedded in a matrix (in our case an amorphous carbon matrix). The nanometric size of the particles in addition to their high dilution requires the use of particular measuring techniques. In order to avoid that a scattering signal from the substrate masks that of the clusters, the use of a grazing incidence setup becomes important. The incident beam has a constant angle with the sample surface (smaller than 1°). This value is close to the sample's critical angle (clusters and matrix) to control the penetrated thickness of the X-rays within the sample and thus avoid, as much as possible, a signal from the silicon substrate. The measurement of scattering spectra is achieved by scanning the detector for different values of angles in the plane of the sample. In fact,

according to the Bragg equation we expect to have a diffracted beam where: $\lambda = 2d_{hkl}\sin\theta$ where d_{hkl} is the inter-atomic distance corresponding to the Miller indices h, k and l, λ is the X-ray wavelength and θ is the angle between the incident and diffracted beams.

The experimentally measured intensity for a given X-ray scattering is proportional to $|F(hkl)^2|$ and hence it is $|F(hkl)|$. This quantity is referred to as the "geometrical structure factor" as it depends only on the positions of atoms and not on any differences in their scattering behaviour. When the nature of the scattering, including any phase change, is identical for all atoms, this results is known as Friedel's law [89]. In the 1930, Coster *et al*. [90] performed an experiment with zincblende using X-ray wavelengths selected to lie close to the absorption edge of zinc, and this resulted in a small phase change of the X-rays scattered by zinc atoms and not sulfur this demonstrating the failure of Friedel's law. The different resonance that leads to this effect has become known as anomalous dispersion.

An electron of an atom can be ejected when a photon has a sufficient energy. A heavy atom has K and L, or even M, edges in the wavelength range which is useful for crystallography. The atomic scattering factor for X-rays of that atom in the resonant condition becomes complex, that is altering the normal scattering factor in amplitude and phase. The anomalous dispersion coefficients f' and f" are used to describe this effect. These two coefficients are wavelength dependent. Hence for the heavy atom we have:

$$f = f_0 + f'(\lambda) + if"(\lambda) \tag{2.17}$$

This equation thereby serves to correct for the standard, simpler, model of X-ray scattering. Normal scattering is basically determined by the total number of electrons in the atom and which takes no account to the absorption edge resonance effects. For a heavy atom this is not the situation for the used wavelength. For the light atoms (C, N, O and H) their corrections to the normal scattering are negligible. A free atom (without neighbours) has a relatively simple form for the variation with wavelength of f' and f". The edge wavelength is then where the scattering factor becomes complex. A bound atom has neighbours which can scatter back the ejected photoelectron and thereby seriously modulate the absorption effect and also alter therefore the X-ray scattering anomalous dispersion coefficients. Furthermore the values can become dependent on direction as there can be for example a high density of neighbours in one direction or plane over another. Table 2.1 lists the values (in electrons) of the dispersion corrections of a few elements for Copper Cu Kα radiation, while figure 2.21 displays the values as a function of the atomic number Z.

Element	C	Si	V	Fe	Co	Ni	Gd	Pb
Z	6	14	23	26	27	28	64	82
$\Delta f'$	0.017	0.244	0.035	-1.179	-2.464	-2.956	-9.242	-4.818
$\Delta f''$	0.009	0.330	2.110	3.204	3.608	0.509	12.320	8.505

Table 2.1 Dispersion corrections values (in electrons) for a few elements for Copper Cu Kα radiation.

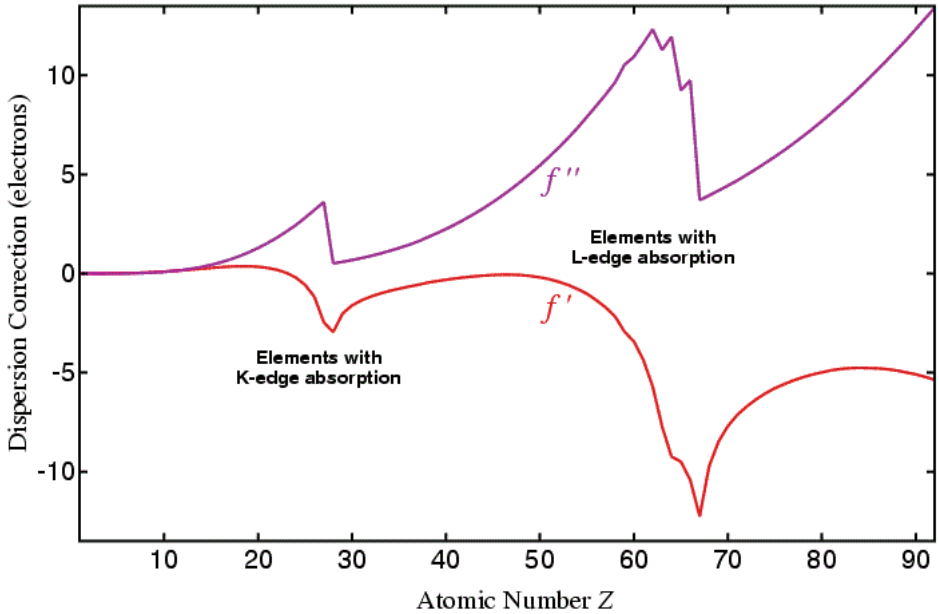

Fig. 2.21 Dispersion corrections as a function of the atomic number Z of Copper Cu Kα radiation.

2.3.4.2 Experimental Setup

The anomalous scattering experiment was performed at the D2am beamline at the ESRF in collaboration with Nils BLANC. The beamline is equipped with two interchangeable instruments a "small angle scattering camera" and a "Kappa Goniometer". The two instruments share photomultipliers, photodiodes and a 2D CDD camera. For our sample geometry the goniometer was used to measure the scattered signal with the help of the detectors. Figure 2.22 shows a schematic of the kappa goniometer.

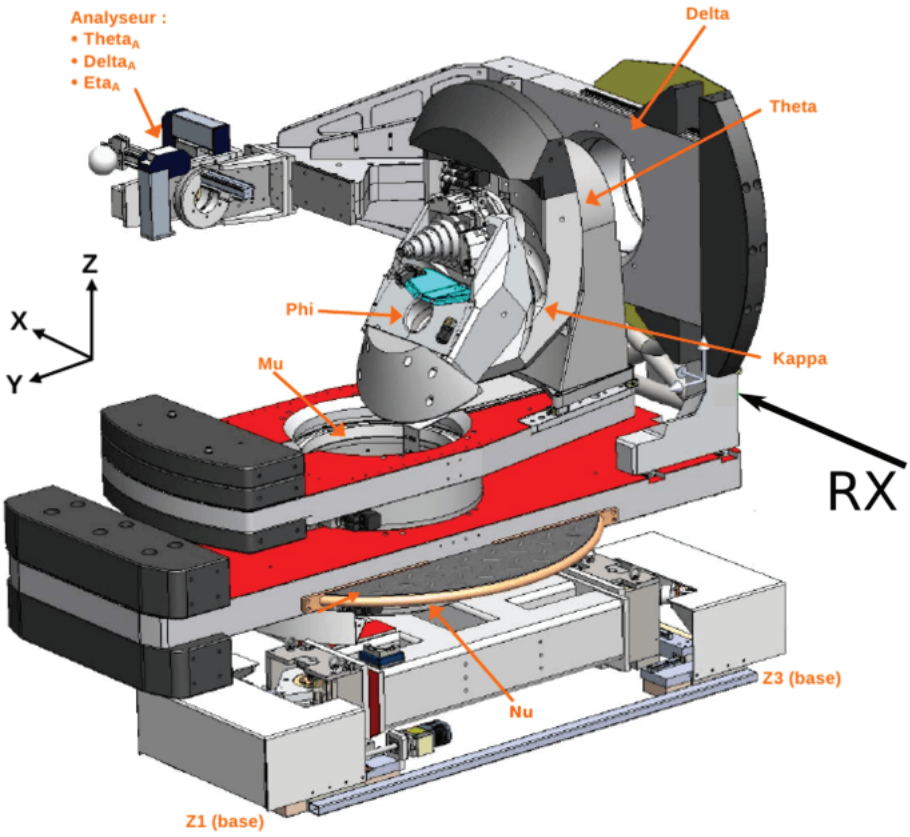

Fig. 2.22 Schematics of the Kappa Goniometer used at the D2am beamline at the ESRF.

With the help of the goniometer, the sample can be oriented through 4 circles of the instrument which can be defined both as physical axis or virtual Eulerian one:

- MU: Sample rotation around a vertical axis (z).
- ETA: Virtual eulerian angle: sample rotation around a horizontal axis perpendicular to the incident beam (y).
- CHI: Virtual eulerian angle: sample rotation around x, it is carried out by THETA.
- PHI: virtual eulerian angle: sample rotation around the sample normal. It is carried by CHI and THETA, so that the sample lies horizontal at chi = 90 (its normal is z) and vertical at chi = 0 (its normal is then y).
- KETA: physical rotation associated with ETA.
- KAPP: physical rotation around the Kappa axis.
- KPHI: physical rotation associated with PHI.

2.3.4.3 Simulation

To simulate an X-ray scattering spectrum of an assembly of atoms (our FeCo/Rh nanoparticles having a diameter of 2-6 nm, thus between a few 100 and 10000 atoms), a simple and effective method to implement is to use the Debye model [91]. This model is widely used to simulate the scattered intensity by a non-crystalline assembly of atoms, such as amorphous solids or liquids, representing the instantaneous position of each atom by a vector $\vec{r}_i$. The intensity is written as the sum of amplitudes scattered by each atom multiplied by the conjugate complex quantity, and can be reduced down to the following equation (as explained by Blanc in his PhD thesis [92]):

$$\langle I(q) \rangle = \sum_{i=1}^{N} \sum_{j=1}^{N} f_i(q) f_j(q) \frac{\sin(q r_{ij})}{q r_{ij}} \tag{2.18}$$

where q is the magnitude of the scattering vector in the reciprocal lattice units, N is the number of atoms, $f_i(q)$ is the atomic scattering factor for atom i and scattering vector q and r_{ij} is the distance between atom i and atom j.

2.4 SQUID magnetometry

2.4.1 Basic principle

The SQUID (Superconducting QUantum Interference Device) measurements in this thesis are done in the Centre de Magnétométrie de Lyon (CML) platform. The apparatus is a MPMS-XL5 SQUID from Quantum Design. This device allows to measure samples having very small magnetizations, typically in the order of 10^{-5} A.m^{-1}. The MPMS-XL5 squid allows for temperature control between 2 K and 400 K and applied magnetic field up to $\pm$ 5 Teslas [93]. A system of RSO (Reciprocating Sample Option) oscillating around a measuring point allows for rapid and precise measurements reaching 10^{-6} A.m^{-1}. The SQUID magnetometer [94, 95] was widely used in this study because it allows the detection of very weak magnetic flux through the employment of operating principles based on superconductivity. A schematics diagram is displayed in figure 2.23. There are three main parts:

- the detection circuit is made up of four L_1 coils, and two coils L_2 and L_{fb} serving as a relay with the two other parts;
- the amplifier and feedback circuits;

- the SQUID loop, made of superconducting material, coupled to the two other parts by mutual inductances M_1 and M_2.

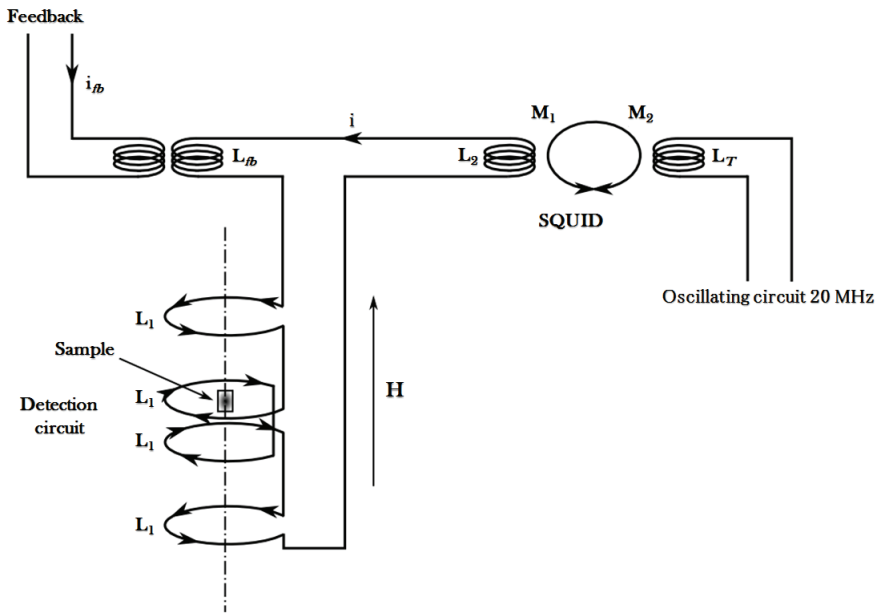

Fig. 2.23 Schematics of a SQUID magnetometer detection loop.

When a homogeneously magnetized sample oscillates between the detection coils L_1, variations in the magnetic flux induce an electric current i in the detection system; this current is proportional to the magnetization of the sample. Its expression is given by:

$$i = \frac{\Delta\Phi}{4L_1 + L_2 + L_{fb}} \tag{2.19}$$

where $\Delta\Phi = k.M$, M the magnetization of the sample. When the current exceeds the Josephson junction's critical current, the SQUID loops allows a magnetic flux proportional to the current i to be injected in the inductance M_1. The second inductance M_2 then couples the SQUID loop with the amplifier circuit that detects a first flux variation. Finally, the feedback circuit injects a current i_{fb} such that the total flux variation detected thereafter is constant. The system works in a Flux-Lock Loop (FLL) mode:

$$\Delta\Phi = M_1(i + i_{fb}) = const. \tag{2.20}$$

Feedback current measurement allows to determine the flux variation which is proportional to the current i and the magnetization M of the sample. The sample is placed in a cryogenic vessel, called a Dewar, whose temperature is controlled with precision. Since all

experimental conditions are controllable, it is then possible to measure the variations of the magnetic moment as a function of the external applied field and temperature.

2.4.2 Model

2.4.2.1 Notations

In order to avoid ambiguity in mathematical expressions, in what follows is the notation for all the terms used in this work:

- $\overrightarrow{B}$ denotes the magnetic induction;
- $\mu_0\overrightarrow{H}$, the applied magnetic field in the plane containing the sample, expressed in tesla (T);
- N_{tot}, the total number of particles in the sample;
- $\overrightarrow{m}(T,\mu_0 H)$, the sample's magnetic moment expressed in A.m^2 at the temperature T and in an applied magnetic field $\mu_0 H$. m_{sat} and m_r are, respectively, the magnetic moment at saturation and remanence of the sample;
- $\overrightarrow{M}$, M_s and M_r, respectively, the magnetization, the saturation magnetization and the remanence magnetization in A/m, defined by $\overrightarrow{M} = \overrightarrow{m}/V$, where V is the sample volume;
- μ_0, the permeability in vacuum of value $4\pi.10^{-7}$ kg.m.A^{-2}.s^{-2};
- k_B, Boltzmann's constant of value 1.3807 10^{-23} J.K^{-1};
- ΔE, the energy barrier to overcome so that a particle's magnetization switches. This energy quantity takes into account the particle's magnetic anisotropy (shape anisotropy, volume and surface magnetocrystalline, magneto-elastic effects);
- χ, the sample's initial magnetic susceptibility, defined by $\left(\frac{dM}{dH}\right)_{H\to 0}$. It is unitless by definition;
- D, denotes the diameter of a particle supposed spherical, D_m, D_{mm} and ω are, respectively, the median diameter, the median magnetic diameter and the dispersion (unitless) in a size distribution $\rho(D)$. Depending on the sample, this size distribution can be modeled by a lognormal function:

$$\rho(D) = \frac{1}{\omega\sqrt{2\pi}}\frac{1}{D}\exp\left[-\frac{1}{2}\left(\frac{\ln(D/D_m)}{\omega}\right)^2\right] \tag{2.21}$$

or a gaussian function:

$$\rho(D) = \frac{1}{\omega D_m \sqrt{\pi/2}} \exp\left[-\frac{1}{2}\left(\frac{D-D_m}{\omega D_m}\right)^2\right] \tag{2.22}$$

where $\omega D_m = \sigma$ is the standard deviation of the distribution.

2.4.2.2 Energy sources

In this section, we will describe the magnetization state at 0 K of a supposedly spherical nanoparticle and discuss its mode of switching. In this case, the magnetization state in a particle is given through minimizing the magnetic energy:

$$E = E_{exchange} + E_{Zeeman} + E_{Magnetostatic} + E_{Anisotropy} \tag{2.23}$$

Minimizing this energy determines the orientation direction of the magnetic moment of the system. It is difficult to satisfy the simultaneous minimization of the four energy terms. Thus, the most favorable state, where the system's energy is minimum, results from a compromise.

Exchange energy

$$E_{exchange} = \int_V A_E \left(\nabla \frac{M}{M_s}\right)^2 dV \tag{2.24}$$

The exchange interaction is the origin of the spontaneous orientation of the moments carried by the atoms. Following the sign of the coefficient of exchange interaction A_E, the material will be either ferromagnetic or antiferromagnetic. This interaction of an electrostatic origin was introduced by Heisenberg in 1929 in his quantum mechanics representation. This type of interaction is strong; however it only acts on close neighbours because it decreases rapidly with distance. Three different types of spontaneous orders can exist:

- The ferromagnetic, where the atomic moments are parallel to each other
- The antiferromagnetic, where the moments are antiparallel with compensating moments
- The ferrimagnetic, where the moments are antiparallel without compensating moments.

These orders exist under a certain temperature, called the Curie temperature (T_C) for the ferromagnetic order and the Néel temperature (T_N) for the antiferromagnetic and ferrimagnetic

orders. Above this temperature, the magnetic order disappears and the material becomes paramagnetic, where the moments exist but are not coupled.

Zeeman energy This energy appears when an external magnetic field $\mu_0\overrightarrow{H}$ is applied. It is basically the interaction between the applied magnetic field and the particle's magnetization.

$$E_{Zeeman} = \mu_0 \int_V \overrightarrow{M}.\overrightarrow{H}\,dV \tag{2.25}$$

Magnetostatic energy The magnetostatic energy, or demagnetizing energy, is the resulting energy from the interaction between the dipoles, on each atom. It is a much weaker energy compared to the exchange energy, but has a longer range. In general, the magnetostatic interaction energy is given by:

$$E_{Magnetostatic} = -\frac{1}{2}\mu_0 \int_V \overrightarrow{M}.\overrightarrow{H_d}dV \tag{2.26}$$

The notion of magnetostatic energy can not be separated from the demagnetizing field. The demagnetizing field is the field created by the magnetization distribution inside the material itself. It is proportional to the opposite direction of magnetization and tends to close the magnetic flux. The demagnetizing field is related to the magnetization by $\overrightarrow{H_d} = -\mathcal{N}\overrightarrow{M}$, where $\mathcal{N}$ is the demagnetizing tensor, which is represented by a symmetric 3×3 matrix.

Anisotropy energy The anisotropy energy can be defined by the natural orientation of the magnetization and consequently the orbital moment, and is generated by different contributions:

- The magnetocrystalline anisotropy energy comes from the interactions of the atomic orbitals with the electric field (crystalline field) created by the charge distribution in their environment. In order to characterize the magnetocrystalline anisotropy energy, the magnetization is expressed as a function of the principal lattice axis according to their symmetries. The energetically favorable direction of spontaneous magnetization is called the easy axis. For a cubic material, the expression is given by:

$$\begin{aligned} E_{anisotropy} = \int_V (&K_1(\cos^2\alpha_1\cos^2\alpha_2 + \cos^2\alpha_2\cos^2\alpha_3 + \cos^2\alpha_1\cos^2\alpha_3) \\ &+K_2\cos^2\alpha_1\cos^2\alpha_2\cos^2\alpha_3 + \ldots)dV \end{aligned} \tag{2.27}$$

  where K_i are the anisotropy constants and α_i are the angles between the magnetization and a crystallographic axis. In the case of a tetragonal material where the axis c plays

a particular role, the anisotropy energy is written in the spherical system:

$$E_{anisotropy} = \int_V \left(K_1 \sin^2\theta + K_2 \sin^4\theta + K_3 \sin^4\theta \cos(4\varphi) + ...\right) dV \tag{2.28}$$

Finally, in systems with a lower symmetry (case of hexagonal close-packed hcp Cobalt, for example), the anisotropy energy is written as:

$$E_{anisotropy} = \int_V \left(K_1 \sin^2\theta + K_2 \sin^4\theta + K_3 \sin^6\theta + K_4 \sin^6\theta \cos\varphi + ...\right) dV \tag{2.29}$$

The predominant term in this case and in the tetragonal case is the second order term, thus in a first order approximation, the system can be represented by a uniaxial anisotropy, and the anisotropy energy becomes:

$$E_{anisotropy} \approx K_1 V \sin^2\theta \tag{2.30}$$

- The magnetocrystalline surface anisotropy energy that originates from the symmetry breaking at the surfaces and interfaces. The atomic magnetic interactions experience a discontinuity at the surface-interface. Thus, surface atom moments will have a tendency to align parallel or perpendicular to the surface plane where their crystallographic environment is changed compared to that of the core atoms. The surface magnetocrystalline anisotropy energy can be described by:

$$E_{anisotropy} = K_s \cos^2\alpha \tag{2.31}$$

  where K_s is the surface anisotropy constant and α is the angle between the atomic magnetic moment and the surface normal.

- The magneto-elastic energy that comes from a deformation of the crystal structure under mechanical stress. In our samples, this anisotropy is neglected. The nanoparticles being preformed in a gas phase, their growth is unconstrained.

In order to optimize the contributions of the different energies, in particular the magnetostatic and anisotropy energies, a magnetic material is divided into uniformly magnetized regions, called Weiss domains, separated by domain walls (Néel or Bloch walls). The magnetic moments are parallel inside these domains and tend to be antiparallel between each other in order to close the field lines (*i.e.* minimize the magnetostatic energy in the vacuum). Figure 2.24 represents a demonstration of magnetic stray fields versus domain walls [96].

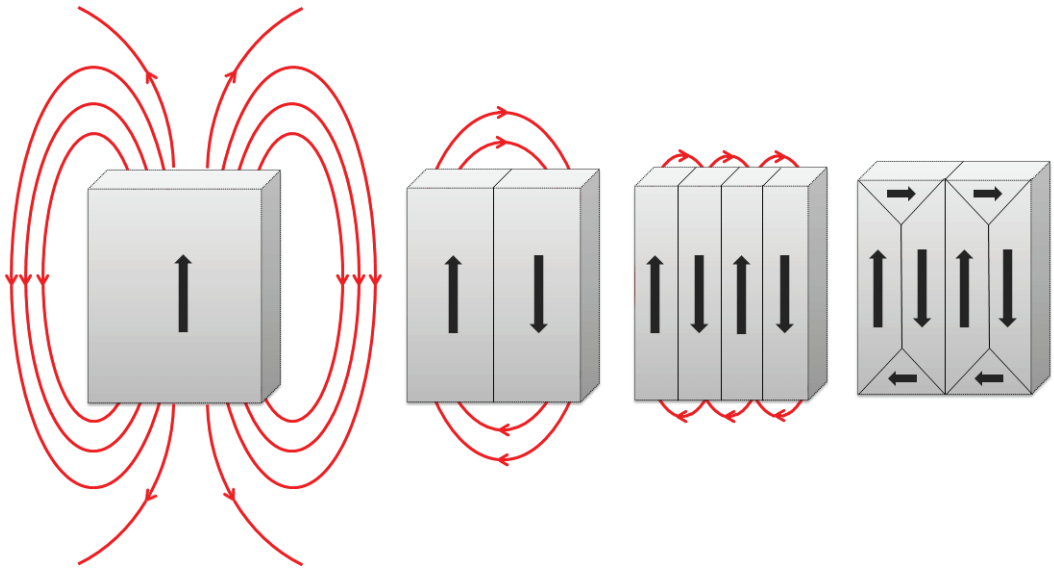

Fig. 2.24 Reducing the magnetostatic energy by the creation of domain walls.

2.4.2.3 Stoner-Wohlfarth macrospin model

Magnetic materials are made up of multiple magnetic domains. These domains are separated by domain walls, as described earlier. However, the creation of magnetic walls cost energy, exchange energy in particular. The fundamental length scales which govern the magnetic properties are the domain wall width δ_m, the exchange length L_{ex} and the magnetostatic length L_s. These length scales are determined from the competition between the internal magnetic forces. The competition between the exchange energy and the magnetocrystalline anisotropy energy defines the domain wall width $\delta_m = \sqrt{A_{ex}/K}$. The competition between the exchange energy and the magnetostatic energy (demagnetizing field) defines the exchange length $L_{ex} = \sqrt{2A_{ex}/\mu_o M_S{}^2}$ and the magnetostatic length is $L_s = \sqrt{A_{ex}/2\pi M_S{}^2}$, where K is the magnetic anisotropy constant and A_{ex} is the exchange length constant within a grain.

For spherical particles, we define the critical radius R_c [97] which is determined by the balance of domain wall energy and magnetostatic energy as

$$R_c = 36\frac{L_{ex}{}^2}{\delta_m} = \frac{36\sqrt{A_{ex}K_{eff}}}{\mu_0 M_S{}^2} \tag{2.32}$$

where K_{eff} is the effective anisotropy. R_c determines the radius limit below which a particle is single domain. In addition, we define the coherent radius $R_{coh} = 5L_{ex}$. The coherent radius presents the limit below which the magnetic reversal of the particle is coherent, which implies the all the magnetic moments carried by the atoms inside the particle rotate at the same time. For the nanoparticles studied in this work ($R < 5$ nm), their radii are inferior to

R_c and $Rcoh$ (see table 2.2 taken from [98]). This means that all the atomic moments in a particle are represented by one magnetic moment, known as the macrospin. The macrospin is thus defined as $m_{NP} = m_{at}N_{at}$ where m_{at} is the moment of an atom and N_{at} is the number of atoms in a particle. The coherent reversal of a mono-domain magnetic moment is described by the Stoner-Wohlfarth model [99, 100].

	A_E (10^{-12} J.m^{-1})	δ_m (nm)	l_{ex} (nm)	M_S (kA.m^{-1})	R_c (nm)	R_{coh} (nm)	K_{eff} (kJ.m^{-3})
Cobalt	10.3	4.5	2.0	1350	34	10	530
Iron	8.3	12.7	1.5	1720	6	7.5	48

Table 2.2 Cobalt and iron magnetic parameters at ambient temperature [98].

The macrospin model (or Stoner-Wohlfarth *SW* model) is widely used to simulate and model the magnetization reversal of ferromagnetic nanoparticles. It is a simple model based on several hypothesis. The nanoparticles are described geometrically as elongated ellipsoids, where the major axis and the easy axis coincide (Figure 2.25). The anisotropy is considered uniaxial with a volume, shape and/or magnetocrystalline nature. The anisotropy introduces an energy barrier (ΔE) that must be overcome for the reversal of the magnetic moment to occur. The energy barrier is given by $\Delta E = K_{eff}V$, where K_{eff} is the effective anisotropy constant supposed independent of the volume V. In addition, the SW model supposes a temperature of 0 K, the so-called absolute zero.

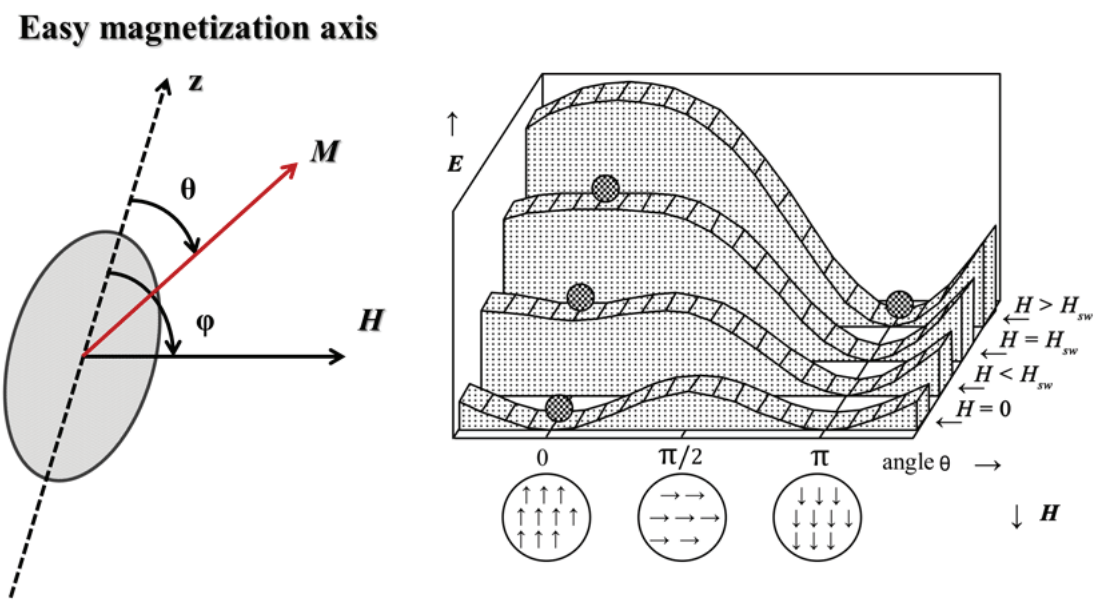

Fig. 2.25 Schematic representation of (Left) a macrospin in an external magnetic field,(Right) a superparamagnetic potential well at different magnetic fields.

When a magnetic field ($\mu_0 H$) is applied, the two energy terms in play are the anisotropy and Zeeman energy. The sum of these two terms constitute the magnetic energy (E) of the nanoparticle. Considering the left diagram of 2.25, we get:

$$E = \Delta E \sin^2\theta - \mu_0 H M_S V \cos(\phi - \theta) \tag{2.33}$$

The reversal field, where the energy barrier disappears in the particular case of $\phi = \pi$ or $\pi/2$, is obtained for:

$$H = H_a = \frac{2K_{eff}}{\mu_0 M_S} \tag{2.34}$$

where H_a is called the anisotropy field of the particle.

Figure 2.26 represents the evolution of the component of the normalized magnetization (in the direction along the magnetic field) ($M_H = \vec{M}.\vec{H}/\|\vec{M}\|\|\vec{H}\|$) as a function of the applied magnetic field.

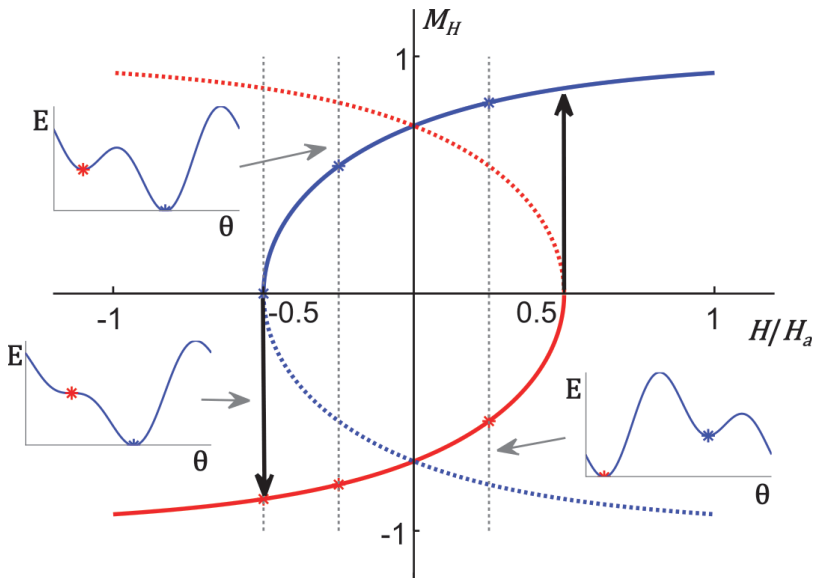

Fig. 2.26 An example of solution for the Stoner-Wolhfarth model for two positions of easy magnetization. The continuous line represents the positions of the energy minimum; the dashed line, the local energy minima. The energy profiles for three different applied magnetic fields are represented.

The equation 2.33 allows determining numerically the hysteresis loop described by the magnetization component in the direction of the applied field for a single particle. In order to calculate for a given magnetic field the stable values of magnetization, it is necessary to minimize the total energy and to determine its critical values.

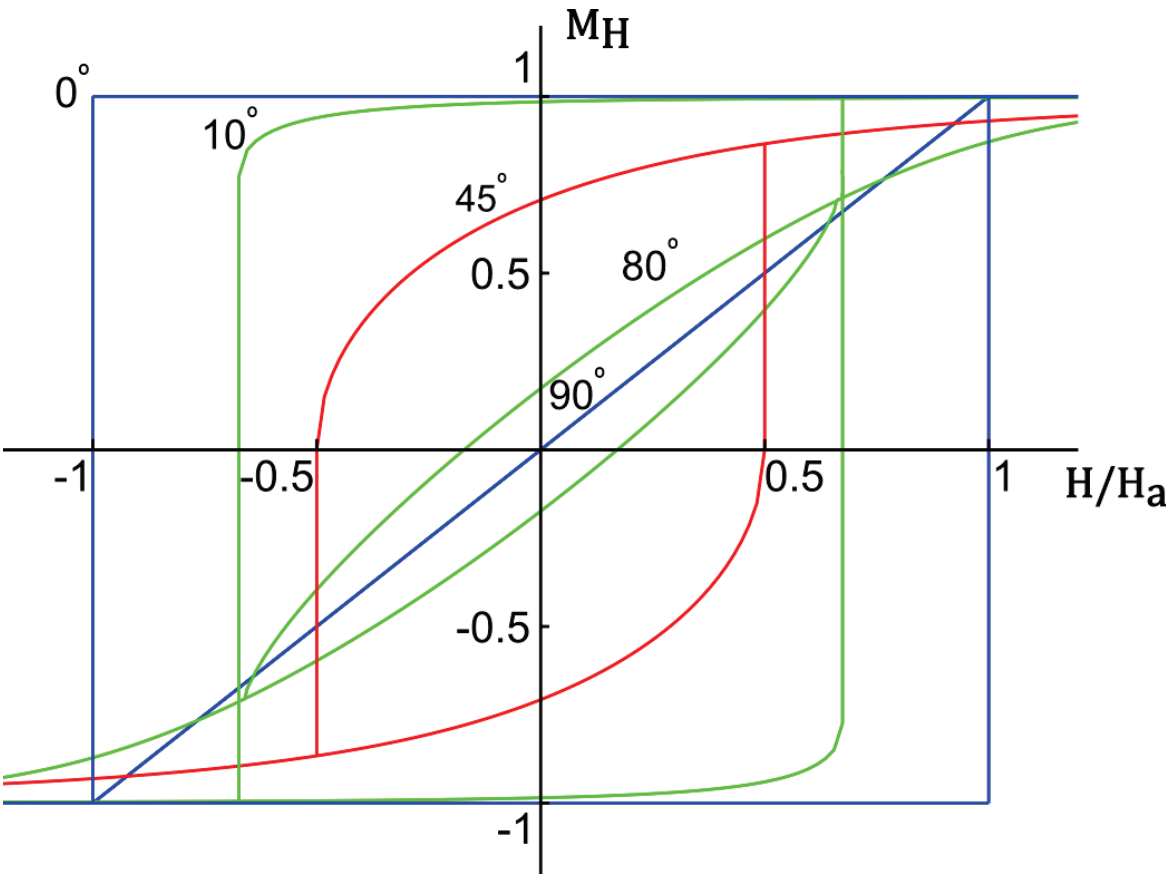

Fig. 2.27 Magnetization curves for the Stoner-Wohlfarth model for various angles ϕ between the applied field direction and the easy axis.

In figure 2.27, the hysteresis loops for a single particle are presented as a function of the applied field H and the angle ϕ (from 0° to 90°). The value of H that verify:

$$\left(\frac{\partial E}{\partial \theta}\right)_{\theta=\theta_0} = 0 \quad \text{and} \quad \left(\frac{\partial^2 E}{\partial \theta^2}\right)_{\theta=\theta_0} > 0 \tag{2.35}$$

is known as the switching field. The switching field H_{sw} corresponds to the magnetization reversal by applying an external magnetic field H having an angle ϕ with the easy axis of magnetization:

$$H_{sw}(\phi) = H_a \left(\sin^{\frac{2}{3}}(\phi) + \cos^{\frac{2}{3}}(\phi)\right)^{-\frac{3}{2}} \tag{2.36}$$

From equation 2.36 it can be noted that the switching field does not depend on the particle's volume. The anisotropy and switching fields are identical for all particle sizes. The obtained curve represents, in polar coordinates, the Stoner-Wohlfarth astroid (Figure 2.28) [99]. This curve represents the switching (reversal) field of the particle's magnetization in the space of the applied magnetic field. The two axes, characteristic of an astroid, correspond to the easy

and hard axis of magnetization. For all fields inside the astroid, the magnetization has two possible orientations (stable or meta-stable), whereas outside the astroid there is only one orientation.

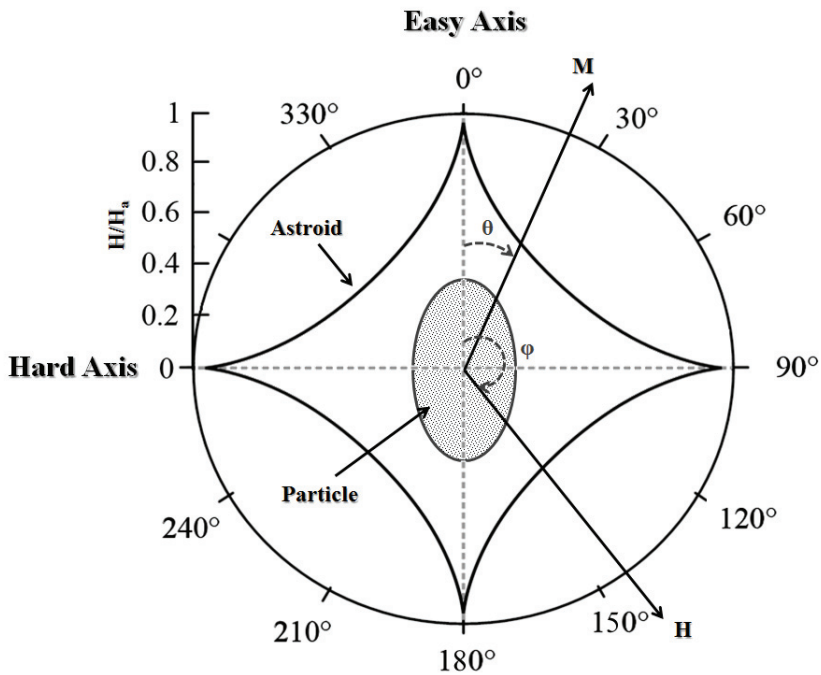

Fig. 2.28 Diagram of the Stoner-Wohlfarth astroid in two dimensions.

2.4.2.4 Superparamagnetism

For single domain nanoparticles, another new magnetic regime is observed which is the superparamagnetism. If we suppose that the nanoparticles have a uniaxial magnetic anisotropy without an applied field, the energy barrier ΔE, presented in figure 2.25, can be overcome by thermal energy ($k_B T$). The magnetic reversal being thermally activated, the relaxation time τ and the reversal frequency ν between the two directions of easy magnetization can be expressed by an Arrhenius law:

$$\tau = \tau_0 e^{\frac{\Delta E}{k_B T}} \tag{2.37}$$

where τ_0 is the relaxation time in the absence of a barrier. τ_0 can be determined from different models [101–104]. Nevertheless, its variation with temperature is overlooked experimentally against the exponential term. Its value is typically in the orders of 10^{-9} – 10^{-11} s. So, if we take into account the experimental measuring time of the magnetization, denoted τ_{mes}, we can put into evidence that for a particle there exist two regimes:

- For $\tau_{mes} >> \tau$, the average magnetization of the measured particle will be zero since the particle's magnetization will be constantly reversing from one direction of the easy axis to the other during the measurement. This is referred to as superparamagnetism; it corresponds to an appearance of paramagnetism even though all the atomic moments in the particle are coupled ferromagnetically.

- For $\tau_{mes} << \tau$, the measured magnetization is different than zero, the particles is labeled as "blocked".

Thus, the progressive transition between the two regimes (blocked and superparamagnetic) is achieved for $\tau \approx \tau_{mes}$. The expression of τ reveals that it is strongly dependent on T such that for a given particle size, the transition temperature between the two states, referred to as the blocking temperature T_B, for which $\tau(T_B) = \tau_{mes}$ is:

$$T_B = \frac{\Delta E}{\mathrm{k_B} \ln(\frac{\tau_{mes}}{\tau_0})} = \frac{K_{eff}V}{\mathrm{k_B} \ln(\frac{\tau_{mes}}{\tau_0})} \tag{2.38}$$

The blocking temperature T_B depends on the size of the nanoparticle, on the anisotropy as well as on the measuring time. For Mössbauer spectroscopy, τ_{mes} is in the order of $10^{-7} - 10^{-10}$ s, for AC-SQUID magnetometry it is in the order of 10^{-5} - 1 s and for DC-SQUID magnetometry in the order of $10 \sim 100$ s. When measuring using a SQUID in DC, $\tau_{mes} = 100$ s and $\tau_0 = 10^{-9}$ s are typically used to calculate the anisotropy energy [105]; equation 2.38 becomes:

$$K_{eff}V = 25\mathrm{k_B}T_B \tag{2.39}$$

This approximation has many limitations. When working with an assembly of nanoparticles having a size distribution, as in our case, it is no longer true to speak of the blocking temperature. For a given temperature, the previous equation can be expressed in terms of blocking diameter below which the nanoparticles are blocked. In fact, the transition between the two regimes (blocked-superparamagnetic) occurs progressively when varying the temperature. This transition can be exploited to precisely characterize the nanoparticles' anisotropy.

2.4.2.5 Nanoparticle assembly

The studied samples are made up of diluted size-selected and non size-selected (neutral) FeCo nanoparticle samples embedded in either an amorphous carbon matrix, or a copper matrix. To interpret the different magnetic curves, several hypothesis were assumed:

- the magnetic moments of a particle is a macrospin, described by the Stoner-Wohlfarth model
- The anisotropy of the nanoparticles is uniaxial with random orientation of the easy magnetization axes from one particle to another
- M_S and ΔE are temperature independent .

The measurements that will be presented were done on assemblies of nanoparticles embedded in a matrix in the 2D or 3D configurations previously established (see section 2.1.4). In both cases, it is possible to question whether or not there are magnetic interactions between the particles. Three types of magnetic interactions could intervene between the particles present in the matrix:

- Dipolar interactions, independent from the nature of the matrix, are long range interactions since they decay as a $1/d^3$, where d is the distance between the particles;
- Ruderman-Kittel-Kasuya-Yosida (RKKY) interactions exist only in metallic matrices. They originate from a parallel or anti-parallel coupling between ferromagnetic layers [106]. This type of interaction is short range as it disappears after 5 nm [107].
- Superexchange interactions are present in isolating matrices (oxydes) [108]. These influences are very short range, a few interatomic distances.

2.4.3 Data treatment

The magnetic response of the nanoparticles was thoroughly investigated using a SQUID. A set of several measurements were performed allowing for a complete characterization of our samples and thus forming a solid base in order to understand the magnetic behaviour of cluster-assembled nanostructures. As was previously established, the particle's volume directly influences its anisotropy energy as well as the energy barrier. Thus, when varying the nanoparticle size the total energy of the system will be the result of combination of all the different energies in play. The aim of the SQUID magnetic measurements is to remove all ambiguities and to shed light on the size-dependence of the anisotropy. In order to study the evolution of the total energy of the system as a function of particle size and concentration, a set of three types of magnetic measurements were realized. Magnetic susceptibility curves in ZFC/FC (Zero Field Cooled/Field Cooled) protocol, magnetization measurements $m(H)$, and magnetic remanence measurements in IRM/DcD (Isothermal Remanent Magnetization/Direct current Demagnetization) protocol. The first two types of measurements, ZFC/FC and $m(H)$,

are simultaneously adjusted using the "Triple-Fit" fitting procedure [105]. Together with the adjustment of the IRM/DcD these magnetic measurements provide a somewhat complete and comprehensive magnetic description of our nanoparticles.

2.4.3.1 Magnetization curves

For an assembly of nanoparticles, magnetization $m(H)$ curves are commonly measured. In our case, the term ”magnetization curves” is not rigorous. In fact, it is the total measured magnetic moment. The response of an assembly of nanoparticles to an external field at a fixed temperature depends on the measurement temperature. If the temperature is below the so called blocking temperature, the measured curve will follow a hysteresis loop. The magnetization cycle is open allowing to measure the coercivity field ($\mu_0 H_C$) as well as the remanence moment (m_r) and the saturation moment (m_S).

In the case where the measurement is done at a temperature T higher than the blocking temperature T_B, the measured response can be described using a Langevin function [109–111] given by:

$$m(H,T) = N_t \int_0^{\infty} \frac{x \mathrm{k_B} T}{\mu_0 H} \left[\coth(x) - \frac{1}{x} \right] \rho(D) dD \tag{2.40}$$

where m is the total magnetic moment of the sample and $x = \frac{\mu_0 H M_S}{\mathrm{k_B} T} \frac{\pi D^3}{6}$, N_t is the number of particles, and $\rho(D)$ is the diameter distribution previously established (equation for lognormal 2.21 and gaussian 2.22). When describing the experimental data using this simple equation, this measurement alone is not sensitive enough to discriminate between variations in the size distribution, such as the median diameter size D_m and the dispersion ω [112, 113].

As can be seen in figure 2.29, adjusting the magnetization curve alone does not give access precisely to the magnetic diameter distribution of the nanoparticles. The curves overlap for three different size distributions, making it impossible to distinguish them. To go a step further, it is necessary to include other magnetic measurements, such as the susceptibility curves, in order to extract the nanoparticles’ properties.

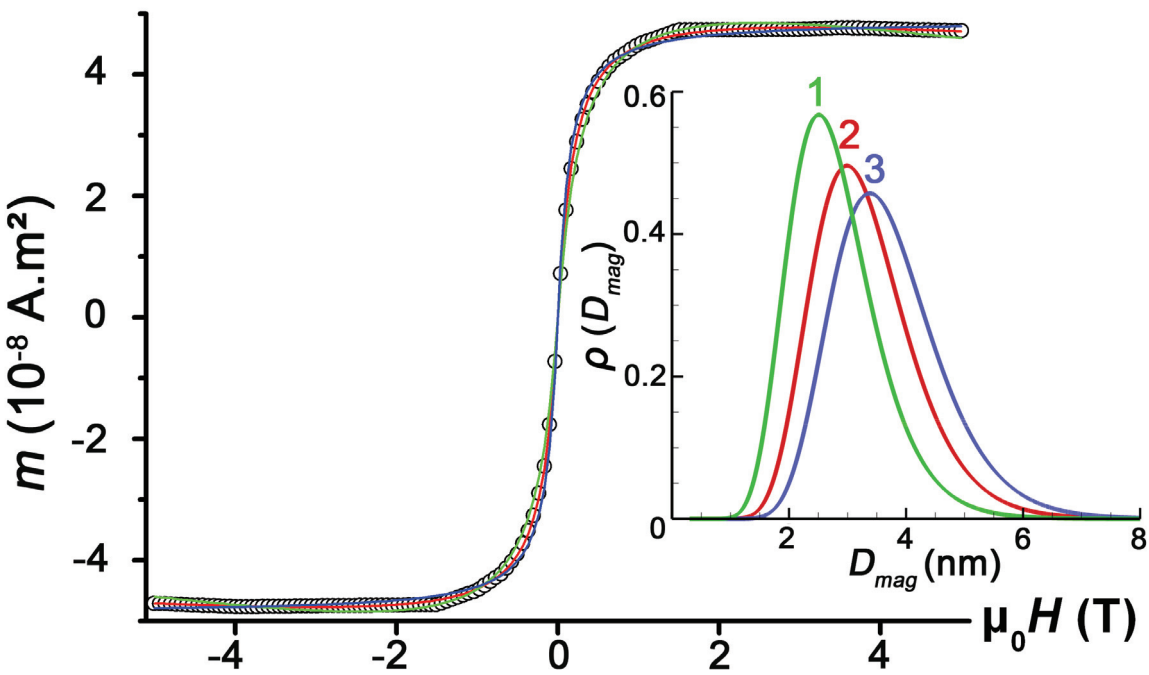

Fig. 2.29 $m(H)$ at 300 K for Cobalt nanoparticles in a gold matrix. The curve can be fitted with several size distributions as is shown in insert.

2.4.3.2 Magnetic susceptibility curves

The acquisition of the susceptibility curves following the ZFC-FC protocol is a typical tool used to determine the magnetic properties of cluster assemblies. These measurements are commonly used since they provide valuable information concerning the magnetic anisotropy energy (MAE) of the nanoparticles. The MAE is a key information related to the energy barrier that governs the magnetization reversal from one direction of easy magnetization to the other. It controls the magnetic stability of the nano-magnets which is an important parameter from an applications' point of view, mainly in the domain of magnetic data storage.

A number of theoretical studies were performed in order to interpret the ZFC-FC curves [114–120]. In particular, a semi-analytical model [105, 121] to simulate the whole temperature range of the FC as well as the ZFC curves. In fact, these curves are often under-exploited to a single value of T_{max} or the ZFC is fitted using two states model [122–126] (abrupt transition from the blocked to the superparamagnetic regime at the blocking temperature T_B)

In the following, we will consider that the nanoparticles have the same magnetization M_s and the same MAE: ΔE. We will introduce a size distribution, as the real case observed using TEM. As such, a distribution of MAE is also introduced. The nanoparticles are described by the Stoner-Wohlfarth model. The system is thus made up of macrospins with their easy

magnetization axis randomly oriented in space. The applied magnetic field is sufficiently small (5mT) to remain in the case of a linear response of the magnetic moment with the field.

2.4.3.2.1 ZFC-FC protocol $m(T)$ measurements following the ZFC-FC protocols were realized in order to determine the magnetic anisotropy of the clusters. First, the sample is cooled down to a low temperature (2 K) without field. The particles are thus in a blocked state with their magnetization randomly distributed homogeneously in all directions of space. Since no external magnetic field was applied, the average magnetization of the sample is zero. A small field $\mu_0 H$ is then applied to remain in the linear response regime where the magnetic susceptibility depends linearly on the applied field. The magnetic moments of the sample is then measured as a function of temperature (Figure 2.30). Thermal energy will allow overcoming the MAE barrier. An increasing number of particles will pass from the blocked state to the superparamagnetic state with a response following $1/T$; this gives the ZFC susceptibility curve shown in figure 2.30.

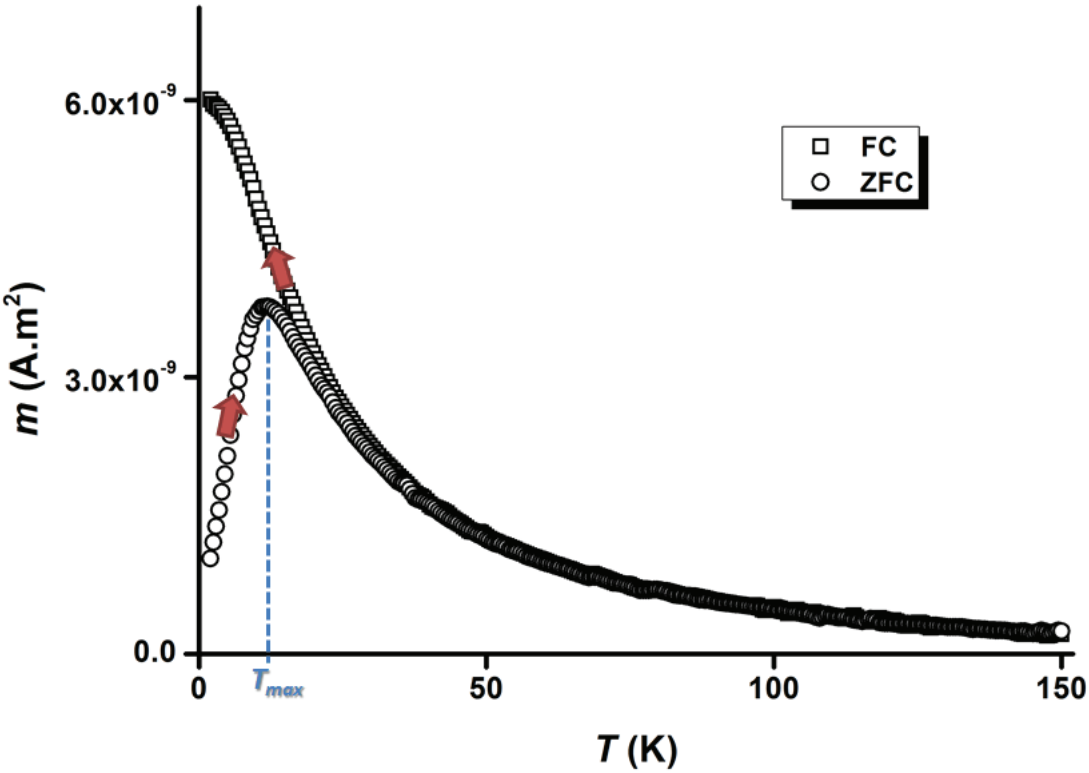

Fig. 2.30 Example of a sample of FeRh nanoparticles embedded in a carbon matrix. These curves present the schematic transition from a blocked to superparamagnetic state around T_{max}.

The FC susceptibility curve is obtained by decreasing the temperature while keeping the previously applied field H. At high temperatures, the particles are superparamagnetic, the ZFC and FC curves superpose on a $1/T$ evolving curve. Once the temperature is low enough, the particles go back to the blocked state.

2.4.3.2.2 Analytical expressions of the ZFC-FC curves It can be shown that the magnetic moment m of an assembly of nanoparticles verifies the following differential equation

$$\frac{1}{\nu}\frac{dm}{dt} + m = \frac{\mu_0 H {M_s}^2 V^2}{3\mathrm{k_B}T} \tag{2.41}$$

where ν is the reversal frequency of a macrospin and is strongly dependent on temperature:

$$\nu = \nu_0 e^{\frac{-\Delta E}{\mathrm{k_B}T}} \tag{2.42}$$

$\Delta E = K_{eff}V$ is the MAE of a particle (height of energy barrier in the absence of an applied field), supposed uniaxial. The variation of ν_0 with temperature is neglected.

A solution to this differential equation allows to write the progressive transition from a blocked to a superparamagnetic regime as proposed by [121]:

$$m_{ZFC} = m_b \exp(-\nu\delta t) + m_{sp}(1 - \exp(-\nu\delta t)) \tag{2.43}$$

$$\begin{aligned} m_b &= \frac{\mu_0 H {M_s}^2 V^2}{3\Delta E} && \text{the magnetization moment in the blocked regime} \\ m_{sp} &= \frac{\mu_0 H {M_s}^2 V^2}{3\mathrm{k_B}T} && \text{the magnetization moment in the superparamagnetic regime} \end{aligned} \tag{2.44}$$

where ν is defined in equation 2.42 and δt is defined by [127]

$$\delta t = \frac{\mathrm{k_B}T^2}{v_t \Delta E} \tag{2.45}$$

it is the effective measuring time related to the speed of temperature variation v_t (K/s) encountered in the experimental measurement. The expression 2.43 takes into account the progressive transition between the two regimes.

In this section, we are interested in the realistic case where we measure the magnetic susceptibility of a sample made up of an assembly of nanoparticles with a size distribution. In the framework of the widely accepted hypothesis, we consider that all the particles have the

same anisotropy constant K_{eff}. Thus, the distribution of the MAE $= \Delta E$ originates directly from the particles' size distribution $\rho(D)$. Strictly speaking, the blocking temperature is defined only in the case of a given MAE. When we consider an assembly of nanoparticles with a distribution of MAE, the ZFC curve present a susceptibility peak at a temperature T_{max}. The term "blocking temperature" of a sample is not correct, physically speaking. Even less to equate T_B and T_{max}. Generally, it is difficult to extrapolate how the contribution of each particle size will add up to form the previously mentioned susceptibility peak. The resulting ZFC curve is strongly dependent on the detailed size distribution within the nanoparticle assembly.

In order to perform the fit, to extract the values of the physical parameters (in particular, the effective anisotropy constant K_{eff}), it is necessary to simulate numerous theoretical curves in a short time. This implies to use simple analytical expressions. From the progressive model 2.43, the following equation is obtained for the total magnetic moment [105, 121]:

$$m_{ZFC}(T) = N_t \int_0^{\infty} \left[m_b e^{-\nu(T)\delta t(T)} + m_{sp} \left(1 - e^{-\nu(T)\delta t(T)} \right) \right] \rho(D) dD \tag{2.46}$$

or

$$m_{ZFC}(T) = N_t \int_0^{\infty} \frac{\mu_0 H {M_S}^2 V}{3K_{eff}} \left[e^{-\nu(T)\delta t(T)} + \frac{K_{eff} V}{\mathrm{k_B} T} \left(1 - e^{-\nu(T)\delta t(T)} \right) \right] \rho(D) dD \tag{2.47}$$

The FC curve can be described by the same equation considering a different initial condition when T tends to 0 defined by $M_0 = m_{FC}(T \to 0)/(N_T V)$. The corresponding equation becomes:

$$m_{FC}(T) = N_t \int_0^{\infty} \left[M_0 V e^{-\nu(T)\delta t(T)} + \frac{\mu_0 H {M_s}^2 V^2}{3\mathrm{k_B} T} \left(1 - e^{-\nu(T)\delta t(T)} \right) \right] \rho(D) dD \tag{2.48}$$

Using this equation implies that the same curve is obtained when measuring the FC curve with an applied external field when starting from low temperature or high temperature. This was verified experimentally for FC (T$\nearrow$) and FC(T$\searrow$).

2.4.3.3 Triple-fit procedure

In order to accurately determine the magnetic anisotropy and the size distribution from the magnetic measurements, it was necessary to develop a fitting procedure that can simultaneously adjust the ZFC-FC susceptibility curves and the magnetization $m(H)$ at high temperature. This was achieved using a semi-analytical model [112]. This triple fit allows

to precisely determine the common parameters between the three equations: the number of particles, the median diameter, the diameter dispersion and the effective magnetic anisotropy constant. Figure 2.31 shows that only one size distribution can fit at the same time the ZFC-FC susceptibility curves and the magnetization curve $m(H)$ at all temperatures. The triple fit thus reduces the solution range of the different parameters and the uncertainty on their values. In addition, the size distribution obtained using the triple fit perfectly corresponds to the size histogram obtained from TEM observations in the case of Cobalt nanoparticles embedded in a gold matrix.

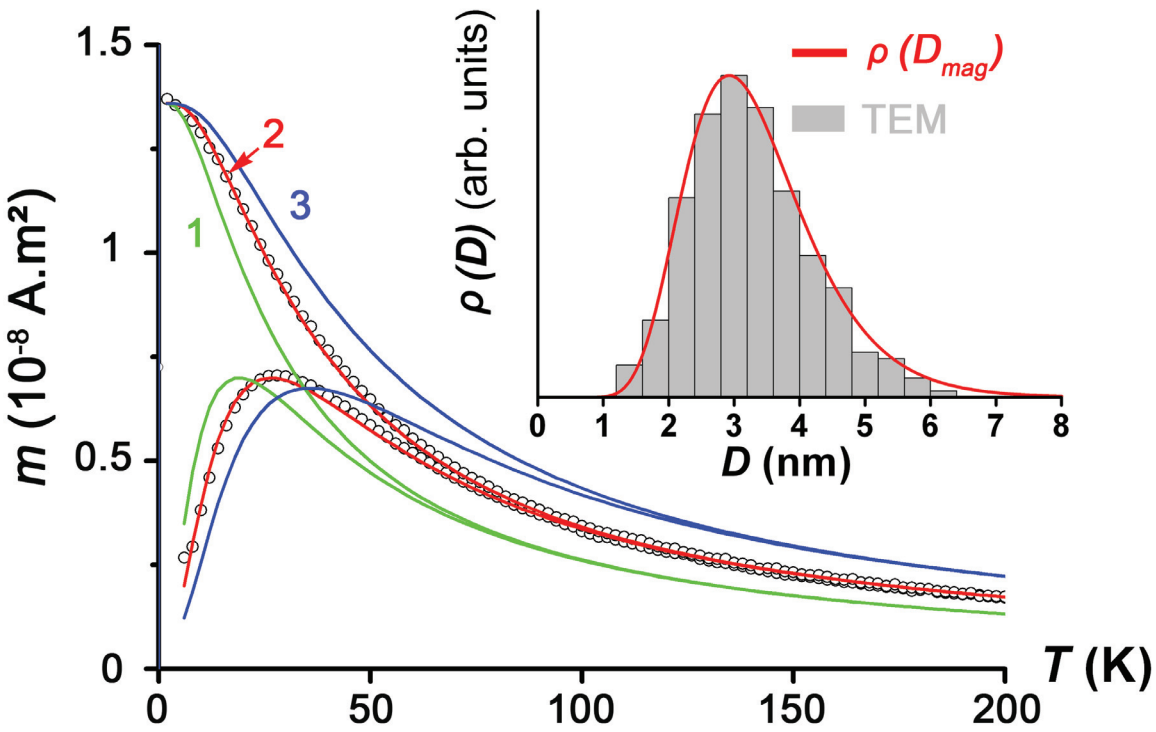

Fig. 2.31 ZFC-FC susceptibility curves for a sample of Cobalt in gold matrix. The red curve corresponds to the triple fit. The two other curves correspond to the fitting based on the size distributions of figure 2.29. The insert present the size distributions deduced from the triple fit and TEM observations.

2.4.4 Hysteresis loops (low temperature)

In order to completely understand the magnetic reversal phenomena, it is evident that the next step will be modeling of the magnetic hysteresis loops at low temperature. Hysteresis loops provide several information; depending on the state of the nanoparticles, blocked or superparamagnetic, the hysteresis loops are different. At low temperature, the particles have open loops (at least for a portion of them, in the case of a size distribution) since

they are in a blocked state. The loops thus allow measuring the coercive field ($\mu_0 H_c$) as well as the ratio between the remanent moment (m_r) and the saturation moment (m_s). The Stoner-Wohlfarth model permits to trace the hysteresis loops as a function of the orientation of the applied field for a macrospin at temperature of T = 0 K in the simple case of a uniaxial second order anisotropy. The magnetization curves can be traced in the case of an assembly of nanoparticles with a random distribution of the easy axis of magnetization (see figure 2.32). The loops are independent of the size of the nanoparticles, the ratio $M_r/M_s = 0.5$ and $\mu_0 H_c \sim K_{eff} M_s$. Experimentally, this ideal case is impossible to achieve. The temperature is often limited to 2 K, in conventional magnetometers, and thus requires taking into account the temperature and the size distribution. In addition, the uniaxial approximation is often inexact in the case of small particles [128] and the magnetic interactions between particles can not be neglected except in the case of highly diluted samples.

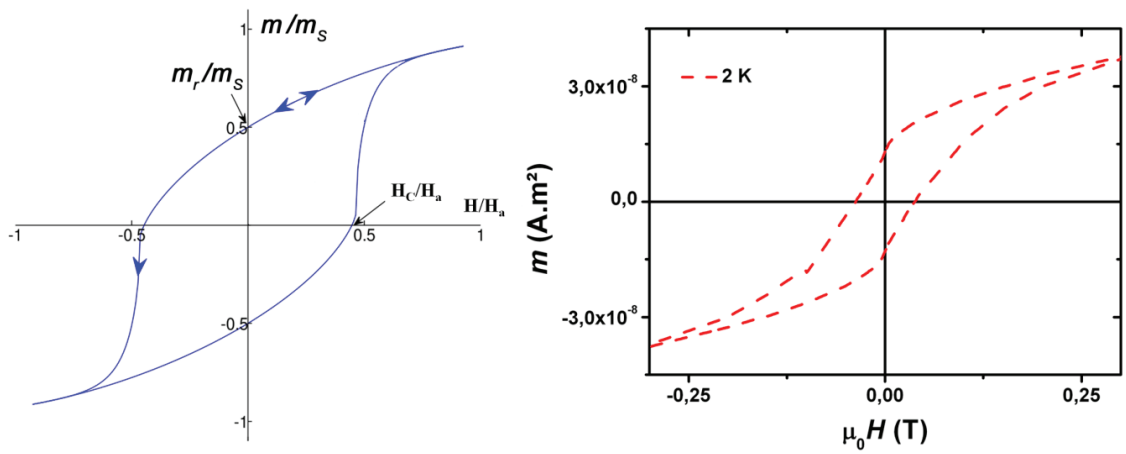

Fig. 2.32 Hysteresis loop at 0 K in the Stoner-Wohlfarth model for an assembly of three dimensional particles having randomly oriented uniaxial anisotropies (left). An example of hysteresis loops at low temperature (2 K) for an assembly of Co nanoparticles embedded in a Cu matrix (right).

Nevertheless, the hysteresis loops at 2 K offer a good indication of the anisotropy of the nanoparticles (which gives access to a lower limit for the value of K_{eff} through the coercive field) and allows verifying that $m_r/m_s < 0.5$. If we consider an assembly of nanoparticles having a given anisotropy, when the temperature increases, H_c decreases as well as the ratio m_r/m_s due to the fact that, on the one hand, some particles become superparamagnetic and secondly H_c decreases for the blocked particles. If $m_r/m_s > 0.5$, there can be different reasons: a non-random distribution of the anisotropy axis, a cubic anisotropy or interactions between the particles of ferromagnetic type.

There are several approaches to simulate the hysteresis loops at finite temperatures using the Néel relaxation [101] but applied to a monodisperse distribution [129] or without taking into account the superparamagnetic particles [130–132]. To simulate a hysteresis loop of particles with a non-uniaxial anisotropy, the switching field must be determined in the three spatial directions and not only in the plane containing the easy magnetization axis. For this, we can rely on a numerical approach [133] or a geometric method called the astroid method [134, 135]. In the latter, a direction of the magnetization $M(\theta, \varphi)$ is fixed and we search, varying the applied magnetic field, the points for which the energy barrier becomes zero and hence magnetization reversal of the particle occurs.

2.4.4.1 Uniaxial anisotropy of the second order

In what follows, we define:

- K_1, the uniaxial anisotropy constant of the second order ($K_1 < 0$), the easy magnetization axis is along z.
- θ_h and θ, are the angles between the easy magnetization axis and respectively the applied magnetic field and the direction of magnetization (see figure 2.33)
- φ_h and φ, are the angles between the x axis and the projections of respectively the applied magnetic field and the direction of magnetization (see figure 2.33).

The simulation is also based on the hypothesis of the Stoner-Wohlfarth model, *i.e.* macrospin.

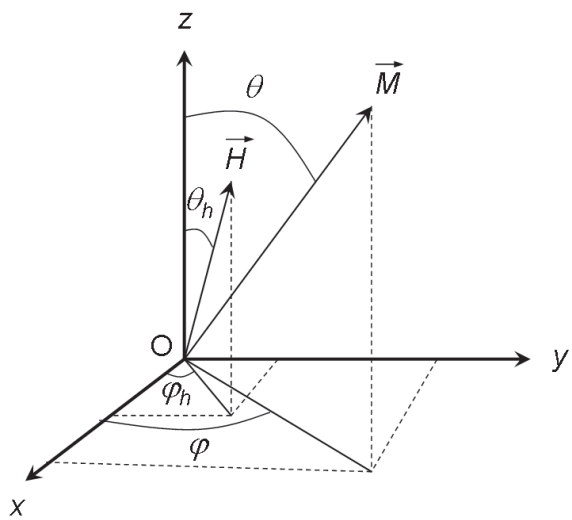

Fig. 2.33 System of axes used in the calculations. The easy magnetization axis is along z direction.

In the context of fitting the experimental data, it is necessary to obtain an algorithm capable of rapidly simulating the data. Considering only the blocked particles, the hysteresis loop can be split into two branches. A loop starts at a high magnetic field; where all the magnetic moments are aligned along this applied field. In order to simulate this first part, from H_{max} to $H = 0$, it is sufficient to minimize the magnetic energy density to find the orientation of the magnetic moments at $T = 0$ K (we always assume that when the particles are blocked, their magnetic moments stay in the energy minimum to avoid introducing a partition function). The energy density (J/m^3) is given by:

$$E_d = G(\theta) - \mu_0 \overrightarrow{H}.\overrightarrow{M} \tag{2.49}$$

where $G(\theta)$ is the magnetic anisotropy function. In the uniaxial case, it is defined by:

$$G(\theta) = K_1 {m_z}^2 = K_1 \cos^2\theta \tag{2.50}$$

with m_z the projection of the normalized magnetic moment on the easy magnetization axis. In this expression of the magnetic anisotropy $K_1 < 0$ compared to equation 2.30. The second part from $H = 0$ to $-H_{max}$ is more complicated since the magnetization reversal depends on the temperature and θ_h. Based on the SW model, the switching field at $T = 0$ K is written as:

$$H_{sw}(0) = H_a \left(\sin^{\frac{2}{3}}(\theta_h) + \cos^{\frac{2}{3}}(\theta_h)\right)^{-\frac{3}{2}} \tag{2.51}$$

where H_a is the previously defined anisotropy field. Néel [101] proposed an energy barrier that depends on the applied field, that gives when applied to the SW model:

$$\Delta E(H) = |K_1| V \left(1 - \frac{H}{H_{sw}(0)}\right)^{\alpha} \tag{2.52}$$

The value of α depends on H and θ_h. Analytically $\alpha = 2$ for $\theta_h = \pi$ or $\pi/2$, *i.e.* when the applied field is along the easy magnetization axis or perpendicular to the latter. For the other angle values between the anisotropy axis and H, α can be calculated by $\alpha = 0.86 + 1.14 H_{sw}/H_a$ [131]. Victoria [136] showed that $\alpha = 1.5$ is also a good approximation for small fields. Here, we use $\alpha = 1.5$, as a matter of fact, using the value of α given by Pfeiffer *et al*. [131] does not significantly impact the curves.

From the previous equation and the relaxation time, the following equation can be obtained:

$$\mathrm{k_B} T \ln(\frac{\tau}{\tau_0}) = K_1 V \left(1 - \frac{H}{H_{sw}(0)}\right)^{\alpha} \tag{2.53}$$

The switching volume (V_s) is thus given as:

$$V_s(T,\theta_h,H) = \frac{25k_BT}{|K_1|\left(1-\frac{H}{H_{sw}(0)}\right)^{\alpha}} \tag{2.54}$$

with the approximation of $\ln(\frac{\tau}{\tau_0}) = 25$. In other words, at a given temperature, field and θ_h, the moments of particles with $V \leq V_s$ are switched. The last step consists, from equation 2.49, on determining the direction of magnetization. Hysteresis loops were simulated at different temperatures in order to validate this method. Figure 2.34a shows the simulations of hysteresis loops for monodispersed particles of 3 nm between 0 and 12 K. The anisotropy constant was chosen equal to 1 MJ.m^{-3} to avoid all superparamagnetic contributions in this temperature range. The curves are in complete agreement with other results obtained in literature [129, 137, 138].

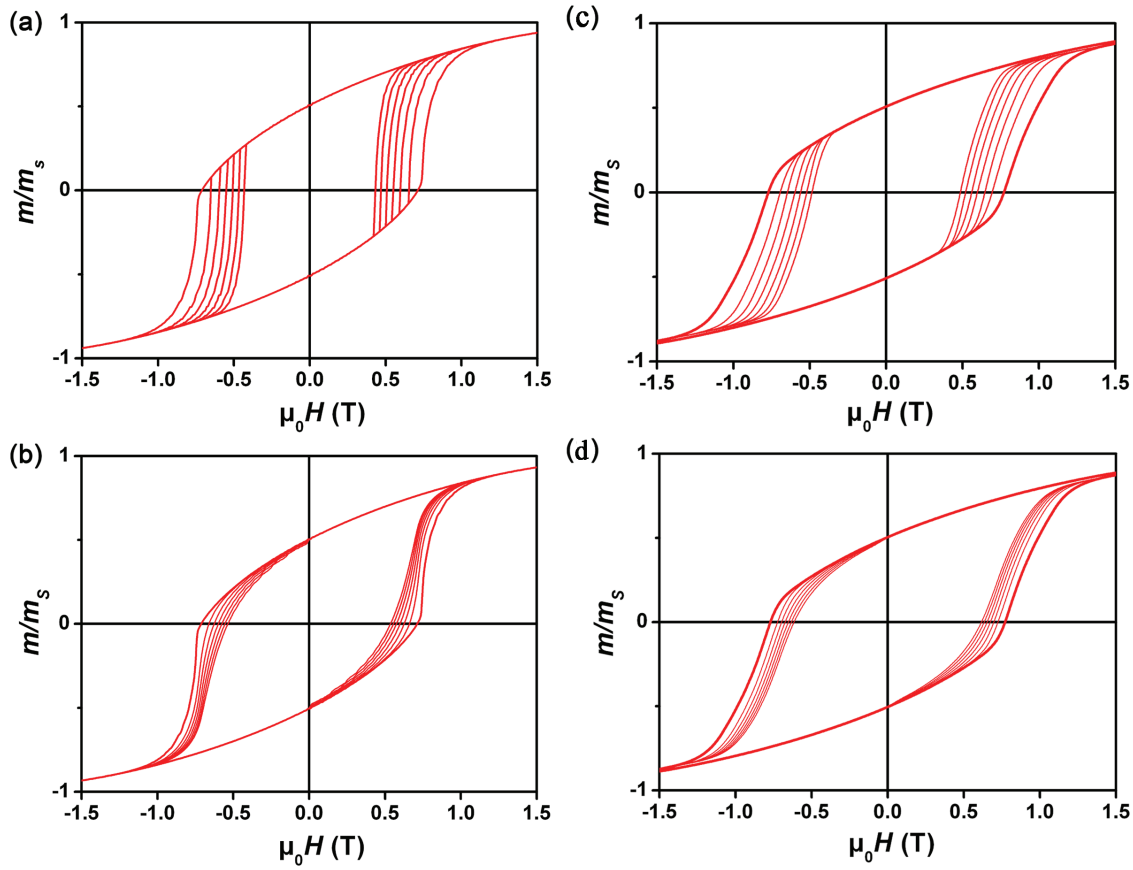

Fig. 2.34 Simulation of hysteresis loops at 2, 4, 6, 8, 10 and 12 K in the case of a uniaxial anisotropy without (a) and with a size distribution (b); in the case of a biaxial anisotropy $|K_2/K_1| = 0.5$ without (c) and with a size distribution (d).

From the switching volume, it is simple to include size effects. In figure 2.34b, hysteresis loops with a lognormal size distribution are presented with a mean diameter of 3 nm and a dispersion of 0.4. The size distribution has the effect of smoothing the curve at a finite temperature. As the temperature increases, the portion of particles in the superparamagnetic state increases as well. For values larger than 12 K, the ratio m_r/m_s decreases, signifying that the superparamagnetic contribution is no longer negligible. It should be noted that the model presented here is only valid in the case where all the particles are in the blocked regime.

2.4.4.2 Biaxial anisotropy of the second order

For all previous magnetic analysis, a uniaxial anisotropy was assumed, however, we know from μ-squid measurements on single magnetic nanoparticles, realized by M. Jamet *et al.* [128], that cobalt nanoparticles having a truncated octahedron form with supplementary facets have a biaxial anisotropy. The adjustment of the 3D astroid, with a geometrical approach shows a ratio of 0.5 between the constants of anisotropy. In addition to the supplementary facets, the particles being not perfectly spherical have a shape anisotropy. This anisotropy can be expressed in the case of an ellipse by a biaxial anisotropy of the second order. The commonly used uniaxial model is not necessarily realistic. In the case of biaxial anisotropy, the particles possess an easy magnetization axis as well as a hard magnetization axis.

$$G(\theta) = K_1 {m_z}^2 + K_2 {m_y}^2 = K_1 \cos^2 + K_2 \sin^2\theta \sin^2\varphi \tag{2.55}$$

with z the easy magnetization axis, y the hard axis and x the average axis and $K_1 < 0 < K_2$. Contrary to the uniaxial case, there is no analytical expression for the switching field (H_{sw}) in the field space in the biaxial case. The geometrical approach is used to determine the switching field of the particle, regardless of the angle of the applied external field [135]. The rest of the algorithm is identical with respect to the uniaxial case. The hysteresis loops in the biaxial case with $K_1 = -1$ MJ.m^{-3} and $K_2 = 0.5$ MJ.m^{-3} are presented in figure 2.34. Figure 2.34c shows the monodisperse case whereas 2.34d shows the hysteresis loops for a lognormal size distribution with a mean diameter of 3 nm and a dispersion of 0.4. Similar to the uniaxial case, adding a size distribution tends to smooth the curve especially as the temperature increases.

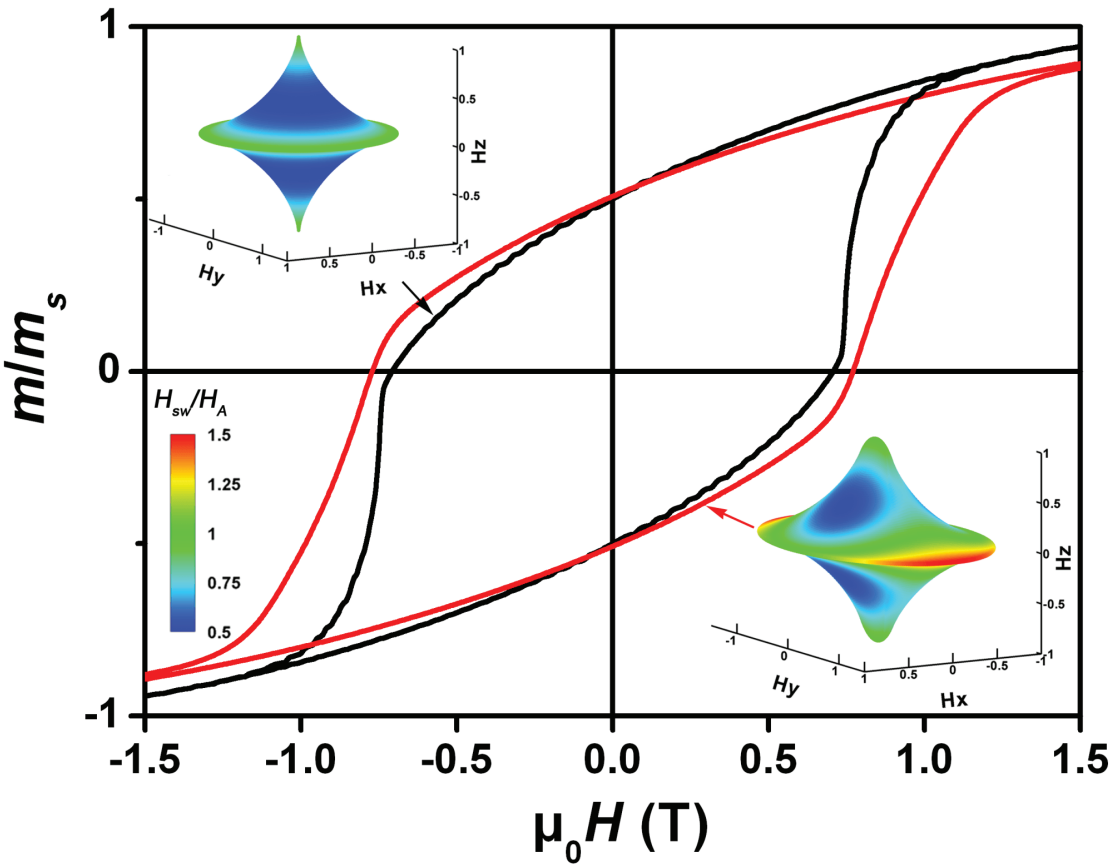

Fig. 2.35 Numeric simulation of hysteresis loops at 0 K in the uniaxial case ($K_2 = 0$) (black) and biaxial ($|K_2/K_1| = 0.5$) (red). The corresponding astroids are shown in insert.

Figure 2.35 compares two hysteresis loops at 0 K in the uniaxial and biaxial anisotropy cases. The ratio of m_r/m_s is identical in the two anisotropy cases as expected. Concerning the switching, it is less abrupt in the biaxial case, this is due to a larger distribution of switching fields. In addition, the approach to saturation is different in the two types of anisotropy. For the biaxial anisotropy, saturation is reached for a larger magnetic field value than for the uniaxial case. This slow saturation is due to particles having their hard axis y close to the direction of the applied field and thus needing a larger field to be saturated in the direction of the applied field.

To go a step further, in order to simulate experimental hysteresis loops with a size distribution, the percentage of superparamagnetic particles in the size distribution is estimated based on the experimental and triple-fit values as well as the IRM simulated values. The superparamagnetic contribution is then calculated using equation 2.40. The overall hysteresis loop is plotted and compared to the experimental data; the model used is explained in the next section.

2.4.4.3 Superparamagnetic contribution

Since the measurements are performed at 2 K, a portion of the nanoparticles present in the sample remain superparamagnetic. Thus, when simulating the hysteresis loops at 2 K their contribution must be taken into account. For a given sample, the total magnetic moment ($\mu_0 H \to \infty$) is given by the following equation:

$$m_{total} = N_T \int_0^\infty M_s V \rho(D) dD \tag{2.56}$$

where M_s is the saturation magnetization, $V = \frac{\pi D^3}{6}$ is the particle volume, D the particle diameter, N_T the number of particles in the sample and $\rho(D)$ is the diameter distribution. The limit volume between the superparamagnetic and blocked particles is given by:

$$V_{lim} = \frac{25 \mathrm{k_B} T}{K} \tag{2.57}$$

where $\mathrm{k_B}$ is the Boltzmann's constant and K is the anisotropy. The total magnetic moment can thus be written as:

$$\begin{aligned} m_{total\,(\mu_0 H \to \infty)} &= m_{SP\,(\mu_0 H \to \infty)} + m_{B\,(\mu_0 H \to \infty)} \\ &= N_T M_s \int_0^{V_{lim}} V \rho(D) dD + N_T M_s \int_{V_{lim}}^\infty V \rho(D) dD \end{aligned} \tag{2.58}$$

here, m_{SP} represents the moment of the superparamagnetic particles and m_B the moment of the blocked ones. We can write:

$$1 = \frac{\int_0^{V_{lim}} V \rho(D) dD}{\int_0^\infty V \rho(D) dD} + \frac{\int_{V_{lim}}^\infty V \rho(D) dD}{\int_0^\infty V \rho(D) dD} \tag{2.59}$$

where the first term is the percentage of magnetic moment due to the superparamagnetic particles and the second term is the percentage of the magnetic moment due to the blocked ones, *i.e.* the portion of the magnetic moment at saturation due the blocked particles is equal to 1 minus the portion of the superparamagnetic particles. The superparamagnetic moment is described by the Langevin function $Ł(x)$. The normalized superparamagnetic moment is thus written as:

$$\begin{aligned} m_{SP,norm} &= \frac{m_{SP}}{m_{SP\,(\mu_0 H \to \infty)}} \\ &= \frac{N_T M_s \int_0^{V_{lim}} V Ł(x) \rho(D) dD}{N_T M_s \int_0^{V_{lim}} V \rho(D) dD} \end{aligned} \tag{2.60}$$

For a given sample the superparamagnetic contribution, in percentage, at saturation is thus given by:

$$\begin{aligned} m_{SP} &= \% \text{ of superparamagnetic contribution} \times m_{SP,norm} \\ &= \frac{\int_0^{V_{lim}} V\rho(D)dD}{\int_0^{\infty} V\rho(D)dD} \times \frac{\int_0^{V_{lim}} V\text{Ł}(x)\rho(D)dD}{\int_0^{V_{lim}} V\rho(D)dD} \\ &= \frac{\int_0^{V_{lim}} V\text{Ł}(x)\rho(D)dD}{\int_0^{\infty} V\rho(D)dD} \end{aligned} \tag{2.61}$$

From equations 2.59 and 2.61,the total normalized theoretical moment is then written as:

$$m_{T,theo,norm} = (1 - \frac{\int_0^{V_{lim}} V\rho(D)dD}{\int_0^{\infty} V\rho(D)dD}) \times m_{sim,norm} + \frac{\int_0^{V_{lim}} V\text{Ł}(x)\rho(D)dD}{\int_0^{\infty} V\rho(D)dD} \tag{2.62}$$

where $m_{sim,norm}$ is the normalized simulated hysteresis loop at 2K, using the triple-fit and the IRM simulation values. So, the $m_{T,theo}$ from equations 2.56 and 2.62 is given by:

$$\begin{aligned} m_{T,theo} &= m_{T,theo,norm} \times m_{total} \\ &= \left[(1 - \frac{\int_0^{V_{lim}} V\rho(D)dD}{\int_0^{\infty} V\rho(D)dD}) \times m_{sim,norm} + \frac{\int_0^{V_{lim}} V\text{Ł}(x)\rho(D)dD}{\int_0^{\infty} V\rho(D)dD} \right] \\ &\quad \times N_T M_s \int_0^{\infty} V\rho(D)dD \end{aligned} \tag{2.63}$$

Since, the two branches of the hysteresis loops are symmetric with respect to the origin, it is sufficient to fit only one branch from $\mu_0 H \to \infty$ to $\mu_0 H \to -\infty$ to obtain the complete hysteresis loop with superparamagnetic contribution. It is possible to fit the hysteresis loop using the following equation:

$$m_{T,fit} = \left[(1 - A) \times m_{sim,norm} + A \frac{\int_0^{V_{lim}} V\text{Ł}(x)\rho(D)dD}{\int_0^{v_{lim}} V\rho(D)dD} \right] \times N_T M_s \int_0^{\infty} V\rho(D)dD \tag{2.64}$$

where A is a fitting parameter that correspond to the percentage of the superparamagnetic contribution to the total magnetic moment in the sample.

Figure 2.36 shows an example of a fit for the hysteresis loop at 2 K for as-prepared non mass-selected Co nanoparticles.

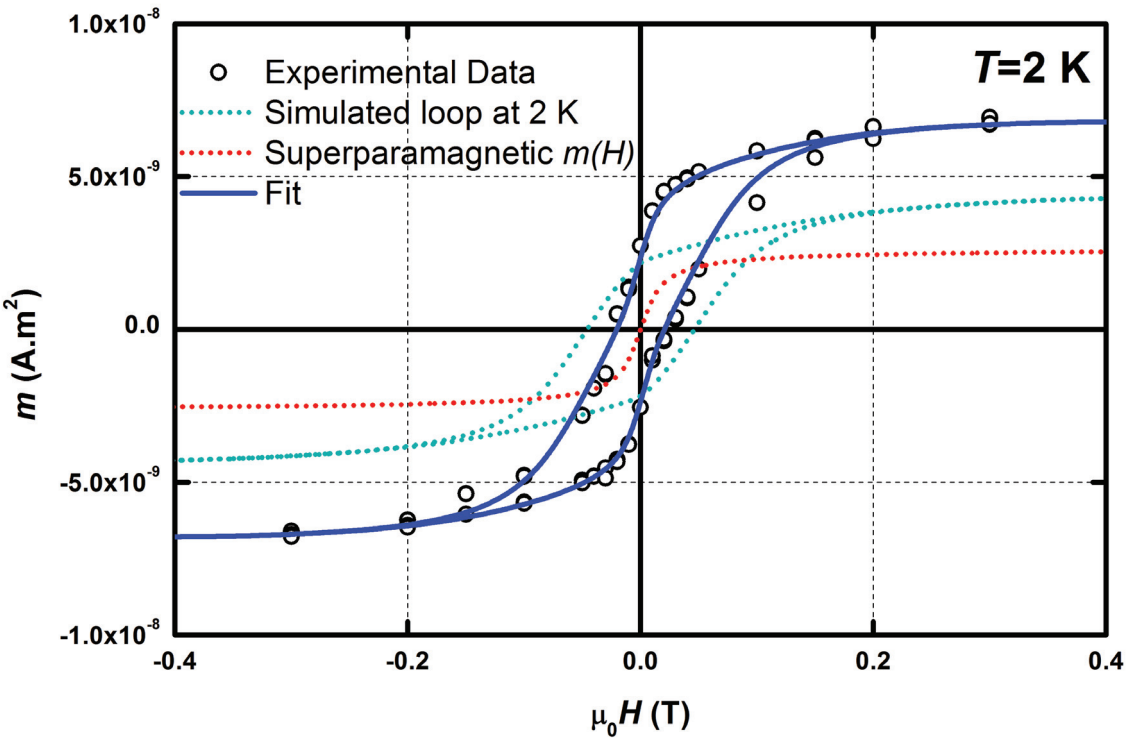

Fig. 2.36 Example of a fit for the hysteresis loop at 2 K of an as-prepared non mass-selected Co nanoparticles sample.

The simulated hysteresis loop at 2 K and the magnetization curve $m(H)$ were obtained using the same parameters as the fit (presented in chapter 4). Adjusting the value of A, it is possible to closely fit the experimental points (here $A = 35$ %).

2.4.5 Remanence measurements

2.4.5.1 IRM-DcD background

The Isothermal Remanent Magnetization (IRM) curve corresponds to a series of measurements of the remanent magnetization of an initially demagnetized sample. The measurement is done at remanence, an external magnetic field $\mu_0 H$ is applied then nullified ($\mu_0 H = 0$) at a fixed temperature after which the sample magnetization is measured. The complete curve is obtained by repeating the process of applying a field, nullifying and measuring while increasing H progressively (see figure 2.37). The acquisition process is longer than that of a typical hysteresis loop since the applied field H must be returned to zero field before doing each measurement. On the contrary, returning the field to zero allows for the measurement of only the irreversible magnetization variations of a sample. In addition, this type of measurement allows to eliminate all diamagnetic (from the substrate, for example), paramagnetic (eventual impurities) contributions as well as contributions from particles in the superparamagnetic state.

The evolution of an IRM at zero temperature comes uniquely from an irreversible change within the sample. In the case of an assembly of macrospins with uniaxial anisotropy, the magnetization reversal of some particles is measured. In the initial state IRM ($H = 0$), the particles' magnetic moments are randomly oriented, such that, statistically, the moment provided by each particle is compensated by another one. When a field is applied this symmetry is broken and one direction becomes more favourable than the others (in the half-sphere defined by the direction of the applied field H). Thus, half the particles are found in the initially stable potential well, while the other half is in the initially metastable well. The increase of the applied field H corresponds to a decrease in the energy barrier that needs to be crossed to pass from the metastable to the stable potential well. Thus, implying an increasing dissymmetry in the proportion of particles magnetized in the field direction with respect to the opposite direction. Finally, at $T = 0$ K and in the uniaxial case, the energy barrier vanishes for $H > H_a$. All the moments that pointed initially in the direction opposite of the field H have necessarily flipped. At a larger field, the IRM is identical to the hysteresis loop at $H = 0$ after saturation of the sample. This implies that $IRM(H = \infty) = m_r$.

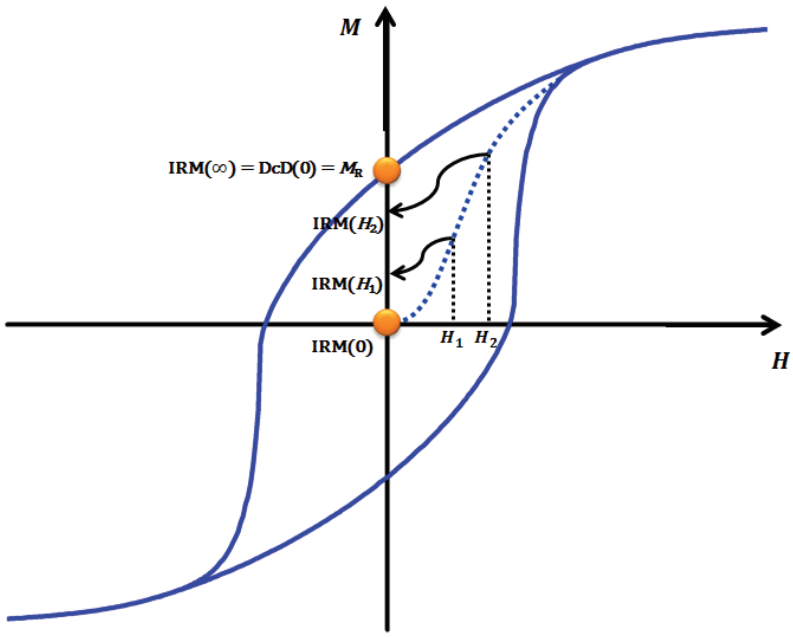

Fig. 2.37 Schematic representation of the IRM measurement.

The complementary measurement of the IRM is the Direct current Demagnetization (DcD). It corresponds to a progressive demagnetization of a sample that was initially brought to remanence after saturation in one direction. The measurement is carried out by applying an increasing field in the opposite direction, and measuring the sample's magnetization after nullifying the field ($\mu_0 H = 0$). Similar to the IRM protocol, this measurement is sensitive to the irreversible magnetization variations in the sample. Thus, it has the same physical process as the IRM curve, the difference comes uniquely from the initial state. Here, the sample is initially saturated by applying a field in the opposite direction to the one used for the acquisition of the DcD curve. The moments of all the particles are initially pointing in the same half-sphere (DcD($H = 0$) = m_r). For a sufficiently large applied field (at $T = 0$ K and for $H > H_a$), all the magnetic moments will be switched (thus (DcD($H = \infty$) = $-m_r$). In this case, the reversal concerns all the particles, whereas in the case of the IRM it concerns only half. If in the case of the IRM N particles have switched with a field H, $2N$ particles will switch in the case of the $DcD(H)$ measurement. Since the starting point of the IRM is a demagnetized state, while it is the remanent state for the DcD, the following fundamental equality can be deduced:

$$DcD = m_r - 2IRM \tag{2.65}$$

It should be noted that this equality is valid regardless of the temperature, the particle's size distribution, the anisotropy distribution, the nature of the anisotropy of the particles, and even if the magnetization reversal is achieved in an incoherent manner. On the other hand, the only hypothesis necessary for the validity of this equality is the absence of interactions between the magnetic particles. The reversal of each particle must depend only on the applied field and not on the state of the other particles. If this hypothesis, which is in practice very binding, is not verified, the magnetization reversal of the magnetic moments will depend on the environment and thus on the initial state of magnetization of the sample. A dissymmetry is thus observed between the magnetization reversal of the DcD and IRM curves and the equation 2.65 is no longer valid. Thus, the invalidity of this equality reveals the presence of magnetic interactions in the sample. This criterion is widely used to characterize the interactions in an assembly of nanoparticles, nanofilaments or thin films [139–147]. The magnitude Δm is considered in this case and is defined as:

$$\Delta m = DcD(H) - (m_r - 2IRM(H)) \tag{2.66}$$

This magnitude corresponds to the difference between the number of moments that switch in the IRM measurement and those that switch in the DcD measurement as a function of field. Thus, a negative value for Δm signifies that the magnetic moment is most easily switched when the initial state is the remanent state (the magnetic moment of all the particles point in the same half-sphere). Considering only one direction, this means that for the moment for a given particle, the switching from $+z$ to $-z$ direction is easier when the other particles have a global magnetic moment directed towards $+z$. This translates to demagnetizing interactions (as the case of dipolar interactions). On the contrary, a positive Δm means that it is harder to switch the magnetic moments when its neighbours have a global orientation in the same direction. This translates to magnetizing interactions (as the case of exchange interactions of the ferromagnetic type). Another way to present the Δm is the Henkel graph [148]. Figure 2.38 shows the theoretical IRM, DcD and Δm curves for an assembly of randomly oriented uniaxial macrospins and without interactions ($\Delta m = 0$). We will therefore use:

- $\Delta m < 0$, demagnetizing interactions
- $\Delta m > 0$, magnetizing interactions
- $\Delta m = 0$, no interactions.

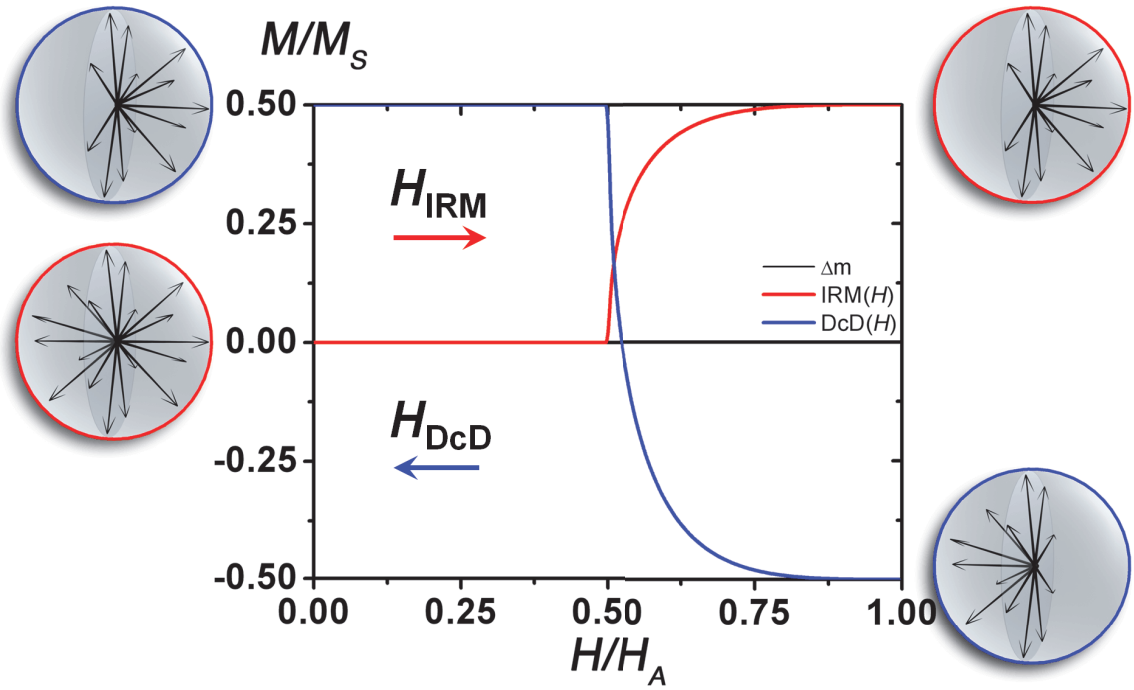

Fig. 2.38 IRM, DcD and Δm curves calculated at $T = 0$ K for an assembly of randomly oriented uniaxial macrospins.

2.4.5.2 Analytical expressions

2.4.5.2.1 Expressions at zero temperature As in the case of low temperature hysteresis loops, for the remanent measurements the Stoner-Wohlfarth model is considered. θ_h and θ are the angles between the easy magnetization axis and respectively the applied magnetic field and the magnetization direction. An assembly of N_{tot} macrospins considered where the magnetization axis is randomly oriented, the uniaxial anisotropy constant K_{eff} is the same and the saturation magnetization M_s is also the same ($m_s = M_s V$ for all macrospins). The anisotropy field H_a is thus the same for all particles:

$$H_a = \frac{2K_{eff}}{\mu_0 M_s} \tag{2.67}$$

At zero temperature, a macrospin only switches if the applied field is larger than the switching field ($H_{sw}(\theta_h)$).

$$H_{sw}(\theta_h) = H_a \left(\sin^{\frac{2}{3}}(\theta_h) + \cos^{\frac{2}{3}}(\theta_h) \right)^{-\frac{3}{2}} \tag{2.68}$$

The particles for which $\theta_h = \pi/4$ are the first to switch, and require to have an applied field such that $H > H_a/2$. Thus, no particle will switch as long as $h = H/H_a$ is smaller than 1/2. Similarly, since the maximal switching field is H_a, for an applied field $H > H_a$, all the particles that initially point in the same half-sphere opposite to the direction of H will switch (which corresponds to half the particles). The particles are thus pointing in the same half-sphere, which corresponds to a remanent moment of $m_r = N_{tot} m_s/2$. Which leads to:

$$\begin{aligned} IRM(H) &= 0 \text{ for } H \in [0, H_a/2] \\ IRM(H) &= N_{tot} m_s/2 \text{ for } H > H_a \end{aligned} \tag{2.69}$$

For the $H \in [H_a/2, H]$ zone, only particles with certain range of θ_h may switch. This range of angles is $[\theta_{h1}, \theta_{h2}]$, where the two limits depend on H. The moments of the particles whose angles between the anisotropy axis and the applied field are within the interval $[\theta_{h1}, \theta_{h2}]$ (see figure 2.39) and which are in the potential well corresponding to the stable position are no longer compensated for by the moments between $\theta_{h1} + \pi$ and $\theta_{h2} + \pi$, which gives:

$$IRM(H) = 2 \int_{\theta_{h1}(H)}^{\theta_{h2}(H)} N_{tot} m_s \cos\theta_h \rho(\theta_h) d\theta_h \tag{2.70}$$

and since $H_{sw}(\theta_h)$ is symmetric with respect to the angle $\theta_h = \pi/4$ (see figure 2.39), the expression simplifies into:

$$IRM(H) = \frac{N_{tot} m_s}{2} \frac{1 - x^3}{1 + x^3} \tag{2.71}$$

with

$$x = \left((1 + 2h^2) - \sqrt{12h^2 - 3} \right) / (2 - 2h^2) \text{ and } h = \frac{h}{H_a} \tag{2.72}$$

This expression was used to simulate the IRM curves in figure 2.39. It is important to note that similar to the hysteresis loops at zero temperature, the IRM curve has no dependence on the size of the particles. In fact, the switching field H_{sw} depends on K_{eff} and not on V. Thus, the curve is identical with or without a size distribution $\rho(V)$. It is only at finite temperatures that the effects of a size distribution are visible.

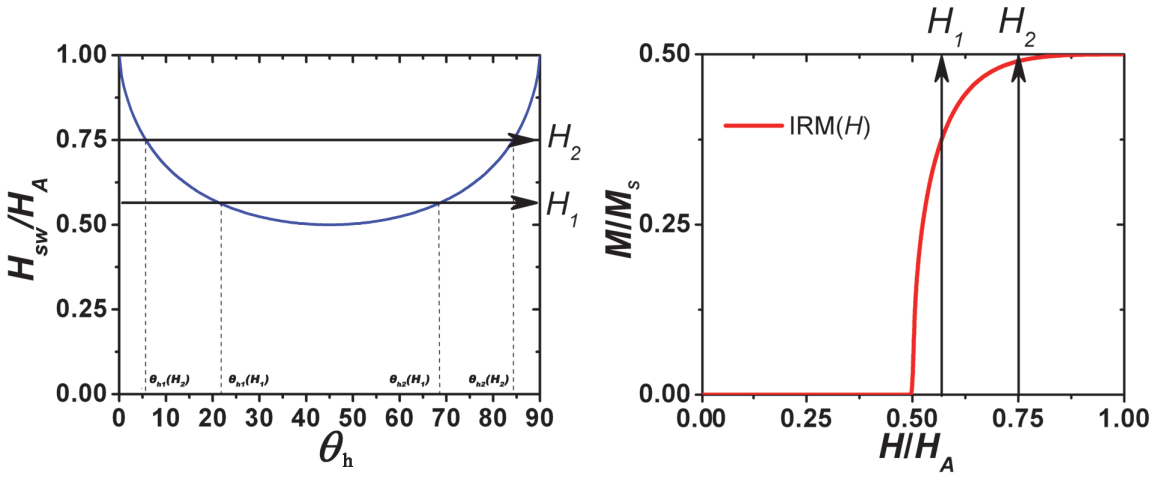

Fig. 2.39 Numerical simulation of an IRM curve at 0 K (right) for a 3D assembly of uniaxial macrospins deduced from the switching field H_{sw} (left).

For the DcD curve and in the absence of magnetic interactions, equation 2.65 allows to directly obtain the $DcD(H)$ curve from the $IRM(H)$:

$$DcD(H) = m_r - 2IRM(H) \tag{2.73}$$

For:

$$\begin{aligned} DcD(H) &= m_r \text{ for } H \in [0, H_a/2] \\ DcD(H) &= -m_r \text{ for } H > H_a \end{aligned} \tag{2.74}$$

In the interval where $DcD(H)$ passes from m_r to $-m_r$, *i.e.* for $H \in [H_a/2, H]$, the equation becomes:

$$DcD(H) = \frac{N_{tot} m_s}{2} \frac{3x^3 - 1}{1 + x^3} \tag{2.75}$$

2.4.5.2.2 Temperature integration When the temperature is not zero, it is no longer necessary to cancel the energy barrier to switch the macrospin from the metastable well to the stable one. The reversal becomes statistically possible with the help of the thermal energy. The Néel relaxation model is used to take into account the thermal energy that can reverse the magnetization. Taking into account the temperature contribution, the calculation is similar to the case of low temperature hysteresis loops. Equation 2.53 is modified in order to determine a temperature dependent switching field.

$$H_{sw}(T) = H_{sw}(0) \left\{ \left[1 - \frac{25 k_B T}{K_1 V} \right]^{1/\alpha} \right\} \tag{2.76}$$

Neglecting the dependence of the energy barrier on θ_h and H, leads to:

$$H_{sw}(T) = H_{sw}(0)\gamma(T)$$
$$\text{with } \gamma(T) = \left\{ \left[1 - \frac{25k_B T}{K_1 V} \right]^{1/\alpha} \right\} \tag{2.77}$$

It should be noted that the switching field is zero if $K_1 V = 25k_B T$. Thus, in a coherent manner, the switching field of superparamagnetic particles is zero. The particles do not add any contribution to the IRM curve since they have a reversible behaviour. The IRM curve is given by the same formula as before, the only difference is that x must be calculated with a reduced field h that takes into account the temperature.

2.4.5.2.3 Size distribution In order to take into account the size distribution, it is sufficient to numerically integrate the contribution of each size. Taking $\rho(V)$ as the size distribution, the expression of IRM becomes:

$$IRM(H) = \int_0^\infty IRM(V,H)\rho(V)dV \tag{2.78}$$

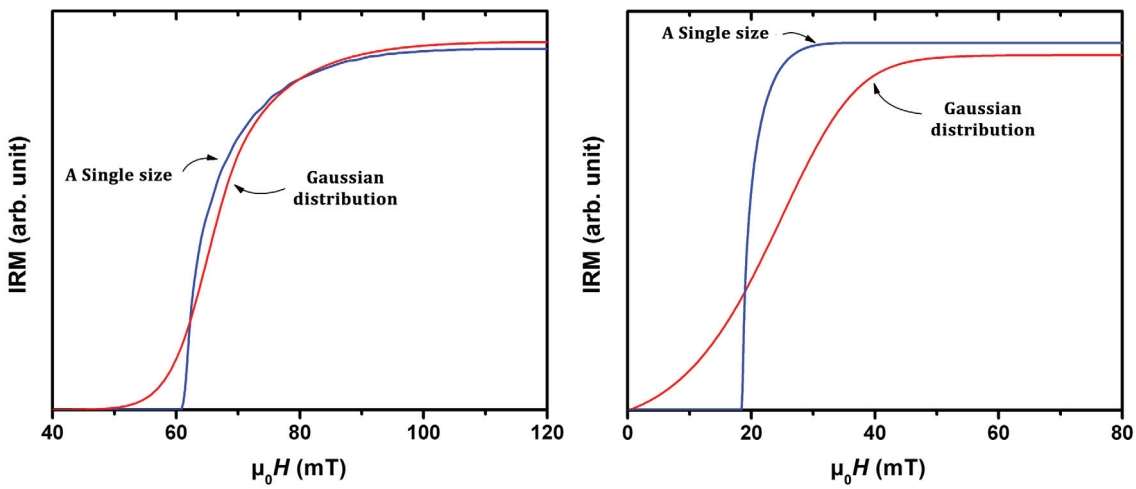

Fig. 2.40 Simulated IRM curve, at 2 K, for an assembly of particles with a Gaussian size distribution with a mean diameter of 4 nm (left) and 2.5 nm (right) with a dispersion of 8%, as well as for a single size.

Figure 2.40 presents simulated IRM curves at 2 K for Gaussian size distribution centered around 2.5 and 4 nm with a relative dispersion of 8%. The size distribution has the effect of smoothing the curve. The contribution of each size of particles by their volume is taken

into account in equation 2.78. Taking, as an example, the case of a given K_{eff} (*i.e.* a given anisotropy field), the largest particles have the highest switching field. The transition zone thus moves to the strong fields when the particles size increases (with a constant relative dispersion), as can be seen in figure 2.41. The large particles contribute more to the signal compared to the smaller ones. In addition, an increase of the size dispersion not only has the effect of increasing the transition zone, but also shifting of the zone towards larger fields (so long as the mean size and the mean switching field remain unchanged), as shown in figure 2.41.

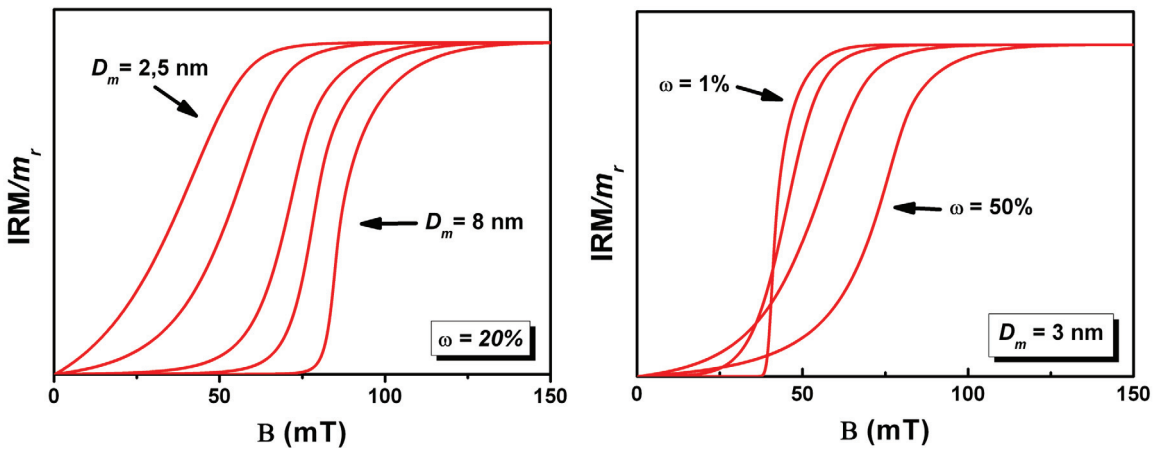

Fig. 2.41 Simulated IRM curve at 2 K, normalized with respect to m_r, for an assembly of particles with a Gaussian size distribution. (Left) The effect of changing the mean diameter: D_m takes the values of 2.5, 3, 4, 5 and 8 nm successively while the relative dispersion is fixed to ω = 20 %. (Right) The effect of changing the relative dispersion: ω takes the values 1 %, 8 %, 20 % and 50 % while D_m is fixed to 3 nm.

Finally, with respect to the ZFC/FC curves where only the product $K_{eff}V$ has an influence on the shape of the curve, a variation of K_{eff} (with MAE constant) modifies the IRM curve in a notable manner. While in the ZFC-FC case, the couples (K_{eff},V) and ($K_{eff}/2$,$2V$) give a curve with the same shape, in the case of the IRM, these two parameter couples give two completely different IRM curves (see figure 2.42). In this case, the IRM measurements are complementary to the ZFC/FC susceptibility curves which themselves bear the signature of the magnetic anisotropy by means of a thermal switching.

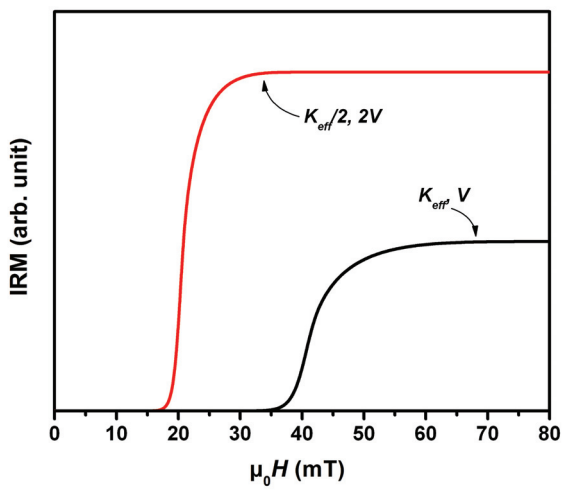

Fig. 2.42 Comparison of IRM curves for the couples (K_{eff},V) and ($K_{eff}/2$,$2V$).

2.4.5.2.4 Anisotropy constant distribution The expression for the IRM curve in the case of an anisotropy constant dispersion is given by:

$$IRM(H) = \int_0^{\infty} IRM(K_{eff}, H)\rho(K_{eff})dK_{eff} \tag{2.79}$$

As can be seen from figure 2.43, the dispersion of K_{eff} widens the transition zone of the IRM without a significant shifting of the inflection point (contrary to the case of size dispersion, here all the K_{eff} contribute with the same weight to the IRM curve).

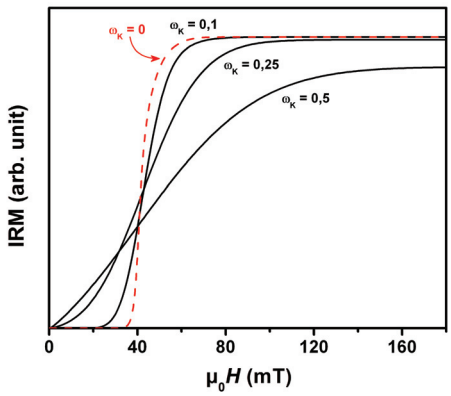

Fig. 2.43 Simulated IRM curve at 2 K for a particle assembly of a 3 nm diameter with a Gaussian anisotropy constant distribution $\rho(K_{eff})$ centered at 120 kJ.m^{-3} and for different relative dispersions $\omega(K)$.

2.4.5.2.5 Case of biaxial anisotropy It is possible to integrate a biaxial anisotropy of the second order in the IRM simulations. Nevertheless, the analytical expression presented in the case of a low temperature hysteresis loop can not be used since H_{sw} is no longer symmetric with respect to $\pi/4$. Similar to the case of the hysteresis loops, the method of Thiaville [134, 135] is used based on a geometrical approach to determine the switching field of a particle, for any given angle of the applied external field. Figure 2.44 compares the IRM curves at 0 K in the cases of uniaxial and biaxial anisotropies with $K_1 = -1$ MJ.m^{-3} and $K_2 = 0.5$ MJ.m^{-3}. In the biaxial case, the reversal is less abrupt. The latter is due to a larger distribution of switching fields.

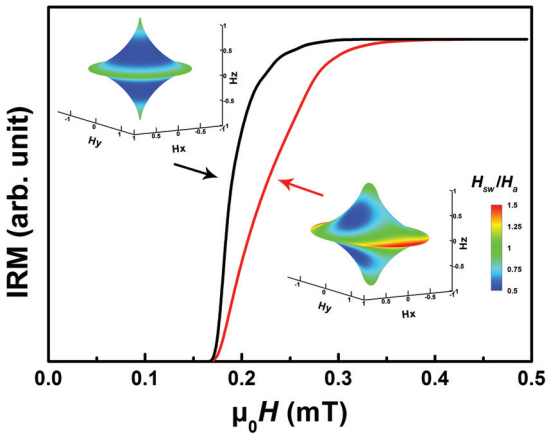

Fig. 2.44 Simulated IRM curves at 0 K in the case of uniaxial ($K_2 = 0$) (black) and biaxial ($|K_2/K_1| = 0.5$) (red) anisotropies. The corresponding astroids are presented in insert.

CHAPTER 3

STRUCTURE AND MORPHOLOGY OF NANOPARTICLE ASSEMBLIES EMBEDDED IN A MATRIX

The structure of the nanoparticles is often different from that of the bulk. Indeed, the structure is determined by the confinement effects at the surface. In a nanoparticle of Co, Fe or FeCo having a 3 nm diameter, 40 % of the atoms are on the surface where the breaking of atomic bonds increases the overall energy of the system. As such, the particles will adopt a crystalline structure, interatomic distance and a morphology (facets for example) that will minimize their total free energy, including surface and magnetic energies. It is thus necessary to understand the structure of nanoparticles in order to reach a better understanding of their magnetic properties. In particular, the crystalline structure sets the internal symmetries in the nanoparticles and consequently the easy magnetization direction. Associated to the structure, the interatomic distance which is an important parameter of the band structure of metals determines the exchange coupling constant, so the magnetic moment per atom and the Curie temperature of the system. It also influences the sign and intensity of the magnetic crystalline anisotropy constants. In addition, the morphology of the particles determines the shape and surface magnetic anisotropy that can dominate all the other anisotropy terms at this scale. We will thus describe in this chapter in a detailed manner the structure of the deposited nanoparticles.

3.1 Structure and morphology of the nanoparticles

In almost all of the studies that have already been performed on small particles, the interatomic distance is reduced when the size decreases. The first experimental evidence was achieved by Apai *et al*. [149] on copper and nickel particles smaller than 4.5 nm deposited on an amorphous carbon substrate. This study using X-ray absorption (EXAFS) has shown a contraction of the lattice parameters reaching 10 %. The same observations were made

by Montano *et al*. on copper particles embedded in a silver matrix [150]. In this case, the variation of the lattice parameter was only effective for sizes lower than 1.5 nm. Recently, Balerna *et al*. demonstrated a contraction of the interatomic distance in gold particles inversely proportional to the grain diameter [151]. These effects were theoretically confirmed in Iron clusters Fe_N (N<=9, N=11, 13, 19) when allowing a uniform relaxation in the lattice parameter. The contraction varies between 2 and 4 % [152]. Other $ab-initio$ studies allowing a complete relaxation of the structure were done on Co and Fe clusters containing a maximum of 7 atoms and gave the same results [153, 154].

In addition, the clusters' crystalline structure strongly depends on the size and environment of the particles. For cobalt clusters, a metastable cubic structure was observed by Respaud *et al*., in nanoparticles having a diameter smaller than 2 nm [126] identified as ε-cobalt with a unit cell similar to that of β-Manganese by Dinega *et al*. [155]. The particles were prepared by chemical means and stabilized in a polymer [156]. The discovery of this new phase reveals the critical role of ligands and surfactants on crystals grown in a solution at low temperature. This structure was also observed by Dureuil *et al*. for a portion of small Cobalt nanoparticles prepared by atomic deposition of cobalt atoms evaporated by pulsed laser ablation (PLD) on an alumina substrate [157]. When the size increases, or after annealing, the particles adopt a more stable and compact structure of face centered cubic (fcc) type. This was observed for different synthesis techniques, both physical and chemical: laser vaporization and condensation by an inert gas (as is used in this work) [59–61] or by the chemical method of reverse micelles [158]. It should be noted that this structure is the cobalt bulk stable structure for a temperature $T > 670$ K. In the case of clusters, it is the surface effects that stabilize this crystalline structure. In a wide size range (from 10 to around 100 nm), both the fcc and hexagonal close compact (hcp) of bulk cobalt coexist. The presence of stacking faults thus allows some particles to have the two structures [159]. For large particles, the final structure is the cobalt bulk hexagonal close packed compact structure. For iron particles, the bulk bcc structure (α-Fe) is systematically observed for all sizes [159]. Nevertheless, the unstable fcc structure (γ-Fe) can be observed at $T < 300$ K in thin films epitaxy on adapted substrates [160] such as copper (111). The fcc structure is the bulk stable structure of iron at $T > 1184$ K and can be ferromagnetic, antiferromagnetic or non-magnetic depending on the lattice parameter value [161].

Moreover, at the nanoscale, in order to minimize their surface energy, crystallized particles have facets. The different crystalline planes do not have the same surface energy. To study the morphology of the particles, a simple geometric model, the Wulff theorem [162], allows

to predict the stable shapes of the fcc and bcc structures. In this model, the minimization of the free surface energy is given by the relation:

$$\frac{\gamma_i}{h_i} = constant \tag{3.1}$$

where γ_i is the surface energy of the facet i, h_i is the distance between the facet i and the polyhedron center. An atom tends to have the maximum number of neighbours to minimize his energy; we obtain in the case of a fcc structure the different surface energies: $\gamma_{111} < \gamma_{100} < \gamma_{110}$. The stable shape for of a fcc particle is thus [163]:

- truncated octahedron if:

$$\frac{\gamma_{110}}{\gamma_{111}} > \sqrt{\frac{3}{2}} \quad \text{and} \quad \frac{\gamma_{100}}{\gamma_{111}} > \frac{\sqrt{3}}{2} \tag{3.2}$$

- cuboctahedron if:

$$\frac{\gamma_{110}}{\gamma_{111}} > \sqrt{\frac{3}{2}} \quad \text{and} \quad \frac{\gamma_{100}}{\gamma_{111}} < \frac{\sqrt{3}}{2} \tag{3.3}$$

In the case of cobalt with a fcc structure, $\gamma_{100}/\gamma_{111} = 1.03 > \sqrt{3}/2$ [164] so the stable shape is a truncated octahedron (see figure 3.1). In the case of Iron with a bcc structure, the (110) facet is the most dense facet and the shape at equilibrium is the rhombic dodecahedron (see figure 3.1) presenting 12 (110) facets.

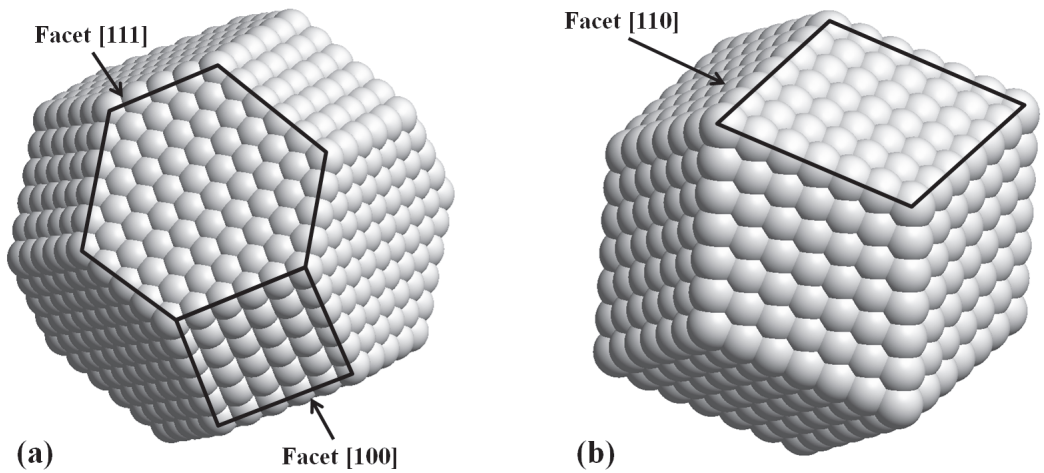

Fig. 3.1 Stable shape for a face centered cubic: truncated octahedron (a) and a body centered cubic: rhombic dodecahedron (b).

In the case of FeCo, the bulk bcc structure (α) is observed in the case of small FeCo particles (5-12 nm) [165] as well as in large sized particles (20 nm) [42] for equimolar

$Fe_{0.5}Co_{0.5}$. In the case of thin films, Burkert *et al*. investigated the possibility of increasing the magnetic anisotropy by tetragonally distorting the lattice parameters using epitaxial growth of alternating films of Fe and Co on a Ru buffer [27]. Ohnuma *et al*. managed to obtain the phase diagram for the FeCo binary alloy in thin films [16]. For the bulk equimolar FeCo alloys, the bcc phase is known to be stable up to a temperature of 985°C with a chemically disordered A2 phase (α). A chemically order B2 phase (CsCl-type, α') exists below a temperature of 730°C. To go a step further, density-functional $ab-initio$ calculations were carried on using the SIESTA code [166] in collaboration with Aguilera-Granja *et al*. (private comm.) to perform first principles electronic, magnetic and structural calculations on rhombic dodecahedron FeCo nanoparticles in the CsCl-B2 phase as a function of size. Table 3.1 presents the values obtained from the SIESTA code for the interatomic distances, magnetic moments per atom as well as the number of holes for the different FeCo cluster sizes in CsCl-B2 phase and depending on the central atom. Figure 3.2 shows the two schematics of a 15 atoms or 65 atoms clusters with different central atom (Fe or Co).

Number of atoms	Central atom	Fe-Fe	Co-Co	Fe-Co	m_{Fe}	m_{Co}	m_{av}	n_{Fe}	n_{Co}
15	Fe	2.74	2.86	2.42	3.32	2.09	2.67	3.24	2.13
	Co	2.89	2.67	2.41	3.47	2.17	2.87	3.29	2.12
65	Fe	2.89	2.77	2.45	3.02	1.76	2.40	3.22	2.10
	Co	2.89	2.80	2.47	3.02	1.77	2.38	3.23	2.11
175	Fe	2.89	2.81	2.47	2.92	1.67	2.29	3.22	2.11
	Co	2.89	2.82	2.47	2.93	1.67	2.30	3.22	2.10
Bulk FeCo	-	2.90	2.90	2.51	2.88	1.69	2.29	3.26	2.17

Table 3.1 Interatomic distances, magnetic moments and number of holes obtain for FeCo CsCl-B2 phase clusters with three different sizes depending on the central atom (see figure 3.2).

In addition, figure 3.3 shows the evolution of the interatomic distances (Fe-Fe, Co-Co and Fe-Co) for the different sizes in the CsCl-B2 phase. In the figure, the two spots for the same size correspond to the two possible central atom positions (see figure 3.2). For the 15-atoms clusters, depending on the central atom configuration, two different minima were found for the distances d_{Fe-Fe} and d_{Co-Co}. In addition, it can be deduced that as the size of the nanoparticle increases these simulated values converge towards the bulk values presented in the figure 3.3 as horizontal pointed black lines. Moreover, on the same graph, the values for clusters having respectively N=1695, 4641 and 9855 are marked as vertical dashed blue

lines. These values correspond to nanoparticles with sizes around 3.7 nm, 4.3 and 6.1 nm. These three sizes are further discussed in this chapter.

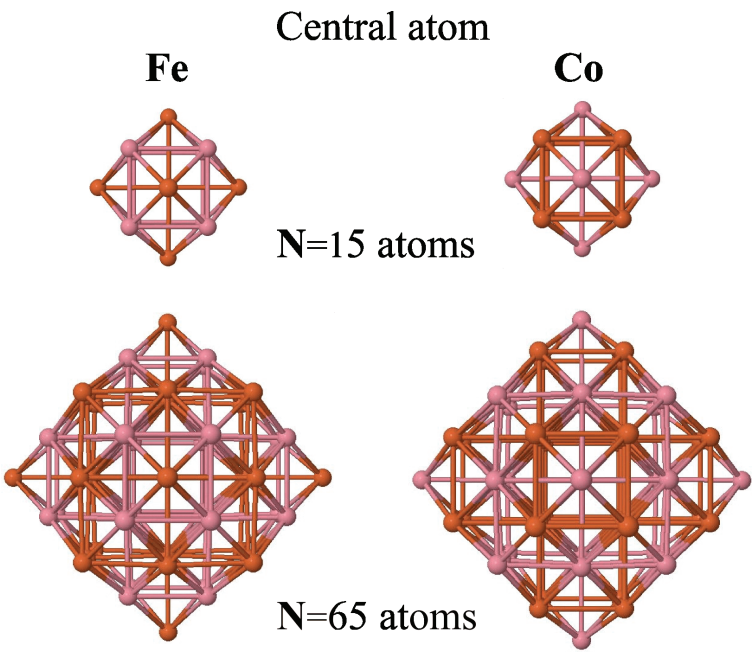

Fig. 3.2 Schematic representation of N = 65 atoms clusters having different central atoms.

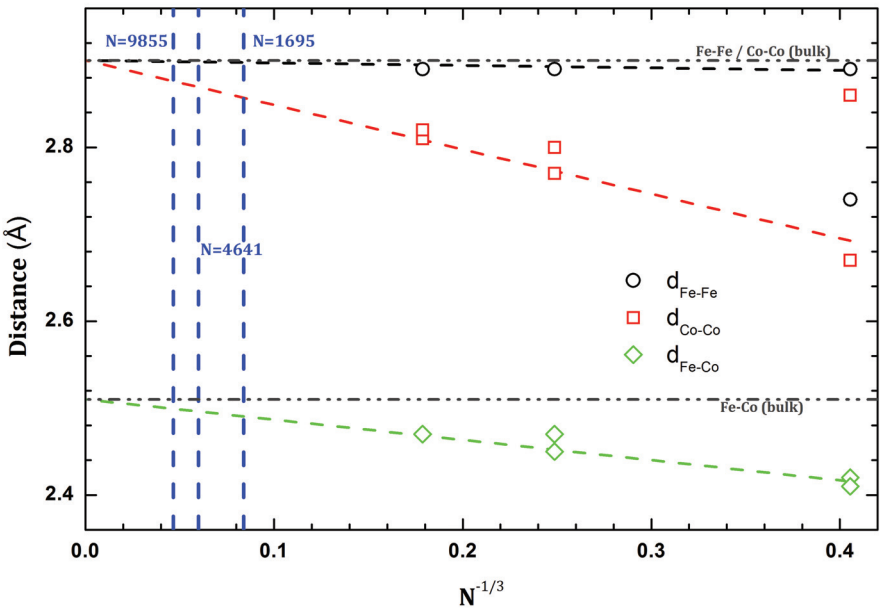

Fig. 3.3 Evolution of the interatomic distances of Fe-Fe, Co-Co and Fe-Co as a function of size from SIESTA calculations.

In order to experimentally study the crystallographic structure of the particles, two main techniques were used: TEM (including HRTEM) and EXAFS.

3.2 Size distribution of clusters

In order to determine the size distribution, the clusters are deposited on a commercial copper grid covered by an amorphous carbon coating (thickness 50 Å) under UHV conditions. Afterwards they are capped by another layer of amorphous carbon of thickness around 20-30 Å to protect them from oxidation. An equivalent cluster thickness of 0.5 Å is deposited in total, which permits to obtain well isolated particles on the carbon film (the diffusion of particles on such amorphous surface being negligible). To image the nanoparticles a diaphragm is placed in the focal plane of the objective lens of the microscope, the nanocrystallized clusters that diffuse the electrons (especially if the atomic number Z of the atoms is high) appear as shadows on the images, the bright background corresponds to the amorphous carbon. The magnification used to obtain the size distribution is 110 000 times. The images are then numerically treated using the *ImageJ* software. We suppose that the clusters have a quasi-spherical shape, the size distribution can be fitted with a lognormal function (equation 2.21) for clusters prepared with the classic source (no mass-selection) or a Gaussian function (equation 2.22) for clusters prepared with the mass selected source. The error made on the particle diameter when treating numerically the images is difficult to estimate, however it does not exceed 5 %.

3.3 Size and composition

3.3.1 Neutral clusters

3.3.1.1 Lognormal distribution

The observations were done on the Centre LYonnais des Microscopies (CLYM) on high resolution microscopes of type TOPCON 002B and JEOL 2010F. The corresponding microscopy images and size distributions are reported in figures 3.4 (a), (b) and (c) for cobalt, iron and iron-cobalt clusters respectively. These figures correspond to neutral clusters (non mass-selected) of Co, Fe and FeCo deposited at 0.01 Å/s. The best fit of the size histograms for neutral deposited clusters is obtained using a lognormal type distribution. During the image treatment of the TEM micrographs, an ellipsoidal shape was used to fit the projections

of the nanoparticles. The area of the latter was used to estimate an average diameter per nanoparticle.

For the pure cobalt clusters, the size distribution is centered at $D_m = 3.3 \pm 0.2$ nm with a dispersion of $\omega = 0.39 \pm 0.03$. For pure iron clusters, the size distribution is centered at $D_m = 3.5 \pm 0.2$ nm with a dispersion of $\omega = 0.24 \pm 0.03$. For the iron-cobalt nanoparticles, the size distribution is centered at $D_m = 3.2 \pm 0.2$ nm with a dispersion of $\omega = 0.45 \pm 0.03$.

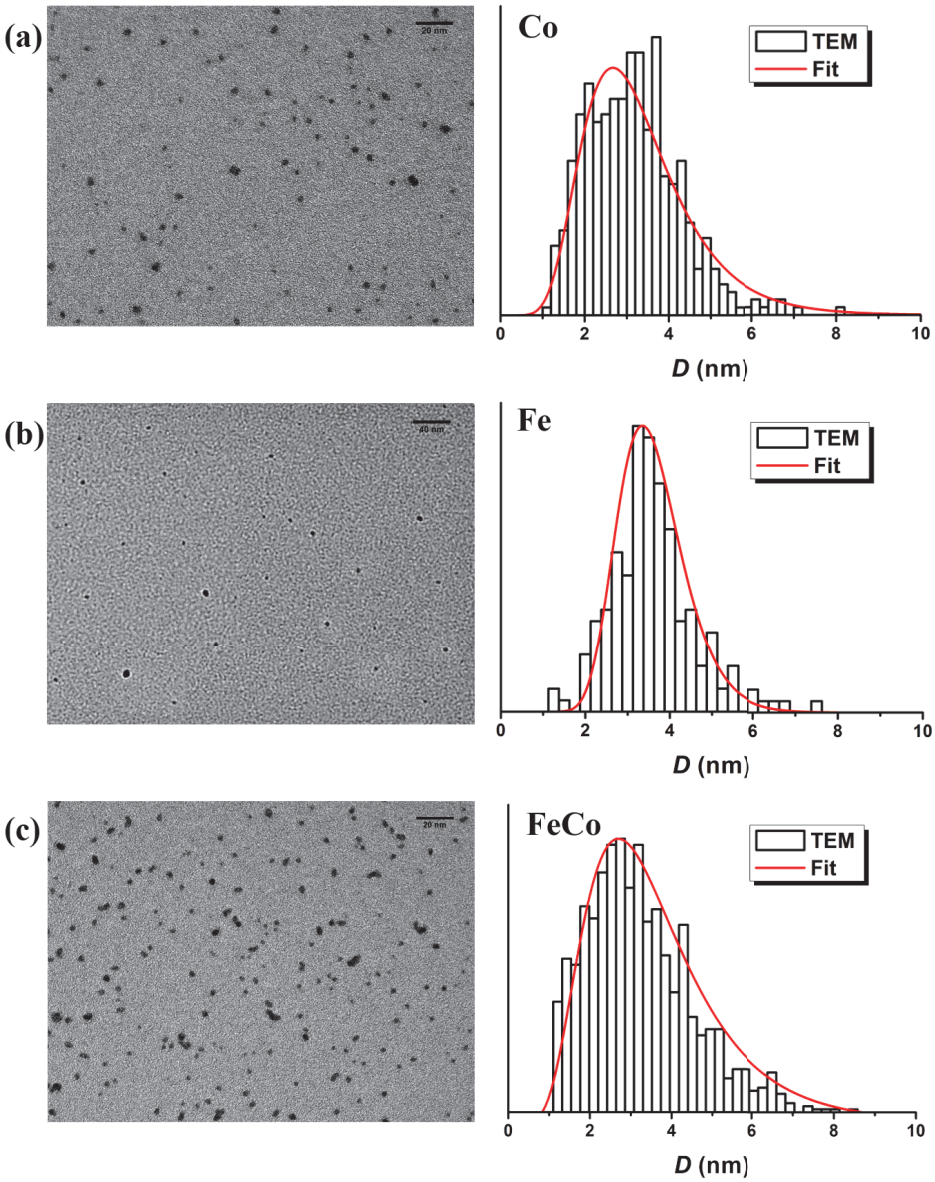

Fig. 3.4 (Left) TEM image of non mass-selected (neutral) Co (a), Fe (b) and FeCo (c) nanoparticles protected by a thin carbon film. (Right) Size histogram deduced from TEM observations as well as its best fit obtained using a lognormal distribution.

3.3.1.2 Morphology

The morphology of the nanoparticles was quantitatively investigated during the image treatment process. The ratio of the two ellipsoid axis (minor and major) is used to estimate the sphericity of the nanoparticles. In table 3.2 the values obtained for the three different systems (Co, Fe and FeCo) are presented. The values obtained were also fitted using a lognormal distribution. The shape of the nanoparticles is more spherical the closer this value is to 1. The nanoparticles in the three cases show an ellipsoidal shape.

	Sphericity	$\omega_{Sphericity}$
Co	1.23 $\pm$0.1	0.14 $\pm$0.03
Fe	1.29 $\pm$0.1	0.14 $\pm$0.03
FeCo	1.28 $\pm$0.1	0.16 $\pm$0.03

Table 3.2 Average value and dispersion of the particles' sphericity (major to minor axis ratio).

3.3.1.3 Composition

In addition, several nanoparticles were analyzed using EDX (Energy Dispersive X-ray analysis). In all three cases, the EDX analysis showed no sign of oxidation of the nanoparticles. For the case of FeCo, the iron to cobalt composition was also verified. Figure 3.5 presents an EDX spectrum for a FeCo nanoparticle. Using this technique, a composition of 40 % Fe to 60 % Co was determined as an average over several nanoparticles. To go further, RBS (Rutherford BackScattering spectroscopy) was also performed on an equivalent sample. Using the latter, a composition of 47 % Fe to 53 % Co was obtained for as-prepared samples and a composition of 49 % Fe to 51 % Co was obtained on a sample annealed at 500°C under ultra high vacuum conditions, as shown in figure 3.6 [167].

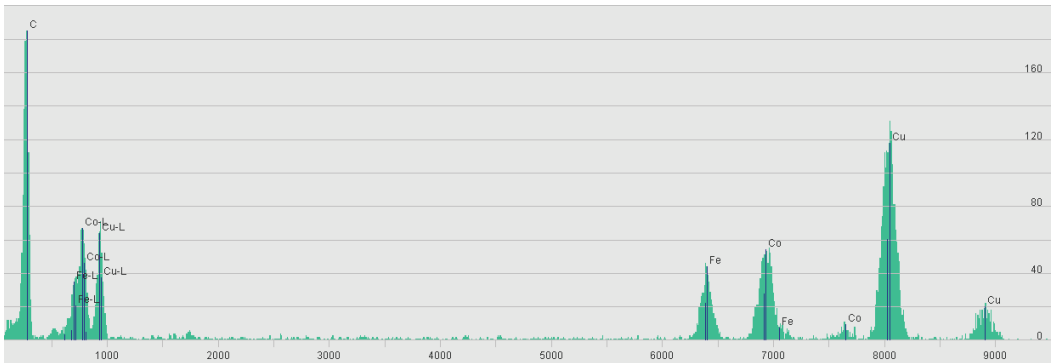

Fig. 3.5 EDX spectrum for a FeCo nanoparticle.

RBS was also used to verify the concentration of nanoparticles present in the carbon matrix. For SQUID magnetometry and in order to avoid magnetic interactions (chapter 4) highly diluted samples are needed. The concentration of FeCo to carbon was obtained to be 1 at. % of FeCo in carbon. This sample was prepared by co-depositing both the FeCo nanoparticles as well as the carbon matrix at the same time while simultaneously controlling the rate of deposition of the FeCo cluster beam and the matrix beam. The quantity of materials deposited was verified with the help of a quartz micro-balance.

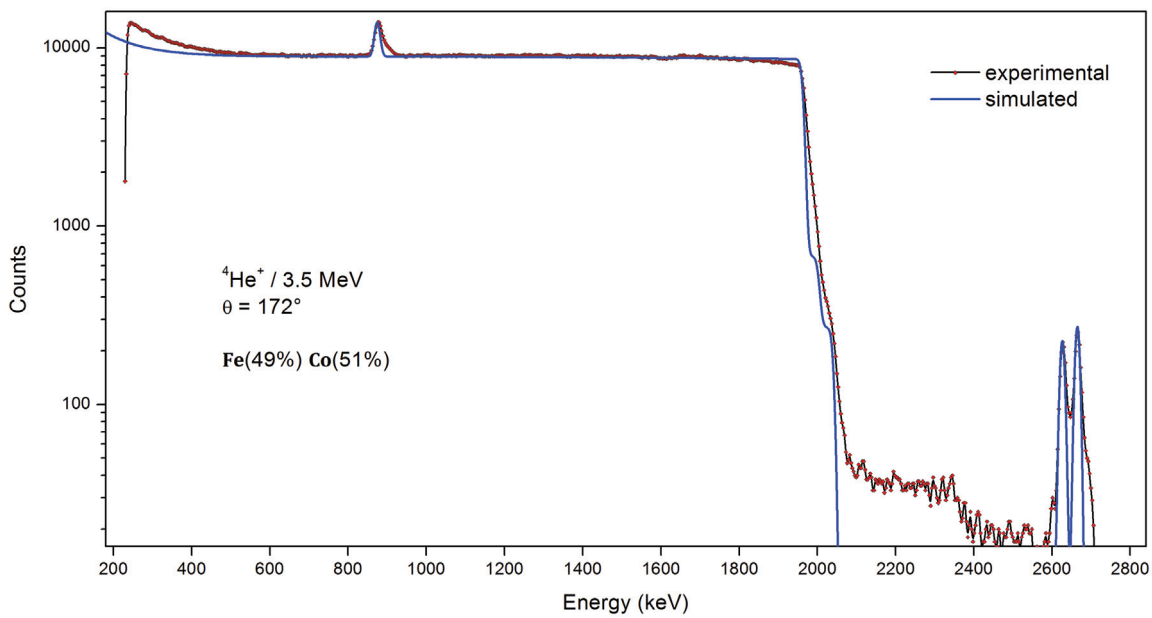

Fig. 3.6 RBS with the corresponding fit for an annealed neutral FeCo sample.

The film's thickness has been precisely calibrated using X-ray reflectivity measurements performed using a Rigaku SmartLab at Ecully, France (see example in figure 3.7). Three different samples containing ten carbon layers were prepared with varying distance of

the carbon evaporator from the Si substrate corresponding to 45 mm, 62 mm and 70 mm. Reflectivity measurements were performed on all samples by Olivier Boisron. The measured curves were fitted using a commercial software *RCRefSimW* [168]. Table 3.3 below sums up the obtained thickness of carbon layer for each distance.

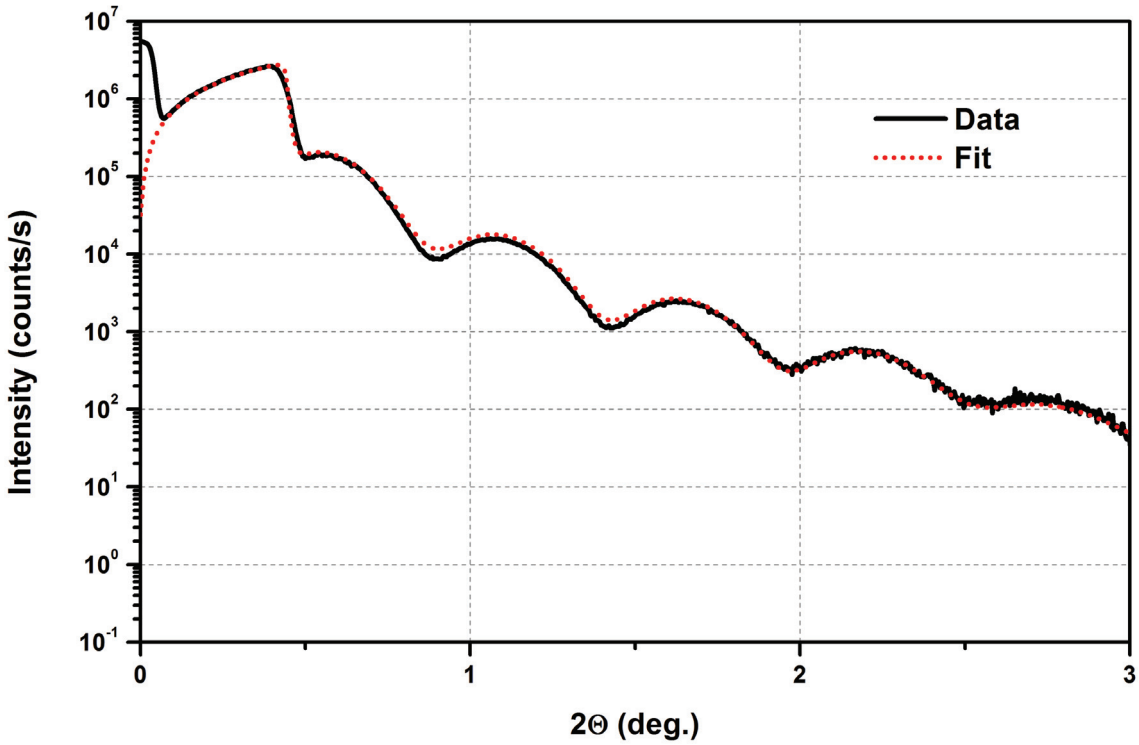

Fig. 3.7 Reflectivity measurements and fit for a sample composed of 5 carbon layers with an evaporator distance of 70 mm. A simple model of 5 carbon layers with the density of carbon of 2.25 g/cm^3 and rugosity of 8 ± 1 Å was used for the fit.

Evaporator distance	Carbon thickness/layer
45 mm	7.31 nm $\pm$0.5
62 mm	3.85 nm $\pm$0.3
70 mm	3.02 nm $\pm$0.2

Table 3.3 Thickness of the carbon layer corresponding to the distance of the evaporator from the sample.

In a sample made up of thin film, the presence of different elements (the film and the substrate), thus different electronic densities, causes a variation of the optical index of the

medium in the direction normal to the layer plane. For the small incidence angles, the X-rays are reflected by the substrate interfering in a constructive and destructive manner with the X-rays reflected by the free surface of the material. The result is a periodic modulation of the reflected intensity and the formation of fringes, called ”Kiessig fringes”. Their spacing is related to the total thickness of the sample.

In addition, for a film of a given chemical element, the intensity of the Kiessig fringes is directly influenced by the rugosity. This technique allowed us to obtain the total thickness of the films deposited on the silicon substrate as well as their rugosity.

3.3.2 Mass-selected clusters

3.3.2.1 Gaussian distribution

In addition to neutrally deposited nanoparticles, mass-selected nanoparticle samples were also studied. For the latter, a quadrupole deviator was used to select only the charged ions in the cluster beam as explained in chapter 2. The rest of the charged particles will be discarded with the help of a diaphragm. The fraction of charged clusters is a small percentage of the cluster beam, significantly increasing the deposition time needed to prepare a sample with enough nanoparticles to perform magnetometry as well as certain synchrotron technique measurements. For this reason, it is important to thoroughly check the size and dispersion of all prepared mass-selected nanoparticle samples before engaging in a lengthy deposition session. For mass selected clusters, our cluster source produces nanoparticles with a Gaussian distribution (equation 2.22) with a dispersion around 10 % [61]. For deposition, the laser power was fixed at 300 mW for all samples; Helium was used as carrier gas with a pressure of 30 mbar. For pure nanoclusters (Co and Fe) two deviations were used, 150 V and 300 V. For the bimetallic FeCo nanoclusters, several voltage deviations were used (75 V, 150 V, 300 V, 450 V, 600 V and 1200 V). During deposition, due to the injection of the Helium carrier gas, the pressure in the three main chambers is respectively around 10^{-5} mbar in the nucleation chamber, 10^{-6} mbar in the deviator chamber and 10^{-8} mbar in the deposition chamber compared to 10^{-7} mbar, 10^{-8} mbar and 10^{-10} mbar in the three chambers, respectively, before the injection of Helium (static vacuum).

3.3.2.2 Size histograms

3.3.2.2.1 Pure clusters For pure Co and Fe clusters, for the 300 V deviation, the obtained deposition rate was 0.001 Å/s; for the 150 V the deposition rate was 0.0001 Å/s with the aforementioned deposition conditions. The corresponding sizes and size dispersions obtained for both mass-selected Co and Fe nanoparticles is reported in the table 3.4. Figure 3.8 shows TEM images for both systems (Co and Fe) for the two selected deviations.

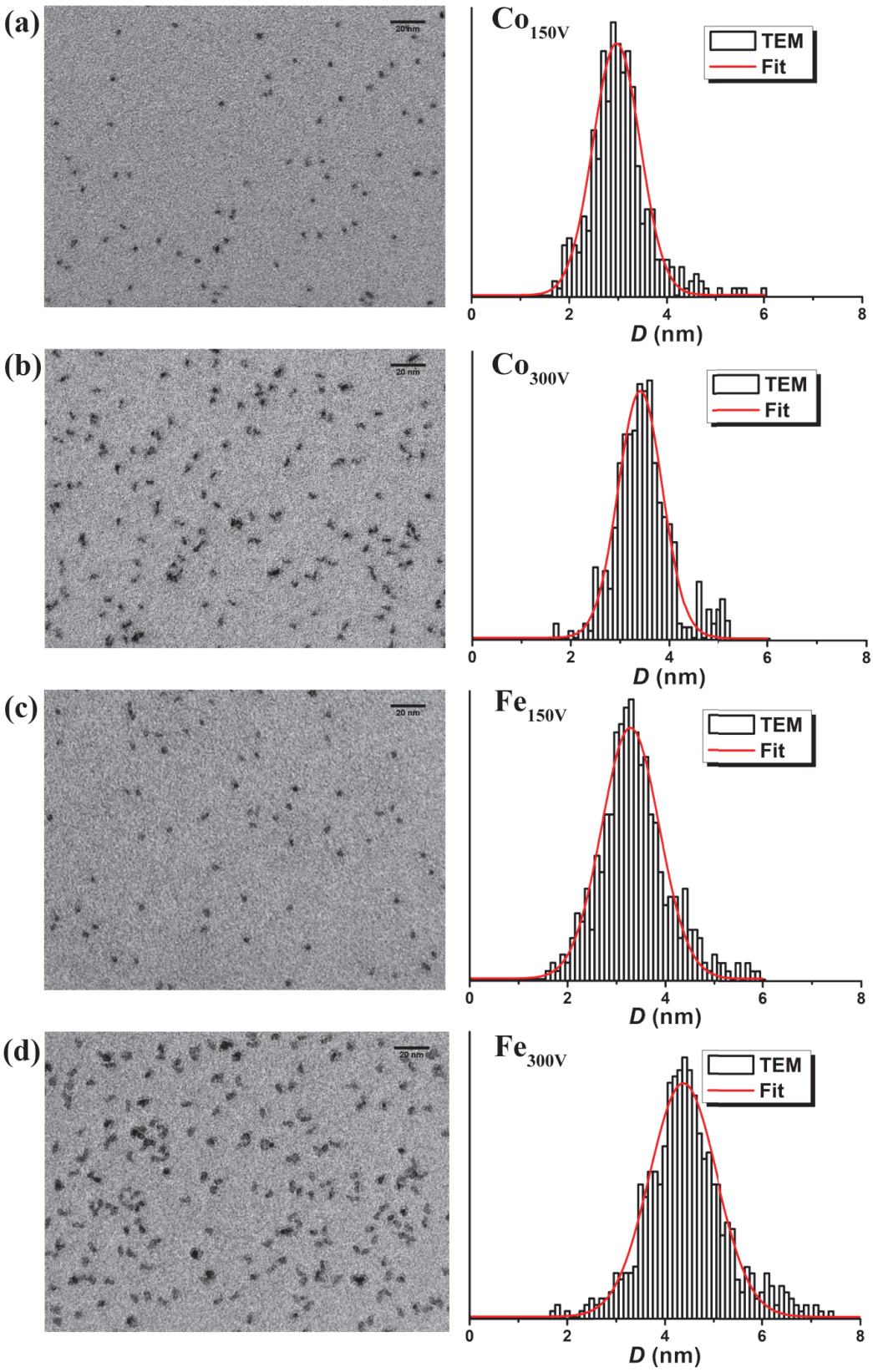

Fig. 3.8 TEM images for mass-selected (a, b) Co and (c, d) Fe nanoclusters and their corresponding size histogram for two voltage deviations, 150 V and 300 V.

	Dm (nm)	ω	**Sphericity**	$\omega_{Sphericity}$
Co 150 V	2.97 ±0.2	0.16 ±0.03	1.41 ±0.1	0.21 ±0.03
Co 300 V	3.41 ±0.2	0.13 ±0.03	1.63 ±0.1	0.27 ±0.04
Fe 150 V	3.28 ±0.2	0.18 ±0.03	1.43 ±0.1	0.22 ±0.03
Fe 300 V	4.37 ±0.2	0.16 ±0.03	1.59 ±0.1	0.25 ±0.04

Table 3.4 Mean diameter and dispersion of mass-selected Co and Fe nanoparticles for two voltage deviations, 150 V and 300 V.

The obtained Gaussian distributions for the two deviations for both Co and Fe samples fit under the envelope of the lognormal distribution of the neutral ones. This proves that by applying a deviation voltage a fraction of the initial lognormal distribution is chosen. Also, the rate of deposition of the voltage assisted deposition strongly depends on the position on the lognormal curve. For larger cluster sizes the rate of deposition drastically drops as was previously shown. For both Co and Fe, increasing the deviation voltage decreased the sphericity of the clusters.

3.3.2.2.2 As-prepared FeCo clusters For bimetallic FeCo clusters, a series of six samples of increasing deviation voltage were prepared from 75 V to 1200 V. These samples were prepared using the same conditions as for the pure clusters. In addition, using a carrier gas mixture of Argon and Helium (12 mbar Ar + 18 mbar He) two samples were prepared using 300 V and 450 V deviations. In the table 3.5 we report the obtained values for all deviation voltages and deposition conditions for the as-prepared samples.

	Deviation	***Dm*** (nm)	ω	**Sphericity**	$\omega_{Sphericity}$
Normal Condition	150 V	3.69 ±0.2	0.13 ±0.03	1.37 ±0.1	0.16±0.03
	300 V	4.27 ±0.2	0.12 ±0.03	1.47 ±0.1	0.24±0.04
	450 V	5.82 ±0.2	0.10 ±0.03	1.66 ±0.1	0.27±0.05
	600 V	6.08 ±0.2	0.1 ±0.03	1.65 ±0.1	0.24±0.04
	1200 V	8.85 ±0.2	0.09 ±0.03	1.83 ±0.1	0.36±0.05
Gas Mixture	300 V	6.17 ±0.2	0.09 ±0.01	1.64 ±0.1	0.24±0.04
	450 V	7.65 ±0.2	0.08 ±0.01	1.67±0.1	0.32±0.05

Table 3.5 Mean diameter and sphericity and their corresponding dispersion of mass-selected FeCo nanoparticles for voltage deviations between 150 V and 1200 V.

The values of the sphericity and its corresponding dispersion are also tabulated in table 3.5. The sphericity was obtained from the ratio of the major to minor axis of the ellipsoidal fit. The latter was fitted using a lognormal type distribution. The corresponding TEM images are presented in figure 3.9.

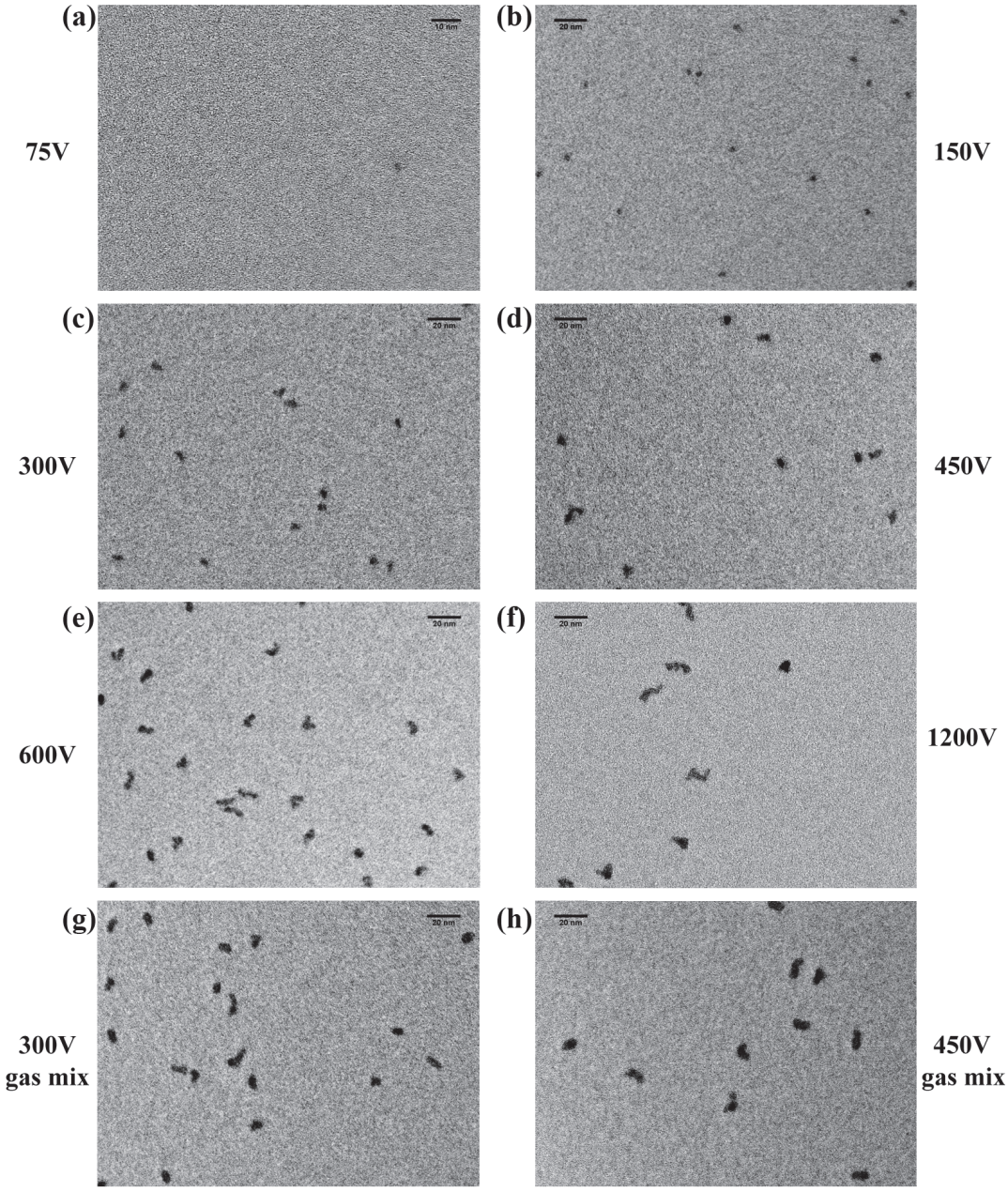

Fig. 3.9 TEM images for mass-selected FeCo nanoparticles obtained under deposition conditions for deviation voltages of (a) 75 V, (b) 150 V, (c) 300 V, (d) 450 V, (e) 600 V and (f) 1200 V; (g) and (h) represent nanoparticles for deviation voltages of 300 V and 450 V respectively obtained with a gas mixture of Argon and Helium.

From these mass-selected FeCo nanoparticles, three main sizes were selected for further investigation corresponding to the voltage deviations of 150 V, 300 V and 600 V. For the 75 V deviation, the nanoparticle size was very small and required heavy image treatment to enhance the particle background contrast (as seen in figure 3.9a); it was thus very difficult to quantify it properly. Moreover, the deposition rate with optimal working conditions was 3.5×10^{-5} Å/s. This means that it would require a continuous deposition lasting for a few days in order to have a minimum quantity for a measurable magnetic signal. Furthermore, during TEM imaging and due to the low contrast and low particle density, it was very difficult to find and image the particles prepared with this deviation. The 450 V deviation gave a size distribution that overlaps with the 600 V one; thus the latter was chosen. It should be noted that for a deviation voltage higher than 300 V, the FeCo nanoparticles exhibited ramified structures rather than spherical ones. Finally, for the 1200 V deviation, the clusters had highly ramified structures with a low deposition rate of 9×10^{-4} Å/s.

Alayan *etal*. discussed in detail the formation of ramified or fractal platinum particles generated using a cluster beam [62]. The particle morphology changes from a spherical to a ramified structure depending on the growth kinetics which are governed by external parameters (laser power, gas pressure, *etc*...). This transition is observed when the cluster size increases beyond a critical diameter d_c (about 2.5 nm for platinum particles) that depends on cluster elements.

For the FeCo nanoparticles achieved with a gas mixture of $Ar_{12}He_{18}$, for both 300 V and 450 V deviations, the deposition rate was very small compared to the case of pure He carrier gas ($\approx 1 \times 10^{-3}$ Å/s) with 7×10^{-5} Å/s and 3×10^{-5} Å/s, for the 300 V and 450 V respectively.

3.3.2.2.3 Annealed FeCo clusters To go a step further, for the three chosen deviation voltages (150 V, 300 V and 600 V) TEM grids were annealed under UHV conditions at a temperature of 500°C for 2 hours. The annealed samples were re-imaged for conventional size histograms as well as for high resolution transmission electron microscopy (HRTEM). For the 150 V sample, complications during the annealing process led to a sample deterioration. As for the 300 V and 600 V deviation samples, figure 3.10 shows the obtained TEM images as well as the corresponding size histograms. Table 3.6 reports the values obtained for the size histograms.

Deviation	Dm (nm)	ω	Sphericity	$\omega_{Sphericity}$
300 V Annealed	3.89 ±0.2	0.14 ±0.03	1.18 ±0.1	0.09±0.02
600 V Annealed	5.26 ±0.2	0.13 ±0.03	1.19 ±0.1	0.09±0.02

Table 3.6 Mean diameter and dispersion of annealed mass-selected FeCo nanoparticles at 500°C for 2 hours for voltage deviations of 300 V and 600 V, as well as their corresponding sphericity values and its dispersion.

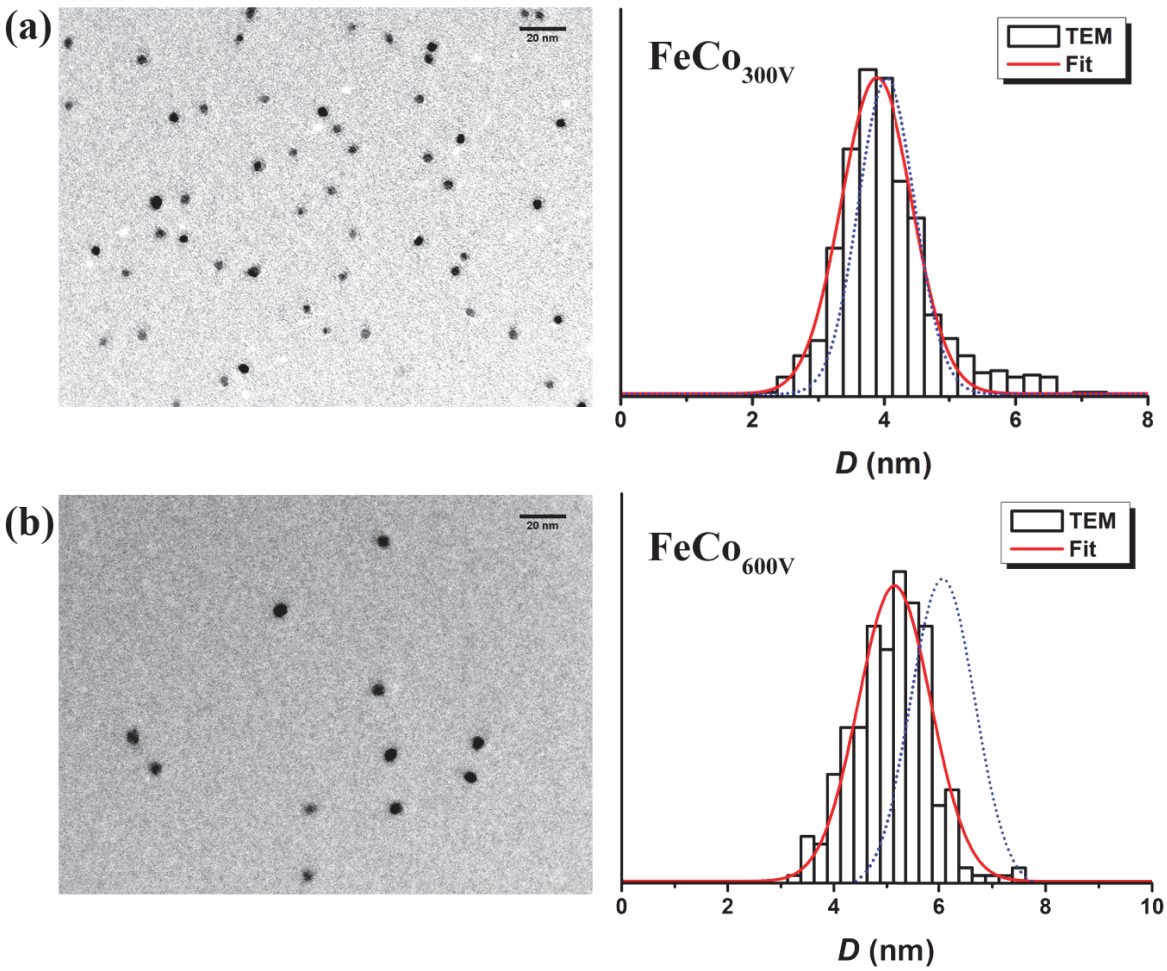

Fig. 3.10 TEM images for annealed mass-selected FeCo nanoparticles at 500°C for 2 hours for deviation voltages of (a) 300 V and (b) 600 V, and their corresponding size histogram as well as that of the size histogram for the as-prepared particles of the same deviation in dotted line.

For the two sizes, after annealing the FeCo nanoparticles exhibited a more spherical shape which was verified from the sphericity values obtained from the nanoparticle projections. In

addition, the average size decreased for both the 300 V deviation, as well as for the 600 V one, the decrease in size is of notable importance (9-13 %) to relate to a more dense structure upon annealing (further investigated from EXAFS measurements). This shrinking of the nanoparticles is likely due to their initial shape. For the 300 V nanoparticles the shape was already quasi-spherical, thus annealing only slightly affected their projected size. Whereas for the 600 V deviation, the FeCo nanoparticles exhibited, as previously noted, ramified structures. Upon annealing, the particle shape changed to the more energy favorable spherical shape, thus their projected size was notably affected.

3.4 High resolution transmission electron microscopy

In addition to conventional TEM images, HRTEM images were systematically taken for the three main nanoparticle sizes. The samples were imaged in HRTEM both as-prepared and after annealing for the 300 V and 600 V deviations. Figure 3.11 shows HRTEM images for the as-prepared 300 V and 600 V nanoparticle sizes; figure 3.12 shows HRTEM images and their corresponding Fast Fourier transforms (FFT) for annealed 150 V, 300 V and 600 V nanoparticle sizes.

3.4.1 As-prepared nanoparticles

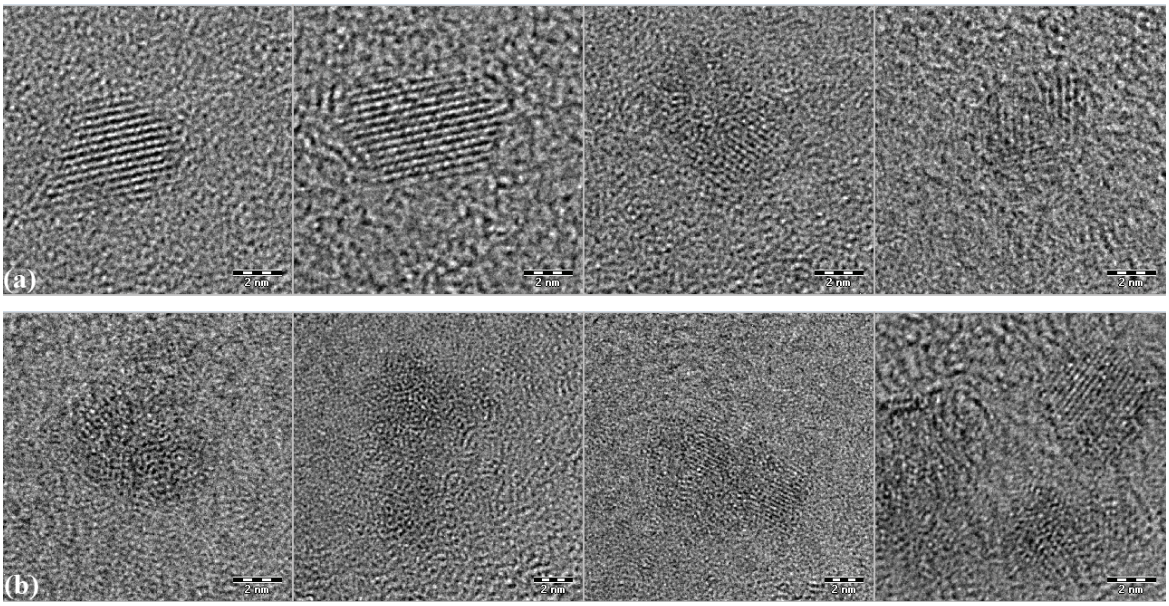

Fig. 3.11 HRTEM images for as-prepared FeCo nanoparticles for deviation voltages of (a) 300 V and (b) 600 V.

From the HRTEM images, it is clear that not all the nanoparticles are well crystallized. In fact, for the 300 V deviation, almost half of the imaged particles do not show a clear crystallographic structure. The nanoparticle to background contrast is not very good. The contrast between the iron and cobalt atoms making up the nanoparticles with a $\Delta Z = 1$ it is absolutely impossible to distinguish between the two atoms with the state of the art imaging techniques. For the 600 V deviation, the clusters exhibit no crystallographic or polycrystalline structures. Using FFTs it was possible to extract some crystallographic information from the images. In the case of:

- 300 V deviation: the FFT gave lattice distances of 3.48 Å, 2.31 Å and 1.65 Å. These distances correspond to a carbide formation, more specifically cementite (Fe_3C); these distances correspond to [020], [210] and [230] Miller indices ([*hkl*]) respectively [169].
- 600 V deviation: the nanoparticles exhibited almost no crystallographic structure. The FFT gave only inconclusive results on the probably disordered structure of these nanoparticles.

3.4.2 Annealed nanoparticles

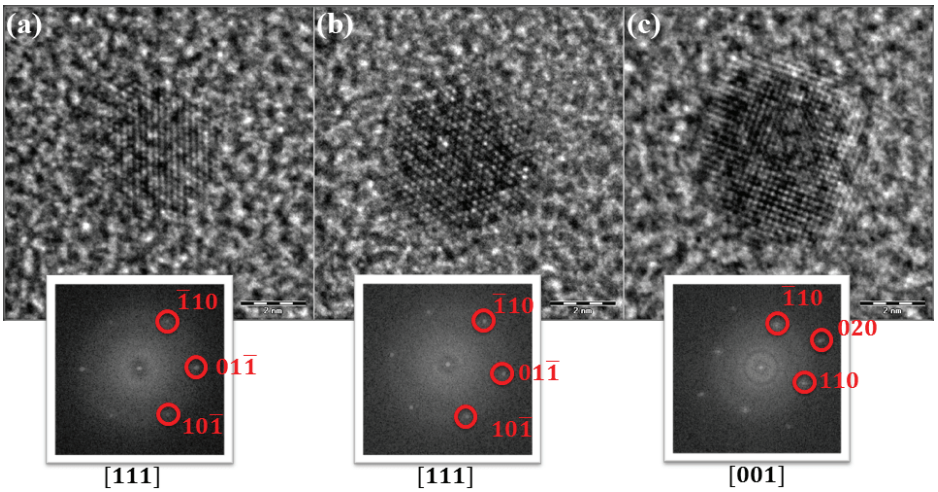

Fig. 3.12 HRTEM images for annealed FeCo nanoparticles for deviation voltages of (a) 150 V, (b) 300 V and (c) 600 V along with their corresponding FFT.

After annealing, a bcc structure is observed for some nanoparticles. In figure 3.12, HRTEM images for the different deviation voltages exhibit a FFT that corresponds to the expected bcc structure. As can be observed, the bcc signature can be viewed following different orientations of the clusters. In some cases, a graphitization of the carbon around the nanoparticles was

observed. In addition, while working in high resolution mode, the electron energy used is significantly higher than normal TEM mode. As such, prolonged exposure of the samples to the electron beam (sometimes for just a few seconds) can lead to the contamination of the sample. It should also be noted that the number of crystallized particles depended on the size. For the small sizes, fewer nanoparticles were crystallized. While for the larger sizes, more particles were crystallized.

3.5 Anomalous scattering spectroscopy

The previous techniques have put into evidence that the annealed FeCo nanoparticles, mainly the 600 V deviation size (6 nm particles), have an irrefutable bcc structure. However, due to the low atomic number difference ($\Delta Z = 1$) between Fe and Co atoms it was not possible to prove that the observed structure was the chemically ordered CsCl-B2 phase even though it is the bulk standard for equimolar FeCo alloys. In order to go further and prove without ambiguity the existence of this chemical order, we decided to use anomalous diffraction to experimentally increase the ΔZ between Fe and Co atoms by changing the X-ray energy. Synchrotron radiation was required, first, due to the small size of the nanoparticles and to their dilution, it is very challenging to perform diffraction spectra. In addition, classical diffractometers are limited to the X-ray energy defined by the anode element (Fe, Co, Cu, Mo, *etc*...) making it impossible to change the energy of the X-rays. Anomalous X-ray Diffraction (AXD) has the advantages of synchrotron radiation techniques for chemical selectivity and high photon flux, as previously explained in details in chapter 2.

3.5.1 Simulation

Before the actual experiment on the synchrotron, the anomalous x-ray diffraction signal was simulated for two similar system, FeCo and FeRh. Both systems, in the bulk, present the chemically ordered CsCl-B2 phase. In the case of FeRh, there already exists a strong atomic difference between the two elements ($\Delta Z_{FeRh} = 19$) compared to the case of FeCo ($\Delta Z_{FeCo} = 1$). For both systems, a B2-phase CsCl structure was assumed for the simulation. The work of Blanc *et al*. [92] on $L1_0$ CoPt nanoparticles was adopted to take into account chemically ordered nanoparticles in the CsCl-B2 phase. The energy (or wavelength) used in the simulation was chosen so as to have the largest anomalous contrast between the two elements, Fe and Rh (or Co). The values for both $f'(E)$ and $f''(E)$ are well known and tabulated for these atoms [170]. In figure 3.13, these values are traced near the K-edge of both Fe and Co atoms.

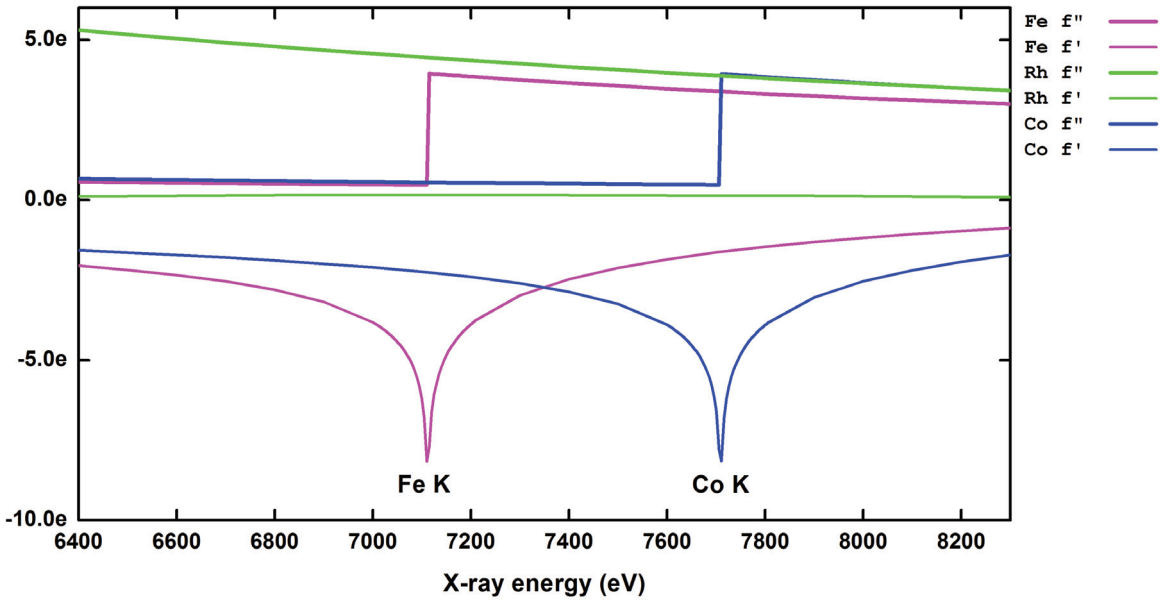

Fig. 3.13 Anomalous scattering coefficients $f'(E)$ and $f"(E)$ for Fe, Co and Rh elements as a function of photon energy (and wavelength).

From the 3.13 plot, the photon energy for which the anomalous contrast is the largest is just before the Fe:K-edge. For a photon energy of $E = 7.108keV$, from the values of f'_{Fe} and f'_{Co} we have a anomalous contrast of around 9 instead of the atomic contrast of $\Delta Z_{FeCo} = 1$. Figures 3.14a and 3.14b show the simulated values for the FeRh and FeCo systems respectively for different nanoparticle sizes in a rhombic dodecahedron, figure 3.1b. The size of the nanoparticles is governed by the number of atoms per edge m ($m = 12$ correspond to nanoparticles with a size around 5 nm).

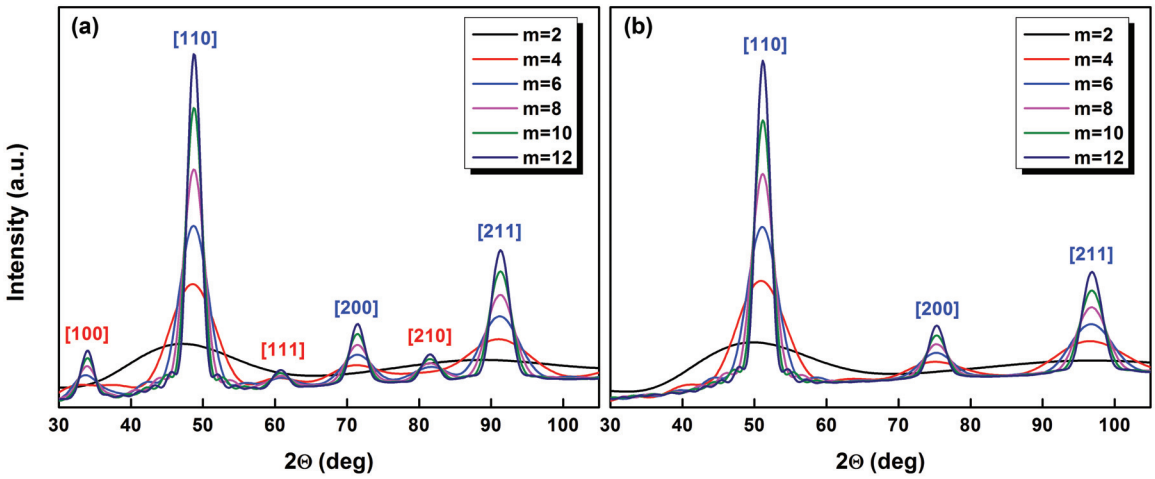

Fig. 3.14 Simulated X-ray scattering curves for CsCl-B2 phase (a) FeRh and (b) FeCo systems for different nanoparticle sizes.

From the simulations, we can see the peaks corresponding to a typical rhombic dodecahedron bcc structure ([110], [200] and [211]) for both systems. In the case of FeRh, in addition to the bcc peaks, we see three additional superlattice reflection peaks ([100], [111] and [210]), signature of a CsCl-B2 phase structure. Comparing the two systems, we can see that in the case of FeCo, it will be very difficult to extract the superlattice reflection peaks for small nanoparticles (up to $m = 12$). Nevertheless, these simulations remain approximations and do not take into account any corrections parameters needed to reach experimental accuracy. Furthermore, it can be noted from these simulations how the form of the peaks is slowly approaching a Dirac shape, which is the case of the bulk. For small m values it was impossible to distinguish the structure peaks or the superlattice peaks. As the size of the particles increase (m increased) the peaks started to get thinner and more distinguishable. For a rhombic dodecahedron FeCo, $m = 12$ corresponds to a nanoparticle with a diameter $D = 5.2$ nm.

For calculated values of FeCo X-ray diffraction, it is reported that an intensity of less then 1% is expected for the appearance of superlattice structure of FeCo [171]. In addition, actual experimental values obtained on FeCo powder diffraction by Baker show no sign of superlattice structure [172]. On the other hand, anomalous diffraction on FeCo based magnet performed by Willard *et al*. show the appearance of the superlattice reflections [173–175].

3.5.2 Experiment

The scattering experiments were performed on the D2am beamline at the ESRF (Grenoble, France) with the help of N. Blanc. Due to the limited time frame (24 hours of beamtime), it was only possible to measure one sample. Thus, the sample which corresponds to FeCo nanoparticles mass-selected with a deviation voltage of 600 V and annealed at $500°C$ for two hours. From the initial simulations we found that the best anomalous contrast is expected for X-ray energies near 7.1 keV. The incidence angle was optimized so as to have no signal from the Si substrate, or at least as low as possible; as such an angle $\alpha_i = 0.2°$ was chosen after some calibrations. The X-ray energy was fixed at 7.108 keV. The sample was measured for 2θ angle between 30° and 105°. Figure 3.15 shows the measured X-ray scattering spectrum for our FeCo sample. From the measured spectrum we can see three peaks which correspond to bcc-like structure peaks. The observation of these three peaks show the very good crystallinity of the annealed FeCo 600 V sample.

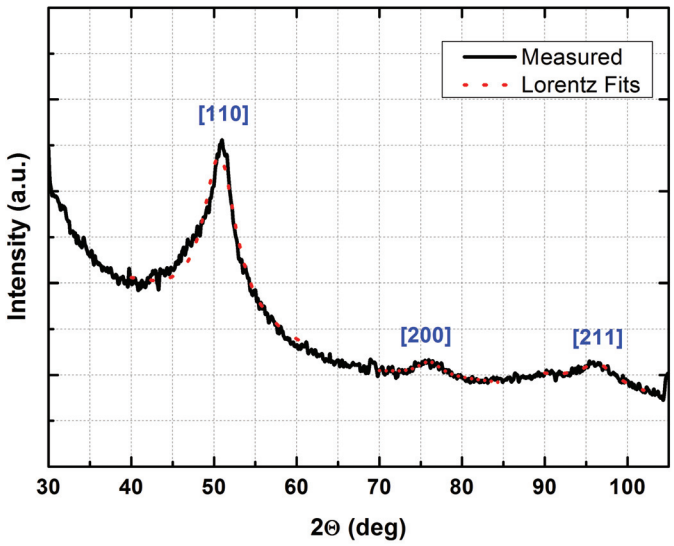

Fig. 3.15 Measured X-ray scattering spectrum for 600 V deviated FeCo annealed at 500°C with the corresponding fits of the peak.

The peaks in the above spectrum were isolated and fitted using a Lorentz type function. Using the Debye-Scherrer equation [176, 177], the size of the nanoparticle is estimated based on the width of the scattered peaks.

$$\tau = \frac{K\lambda}{\beta \cos\theta} \tag{3.4}$$

where τ is the size of the nanoparticle, K is a dimensionless shape factor (approximated as $K = 0.9$), λ is the X-ray wavelength, β is the full width at half maximum (FWHM) of the peak and θ is the Bragg angle. The corresponding values obtained for both the Lorentz fit and the obtained estimated diameter are presented in table 3.7.

	2θ **(deg)**	FWHM (deg)	$D_{Scherrer}$ **(nm)**
[110]	50.7	4.83	4.13
[200]	76.1	3.46	6.60
[211]	96.5	5.36	5.04

Table 3.7 Values obtained for the Scherrer diameter ($D_{Scherrer}$) as well as the peak position and width for the X-ray scattering spectrum.

Averaging the diameter values obtained from the three peaks we obtain $D_{Scherrer} =$ 5.25 nm which is consistent with the results obtained from TEM microscopy for annealed

FeCo nanoparticles with a deviation voltage of 600 V. Nevertheless, the above values show that with this technique the error on the estimated diameter is very large ($\pm$ 1 nm).

Using anomalous scattering on FeCo nanoparticles did not provide conclusive information on the chemical order of the nanoparticles. Thus, in order to evidence the expected chemically ordered CsCl-B2 phase we performed a series of EXAFS measurements on our samples (neutral and mass-selected) at both Fe and Co sites.

3.6 EXAFS spectroscopy

In this section, we will present the results obtained for X-ray absorption measurements on cobalt, iron and iron-cobalt nanoparticles embedded in an amorphous carbon matrix. We will start first with the results obtained on neutral particles (no mass-selection) then we present the size study. The aim of using this technique is to clarify and better understand the crystallographic structure of the nanoparticles and the nature of the interface matrix-nanoparticles at each site (Co and Fe).

For a given absorber element, the X-rays absorption coefficient presents oscillations characteristic of the crystallographic structure of the material. These oscillations are called Extended X-ray Absorption Fine Structure (EXAFS). The analysis method for these oscillations was described in chapter 2.

The X-ray absorption measurements were carried out at the BM30B Frame beamline at the ESRF in Grenoble, France. For X-ray absorption spectra, the quantity of materials needed to obtain a quantifiable signal is significantly larger than that needed for TEM. An average of 1 nm of equivalent thickness of nanoparticles is needed in order to get a detectable signal.

3.6.1 Bulk metallic foil references

In addition to performing absorption measurements on Fe, Co and FeCo cluster samples, bulk-reference Fe and Co foils were measured. Figure 3.16 shows the normalized absorption spectra of the two reference samples; figure 3.17 shows their Fourier Transform and figure 3.18 shows the EXAFS oscillations and the corresponding fits. Table 3.8 contains the fitted values for the reference systems. These values are necessary to obtain the value for ${S_0}^2$ for both Fe and Co. This value is known as the passive electron reduction factor [68]. It strongly depends on the experimental conditions, and as such it can be extrapolated from the reference sample, if measured at the same time as the samples and under the same conditions.

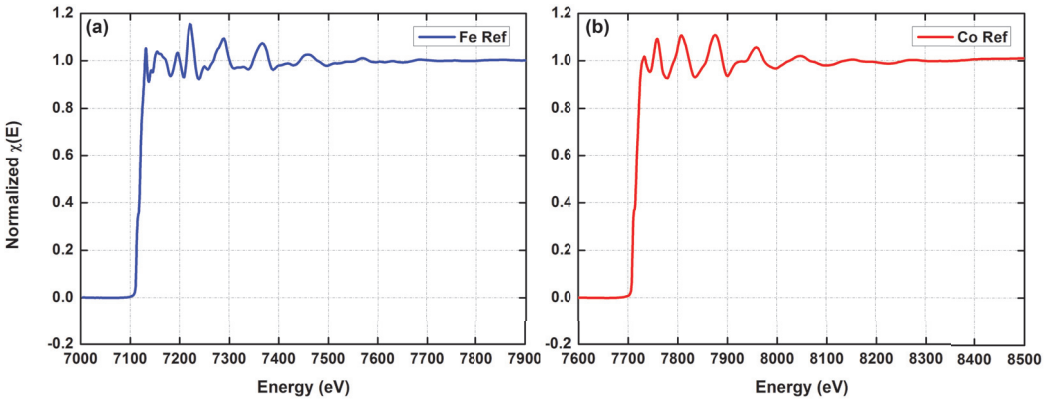

Fig. 3.16 Normalized absorption spectra of (a) bcc Fe and (b) hcp Co bulk reference foils.

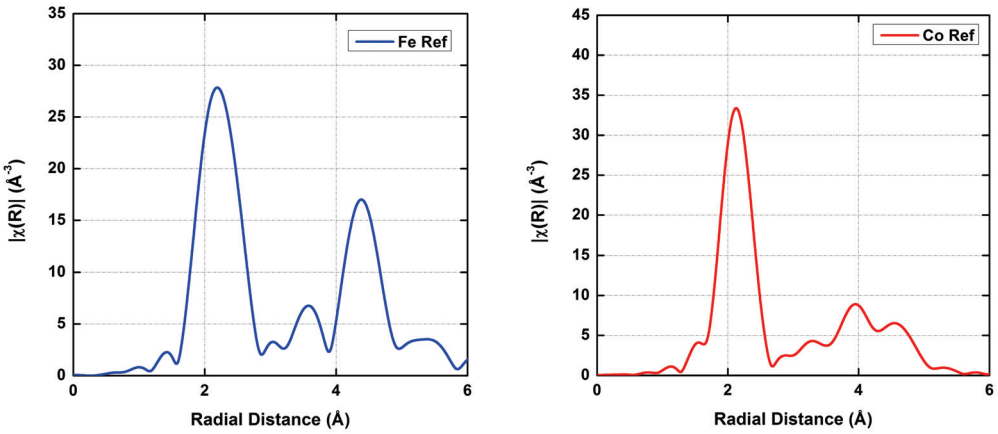

Fig. 3.17 Radial distribution of EXAFS oscillations for (a) bcc Fe and (b) hcp Co bulk reference foils.

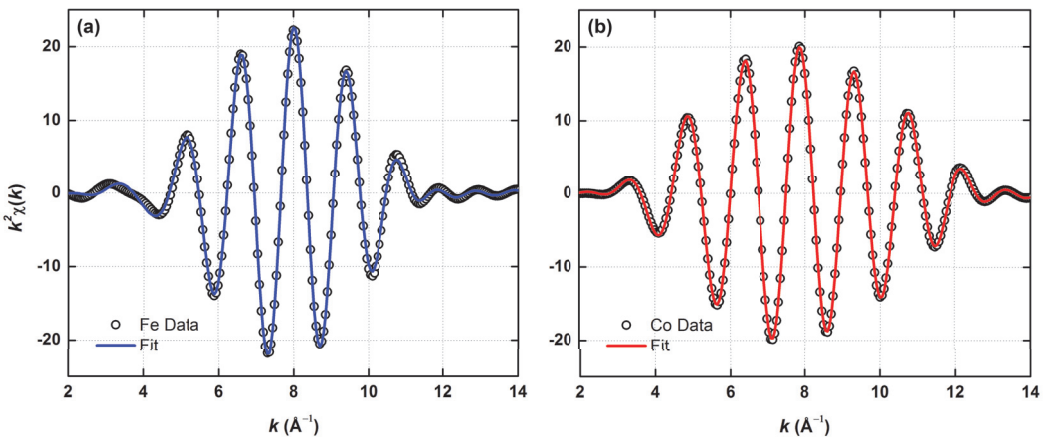

Fig. 3.18 EXAFS oscillations of (a) bcc Fe and (b) hcp Co bulk reference foils as well as their corresponding fits.

Sample	Atom	Degeneracy	$S_0{}^2$	σ^2	R (Å)
Fe Reference	Fe.1	8	0.795	0.00492	2.47 ± 0.02
	Fe.2	6	0.795	0.00556	2.85 ± 0.02
Co Reference	Co	12	0.814	0.00635	2.49 ± 0.02

Table 3.8 Fitting parameters for the bcc Fe (first and second neighbours) and hcp Co bulk-reference foils.

The above data adjustments were achieved using a bcc crystal for Fe reference with the Fe bulk values and using an hcp crystal for the Co reference. Figure 3.17 shows the difference between the Fourier Transform for a bcc structure and a hcp one. For all the fits that follow, the number of neighbours for atoms at the Fe edge is divided by $S_0{}^2{}_{Fe} = 0.795$, and at the Co edge $S_0{}^2{}_{Co} = 0.814$.

3.6.2 Neutral clusters

In the case of neutral clusters, two FeCo samples were prepared having a total equivalent thickness of clusters of around 1.6 nm. The samples were prepared in the 2D configuration with alternating layers of amorphous carbon (2 nm) and FeCo nanoparticles with 8 Å equivalent thickness with a total of eight layers of nanoparticles. The samples were both capped with amorphous carbon. One was annealed under UHV conditions at a temperature of $500°C$ for two hours, while the other was left as-prepared. Both samples were measured at the Co:K edge and Fe:K edge.

It should be noted that the magnetic signal of these two samples was thoroughly characterized (reported in chapter 4). In addition, the previously reported RBS data for neutral clusters were later performed on these same two samples (see section 3.3.1.3).

Figure 3.19 shows the radial distribution for Co:K and Fe:K edges for as-prepared and annealed samples.

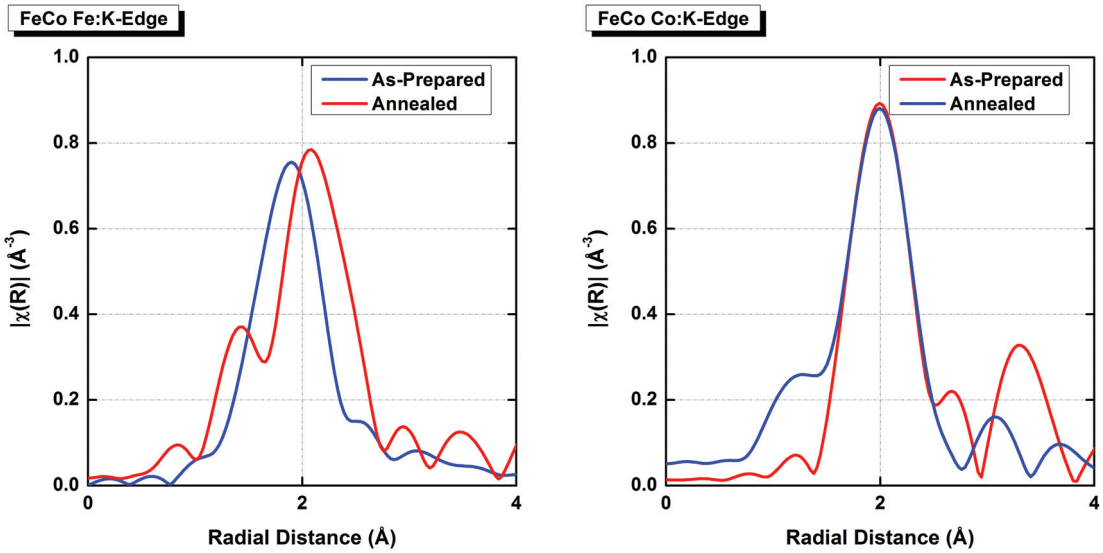

Fig. 3.19 Radial distribution of EXAFS oscillations for (left) Fe:K edge and (right) Co:K edge for as-prepared (blue line) and annealed (red line) neutral FeCo samples.

From qualitative analysis of the non-corrected radial distributions, we can see, at the Fe:K edge, a shift of the principal peak after annealing accompanied by an increase in amplitude of the principal peak due to ordering of the local environment of the Fe atoms. For the Co:K edge, we observe the decrease after annealing of a shoulder-like structure due to carbon neighbours before the main peak (at 2 Å). This is likely due to the demixing of cobalt and carbon atoms previously observed in pure Co nanoparticles embedded in a carbon matrix [178].

A more quantitative analysis can be obtained from the simulation of EXAFS oscillations (through the inverse Fourier Transform $\mathrm{FT}^{-1}\chi(R)$ filtered around 1-3 Å) and is detailed below in figures 3.20, 3.21 and tables 3.9, 3.10.

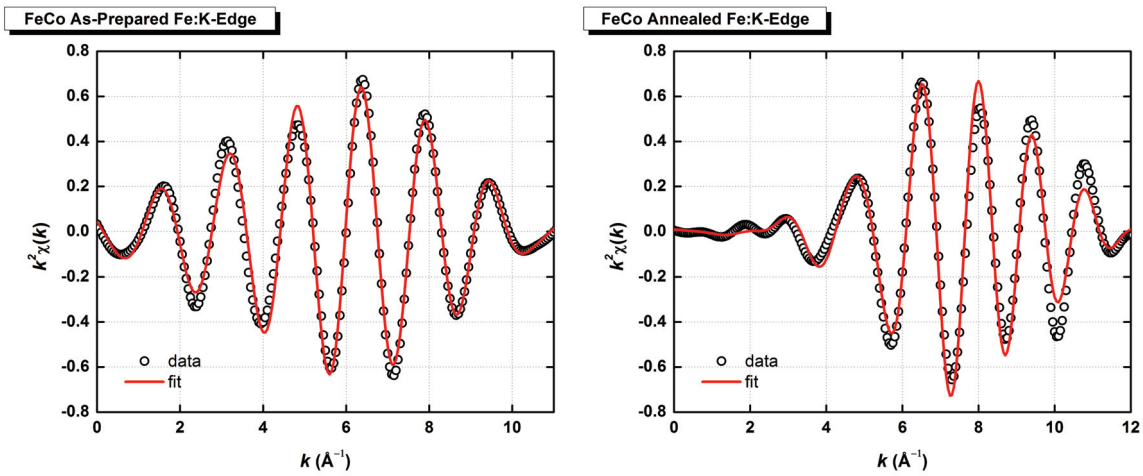

Fig. 3.20 EXAFS oscillations for as-prepared (left) and annealed (right) neutral FeCo nanoparticles at the Fe:K-edge with their corresponding best fits.

	Path	Number of Nearest Neighbours	σ^2	R (Å)
As-Prepared	Fe-Fe	1.5	0.0077	2.52 ± 0.2
	Fe-Co	1.5	0.0075	2.41 ± 0.2
	Fe-C	2	0.0059	2.25 ± 0.2
Annealed	Fe-Fe	4.4	0.0130	2.78 ± 0.2
	Fe-Co	5.9	0.0151	2.47 ± 0.2
	Fe-C	0.7	0.0059	1.99 ± 0.2

Table 3.9 Values obtained the for best fits of the EXAFS oscillations for as-prepared and annealed neutral FeCo nanoparticles at the Fe:K-edge.

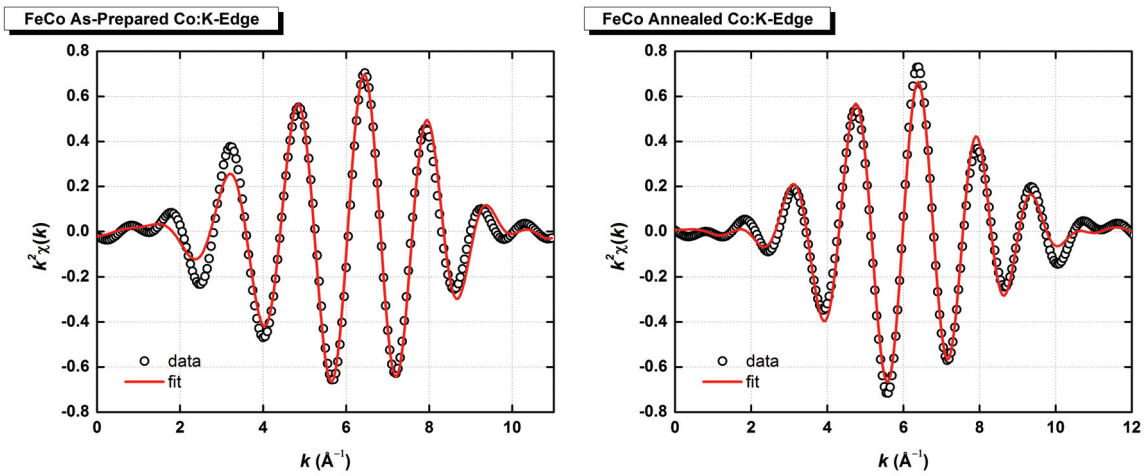

Fig. 3.21 EXAFS oscillations for as-prepared (left) and annealed (right) neutral FeCo nanoparticles at the Co:K-edge with their corresponding best fits.

	Path	Number of Nearest Neighbours	σ^2	R (Å)
As-Prepared	Co-Co	1.7	0.0074	2.45 ± 0.2
	Co-Fe	1.7	0.0076	2.41 ± 0.2
	Co-C	0.6	0.0059	2.19 ± 0.2
Annealed	Co-Co	4.1	0.0278	2.74 ± 0.2
	Co-Fe	5.4	0.0126	2.47 ± 0.2
	Co-C	0.7	0.0059	1.99 ± 0.2

Table 3.10 Values obtained for the best fits of the EXAFS oscillations for as-prepared and annealed neutral FeCo nanoparticles at the Co:K-edge.

During the fitting of the EXAFS oscillations on FeCo nanoparticles, it was necessary to add a contribution of the neighbouring atom of the matrix, that is the carbon environment, to obtain a high quality fit. The evolution of the contribution of Fe-C (respectively Co-C) interatomic distance is presented in the tables above alongside the nanoparticle absorber distances (Fe-Fe, Fe-Co and Co-Co).

In the case of the as-prepared nanoparticles, a first-shell coordination was used to simulate the EXAFS oscillations. In a first coordination shell, only the first nearest neighbours are considered. This is usually used in the cases where only a single peak is obtained in the

FT which is the case here. The first shell coordination was used since we expect to have a chemically disordered A2 phase structure. Thus, for any given atom (Fe or Co) there is a 50% chance to have a Fe or Co atom as nearest neighbour (NN). As such, the interatomic distance for the absorbed atoms was initialized at $R_1 = 2.484$ Å and $R_2 = 2.868$ Å which corresponds to the distance for the NN in the bulk FeCo alloy [26]. The fits obtained on the neutral as-prepared FeCo nanoparticles displayed some differences mainly in that the interatomic distance for Co-Co is smaller than the Fe-Fe one ($d_{Fe-Co} < d_{Co-Co} < d_{Fe-Fe}$).

The number of nearest neighbours for a given atom in a perfect B2 FeCo crystal is $8+6 = 14$ (figure 3.22). A Fe atom has 6 Fe neighbours and 8 Co neighbours. In nanoparticles, this number of nearest neighbours is no longer valid. Since in nanocrystals, there are more atoms on the surface of the nanocrystallites than in their core. Thus, the average number of nearest neighbours is smaller in this case since the surface atoms will have less metallic neighbours than the core atoms. Thus, for small nanoparticles, the number of nearest neighbours is smaller depending on the size. In addition, from the FT of our samples only one peak is present in the FT and the position of the peak for the as-prepared samples is smaller compared to the annealed ones. This suggests that i) the average number of nearest neighbours that we are able to detect is smaller, ii) we are only able to detect neighbours at the R_1 distance, *i.e.* d_{Fe-Co} (d_{Co-Fe}). For a bulk structure, this distance corresponds to 8 neighbours, whereas for nanocrystals this value will be smaller.

In the case of the as-prepared nanoparticles, the number of NNs at both edges is around 5 atoms. However, after annealing the number of NNs increases to 11 at the two edges. This increase of number of NNs is in direct correlation with the crystal coordination and ordering. Thus, after annealing, the nanoparticles are better crystallized.

For the annealed samples a chemically ordered CsCl-B2 phase structure was used to fit the EXAFS oscillations. The fit was possible on both edges (Co and Fe) and gave similar values further verifying the validity of our used model. The Fe-Co and Fe-C (resp. Co-C) distances are also in agreement at both edges. For a chemically ordered CsCl-B2 phase structure, if we consider an iron atom in the bulk, the cobalt and iron NNs of this atom will have a ratio of NN $\frac{Co}{Fe} = \frac{8}{6} = 1.333$ (see illustration in figure 3.22). We get, at the Fe edge, the ratio of NN $\frac{Co}{Fe} = \frac{5.9}{4.4} = 1.34$ and at the Co edge the ratio of NN $\frac{Co}{Fe} = \frac{5.4}{4.1} = 1.32$. Notice that in our case:

$$d_{Fe-Co} = R_1 = 2.47 \text{ Å}$$

different from

$$d_{Fe-Fe} \times \sqrt{3}/2 = 2.41 \text{ Å or } d_{Co-Co} \times \sqrt{3}/2 = 2.37 \text{ Å}$$

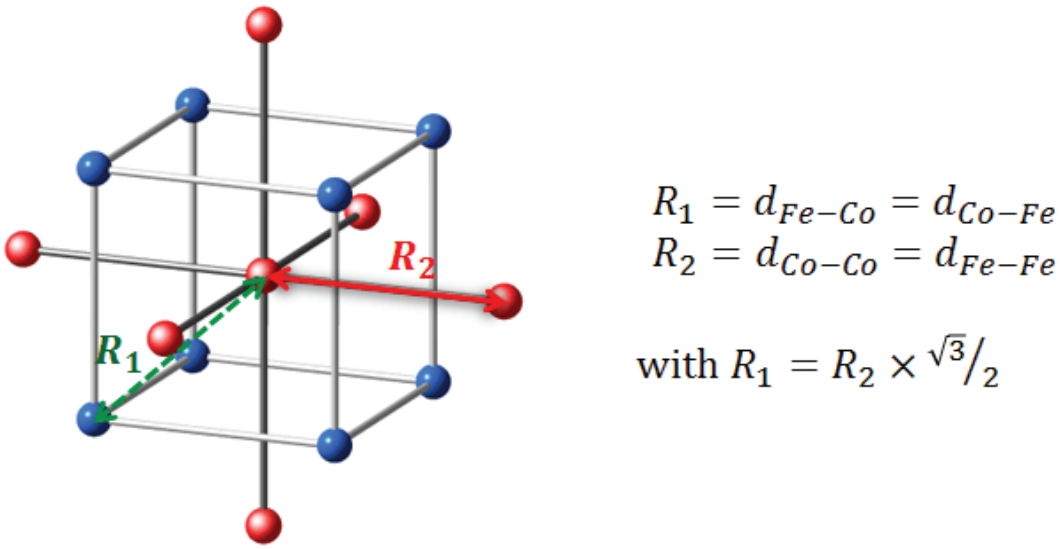

Fig. 3.22 A chemically ordered B2 phase CsCl unit cell for two different species of atoms.

In addition, although the fits presented here are the best fits obtained, it is clear that there are contributions which are not taken into account. First of all, the samples are made up from neutral FeCo nanoparticles, that is the size distribution for the particles in these samples have a large size dispersion of 45 %. Thus, the measured EXAFS signal is the super position of all nanoparticle sizes from 2 nm to 5 nm. If we consider a rhombic dodecahedron system a 2 nm sized particle has around 369 atoms, 52 % of which are on the surface, compared to around 6095 atoms for the 5 nm particle, of which only 23 % are on the surface. These values are calculated using the equations for a rhombic dodecahedron (according to the theory of Wulff [162]) below, where m is the number of atoms per edge ($m = 5$ for particles of 2 nm and $m = 12$ for particles of 5 nm). As for the size of the particles, they are estimated using the bulk FeCo lattice parameter of 2.868 Å.

$$\begin{aligned} N_{Total} &= (2m-1)(2m^2-2m+1) \\ N_{Surface} &= 12m^2-24m+14 \end{aligned} \tag{3.5}$$

Since these particles are embedded in a carbon matrix, these surface atoms are in direct contact with the matrix. Moreover, from magnetic studies performed on Co nanoparticles [178] we know that for the as-prepared particles, the amorphous carbon, even though inert does interact with the atoms at the particle-matrix interface.

In fact, a number of articles discuss the effects that arise from the presence of carbon atoms at the surface of nanoparticles used as catalysts. For instance, Diarra *et al*. predicts the carbon solubility in nickel nanoparticles using a grand canonical Monte Carlo study [53, 54].

By using tight-binding calculations, they showed that carbon solubility becomes larger for smaller nanoparticles. Magnin *et al*. predicts that the same effects are expected for Fe and Co nanoparticles [55]. In these studies, the nanoparticles are used as catalysts for the formation of carbon nanotubes.

Kuzentsov *et al*. used XRD to study the activation of Fe, Co and FeCo catalysts for the growth of multi-walled carbon nanotubes [51]. In this study, they show how catalysts containing Fe demonstrates the simultaneous formation of Fe-C alloys and their transformation into the stable cementite (Fe_3C); while for the FeCo alloyed nanoparticle catalysts, no carbide formation is formed, whereas the diffusion of carbon through the metal particle is high providing much higher activity as a catalyst. For the latter, they argue that the Co additions prevent the formation of stable iron carbides.

Mazzucco *et al*. observed how the type of iron carbide affects the activation or inhibition of carbon nanotube formation [56]. They found that a cementite carbide activates the nanotube growth while a Hägg carbide (Fe_5C_2) inhibits the growth. Hardeman *et al*. also report the effect of the FeCo catalyst on the growth of carbon nanotubes [52]. They observe how the absence of a stable carbide promotes an effective carbon diffusion through the metal particles providing much higher activity for FeCo catalysts compared to Fe catalyst where iron carbides are more favourable.

Thus, in order to clarify these size effects a detailed EXAFS study for mass-selected FeCo nanoparticles with deviations of 150 V, 300 V and 600 V was performed for as-prepared and after annealing at the BM30B Fame beamline in collaboration with O. Proux.

Six FeCo samples were prepared; two samples for each deviation voltage (150 V, 300 V and 600 V). In addition to the FeCo mass-selected samples, two samples of deviation voltage of 300 V were prepared for each reference (Co and Fe). Furthermore, a detailed study of the iron carbide is discussed below.

3.6.3 Iron carbide

In this section, we will discuss in details the presence of carbon in the sample. Before talking about the iron-carbon (carbide) alloys let us discuss the cobalt-carbon alloys stability. Ishida *et al*. plotted the phase diagram for the Co-C alloy [179] as a function of the atomic percent of carbon and cobalt and as a function of temperature. Figure 3.23 presents this phase diagram.

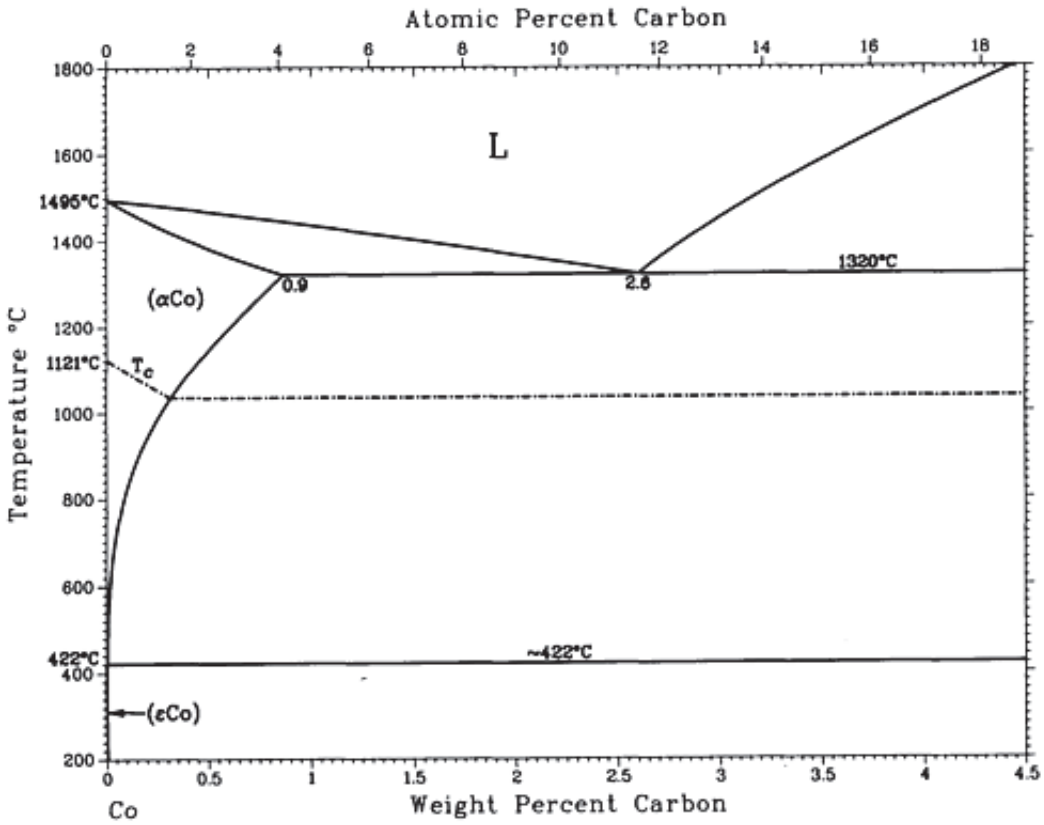

Fig. 3.23 Phase diagram for Co-C alloy as a function of temperature and atomic composition.

The phase diagram shows that cobalt and carbon are immiscible for almost all temperature. Two metastable phases are present for compositions of 6 % in weight (Co_3C) and 9 % in weight (Co_2C) [179] between temperature of 450 and 500°. Thus, at isothermal equilibrium and due to kinetic effects cobalt and carbon do not mix. For the as-prepared particles it might not be the case due to the diffusion of carbon into structural defects in the particle present during the deposition phase. However, after annealing at 500°C carbon is completely demixed from the cobalt particles as previously referenced by Tamion *et al*. [178].

On the other hand, iron and carbon atoms are known to be miscible and form different kinds of carbides depending on their composition and temperature. Okamoto compiled a

complete phase diagram for the Fe-C system which includes all the stable and metastable phases [180]. Figure 3.24 represents the phase diagram for Fe-C along with the stable carbides presented in table 3.11. There are four main stable carbides: the Cementite [181, 182], the Hägg carbide [181, 183], the ε-carbide [181, 182] and the η-carbide [181, 182].

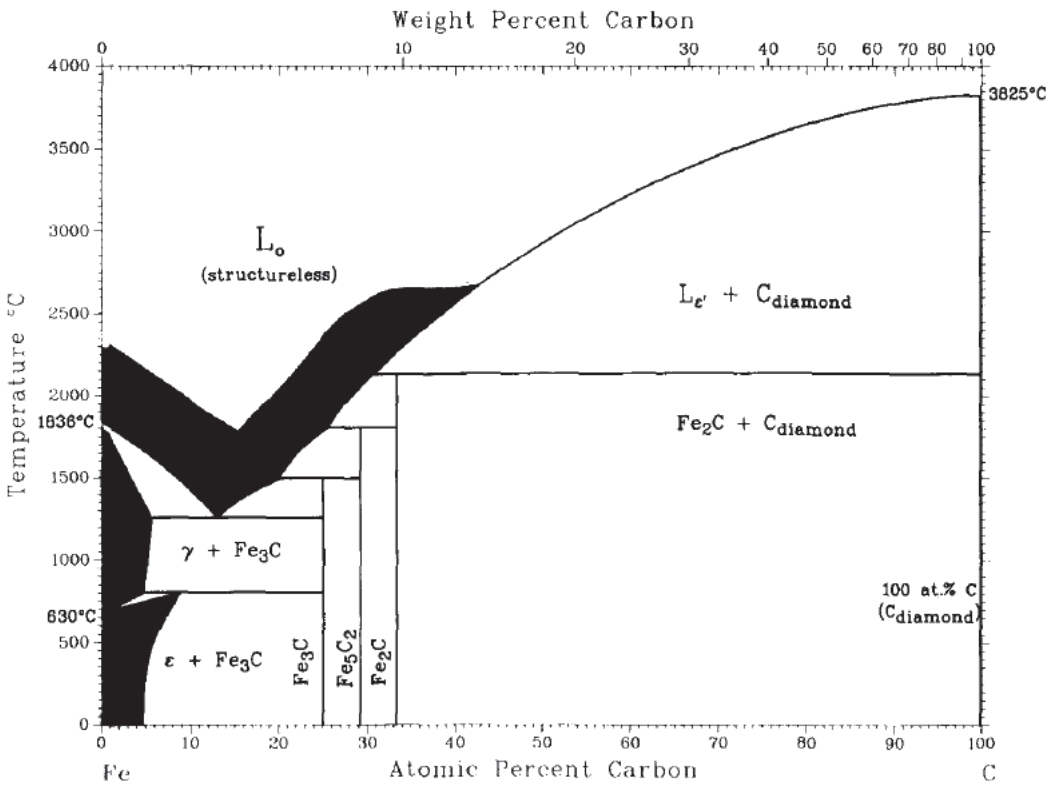

Fig. 3.24 Phase diagram for Fe-C alloy as a function of temperature and atomic composition.

Carbide Compound (% at. C)	Formula	Space Group	a (Å)	b (Å)	c (Å)	α (deg)	β (deg)	γ (deg)
Cementite (25%)	Fe_3C	P n m a (62)	4.5133	5.0679	6.7137	90	90	90
Hägg carbide (28.6%)	Fe_5C_2	C 2/c (15)	11.504	4.524	5.012	90	97.60	90
ε-carbide (33%)	Fe_2C	P 6 3 2 2 (182)	4.767	4.767	4.354	90	90	120
η-carbide (33%)	Fe_2C	P n n m (58)	4.687	4.261	2.830	90	90	90

Table 3.11 Fe-C carbides, their composition, space group and lattice parameters.

Looking at the path parameters generated for single scattering using the FEFF code [184], the distance Fe-C for the different carbides are very close. Thus, it is extremely difficult to distinguish the type of carbide present from the resulting fit distance of the Fe-C distances. Table 3.12 shows the scattering paths with the highest probabilities for the different paths and the corresponding Fe-C distance.

Carbide Compound	Distance (Å)
Cementite	2.0784
Hägg carbide	1.9766
ε-carbide	1.9259
η-carbide	1.9441

Table 3.12 Fe-C distances expected for the different carbides.

From the above table, the difference between the largest and smallest distance for the different carbides is $\Delta D = 0.1343$ Å. This value is too small to be quantifiable in disordered carbide (Debye-Waller factor > 0.01). Thus, fitting the EXAFS oscillations does not provide conclusive information on the type of the iron carbide present in the samples. Nevertheless, plotting the Fourier Transform of the EXAFS oscillations for the different carbides shows how the form of the radial distribution at the Fe:K-edge evolves for the different cases. Figure 3.25 presents the simulated radial distribution for the different carbides as a function of the Debye-Waller factor [184].

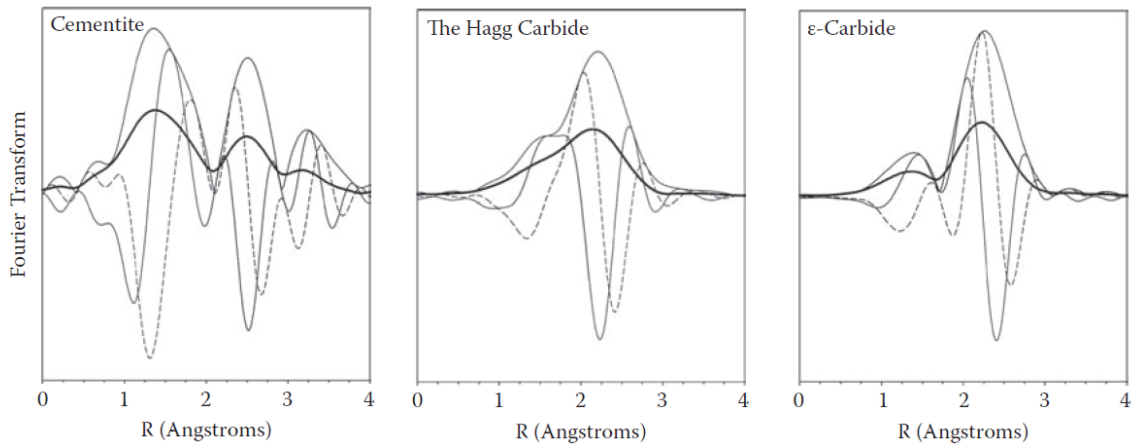

Fig. 3.25 Simulated radial distributions of EXAFS oscillations for the iron carbide systems for a Debye-Waller factor of 0.000 (light solid line) and Debye-Waller factor of 0.010 (thick solid line).

From qualitative analysis of the above figures, it is possible to predict the type of carbide with the position and separation of the coordination peaks. In addition to an obvious attenuation of the coordination peaks, a shift to lower distance is observed with increasing degree of disorder, as modeled by using the values of the Debye-Waller factor from 0 to 0.010.

3.6.4 Mass-selected clusters

For what follows, the cluster samples were mass-selected using the clusters source with the quadrupole deviator. For the pure cluster samples, that is Fe particles and Co particles, only one voltage deviation of 300 V was used with the same parameters as in the case of TEM samples. For the FeCo clusters, three sizes where chosen corresponding to the voltage deviations of 150 V, 300 V and 600 V having the same size and size distribution as there counterparts investigated using TEM. The latter was assured first by preparing the samples for TEM and EXAFS measurements at the same time, and also by using the same deposition parameters including the deposition time per layer of clusters. For what follows, we will refer to the mass-selected samples by the nomenclature presented in the table 3.13.

Name	Deviation voltage	TEM diameter (nm)	ω
$FeCo_{3.7}$	150 V	3.7 ±0.2	0.13 ±0.03
$FeCo_{4.3}$	300 V	4.3 ±0.2	0.12 ±0.03
$FeCo_{6.1}$	600 V	6.1 ±0.2	0.07 ±0.03
$Co_{3.4}$	300 V	3.4 ±0.2	0.13 ±0.03
$Fe_{4.4}$	300 V	4.4 ±0.2	0.16 ±0.03

Table 3.13 List of mass-selected FeCo, Co and Fe samples.

The samples were made up of a 2D configuration of alternating layers of clusters and amorphous carbon matrix with a total of 28 layers of clusters for EXAFS samples. All samples were capped with an amorphous carbon layer to prevent them from oxidation. For each voltage deviation, two samples were prepared one after the other. Since the samples are deemed identical, for each pair one was annealed at 500°C for two hours under UHV conditions while the other was left as-prepared. For the carbon matrix, a new carbon evaporator developed in our group was used (patent number WO/2014/191688). The average thickness of each carbon layer is between 2 and 3 nm.

3.6.4.1 Pure clusters

In order to better separate the contributions of the annealing, alloying as well as the size effects, it was necessary to investigate both pure nanoparticle samples as well as bimetallic ones. The results obtained for the Fe and Co systems are presented below. For the iron particles two $Fe_{4.4}$ samples and for the cobalt particles two $Co_{3.4}$ samples were prepared (one kept as-prepared and the other annealed). The energy shift fitting parameter is not included in the tables below (see chapter 2). For each measurement, this shift was fixed to be equal for all pathways. Moreover, this value was restrained between $-12eV < E_0 < +12eV$.

3.6.4.1.1 Fe system Figure 3.26 shows the evolution of the radial distribution after annealing of the $Fe_{4.4}$ sample. Figure 3.27 shows the EXAFS oscillations and the corresponding best fits for these samples. The results of the best fits are tabulated in table 3.14.

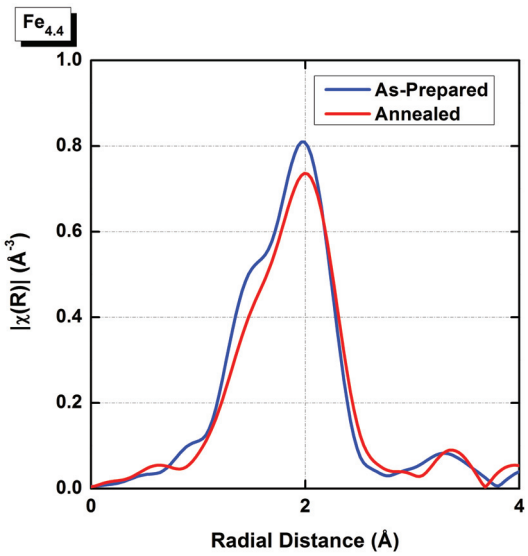

Fig. 3.26 Radial distributions of EXAFS oscillations of the as-prepared and annealed $Fe_{4.4}$ nanoparticles.

From the above figure, we can clearly see that after annealing the crystal coordination in the Fe nanoparticles is reduced. This is evidenced by the decrease of the intensity of the principal peak. A slight shift of this peak towards the right indicates a small dilatation of the interatomic distances. Indeed, this qualitative analysis is quantitatively validated from the obtained best fits presented in figure 3.27 and table 3.14. To go a step further, comparing the shape of the peak with that of the iron carbides (figure 3.25), it appears that in the as-prepared clusters a Hägg carbide form is present. After annealing, the same carbide is still present but with a reduced crystal order.

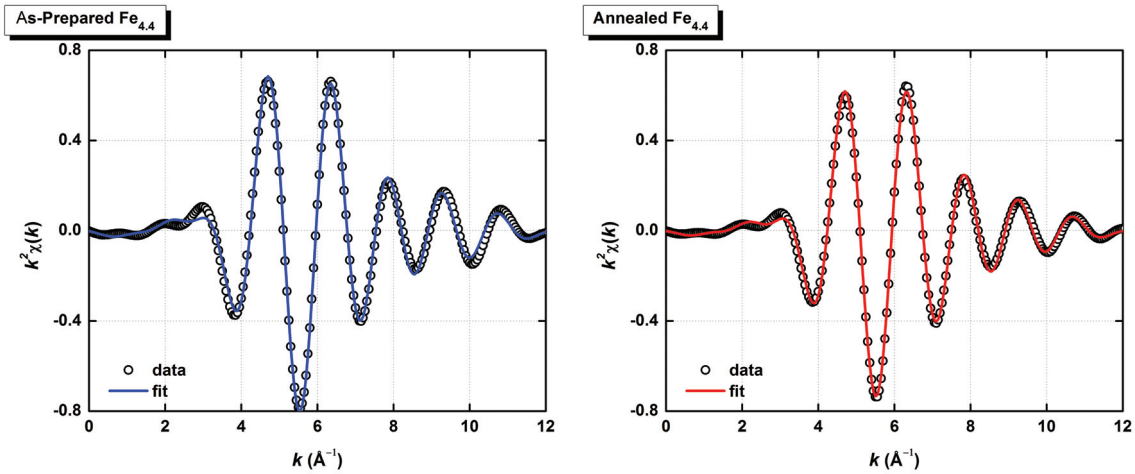

Fig. 3.27 EXAFS oscillations for as-prepared (left) and annealed (right) pure $Fe_{4.4}$ nanoparticles at the Fe:K-edge with their corresponding best fits.

	Path	Number of NNs	σ^2	R (Å)
As-Prepared	Fe-Fe	4.5	0.0133	2.47 ± 0.2
	Fe-C	1.4	0.0048	1.93 ± 0.2
Annealed	Fe-Fe	4.4	0.0138	2.49 ± 0.2
	Fe-C	1.3	0.0061	1.95 ± 0.2

Table 3.14 Values obtained for the best fits of the EXAFS oscillations for as-prepared and annealed pure $Fe_{4.4}$ nanoparticles at the Fe:K-edge.

From the fitting values for the $Fe_{4.4}$, a rather small difference can be noticed between before and after annealing. The crystal coordination remains the same since the number of NNs is almost unchanged as well as the NN distances. The carbon is present in both cases in agreement with the qualitative analysis suggesting that these particles are in fact made up of an iron carbide.

3.6.4.1.2 Co system Figure 3.28 shows the evolution of the radial distribution after annealing of the sample. Figure 3.29 shows the EXAFS oscillations and the corresponding best fits for these samples. The results of the best fits are tabulated in table 3.15.

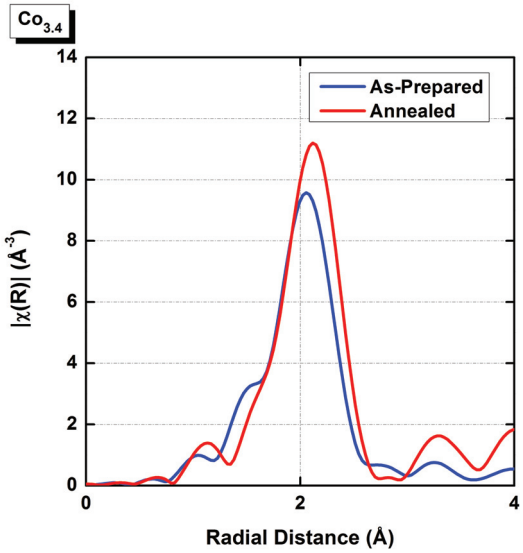

Fig. 3.28 Radial distributions of EXAFS oscillations of the as-prepared and annealed $Co_{3.4}$ nanoparticles.

From the above figure, contrary to the Fe nanoparticles, we can clearly see that after annealing the crystal coordination in the Co nanoparticles is enhanced, this is evidenced by the increase in intensity of the principal peak. A shift of this peak towards the right indicates a clear dilatation of the interatomic distances. Moreover, the shoulder due to the carbon neighbours is reduced. Indeed, this qualitative analysis is quantitatively validated from the obtained best fits presented in figure 3.29 and table 3.15. In addition, from qualitative analysis of the radial distribution, as well as from quantitatively fitted data, it is clear that after annealing there is a demixing of the cobalt and carbon atoms.

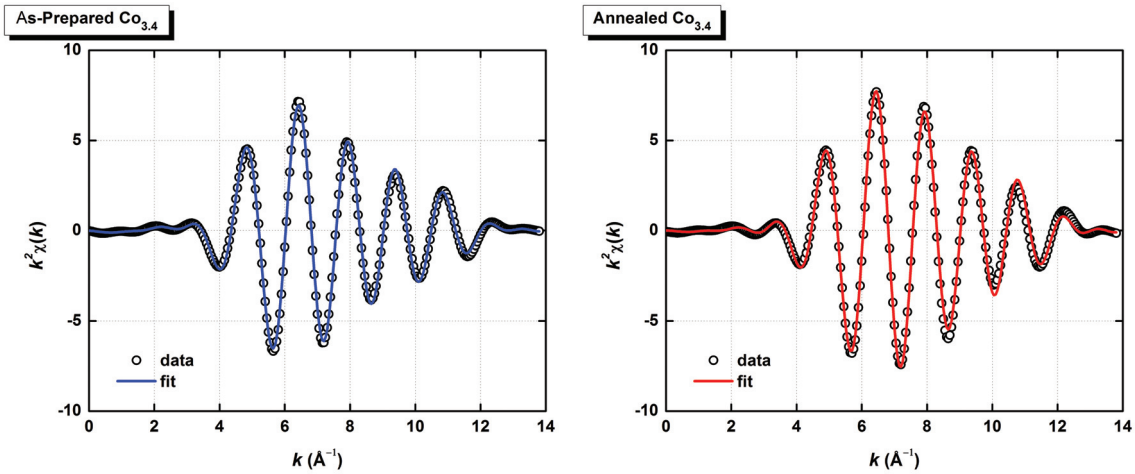

Fig. 3.29 EXAFS oscillations for as-prepared (left) and annealed (right) pure $Co_{3.4}$ nanoparticles at the Co:K-edge with their corresponding best fits.

	Path	Number of NNs	σ^2	R (Å)
As-Prepared	Co-Co	6.2	0.0109	2.46 ± 0.2
	Co-C	1.2	0.0046	1.94 ± 0.2
Annealed	Co-Co	5.7	0.0090	2.48 ± 0.2
	Co-C	0.9	0.0027	2.01 ± 0.2

Table 3.15 Values obtained for the best fits of the EXAFS oscillations for as-prepared and annealed pure $Co_{3.4}$ nanoparticles at the Co:K-edge.

Taking into consideration the results of both the pure iron and cobalt nanoparticles, we can identify two trends. In the case of the iron nanoparticles, annealing increased the crystal disorder and reduced its coordination. Moreover, the Debye-Waller values for the Fe particles exhibited an increase after annealing. From the previous tendencies we can deduce that the carbon atoms, upon annealing, further diffused into the Fe particles. On the other hand, for the cobalt nanoparticles, annealing increased the ordering in the lattice and enhanced the relative coordination between the metal and carbide. Furthermore, the reduction of the Debye-Waller factor further confirms these results. This tendency was previously observed in Co particles from magnetic characterization [178]. We can, thus, establish two behaviours:

- that of the iron particles where annealing increases the diffusion of carbon atoms into the particles

- that of the cobalt particles where annealing demixes the carbon atoms from the particles and expels them back to the matrix.

3.6.4.2 Bimetallic FeCo clusters

The bimetallic FeCo nanoparticle samples were all prepared during the same experiment. For all deviation voltages, two samples were prepared (one left as-prepared and the other one annealed). The list of samples was previously presented in table 3.13. Before delving into the quantitative description of results for each size, we will start a qualitative overview of the as-prepared samples, as well as the annealed one. In addition, the investigation of the XANES signal was established in a collaboration with Yves Joly (Institut Néel, Grenoble; private comm.). The XANES signal at the Fe K-edge for Fe and FeCo (B2) nanoparticles having a diameter of 1.6 nm was simulated. The simulation, shown below in figure 3.30, shows only a slight difference in the XANES shape of the two systems. The observed difference from the simulation is very small and shows that it is quite difficult to distinguish a bcc structure from a chemically ordered CsCl-B2 structure.

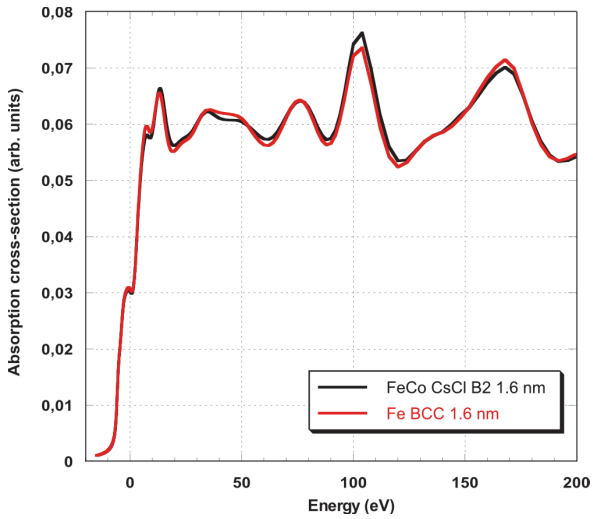

Fig. 3.30 The simulations of the XANES signal for 1.6 nm Fe and FeCo (B2) nanoparticles (performed by Yves Joly, Institut Néel Grenoble) show the difficulties to distinguish a bcc from a CsCl-B2 phase.

3.6.4.2.1 As-prepared Figures 3.31 and 3.32 show the normalized XAS signal and the radial distribution at the Fe and Co K-edges, respectively, for the as-prepared samples for all sizes ($FeCo_{3.7}$,$FeCo_{4.3}$ and $FeCo_{6.1}$).

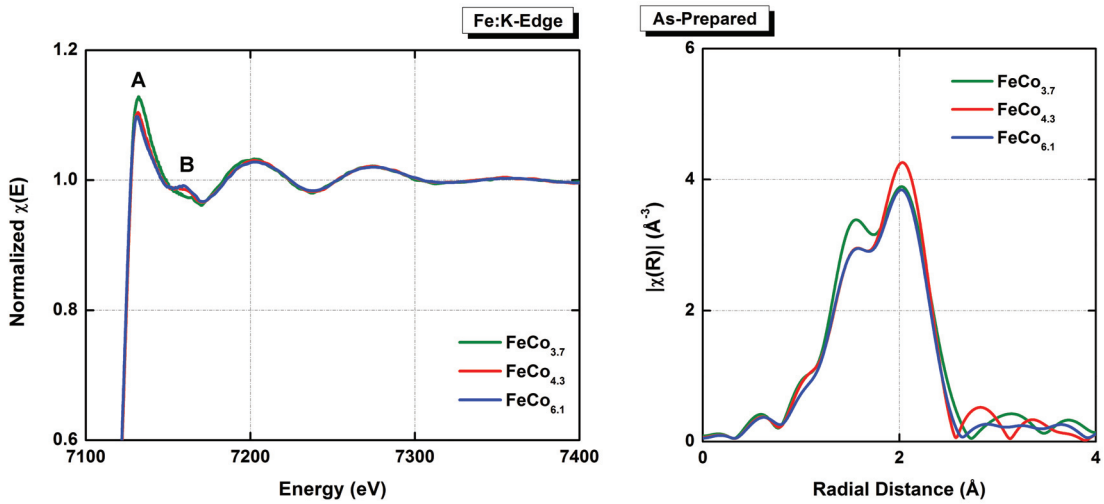

Fig. 3.31 The normalized XAS signal (left) and Radial Distributions of EXAFS oscillations (right) for the as-prepared $FeCo_{3.7}$, $FeCo_{4.3}$ and $FeCo_{6.1}$ samples at the Fe:K-edge.

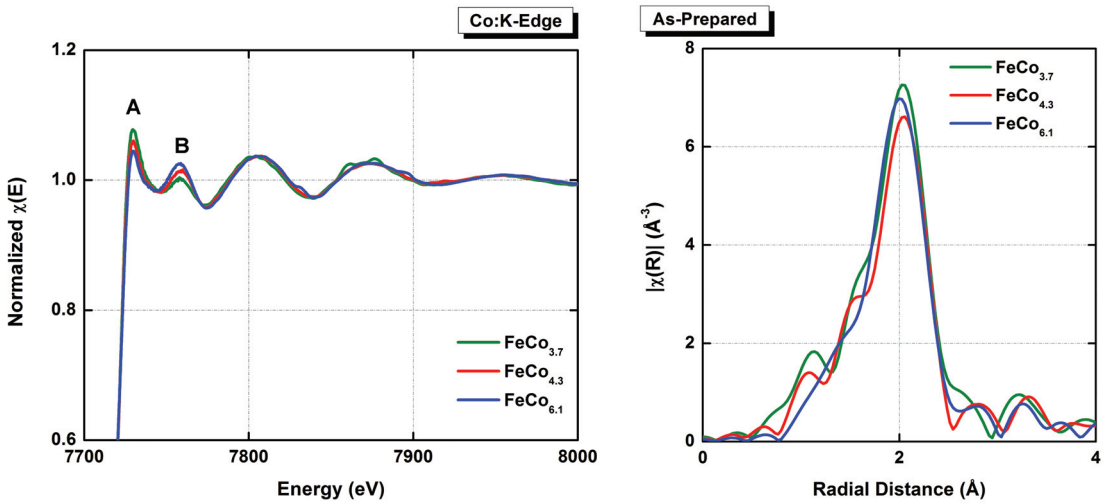

Fig. 3.32 The normalized XAS signal (left) and Radial Distributions of EXAFS oscillations (right) for the as-prepared $FeCo_{3.7}$, $FeCo_{4.3}$ and $FeCo_{6.1}$ samples at the Co:K-edge.

From the normalized XAS signals at both edges, the three nanoparticle sizes exhibit almost the same signature. It is practically impossible to distinguish the difference between the structural information carried by the EXAFS oscillations for the different sizes. Some slight differences can be observed at the X-ray Absorption Near Edge Structure (XANES) except the fact that the smaller the sample size, the higher white line peak (A) and the smaller first oscillation peak (B). The XANES is often used to determine the valence state of the probed atom [185] (Fe or Co in our case). As the amplitude of the white line peak increases,

the carbide signature increases, while the increase of the first oscillation peak indicates a better crystallization (increased ordering). As for the radial distribution, the position of the primary peak is the same for all sizes, with a slight shift for the $FeCo_{6.1}$ sample at the Co K-edge. The pre-peak signal is almost the same with some minor deviation from one size to another. The latter is strongly related to the form of the XANES peak and can be used to determine the type of carbide at the iron edge.

3.6.4.2.2 Annealed Figures 3.33 and 3.34 show the normalized XAS signal and the radial distributions of EXAFS oscillations at the Fe and Co K-edges, respectively, for the annealed samples for all sizes ($FeCo_{3.7}$,$FeCo_{4.3}$ and $FeCo_{6.1}$).

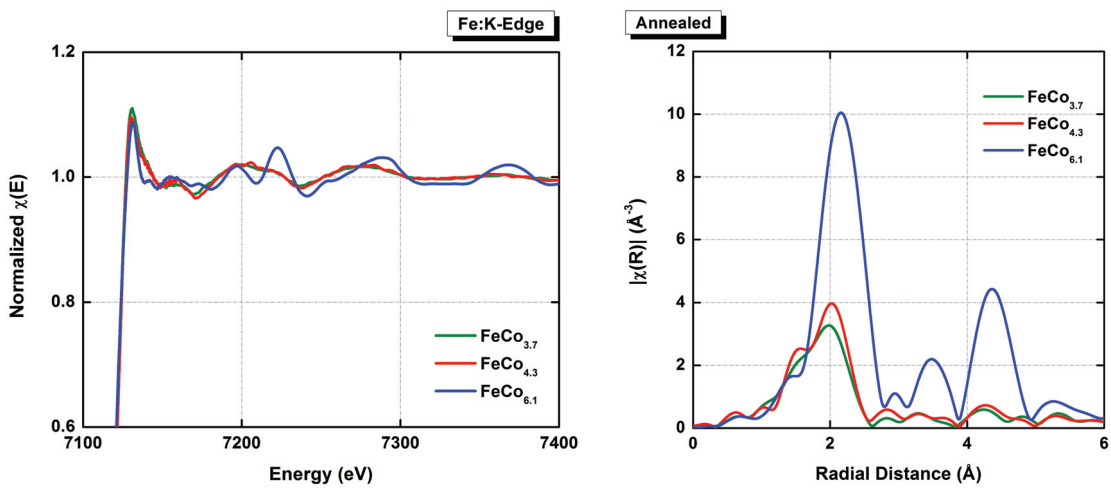

Fig. 3.33 The normalized XAS signal (left) and Radial Distributions of EXAFS oscillations (right) for the annealed $FeCo_{3.7}$, $FeCo_{4.3}$ and $FeCo_{6.1}$ samples at the Fe:K-edge.

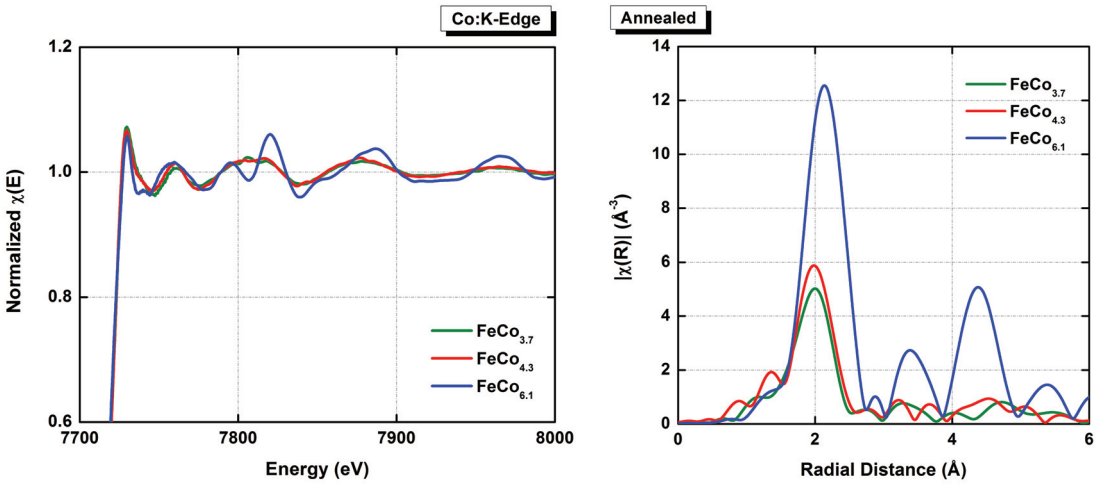

Fig. 3.34 The normalized XAS signal (left) and Radial Distributions of EXAFS oscillations (right) for the annealed $FeCo_{3.7}$, $FeCo_{4.3}$ and $FeCo_{6.1}$ samples at the Co:K-edge.

For the annealed samples, taking into consideration the $FeCo_{3.7}$ and $FeCo_{4.3}$, both samples exhibit almost the same EXAFS oscillations with a slight difference of the XANES edge. On the contrary, for the $FeCo_{6.1}$, the strong structural EXAFS oscillations are completely different of all the other sizes. The same can be observed from the radial distribution. For the smallest nanoparticle samples ($FeCo_{3.7}$ and $FeCo_{4.3}$) the position of the main peak is the same while the pre-peak shows some variations. Comparing the $FeCo_{6.1}$ nanoparticles sample with the smaller sizes, from a first glance, a shift of the primary peak is observed at both edges. In addition, oscillations of the radial distribution are clearly visible up to 6 Å at both edges (see figure 3.35) even comparable to the radial distribution of the metallic Fe foil. It can be compared to the previous studies performed on $L1_0$ CoPt nanoparticles [92, 186] and on B2 FeRh nanoparticles of 3 nm [77, 187] where the crystallographic order was only observed up to 3 Å even for a long-range chemical order coefficient $S = 0.8$.

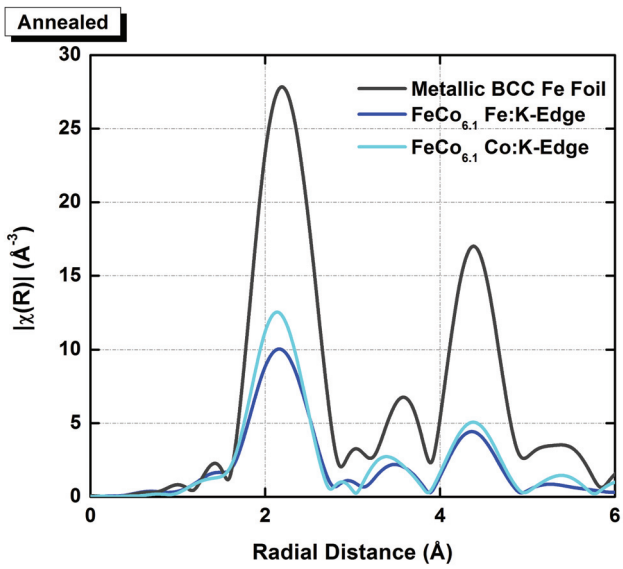

Fig. 3.35 The radial distributions of EXAFS oscillations for the annealed $FeCo_{6.1}$ nanoparticles sample at both Fe and Co K-edges, and for the Fe metallic foil at the Fe K-edge.

For the annealed $FeCo_{6.1}$ sample, comparing the shape of the peaks at both edges, it is clear that a bcc like structure is present in the nanoparticles. The position, intensity and ratio of the peaks is in agreement with that of the Fe metallic foil implying that after annealing of the $FeCo_{6.1}$ a bcc like crystallographic structure is formed but it is difficult to distinguish between a bcc and CsCl-B2 phase FeCo (as seen in figure 3.30).

On to a more detailed quantitative analysis, the EXAFS results are presented below in a separate section for each size (small: $FeCo_{3.7}$, $FeCo_{4.3}$, and large $FeCo_{6.1}$).

The fits for the as-prepared sample were achieved using pathways generated with the "first shell" coordination for each site. Since in the as-prepared case a chemically disordered structure is expected, the number of nearest neighbours being iron or cobalt was set equal. The distances Fe-Co and Co-Fe must be the same for both edges. At larger size, the ratio of the nearest neighbour being iron or cobalt was also fixed in the fit. In addition, the distances Fe-Co and Co-Fe were also set equal. For the qualitative analysis, the shape of the peaks at the Fe edge are also compared to those of the iron carbides presented in figure 3.25.

3.6.4.2.3 FeCo 3.7 nm / FeCo 4.3 nm Figures 3.36 and 3.37 show the evolution of the radial distributions of EXAFS oscillations for the $FeCo_{3.7}$ and $FeCo_{4.3}$ samples, respectively, after annealing, at the two K-edges Fe and Co.

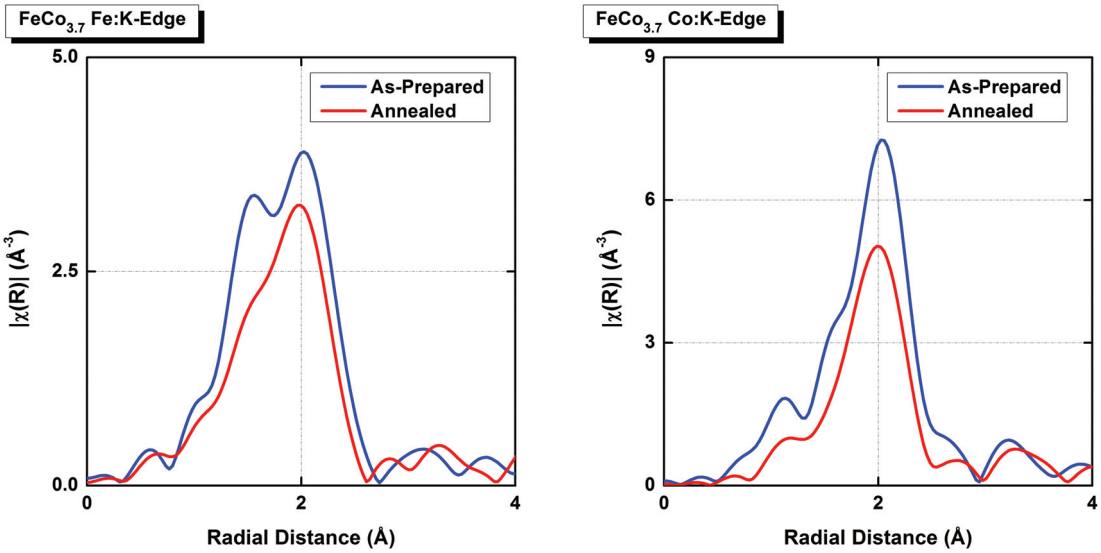

Fig. 3.36 Radial Distributions of EXAFS oscillations for as-prepared (blue) and annealed (red) $FeCo_{3.7}$ nanoparticles at the Fe:K-edge (left) and Co:K-edge (right).

At the iron site, the as-prepared $FeCo_{3.7}$ signal shows two distinct peaks, the principal around 2 Å, the other near 1.5 Å. The shape of the peaks resembles a mixture of cementite and ε-carbide signatures. After annealing, the carbide signal becomes that of a Hägg carbide accompanied by a reduction of the crystal coordination evidenced by a decrease in the intensity of the principal peak. At the cobalt site on the other hand, the annealed signal is almost free of a carbide signal but shows a decreased peak intensity due to a decrease in NN (*i.e.* increase of disorder). This behaviour could be explained by the diffusion of carbon atoms at the iron site into the particle's core; ε-carbide to Hägg carbide Fe-C contribution. While at the cobalt site a demixing of cobalt and carbon is observed.

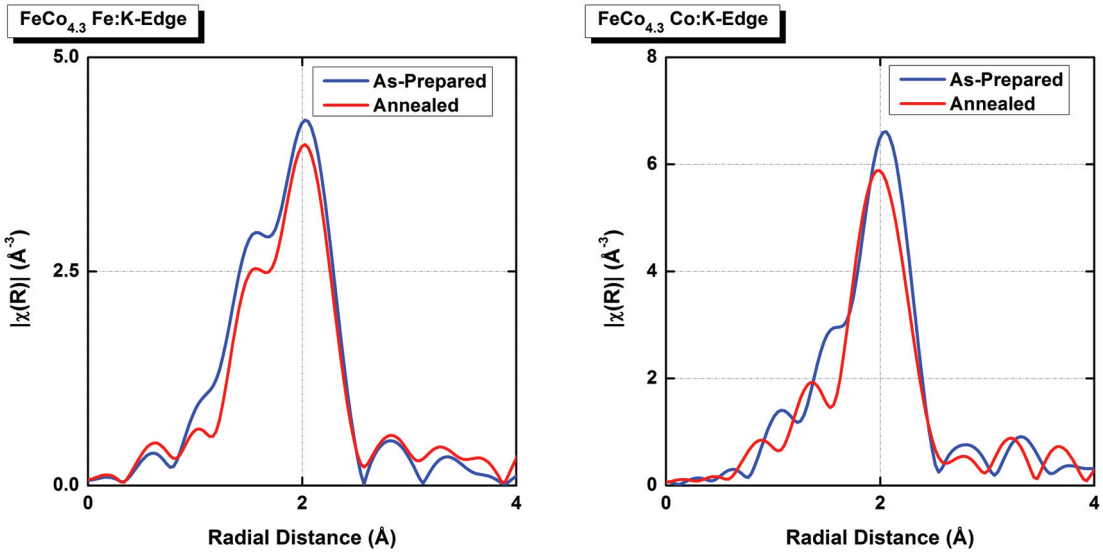

Fig. 3.37 Radial Distributions of EXAFS oscillations for as-prepared (blue) and annealed (red) $FeCo_{4.3}$ nanoparticles at the Fe:K-edge (left) and Co:K-edge (right).

At the iron site, the as-prepared $FeCo_{4.3}$ signal shows a principal peak around 2 Å preceded by a shoulder. The shape of the peaks resembles a Hägg carbide signature. After annealing, the carbide signal is slightly attenuated alongside a decrease in the principal peak intensity signaling a reduction in the crystal coordination. At the cobalt site, the as-prepared signal shows a shoulder before the principal peak signaling the presence of carbon. After annealing however, the principal peak is shifted to the left and the shoulder peak is completely separated from the principal peak.

Comparing the carbon signature, for small nanoparticle sizes ($FeCo_{3.7}$ and $FeCo_{4.3}$), more carbon diffuses into the particle's core resulting in a mixture of carbon phases. After annealing, however, the carbon diffusion seems to be stabilized in the nanoparticles in the form of Hägg carbide. The latter is more prominent at the iron edge than at the cobalt edge suggesting that the carbon is mostly seen by iron atoms. This effect can probably be explained by the positioning of the carbon atoms in interstitial regions in the proximity of the iron sites [53, 181]. The same effect is observed for the medium sized nanoparticles ($FeCo_{4.3}$) where as-prepared particles show a Hägg carbide signature that is attenuated after annealing, with a less prominent presence of a cobalt carbide. For the quantitative fit, only the fit for the $FeCo_{4.3}$ is presented since for the smaller $FeCo_{3.7}$ nanoparticles, the number of NNs is very small and there is high degree of disorder probably due to the high carbon solubility of small sized nanoparticles.

Fe:K-Edge Figure 3.38 shows the EXAFS oscillations and the corresponding best fits for the as-prepared and annealed $FeCo_{4.3}$ samples at the Fe K-edge. The results of the best fit are tabulated in table 3.16.

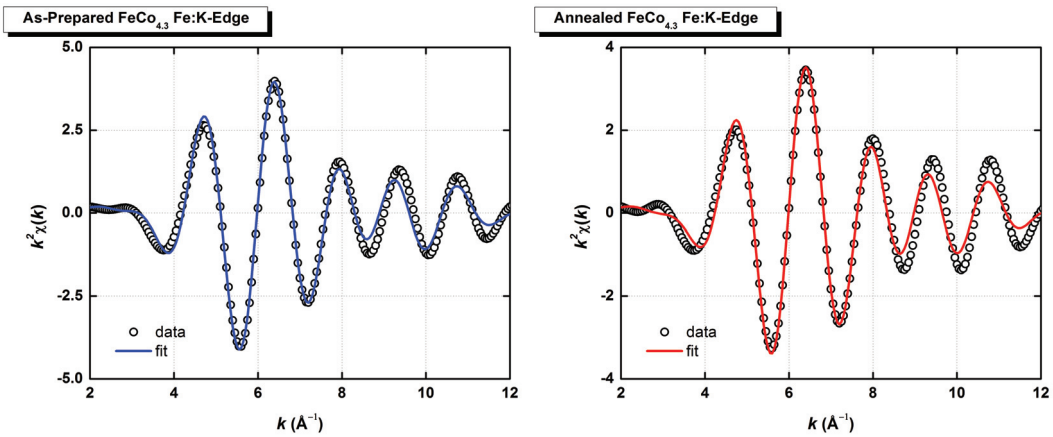

Fig. 3.38 EXAFS oscillations for as-prepared (left) and annealed (right) $FeCo_{4.3}$ nanoparticles at the Fe K-edge with their corresponding best fits.

	Path	Number of NNs	σ^2	R (Å)
As-Prepared	Fe-Fe	2.2	0.0148	2.46 ± 0.2
	Fe-Co	2.2	0.0144	2.46 ± 0.2
	Fe-C	1.5	0.0030	1.93 ± 0.2
Annealed	Fe-Fe	1.4	0.0084	2.52 ± 0.2
	Fe-Co	1.4	0.0082	2.42 ± 0.2
	Fe-C	1.3	0.0030	1.96 ± 0.2

Table 3.16 Values obtained for the best fits of the EXAFS oscillations for as-prepared and annealed $FeCo_{4.3}$ nanoparticles at the Fe K-edge.

The above fits, show for the as-prepared samples have a reduced NN of about 4 compared to the the bulk 8 NN for atoms at the R_1 distance and an equi-chance to have the first neighbour be iron or cobalt with a slightly compacted interatomic distance of around 2.46 Å compared to the FeCo bulk interatomic distance of 2.484 Å. Concerning the carbon presence, a large number of nearest neighbours is present at the iron site. The latter is expected since iron and carbon are expected to have a variety of configurations, as discussed earlier. For the annealed samples, qualitatively the measured signal showed little to no enhancement thus the EXAFS oscillations were fitted using a disordered structure. It should be noted that even

from EXAFS measurements, it is still difficult to distinguish a Co neighbour from a Fe one since the difference in backscattering amplitude and phase shifts between the two species are very small [188, 189], and only the absorbed atom is known with certainty (choice of absorption edge). Nevertheless, the resulting fit shows a tendency to have iron atoms at somewhat longer distances compared to the cobalt atoms for annealed samples, and to the as-prepared values. This distance, however, is slightly larger than that of the bulk (2.484 Å compared to 2.868 Å for the bulk). In addition, the carbide presence at the iron edge is less prominent compared to the as-prepared samples.

Co:K-Edge Figure 3.39 shows the EXAFS oscillations and the corresponding best fits for the as-prepared and annealed $FeCo_{4.3}$ samples at the Co K-edge. The results of the best fit are tabulated in table 3.17.

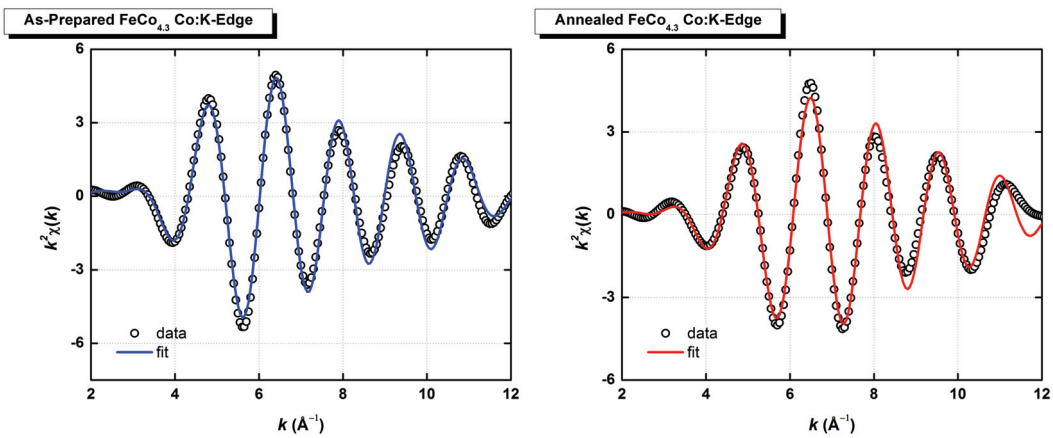

Fig. 3.39 EXAFS oscillations for as-prepared (left) and annealed (right) $FeCo_{4.3}$ nanoparticles at the Co K-edge with their corresponding best fits.

	Path	Number of NNs	σ^2	R (Å)
As-Prepared	Co-Co	2.1	0.0107	2.46 ± 0.2
	Co-Fe	2.1	0.0110	2.46 ± 0.2
	Co-C	1.2	0.0050	1.90 ± 0.2
Annealed	Co-Co	1.3	0.0080	2.41 ± 0.2
	Co-Fe	1.3	0.0082	2.42 ± 0.2
	Co-C	0.7	0.0046	1.95 ± 0.2

Table 3.17 Values obtained for the best fits of the EXAFS oscillations for as-prepared and annealed $FeCo_{4.3}$ nanoparticles at the Co K-edge.

Here the adjustments for the as-prepared sample are consistent with the results found at the Fe:K-edge with even less carbon presence near the cobalt sites. For the annealed samples, however, the Co-Co distance is very close to that of the Co-Fe (or Fe-Co). This decreased distance could be viewed as a contraction of the crystal lattice in the alternating Co-Co planes. In addition, the number of nearest neighbours after annealing is reduced (from 2.12 to 1.34 for the Co and the Fe atoms); the same trend was observed at the iron edge suggesting that a disordered structure persists after annealing. It should be noted that the values obtained from both Fe and Co edges for the Fe-Fe and Co-Co distances follow the same trend as found from the calculations of Aguilera-Granja *et al*. (private comm.) for small size relaxed B2 nanoalloys presented in table 3.1 and figure 3.3, where the Fe-Fe distance is found to be larger than the Co-Co distance.

3.6.4.2.4 FeCo 6.1 nm Figure 3.40 shows the evolution of the radial distributions of EXAFS oscillations for the $FeCo_{6.1}$ after annealing, at the two K-edges (Fe and Co).

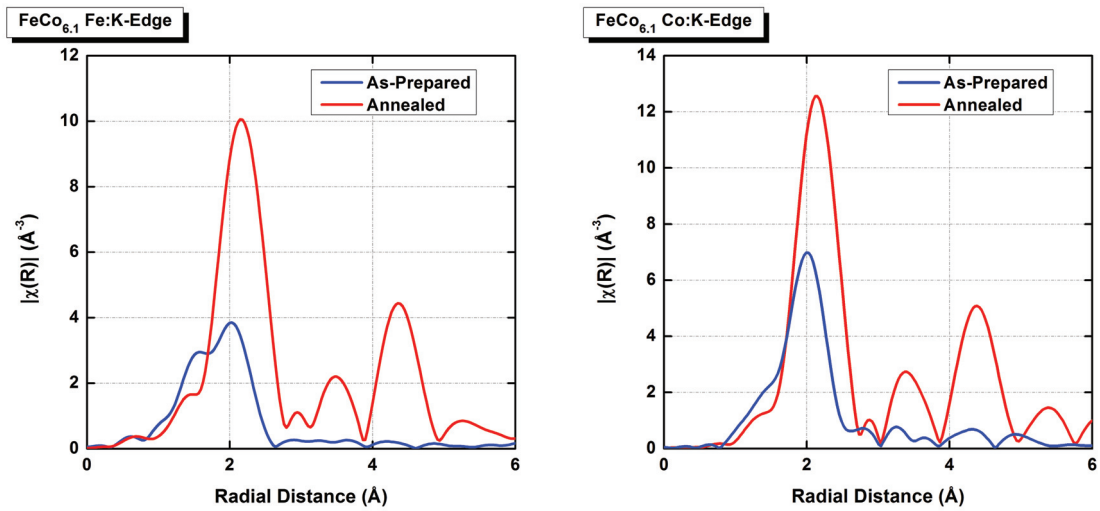

Fig. 3.40 Radial Distributions of EXAFS oscillations for as-prepared (blue) and annealed (red) $FeCo_{6.1}$ nanoparticles at the Fe:K-edge (left) and Co:K-edge (right).

For the largest size, at the iron site the shape of the peak resembles a Hägg carbide signature. After annealing, however, the EXAFS oscillations are completely transformed. The shape of the oscillations closely resembles that of the Fe bcc foil reference oscillations. The first peak of the radial distribution is shifted to the right and its intensity is more than twice as high as the as-prepared principal peak. In addition to the principal peak, two more strong peaks are observed resulting from the second nearest neighbour scatterings in the nanoparticles. Looking at the usual pre-peak (iron carbide shoulder), after annealing this

shoulder is severely diminished. At the cobalt edge, the same behaviour is observed after annealing (see figure 3.40). The carbon signature is even further reduced after annealing. The shape of the oscillations is in agreement at both edges. Overall, the FT of the $FeCo_{6.1}$ EXAFS oscillations at the Co edge has the same shape as the bcc Fe foil at the Fe edge shown in figure 3.35.

Thus, for the larger nanoparticles sizes ($FeCo_{6.1}$), upon annealing the Hägg carbide almost completely disappears suggesting that the carbon presence is only limited to the interface. Moreover, the as-prepared signal at both edges, as seen in figures 3.31 and 3.32, is the very close to that of the $FeCo_{3.7}$ and $FeCo_{4.3}$ nanoparticle samples. Thus, for the as-prepared particles, the Fe carbide is present for all sizes with varying quantity. After annealing, for the sizes smaller than the $FeCo_{6.1}$ almost no enhancement of the crystal coordination is observed, in fact more disorder can be noted due to an increased diffusion of the carbon into the cluster. Whereas for the $FeCo_{6.1}$, after annealing the carbon presence is almost completely suppressed, the crystal coordination shows an prominent evolution and the structure of the FT peaks is almost identical to that of the bcc and consequently the B2 CsCl phase structure. Thus, after annealing carbon solubility decreases as the nanoparticle size is increased. Here-below we present the adjustments for the as-prepared and annealed signals of the $FeCo_{6.1}$ samples for the two K-edges (Fe and Co).

Fe:K-Edge Figure 3.41 shows the EXAFS oscillations and the corresponding best fits for the as-prepared and annealed $FeCo_{6.1}$ samples at the Fe K-edge. The results of the best fits are tabulated in table 3.18.

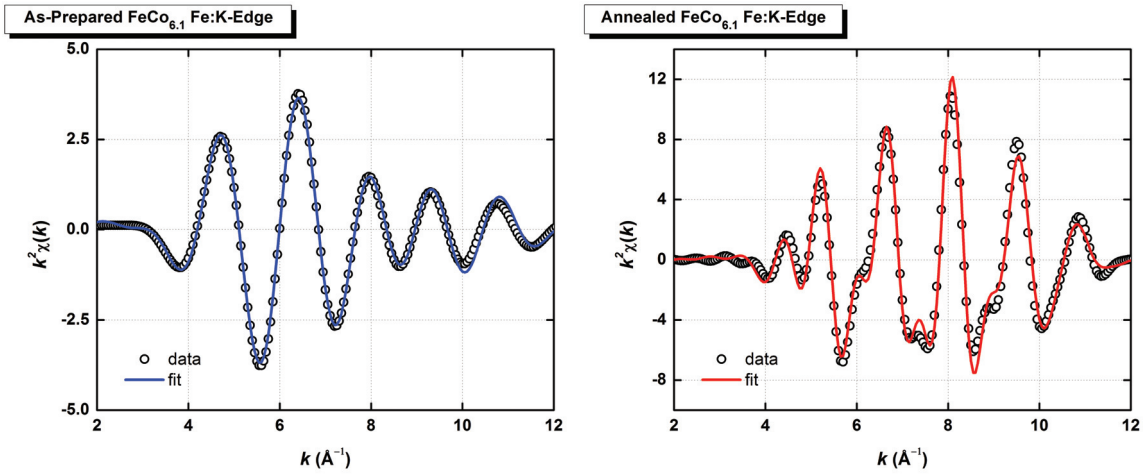

Fig. 3.41 EXAFS oscillations for as-prepared (left) and annealed (right) $FeCo_{6.1}$ nanoparticles at the Fe K-edge with their corresponding best fits.

	Path	Number of NNs	σ^2	R (Å)
As-Prepared	Fe-Fe	0.9	0.0122	2.67 ± 0.2
	Fe-Co	3.7	0.0119	2.46 ± 0.2
	Fe-C	1.5	0.0030	1.94 ± 0.2
Annealed	Fe-Co1	5.1	0.0089	2.46 ± 0.2
	Fe-Fe1	3.8	0.0104	2.80 ± 0.2
	Fe-Co1-Fe1	30.0	0.0107	3.90 ± 0.2
	Fe-Fe2	1.6	0.0119	3.99 ± 0.2
	Fe-Co1-Fe2	30.4	0.0118	4.49 ± 0.2
	Fe-Co2	15.2	0.0118	4.67 ± 0.2
	Fe-Fe3	5.1	0.0121	4.94 ± 0.2
	Fe-Co1-Fe3	10.1	0.0121	4.95 ± 0.2
	Fe-Co1-Fe3-Co1	5.1	0.0121	4.95 ± 0.2
	Fe-C	0.6	0.0273	2.02 ± 0.2

Table 3.18 Values obtained for the best fits of the EXAFS oscillations for as-prepared and annealed $FeCo_{6.1}$ nanoparticles at the Fe:K-edge.

Co:K-Edge Figure 3.42 shows the EXAFS oscillations and the corresponding best fits for the as-prepared and annealed $FeCo_{6.1}$ samples at the Co K-edge. The results of the best fits are tabulated in table 3.19.

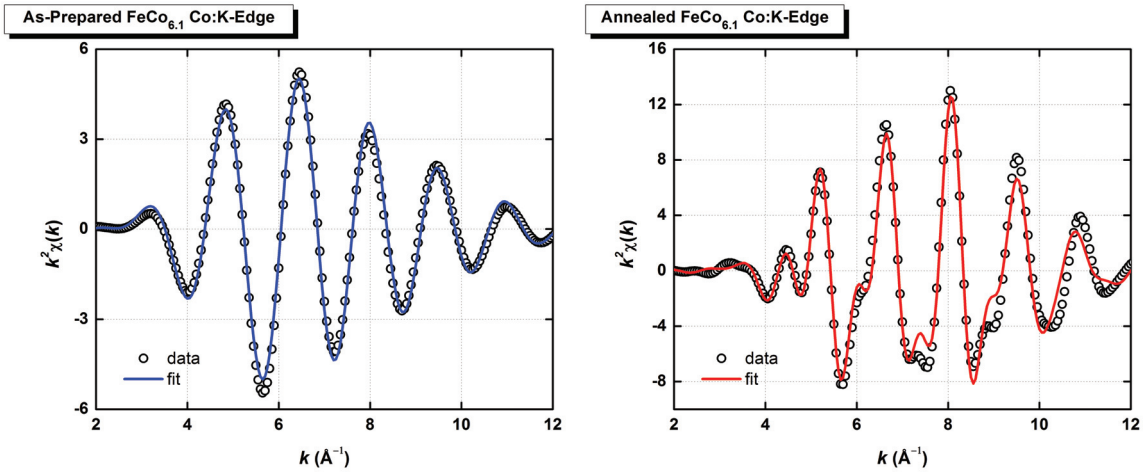

Fig. 3.42 EXAFS oscillations for as-prepared (left) and annealed (right) $FeCo_{6.1}$ nanoparticles at the Co K-edge with their corresponding best fits.

	Path	Number of NNs	σ^2	R (Å)
As-Prepared	Co-Co	1.5	0.0101	2.36 ± 0.2
	Co-Fe	3.7	0.0101	2.46 ± 0.2
	Co-C	0.5	0.0100	1.90 ± 0.2
Annealed	Co-Fe1	4.9	0.0089	2.46 ± 0.2
	Co-Co1	3.7	0.0098	2.81 ± 0.2
	Co-Fe1-Co1	29.7	0.0104	3.90 ± 0.2
	Co-Co2	7.4	0.0113	3.99 ± 0.2
	Co-Fe1-Co2	29.7	0.0114	4.49 ± 0.2
	Co-Fe2	14.8	0.0118	4.67 ± 0.2
	Co-Co3	4.9	0.0115	4.93 ± 0.2
	Co-Fe1-Co3	9.9	0.0115	4.95 ± 0.2
	Co-Fe1-Co3-Fe1	4.9	0.0115	4.95 ± 0.2

Table 3.19 Values obtained for the best fits of the EXAFS oscillations for as-prepared and annealed $FeCo_{6.1}$ nanoparticles at the Co:K-edge.

For the as-prepared sample, it was not possible to fit using the same parameters as that of the smaller $FeCo_{3.7}$ and $FeCo_{4.3}$ ones. Nevertheless, the number of NNs with the opposite species as well as its distance was fixed ($d_{Fe-Co} = d_{Co-Fe}$). At the iron edge, the number of NNs being Fe was small compared to that of the Co and was found at a further distance. At the cobalt edge, the number of NNs being Co is larger than the case of the Fe but at a shorter distance. Carbon is mostly seen by the iron atoms with only a small carbon signature present near the Co atoms.

Notice that the fit for the annealed sample was achieved up to around 6 Å. For this fit, a CsCl-B2 phase structure is used. At the iron edge, the ratio of the first two nearest neighbours is $\frac{6}{8} = 0.75 \simeq \frac{3.79}{5.06}$. The Fe-Co distance of 2.46 Å remains unchanged after annealing, however, the Fe-Fe distance is in accordance with that of the bulk FeCo. After annealing, similar to the iron edge, the cobalt edge shows the same values for the d_{Co-Fe} ($d_{Fe-Co} = 2.46$ Å) that are consistent with the as-prepared sample. The carbon atoms are only seen by the Fe atoms. The ratio of the number of nearest neighbours is also consistent of a 6 to 8 ratio. The ratio of the obtained R_1/R_2 at the two edges is different from $\sqrt{3}/2 \simeq 0.866$:

$$\frac{R_1}{R_2} = \frac{2.46}{2.81} = 0.875 \text{ at the Co edge}$$
$$\frac{R_1}{R_2} = \frac{2.46}{2.80} = 0.878 \text{ at the Fe edge}$$

suggesting a distortion of the lattice locally. To go further, no presence of a carbide signal at the cobalt edge is detected unlike at the Fe edge suggesting that the carbon is mostly seen by the iron atoms in the nanoparticles. So, the carbon atoms occupy mostly interstitial sites near the Fe atoms.

3.7 Discussion

The X-ray absorption and grazing incidence X-ray scattering allows to characterize the samples in their entirety. In fact, compared to high resolution transmission electron microscopy, the entire sample is probed which allows to have more statistics (around 10^{14} clusters per sample). The results discussed in the chapter are validated here on the entire sample:

- Microscopy measurements gave insightful information about the particle's morphology, size and size dispersion. Depending on the studied system, there exists a critical size below which the particles, as-prepared, exhibit a spherical structure. In the case of FeCo, particles whose size is smaller or equal to 4.3 nm are more or less spherical (corresponding to neutral or mass selected with a deviation voltage smaller up to 300

V). For the Fe and Co particles, a spherical shape is observed for the neutral particles and mass selected ones with a deviation of 150 V. Ramified structures begin to form for sizes larger than a critical one for all systems. Annealing in all cases induced a shape change to a more oval or spherical shape. In addition to microscopy observations, EDX and RBS provided conclusive results concerning the equiatomic nature of the FeCo nanoparticles and showed that there exists no evidence of oxidation.

- High resolution TEM images gave evidence that the annealed FeCo particles present a bcc structure for the different sizes. Some evidence of the presence of iron carbide was observed in as-prepared nanoparticles. Anomalous scattering further put in evidence the bcc structure for the large sized $FeCo_{6.1}$ nanoparticles, however the CsCl-B2 phase expected for the FeCo system was cannot be evidenced using these techniques, even from the simulation of scattering curves.

- EXAFS measurements provided different information concerning the local structure near the probed atoms and the nature of its neighbours. For the neutral particles a disordered structure is observed even after annealing with the presence of carbon neighbours near the two sites (iron site and cobalt one). For the mass-selected nanoparticles, a disordered structure persists in the small and medium sized particles ($FeCo_{3.7}$ and $FeCo_{4.3}$) after annealing. The nature of the carbon environment in these particles differs from one size to the other and also after annealing. The large $FeCo_{6.1}$ nanoparticles also showed the same expected disordered A2 structure before annealing with some relaxations, dilated Fe (contracted Co) NN distances compared to the as-prepared FeCo nanoparticles of the smaller sizes. After annealing a clear evolution of the structure is observed. From the FT of the EXAFS oscillations a prominent bcc like structural evolution is observed after annealing at both sites (Fe site, as well as Co site).

R_1/R_2	Fe:K-Edge	Co:K-Edge
Neutral FeCo	0.89 ± 0.14	0.90 ± 0.14
Mass-selected $FeCo_{6.1}$	0.88 ± 0.14	0.88 ± 0.14

Table 3.20 Ratio of the NN distances (R_1/R_2) after annealing for the neutral and mass-selected 6.1 nm FeCo nanoparticles.

Comparing the ratio of R_1/R_2 for the neutral FeCo and the mass-selected $FeCo_{6.1}$ annealed nanoparticles (see table 3.20) to the bulk value of $R_1/R_2 = 0.866$ shows that, at both

edges, the obtained ratio is larger than that of the bulk. At the Co edge, a strong dispersion of the d_{Co-Co} is obtained $d_{Co-Co} = 2.74$ Å (see table 3.10) with $\sigma^2 = 0.03$ for the neutral clusters due to large relaxation for the small sizes (see figure 3.3) whereas the larger $FeCo_{6.1}$ nanoparticles shows less distortion with values of $d_{Co-Co} = 2.81$ Å with $\sigma^2 = 0.01$ close to the bulk value of 2.868 Å with a ratio of $R_1/R_2 = 0.88$ closer to that of the bulk. Moreover, no carbon signal is observed for the larger $FeCo_{6.1}$ nanoparticles at the Co edge.

At the Fe edge, the distance d_{Fe-Fe} is larger due to carbon insertion, mostly in the small nanoparticles since the carbon solubility increases as the size of the nanoparticles decrease. A distortion of the lattice parameters is obtained with a ratio R_1/R_2 in the neutral nanoparticles, larger than the mass-selected $FeCo_{6.1}$ nanoparticles due to the large size dispersion and thus to the carbon presence.

The obtained values of distances $d_{Fe-Fe} > d_{Co-Co}$ (2.67 > 2.36) are in qualitative agreement with the values of Aguilera-Granja *et al*. (private comm.) for relaxed B2 nanoalloys presented in table 3.1 and figure 3.3. The obtained number of NNs for the annealed nanoparticles is larger than that of the as-prepared ones at 6.1 nm. The obtained R_1 values, however, are smaller than that of the bulk as in the small clusters.

From all the obtained data and their corresponding fits, it is safe to say that we have all the "symptoms" of a chemically ordered FeCo in the CsCl-B2 phase from EXAFS expected after annealing For the $FeCo_{6.1}$ nanoparticles. As a conclusion, even if no CsCl-B2 phase signature was observed from the AXD measurements (due to the small nanosize, and the low signal, noise of the superstructure peaks), our results are in agreement with Willard *et al*. who found from EXAFS measurements at both edges exactly the same evolution of FT after annealing of their FeCo based system [173–175]. They performed EXAFS and AXD experiments on FeCo nanoparticles of one order of magnitude larger size (40-60 nm) than our nanoparticles. They observed the same increase in the number of NNs and the structuration of the FT up to 6 Å after annealing at 500°C. In addition, from AXD, due to the large size of their nanoparticles they were able to see the (100) superlattice structure peak signature of a B2 CsCl phase structure. In our case, due to the small size of our FeCo nanocrystals, the broadening of the Bragg diffraction peaks was too large to allow us to isolate the (100) superstructural peak.

In chapter 4, the magnetic properties of the same nanoparticles are presented showing the direct correlation and impact of the structural properties of the particles on their magnetic properties.

Chapter 4

Magnetic properties of nanoparticle assemblies embedded in a matrix

In this chapter we are interested in studying the intrinsic magnetic properties of Co, Fe and FeCo nanoparticle assemblies. In particular, the magnetic anisotropy of assemblies having a fine size distribution as well as their magnetic spin and angular moments. For this work, SQUID magnetometry and XMCD techniques were used. In addition to the intrinsic magnetic properties, a direct correlation between the crystallographic structure and the corresponding magnetic signature is possible in the size selected particles as both studies were performed on the same samples. To go a step further, the influence of the matrix was investigated. The Stoner-Wohlfarth model as well as the adjustment techniques used to describe the magnetic properties of nanoparticle assemblies were discussed in chapter 2.

4.1 Magnetic properties of neutral clusters

The magnetic properties of our nanoparticle samples were measured using a Superconducting QUantum Interference Device (SQUID) magnetometer, specifically a MPMS-XL5 SQUID from Quantum Design. The list of studied samples is detailed in table 4.1.

Sample	Deposition	Cluster thickness	Concentration
FeCo (Annealed)	8 layer 2D	2 Å/layer	10%
FeCo (As-prepared)	8 layer 2D	2 Å/layer	10%
FeCo	co-dep.	16 Å	0.7%
Fe	co-dep.	13 Å	0.5%
Co	co-dep.	20 Å	1%

Table 4.1 List of neutral samples measured in this section.

The first couple of samples as prepared under UHV conditions one after the other; each sample is made up of 8 layers of nanoparticles separated by a layer of amorphous carbon. The first sample was annealed at 500°C for 2 hours while the second sample was left as-prepared. The second series of samples was also prepared under UHV conditions but were co-deposited with the matrix at the same time using an electron gun evaporator on an amorphous carbon crucible. These three samples were measured as-prepared using the SQUID after which they were annealed at 500°C for 2 hours and were re-measured again after annealing with the SQUID. The concentration of nanoparticle to matrix was obtained from RBS measurements on these samples.

We performed magnetization $m(H)$ measurements as a function of the magnetic field at different temperatures. $m(H)$ curves at 2 K show a typical hysteretic behaviour signature of particles in the blocked regime. In chapter 2, we introduced the energy barrier that governs the transition from the blocked to the superparamagnetic regime. This barrier depends on the volume of the nanoparticles and on their anisotropy constant, thus the values obtained for the coercive field H_c are a combination of both effects when $T > 0$ K. In our samples, as seen from TEM observations in chapter 3, the nanoparticles have a lognormal size distribution. At 2 K, the critical size for the transition from the blocked to the superparamagnetic regime is around ~ 2 nm as obtained from equation 2.39 which depends on the value of K_{eff}. This implies that for samples with small particle sizes, the obtained magnetization curves at 2 K is a superposition of the blocked and superparamagnetic nanoparticles magnetic signal.

In addition to the $m(H)$ magnetization measurements, ZFC/FC protocols were performed and the corresponding magnetic susceptibility curves were measured as a function of temperature. For these measurements, an external applied field of 5 mT was used in all samples. These curves were adjusted along with the high temperature $m(H)$ (at least two times higher than T_{max}) using the "Triple Fit" technique described in chapter 2.

Moreover, to ensure that our samples are free from magnetic interactions, IRM/DcD curves were also measured for all samples and the corresponding Δm was determined using equation 2.66. Furthermore, the IRM curves were simulated using the results of the triple fitting of the ZFC/FC and $m(H)$ at high temperature curves. It should be noted that for the IRM simulation, it was necessary to include a K_2 anisotropy component in addition to the K_1 as the magnetization switching using a magnetic field is more sensitive to the presence of a biaxial anisotropy (as described in chapter 2). The IRM fitting values allowed the simulation of the hysteresis loops, at low temperatures (2 K) while taking into account the superparamagnetic particles contribution.

4.1.1 10 % - Concentrated clusters

The two FeCo layered samples have a concentration of clusters to matrix of around 10 % from RBS measurements (see table 4.1). The crystallographic structure of these two samples was discussed in chapter 3. Here we report the different magnetic measurements performed on these two samples. Figure 4.1 shows the ZFC-FC curves of the two samples as well as $m(H)$ at $T = 200$ K.

From Figure 4.1 we obtain a maximum temperature for the as-prepared neutral FeCo nanoparticles of $T_{max}^{As-prepared} = 73$ K, to be compared to a temperature of around $T_{max}^{Annealed} = 150$ K for the annealed sample. Adjusting these data using the "Triple-Fit" technique was unsuccessful. The mean diameter obtained from TEM images on an equivalent as-prepared sample was $D_m = 3.2$ nm.

To go a step further, magnetic remanence measurements were performed using the SQUID. Figure 4.2 shows the obtained IRM/DcD data sets for the as-prepared and the annealed sample, in addition to their corresponding Δm.

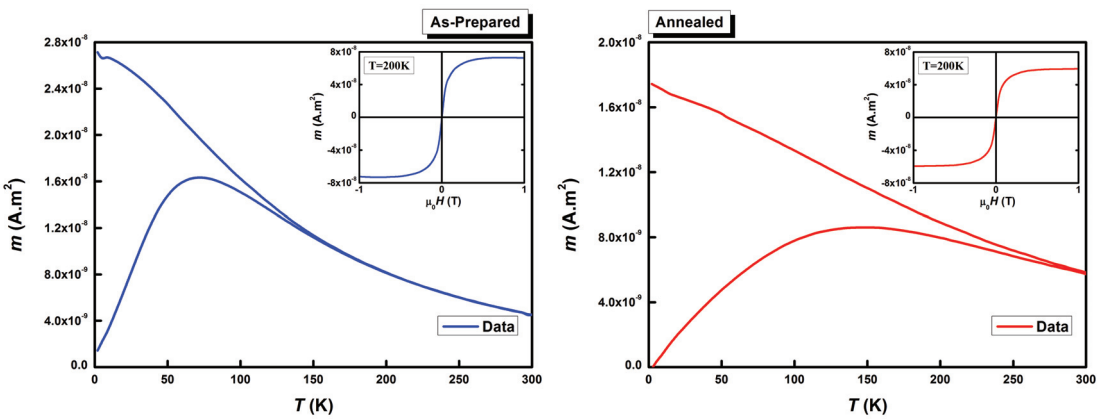

Fig. 4.1 ZFC-FC curves at 5 mT for the (left) as-prepared and (right) annealed samples, and the $m(H)$ at $T = 200$ K are presented in insert.

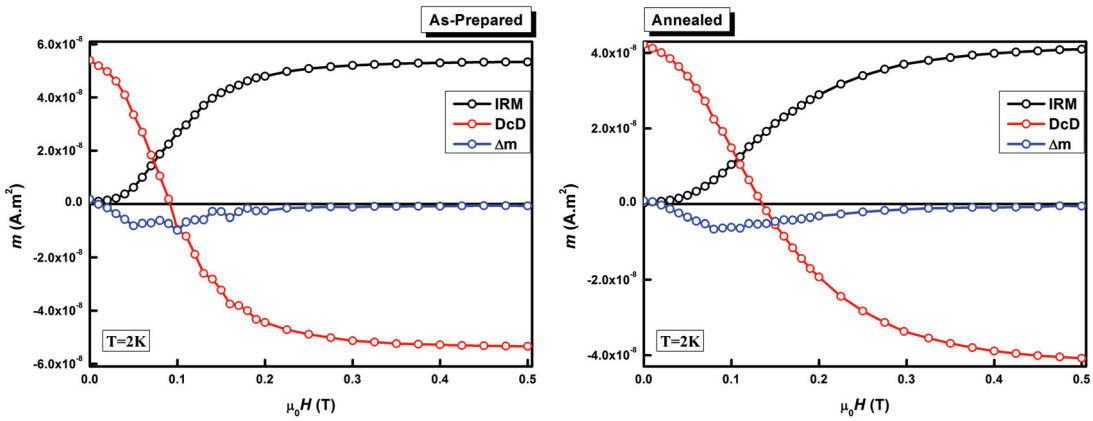

Fig. 4.2 IRM/DcD curves at 2 K for the (left) as-prepared and (right) annealed samples and their corresponding Δm.

From figure 4.2 it is clear that both samples exhibit magnetic interactions evidenced by a negative Δm larger than the background noise. In order to study the intrinsic magnetic properties of our clusters, it is necessary to eliminate all possible magnetic interactions between the clusters. Thus, the sample needs to be sufficiently diluted to minimize the dipolar interactions between the nanoparticles. In addition, the amorphous carbon matrix used in this study insures that we have no interactions of RKKY type.

A number of studies were performed in order to determine the influence of the interactions of nanoparticles on their magnetic properties [190–206]. The interactions are modeled by varying the interparticle distance by different methods: the particles are dispersed in a solvent, in a polymer or in an inorganic matrix and, thus, the distance depends simply on the concentration. In general, all of the presented studies indicate a more or less significant increase of the T_{max} with the increase of dipolar interactions. The amplitude of this variation and the dependence as a function of the distance varies from one study to the other. For hysteresis loops at 2 K, on the other hand, no particular behaviour was observed; the coercive field as well as the m_r/m_s ratio varies depending on the studied system.

To go a step further, in order to better understand the evolution of our sample, we simulated the sample microstructure with all the experimental conditions including the size distribution, the thickness and number of layers. The resulting simulation is presented in figure 4.3. The simulation also takes into account the possible coalescences that could occur in the sample during annealing for particles that are sufficiently close to one another, either only in the same plane, *i.e.* no coalescence permitted between different matrix layers (2D coalescence), or also through the carbon layers (3D coalescence).

For the simulation, a lognormal distribution with a mean diameter $D_m = 3.2$ nm and a dispersion $\omega = 0.45$ was used. The number of layers was set to 8, same as experimentally,

with an equivalent thickness of 2 Å of FeCo. 2D coalescence is permitted only for an edge-edge distance between the particles $D_{edge-edge}$ smaller than 4 Å. The simulation gives an average center-center distance between the particles $D_{center-center} = 6.7$ nm. After coalescence, the obtained histogram was fitted with a lognormal distribution centered around $D_m = 3.3$ nm with a size dispersion of $\omega = 0.48$ (see figure 4.5).

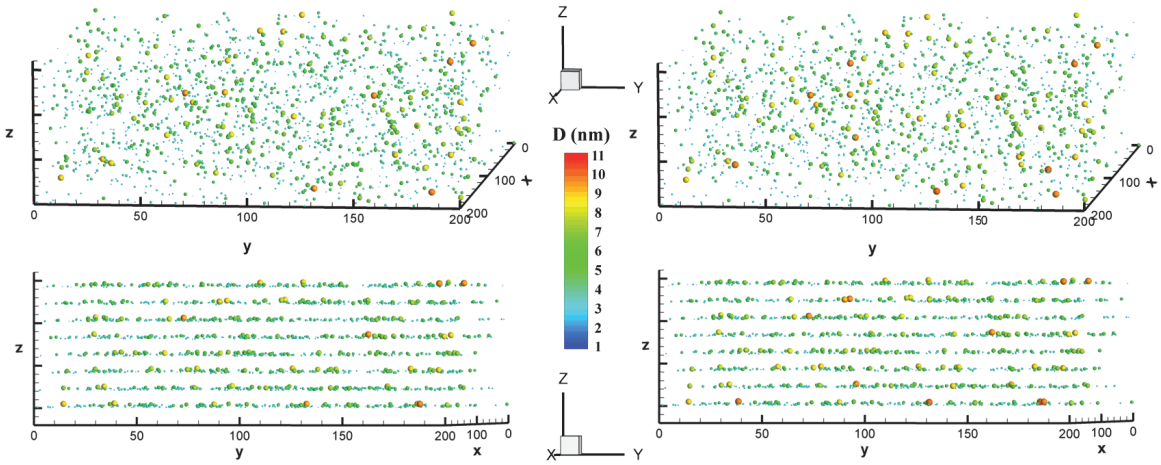

Fig. 4.3 Visual representation of a simulation of the sample before (left) and after annealing (right). The top representations are viewed with an oblique angle while the bottom ones are a cross-sectional view.

In fact, the above simulation does not take into account possible coalescence that could occur vertically (that is traversing the carbon layers, 3D coalescence). Figure 4.3 actually shows a somewhat zoomed-out version of the sample in order to show the eight layers. However, using the real values for the carbon thickness (≈ 3 nm) and nanoparticle concentration obtained from RBS, we obtained the evolution presented in figure 4.4.

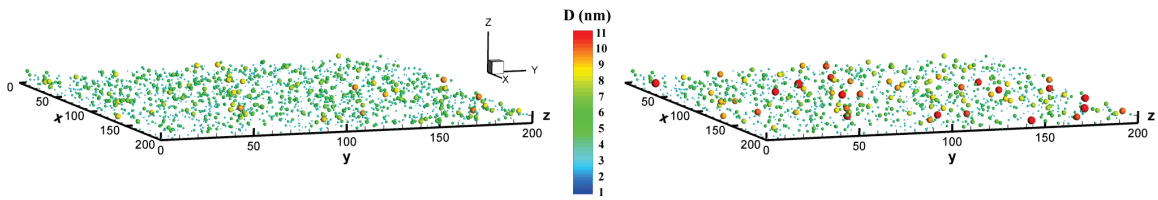

Fig. 4.4 Visual representation of a simulation of the sample before (left) and after annealing (right) viewed from an oblique angle.

The coalescence obtained from the simulation in this case is prominent and the value obtained for the average center-center distance is $D_{center-center} = 4.5$ nm. The obtained size histogram can be described using two lognormal distributions: the first centered around

$D_m = 2.9$ nm with a size dispersion of $\omega = 0.42$ and the second centered around $D_m = 6.3$ nm with a size dispersion of $\omega = 0.32$. The obtained size distributions, for both 2D and 3D coalescence cases, along with the initial size distribution, are plotted in figure 4.5. In addition to the size distributions, figure 4.5 shows the simulated ZFC curves using the size distribution parameters of the coalesced models.

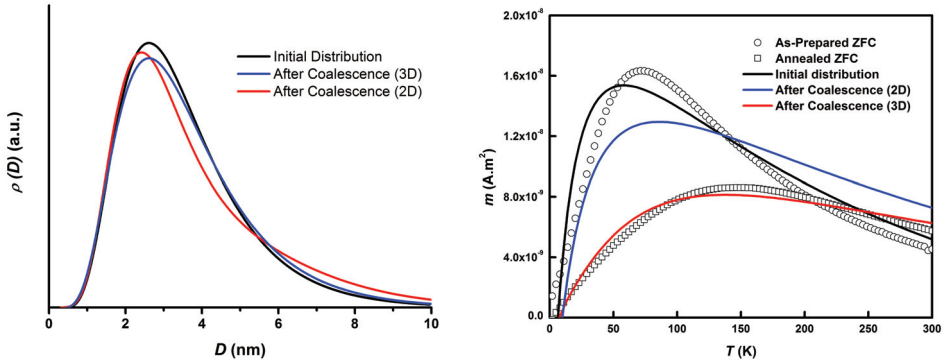

Fig. 4.5 (Left) Size distribution of the as-prepared and coalesced samples. (Right) ZFC of the as-prepared and annealed samples alongside the simulated ZFC curves.

For the above ZFC simulations, the values of diameter and dispersion obtained from the coalescence simulations were used. The initial size distribution closely resembles that of the as-prepared ZFC curve. Whereas the 3D coalescence simulated curve resembles more the annealed ZFC curve. Thus, in the as-prepared samples, if two nanoparticles are very close to one another in the same layer they will merge into one particle. Annealing, on the other hand, allows the coalescence to occur in between carbon layers. For all the simulated curves, the same values of magnetic anisotropy and saturation magnetization were fixed. The above simulations serve to further emphasize the effect of annealing on samples with high nanoparticle to matrix concentration.

4.1.2 1 % - Diluted clusters

As previously emphasized, in order to study the intrinsic magnetic properties of our nanoparticles, it is necessary to have nanoparticle samples that are sufficiently diluted in order to avoid dipolar magnetic interactions as well as possible coalescences in the samples due to annealing. As such, the previous multi-layered deposition technique is limited in terms of the carbon evaporator. At the time of the sample preparation, the available evaporator could only deposit 5 layers of carbon before needing to break the UHV and recharge it [207]. Thus, in order to have a sufficiently diluted sample it was decided to use the co-deposition layout

in which we use an electron gun to evaporate the carbon matrix and co-deposit both the matrix and the clusters at the same time. Two types of samples were prepared using the co-deposition configuration; pure (Fe or Co) cluster samples and bimetallic (FeCo) cluster samples. The obtained data are presented in the next two sections.

4.1.2.1 Pure clusters

Neutral Co clusters Pure cobalt nanoparticles were prepared using the classical LECBD cluster source (no size selection) and co-deposited with an amorphous carbon matrix evaporated using an electron gun. The rate of deposition of both clusters and matrix were controlled so as to have a cluster to matrix dilution of around 1%. Figures 4.6 and 4.7 show the complete magnetic characterization of the sample before and after annealing, respectively.

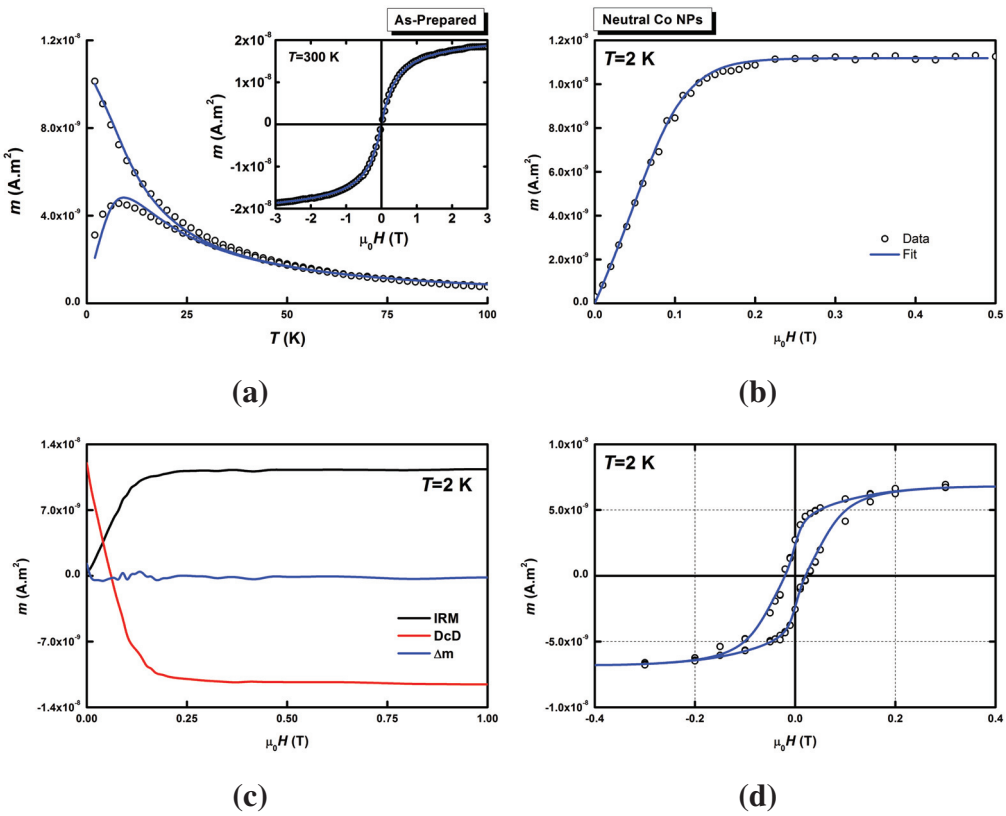

Fig. 4.6 (a) ZFC/FC and $m(H)$ experimental data for neutral as-prepared Co clusters along with their best fits; (b) IRM experimental data with the corresponding biaxial contribution simulation; (c) IRM/DcD curves with the Δm; (d) hysteresis loop at 2 K along with the corresponding simulation.

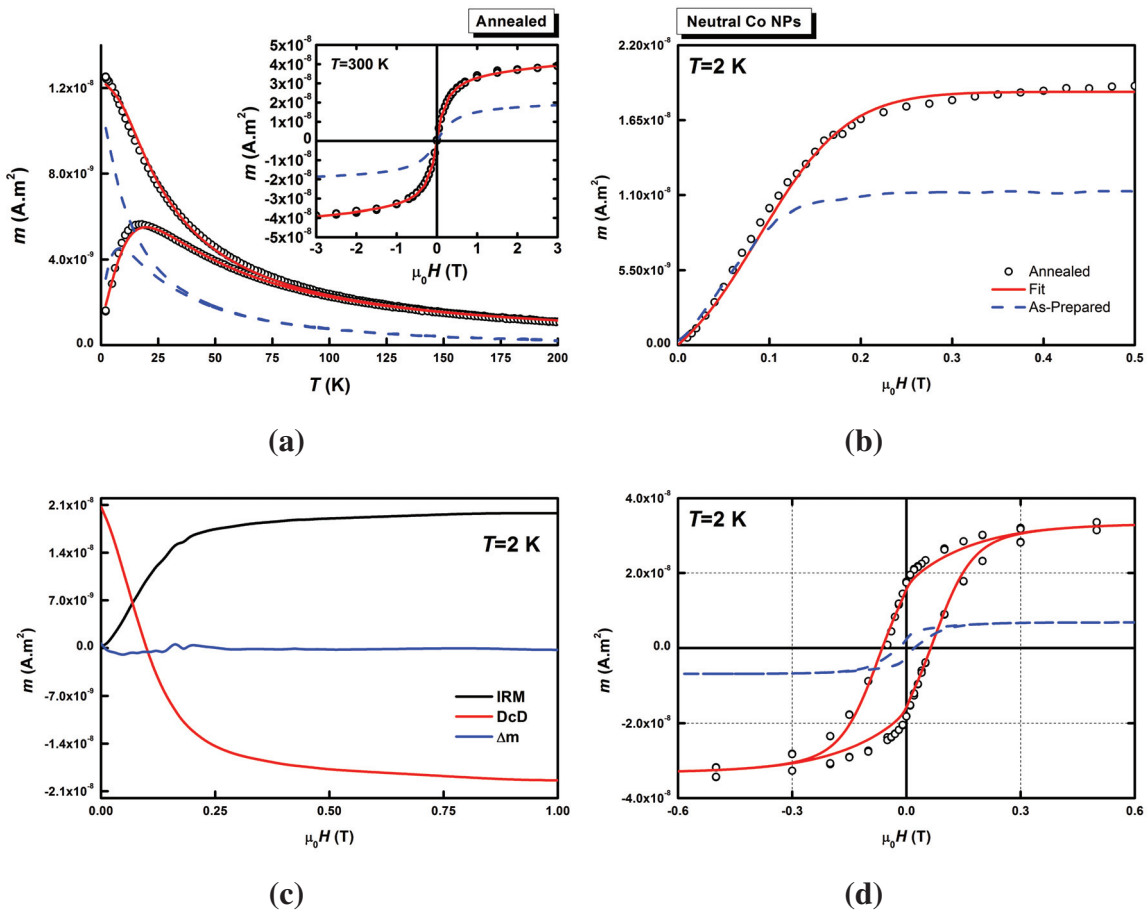

Fig. 4.7 (a) ZFC/FC and $m(H)$ experimental data for neutral annealed Co clusters along with their best fits; (b) IRM experimental data with the corresponding biaxial contribution simulation; (c) IRM/DcD curves with the Δm; (d) hysteresis loop at 2 K along with the corresponding simulation; the dashed line is the as-prepared experimental data.

The corresponding fitting parameters are presented in table 4.2 below.

	T_{max} (K)	$\mu_0 H_C$ (mT)	D_{mag} (nm)	ω_{mag}	K_1 (kJ.m^{-3})	ω_K	K_2/K_1	% SP
As-prepared	8	20	2.6 ± 0.2	0.26 ± 0.02	115 ± 10	0.30 ± 0.05	1.2 ± 0.4	35.9
Annealed	17.5	53	3.1 ± 0.2	0.41 ± 0.02	165 ± 10	0.41 ± 0.05	0.6 ± 0.4	4.6

Table 4.2 Maximums of the ZFC (T_{max}), coercive field ($\mu_0 H_C$) and the deduced parameters from the adjustment of the SQUID measurements for neutral Co nanoparticles embedded in C matrix as-prepared and after annealing as well as the percentage of superparamagnetic magnetic signal at saturation for the low temperature hysteresis loop fit.

The triple-fit for the as-prepared sample gives a slightly reduced size compared to the TEM size histogram. After annealing the expected size distribution is achieved with a demixing of carbon and cobalt atoms resulting in an even higher value of anisotropy (see figure 4.8). In addition and as previously explained, in order to simulate the hysteresis loops at low temperature (2 K) it is necessary to calculate the SP contribution for the particles that are not blocked at 2 K. The latter is also tabulated for the two cases, as-prepared and annealed samples.

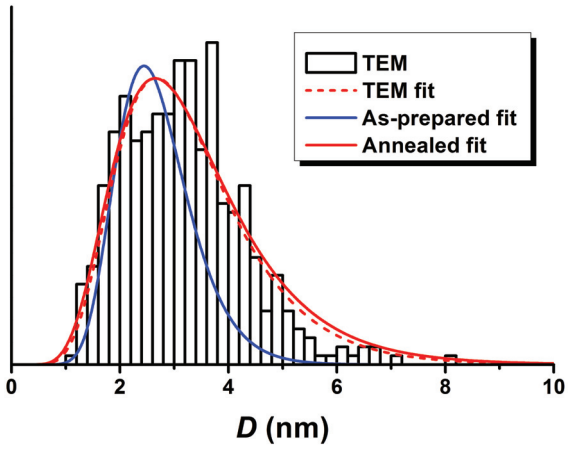

Fig. 4.8 Neutral Co nanoparticles size histogram obtained from TEM observations along with the corresponding fit, as well as the two size distributions obtained from the triple-fit of the as-prepared and annealed neutral Co samples.

To understand the origin of this biaxial contribution, the particle switching in the different measurements must be understood. In the case of the susceptibility curves (ZFC/FC), the particles switching has a thermal origin, the increase in temperature causes an increase in the probability to pass the energy barrier. Since the susceptibility measurements are performed using a weak external field (5 mT) the path chosen by the magnetization to switch can be considered as independent from the direction of the applied field. The magnetization passes the energy barrier where it is the smallest (*i.e.* $\Delta E = K_1 V$). For the IRM, the measurements are performed at a fixed temperature (2 K) and the magnetization switching is due to the applied field. The magnetization follows the path imposed by the external field and switches only if the applied field is larger than the switching field described by the astroid. This difference is particularly important since adding a biaxial contribution completely modifies the IRM curve (see chapter 2) while the effects are not detectable in the susceptibility curves.

In fact, the switching time $\tau = \tau_0 \exp(\Delta E/\mathrm{k_B}T)$ depends on the energy barrier $\Delta E = |K_1|V$ and does not depend on K_2. Even if τ_0 varies as a function of K_2, this dependence is masked by the exponential dependence of τ on K_1. Furthermore, μ-SQUID measurements

performed on Co nanoparticles showed that indeed they may possess a biaxial contribution [128]. Quantitatively, the maximum temperature in the ZFC curves and the coercive field increase significantly. Moreover, the IRM curve is slightly shifted to the right suggesting a larger anisotropy value and the curve saturates at a significantly higher value inferring an increase in the particles' magnetic volume. The same conclusion can be reached from the hysteresis loops at 300 K, which is directly sensitive to the size distribution. The simultaneous fitting of all the curves reveals that in reality, not only does the magnetic anisotropy increase significantly, but also the magnetic diameter of the particles. It should be noted that in both cases the triple-fit, as well as IRM and hysteresis loop simulations at 2 K were obtained with a saturation magnetization of $M_s = 1350$ kA.m^{-1} (the cobalt bulk value for saturation magnetization [98]).

Neutral Fe clusters In the same manner, pure iron nanoparticles were co-deposited along with an amorphous carbon matrix. The sample dilution was kept to around 1% to avoid particle interactions. In the case of the iron, the complete fit was possible using two models due to carbon mixing. In the first model, the saturation moment of the bulk was used ($M_s = 1730$ kA.m^{-1} [98]) and gave a reduced magnetic size. In this case, the nanoparticles can be imagined as a core-shell structure, with the shell being magnetically dead, and the core completely magnetic. For the second model, a reduced saturation magnetization was used ($M_s \simeq 1000$ kA.m^{-1}), calculated from [208, 209]. Here, the nanoparticle is considered to have a homogeneous make up throughout its volume. Figures 4.9 and 4.10 show the obtained experimental data along with the triple-fit adjustments for the as-prepared, as well as, the annealed neutral Fe clusters along with the IRM data and simulation using the two models (core-shell and homogeneous alloy).

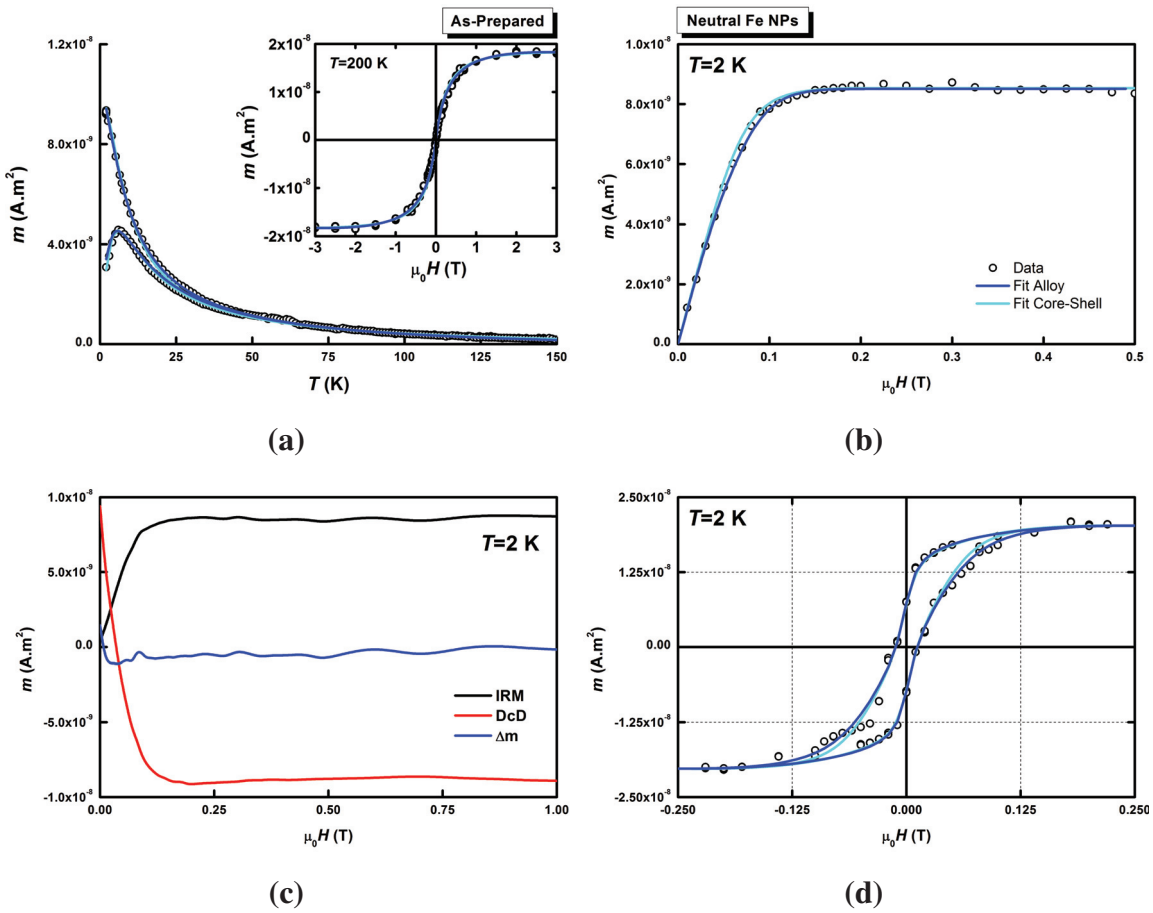

Fig. 4.9 (a) ZFC/FC and $m(H)$ experimental data for neutral as-prepared Fe clusters along with their best fits; (b) IRM experimental data with the corresponding biaxial contribution simulation; (c) IRM/DcD curves with the Δm; (d) hysteresis loop at 2 K along with the corresponding simulation.

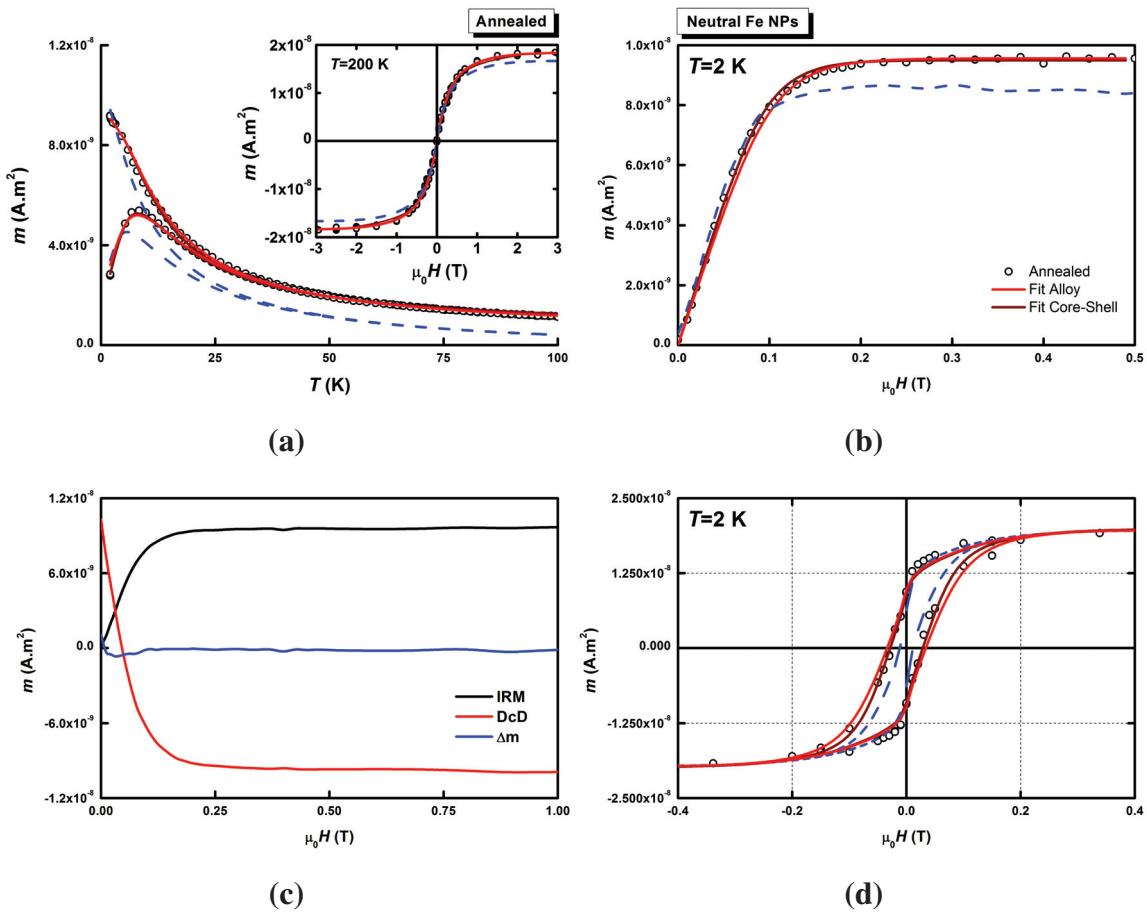

Fig. 4.10 (a) ZFC/FC and $m(H)$ experimental data for neutral annealed Fe clusters along with their best fits; (b) IRM experimental data with the corresponding biaxial contribution simulation; (c) IRM/DcD curves with the Δm; (d) hysteresis loop at 2 K along with the corresponding simulation; the dashed line is the as-prepared experimental data.

The corresponding fitting parameters are presented in table 4.3 below.

		T_{max} (K)	$\mu_0 H_C$ (mT)	D_{mag} (nm)	ω_{mag}	M_s (kA.m^{-1})	K_1 (kJ.m^{-3})	ω_K	K_2/K_1	% SP
Core-Shell	As-prepared	6.5	11	1.8 ± 0.2	0.34 ± 0.02	1730	130 ± 10	0.32 ± 0.05	1.2 ± 0.4	41.9
	Annealed	8.5	24	2.5 ± 0.2	0.25 ± 0.02	1730	120 ± 10	0.40 ± 0.05	1.4 ± 0.4	18.4
Homogeneous	As-prepared	6.5	11	2.7 ± 0.2	0.27 ± 0.02	950 ± 100	70 ± 5	0.42 ± 0.05	0 ± 0.4	34.7
	Annealed	8.5	24	3.0 ± 0.2	0.23 ± 0.02	1000 ± 100	74 ± 5	0.35 ± 0.05	1.2 ± 0.4	13.8

Table 4.3 Maximums of the ZFC (T_{max}), coercive field ($\mu_0 H_C$) and the deduced parameters from the adjustment of the SQUID measurements for neutral Fe nanoparticles embedded in C matrix as-prepared and after annealing in addition to the percentage of SP contribution for the 2 K hysteresis loop.

The complete fitting of all the experimental curves was possible using the two models. At first glance, a slight enhancement of the maximum temperature accompanied by the doubling of the coercive field can be observed after annealing. This increase, however, can be either due an increase of the magnetic diameter or of the particle's anisotropy. Comparing the hysteresis loops at high temperature ($T = 200$ K), a slight increase of the saturation is observed suggesting an increase in the magnetic size. In addition, the two IRM curves, before and after annealing, also show an enhancement that can be due to an increase in either the saturation magnetization M_s, or the magnetic diameter D_m. Moreover, from figures 4.9c and 4.10c, the measured IRM/DcD curves and the calculated Δm show small values for the Δm that are at the noise level. It should be noted that the value obtained from TEM for the mean diameter and dispersion is $D_m = 3.5 \pm 0.2$ nm and $\omega = 0.24 \pm 0.03$.

Core-shell model In the case of the core-shell model, the core is assumed to be completely magnetic with $M_s = 1730$ kA.m^{-1}, that is containing only Fe atoms, while the shell is made up of a magnetically dead iron-carbide with no magnetic contribution (see figure 4.11). The fit, in this case, gives a very small magnetic diameter with a large size dispersion ($D_{mag} = 1.8$ nm, $\omega_{mag} = 0.34$); after annealing the magnetic size increases while the size dispersion narrows ($D_{mag} = 2.5$ nm, $\omega_{mag} = 0.25$). This evolution can be explained by an increase of the core volume, *i.e.* a retraction of the carbide shell. The magnetic anisotropy value remains almost constant with a enlargement of the anisotropy dispersion. As for the ratio of the biaxial (K_2) to uniaxial anisotropy (K_1), it remains almost unchanged. Fitting the hysteresis loops required the addition of a SP contribution. This contribution is halved after annealing which is logical as the obtained diameter, since for small sizes, there are more particles in the SP regime than for larger sizes.

Homogeneous model On the other hand, in the case of a homogeneous alloy model (see figure 4.11), the particle is assumed to be magnetic with a reduced average magnetic moment per atom in the range of the values expected for the cementite [208, 209]. The fit gives a larger initial magnetic diameter ($D_{mag} = 2.7$ nm, $\omega_{mag} = 0.27$) compared to the core-shell fit. After annealing, the diameter slightly increases with a narrowing of the size dispersion ($D_{mag} = 3.0$ nm, $\omega_{mag} = 0.23$). The observed increase in the diameter is consistent with that of the hysteresis loop at high temperature ($T = 200$ K). An explanation is that after annealing, iron atoms expand into carbon-nanoparticle interface increasing the magnetic volume of the nanoparticle. Almost no noticeable evolution of the magnetic anisotropy is observed in this model too. However, the obtained value for the anisotropy is significantly smaller in this model compared to the core-shell one. As for the biaxial contribution, for the

as-prepared particles, the IRM fit is possible with no addition of biaxial component while for the annealed nanoparticles it was necessary. It should be noted that the error on the biaxial contribution is very high and is only used as an indication of whether or not there exits a biaxial contribution in the nanoparticles. Lastly, the SP contribution is also consistent in this model and shows values that are reasonable with the obtained diameter evolution.

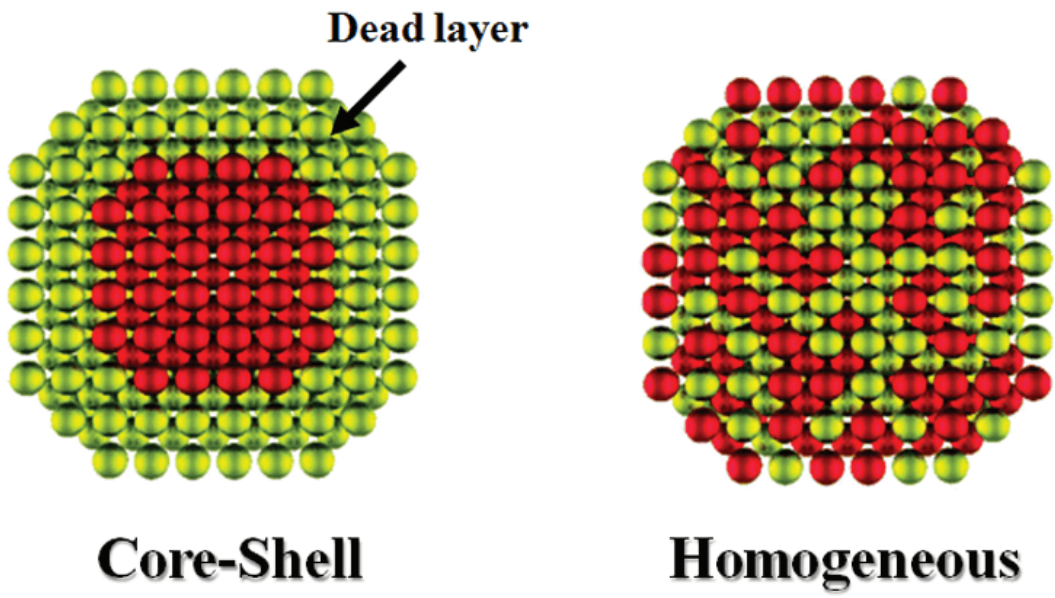

Fig. 4.11 (Left) Core-shell nanoparticle model; (Right) homogeneous nanoparticle model; from F. Calvo [210]

To sum up, if the value of the saturation magnetization M_s is unknown it is impossible to know precisely the intrinsic magnetic properties of the clusters. Moreover, another proposition is that there exists a mix of the two models with a carbon concentration gradient that decreases as we go deeper into the nanoparticle's core. In this case, the magnetization as a function of the diameter $\vec{M}(D)$ could be proportional to the carbon gradient $\vec{\nabla}[c]$. Further investigation of the validity of our two models is examined in the mass-selected nanoparticles section.

4.1.2.2 Bimetallic clusters

In addition to the pure clusters, bimetallic FeCo clusters were prepared from an equi-stoichiometric target source. The magnetic response of the clusters was investigated before and after annealing using the triple-fit technique [167]. In what follows, in addition to the triple-fit, the IRM and the hysteresis loop at 2 K were simulated before and after annealing. Figures 4.12 and 4.13 show the complete magnetic characterization of the sample before and after annealing, respectively. Similar to the pure iron nanoparticles, the iron-cobalt particles' curves were adjusted using the core-shell and the homogeneous alloy model.

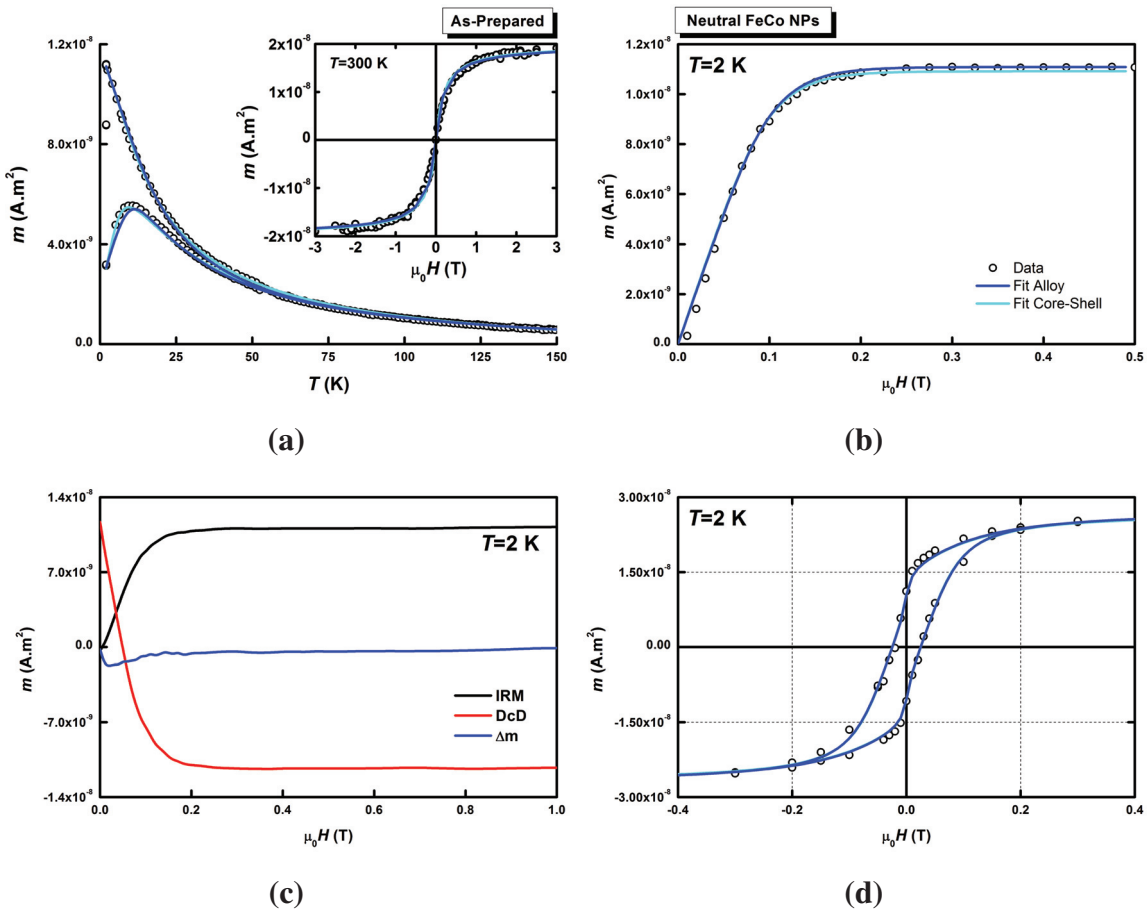

Fig. 4.12 (a) ZFC/FC and $m(H)$ experimental data for neutral as-prepared FeCo clusters along with their best fits; (b) IRM experimental data with the corresponding biaxial contribution simulation; (c) IRM/DcD curves with the Δm; (d) hysteresis loop at 2 K along with the corresponding simulation.

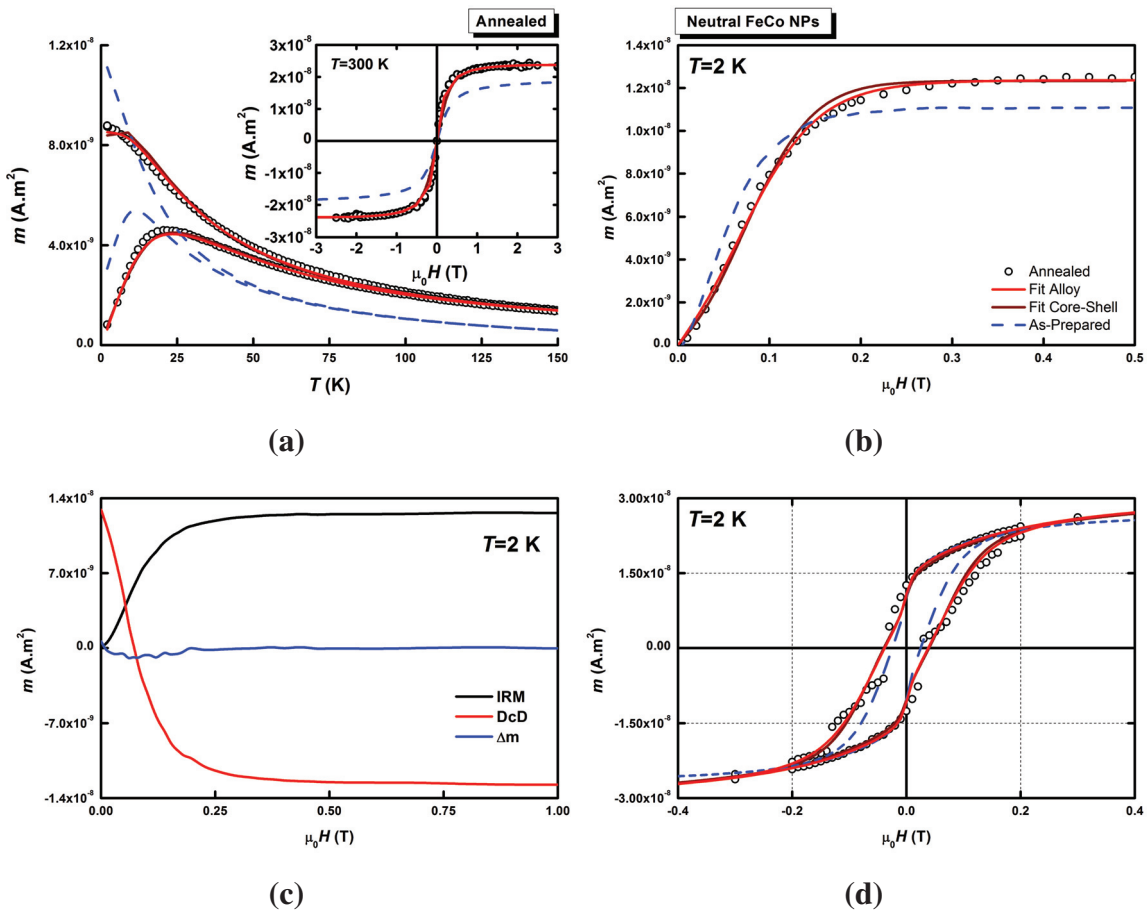

Fig. 4.13 (a) ZFC/FC and $m(H)$ experimental data for neutral annealed FeCo clusters along with their best fits; (b) IRM experimental data with the corresponding biaxial contribution simulation; (c) IRM/DcD curves with the Δm; (d) hysteresis loop at 2 K along with the corresponding simulation; the dashed line is the as-prepared experimental data.

The corresponding fitting parameters are presented in table 4.4 below.

		T_{max} (K)	$\mu_0 H_C$ (mT)	D_{mag} (nm)	ω_{mag}	M_s (kA.m^{-1})	K_1 (kJ.m^{-3})	ω_K	K_2/K_1	% SP
Core-Shell	As-prepared	10	20	2.6 ± 0.2	0.28 ± 0.02	1930	115 ± 10	0.43 ± 0.05	1.4 ± 0.4	17.7
	Annealed	23	34	3.1 ± 0.2	0.24 ± 0.02	1930	200 ± 10	0.3 ± 0.05	0.8 ± 0.4	16.0
Homogeneous	As-prepared	10	20	3.2 ± 0.2	0.32 ± 0.02	900 ± 100	44 ± 10	0.35 ± 0.05	1.2 ± 0.4	18.1
	Annealed	23	34	3.4 ± 0.2	0.27 ± 0.02	1220 ± 100	125 ± 10	0.25 ± 0.05	1.2 ± 0.4	17.6

Table 4.4 Maximums of the ZFC (T_{max}), coercive field ($\mu_0 H_C$) and the deduced parameters from the adjustment of the SQUID measurements for neutral FeCo nanoparticles embedded in C matrix as-prepared and after annealing in addition to the percentage of SP contribution for the 2 K hysteresis loop.

From a qualitative analysis, a clear increase of the maximum temperature as well as the coercive field can be noticed after annealing. The hysteresis loops at high temperature ($T = 300$ K) show a clear increase implying an increase in the magnetic moment. In addition, an evolution of the IRM curve before and after annealing is observed. A shift of the IRM to the right side indicating an increase in the switching field can be inferred. Moreover, figures 4.12c and 4.13c show the measured IRM/DcD curves and the calculated Δm. The Δm values are at the noise level. It should be noted that the value obtained from TEM for the mean diameter and dispersion is $D_m = 3.2 \pm 0.2$ nm and $\omega = 0.45 \pm 0.03$.

Core-shell model The core is assumed to be completely magnetic with $M_s = 1910$ kA.m^{-1} [25], *i.e.* it contains only Fe and Co atoms, while the shell is made up of a magnetically dead iron-cobalt-carbide with no magnetic contribution (see figure 4.11). The fit, in this case, gives a small mean magnetic diameter ($D_{mag} = 2.6$ nm, $\omega_{mag} = 0.28$ as-prepared); after annealing the mean magnetic size increases while the size dispersion narrows ($D_{mag} = 3.1$ nm, $\omega_{mag} = 0.24$). This evolution can be explained by a retraction of the non-magnetic carbide shell and an effective increase of the magnetic core volume. The magnetic anisotropy value almost doubles after annealing with a narrowing of the anisotropy dispersion. Nevertheless, the values obtained for the anisotropy after annealing suggest a better crystallization of the core atoms. As for the ratio of the biaxial (K_2) to uniaxial anisotropy (K_1), it is slightly decreased after annealing. The SP contribution used to fit the hysteresis loops at low temperature ($T = 2$ K) is slightly reduced after annealing in agreement with the evolution of the diameter distribution.

Homogeneous model As for the homogeneous model (used in the fit presented in the article [167]), the particle is assumed to be magnetic with a reduced magnetic moment per atom similar to the cementite values. Thus, the saturation magnetization was fitted and gave a value of $M_s = 900$ kA.m^{-1} for the as-prepared sample that increased to 1220 kA.m^{-1} after annealing. The fit gives a larger initial magnetic diameter and dispersion ($D_{mag} = 3.2$ nm, $\omega_{mag} = 0.32$) compared to the core-shell fit are in agreement with the TEM values. After annealing the diameter marginally increases with a narrowing of the size dispersion ($D_{mag} = 3.4$ nm, $\omega_{mag} = 0.27$). The observed increase in the diameter is consistent with that of the hysteresis loop at high temperature ($T = 300$ K). The magnetic anisotropy in this case almost triples in value after annealing indicating a better crystallization. However, the value is comparable with that of the anisotropy of neutral Co nanoparticles. As for the biaxial contribution, almost no change is observed after annealing. Finally, the SP contribution is

also consistent in the two models and shows values in agreement with the obtained diameter evolution.

To conclude, similar to the case of neutral Fe nanoparticle, for the FeCo nanoparticles it is also impossible to determine which model is the correct one. Thus, to go a step further, XMCD measurements were used to determine the average magnetic moment per atom at the Fe and Co edges presented in the section below, and consequently to extrapolate the saturation magnetization M_s.

4.2 Spin and orbital moments of size-selected clusters

The spin and orbital moments of all size-selected clusters were investigated using the XMCD technique. Measurements at the $L_{2,3}$ edges of both Fe and Co were done on our samples with the collaboration of P. Ohresser and F. Choueikani of the DEIMOS beamline at the SOLEIL synchrotron at Saclay, France. The general principle of the XMCD technique was detailed in chapter 2. In magnetic materials, there exists a difference between the population of spin *up* and spin *down* electrons at the Fermi level. The probability that the p electrons are absorbed in the d band depends on their spin, which gives rise to the dichroism. The difference between the left and right circularly polarized absorption spectra corresponds to the XMCD signal which is proportional to the magnetic moment of the probed atom. The proportionality between the XMCD signal and the magnetic moment is approximate. The error introduced when determining the magnetic moment by XMCD is approximatively 10-20% in the case of Fe and Co [211].

An XMCD signal can be obtained for a single polarization (left of right) by measuring the XAS signal under two opposite directions of the applied magnetic field. The used experimental sequence consists of measuring four spectra for both polarizations and both directions of applied magnetic field (which gives a total of 16 spectra). The measurements are done under UHV conditions (around 10^{-10} mbar), at 2 K with an applied field of $\pm$ 5 T. When applying the sum rules and calculating the magnetic moments, since the samples are made up of randomly oriented nanocrystals, the magnetic dipolar term, that reflects the asphericity of the distribution of spin moments around the absorbing atom, is neglected. The spin and orbital moments were obtained by using the theoretical number of holes (n_h) for FeCo for the d orbital: $n_h = 2.174$ for Co and $n_h = 3.261$ for Fe (calculated using the SIESTA code in collaboration with Aguilera-Granja *et al.*, private comm.) for both the as-prepared and annealed samples. For the pure clusters, the number of holes used is $n_h = 2.49$ for Co and $n_h = 3.39$ for Fe [88].

Two types of samples were prepared: pure clusters (Fe and Co) and bimetallic FeCo clusters. The table 4.5 contains a summary of all the measured samples. Since XMCD is a surface sensitive technique, a 2D sample configuration (see figure 2.4) was used. The samples consisted of 3-4 layers of clusters separated by an amorphous carbon matrix. The cluster layers were made up of around 2 Å of equivalent thickness of clusters leading to a concentration close to 10% volume. For each size, two samples were prepared, one was left as-prepared and the other annealed at 500°C for 2 hours.

Name	Deviation voltage	TEM diameter (nm)	ω
$FeCo_{3.7}$	150 V	3.7	0.13
$FeCo_{4.3}$	300 V	4.3	0.12
$FeCo_{5.8}$	450 V	5.8	0.10
$FeCo_{6.1}$	600 V	6.1	0.07
$Co_{2.9}$	150 V	2.9	0.16
$Co_{3.4}$	300 V	3.4	0.13
$Fe_{3.3}$	150 V	3.3	0.18
$Fe_{4.4}$	300 V	4.4	0.16

Table 4.5 List of mass-selected FeCo, Co and Fe samples.

4.2.1 Pure clusters

For the pure clusters, two voltage deviations were used (see table 4.5). The polarized XAS signals were measured for the cobalt $L_{2,3}$ edge, on $E = 760$ - 860 eV, and for the iron edge $L_{2,3}$ on $E = 690$ - 780 eV.

4.2.1.1 Co clusters

Figures 4.14 and 4.15 show the XMCD signal in as-prepared samples and after annealing for the two sizes, $Co_{2.9}$ and $Co_{3.4}$, respectively.

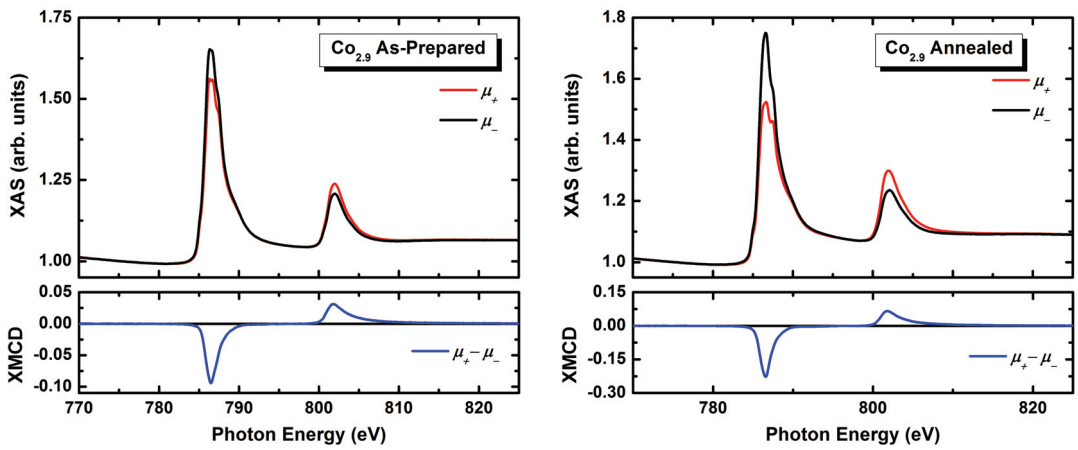

Fig. 4.14 XMCD signal at 2 K at the $L_{2,3}$ Co edge for the as-prepared (left) and annealed (right) mass-selected $Co_{2.9}$ nanoparticles.

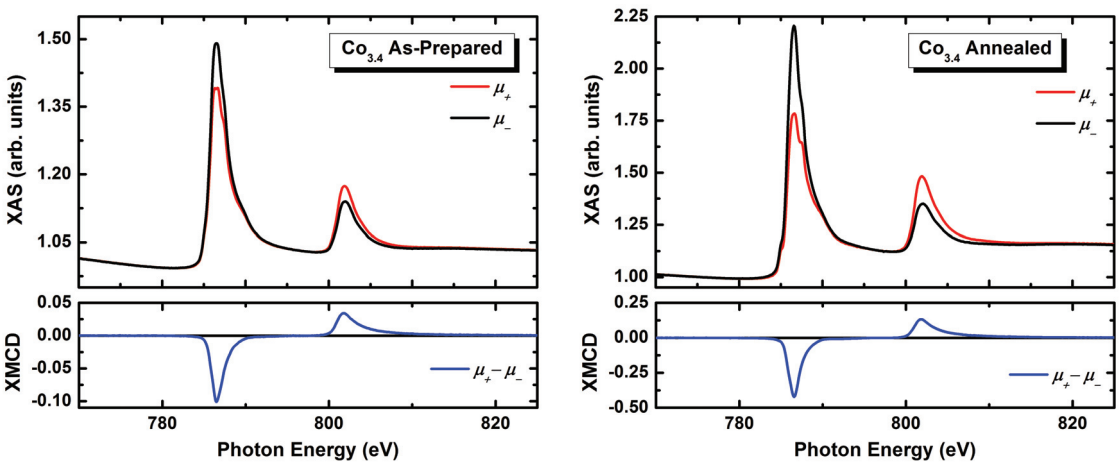

Fig. 4.15 XMCD signal at 2 K at the $L_{2,3}$ Co edge for the as-prepared (left) and annealed (right) mass-selected $Co_{3.4}$ nanoparticles.

The spin and orbital moments deduced from the absorption spectra are presented in table 4.6. After annealing, an increase in the spin and orbital magnetic moments is observed. The values are almost doubled after annealing. For both sizes, the value of the magnetic moments as-prepared is very small and can be considered to be the same due to the uncertainty of the XMCD technique. After annealing the values significantly increase but remain smaller than the expected values for the bulk Co ($\mu_S = 1.62$ μ_B/at. and $\mu_L = 0.154$ μ_B/at. [88]). This goes in favour of a demixing of the cobalt and carbon atoms in full agreement with EXAFS measurements. However, since the bulk moment was not achieved, it is safe to assume that some cobalt and carbon atoms are bonding, causing a small magnetically inactive layer, at the interface for example (smaller after annealing than before).

		μ_L (μ_B/at.)	μ_S (μ_B/at.)	$\mu_L + \mu_S$ (μ_B/at.)	μ_L/μ_S
$Co_{2.9}$	As-prepared	0.04±0.01	0.50±0.10	**0.54±0.11**	0.09±0.02
	Annealed	0.10±0.02	0.92 ±0.28	**1.12±0.30**	0.11±0.02
$Co_{3.4}$	As-prepared	0.06 ±0.01	0.69 ±0.14	**0.75±0.15**	0.08±0.02
	Annealed	0.12 ±0.02	1.19 ±0.24	**1.31±0.26**	0.10±0.02

Table 4.6 Orbital and spin moments of the Co atoms before and after annealing for two nanoparticle sizes, $Co_{2.9}$ and $Co_{3.4}$.

In addition to the XMCD spectra, hysteresis loops were also recorded at the DEIMOS beamline for the samples at low temperature ($T = 2$ K) as well as at high temperature ($T = 300$ K). The spectra were recorded at the L_3 edge for the cobalt atoms by varying the magnetic field. The resulting hysteresis loops at 2 K and 300 K are presented in figures 4.16 and 4.17 respectively.

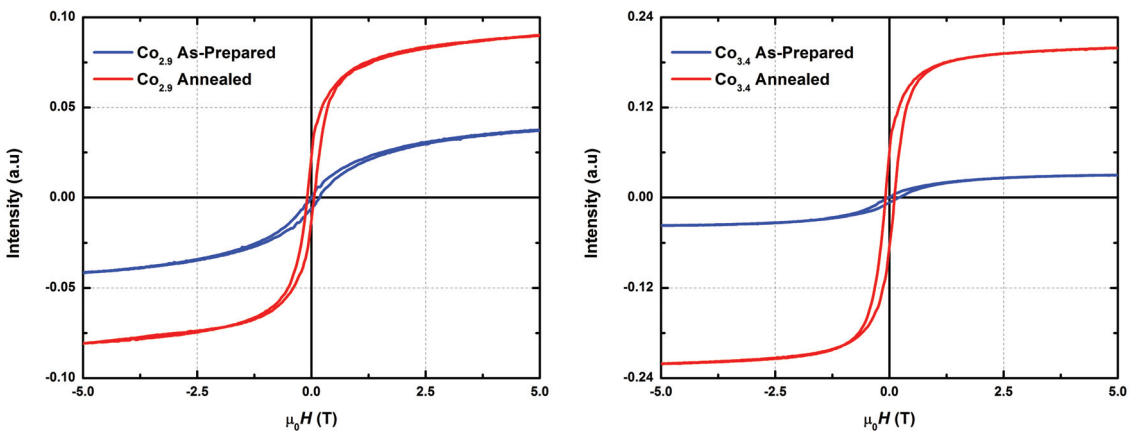

Fig. 4.16 Hysteresis loops of $Co_{2.9}$ (left) and $Co_{3.4}$ (right) nanoparticles measured by XMCD at the Co:L_3-edge at 2 K.

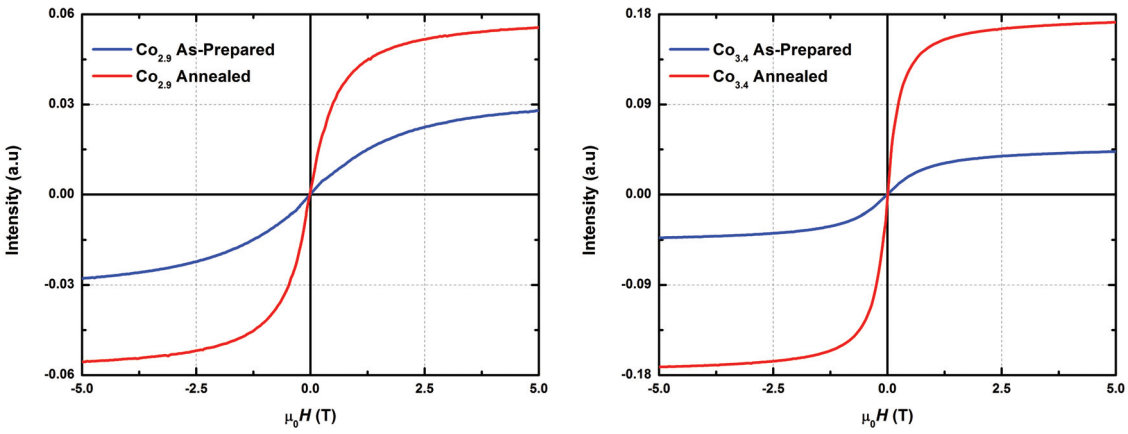

Fig. 4.17 Magnetization curves of $Co_{2.9}$ (left) and $Co_{3.4}$ (right) nanoparticles measured by XMCD at the Co:L_3-edge at 300 K.

For both sizes, annealing induces an enhancement of the magnetization evidenced by the increase of the saturation magnetization at high temperature (300 K) and at low temperatures (2 K). In addition, after annealing the largest particles, the curve has a more squared shape compared to the as-prepared case meaning an increase of the magnetic moment. On the other hand, it seems that the samples are not completely saturated even though the applied field reaches $\pm$ 5 T.

As an example, at saturation, the magnetic moment increases by a factor of 5, for the $Co_{3.4}$ nanoparticles (see figure 4.16 (right)), whereas the magnetization increases by a factor of 2 (see tables 4.6 and 4.10). If we consider that the number of clusters is the same at saturation, we can write:

$$
\begin{aligned}
m_{annealed} &= M_{s_{annealed}} \times V_{annealed} \\
m_{as-prepared} &= M_{s_{as-prepared}} \times V_{as-prepared} \quad \text{with} \quad M_{s_{annealed}} = 2 \times M_{s_{as-prepared}} \\
\frac{m_{annealed}}{m_{as-prepared}} &= \frac{2 \times M_{s_{as-prepared}} \times V_{annealed}}{M_{s_{as-prepared}} \times V_{as-prepared}} = \frac{2V_{annealed}}{V_{as-prepared}} = 5 \\
V_{annealed} &= \frac{5}{2} \times V_{as-prepared} \\
D_{m_{annealed}} &= \sqrt{\frac{5}{2}}^{3} \times D_{m_{as-prepared}} \\
D_{m_{annealed}} &= 1.35 \times D_{m_{as-prepared}}
\end{aligned}
$$

where m is the magnetic moment, M_s is the saturation magnetization, V is the magnetic volume and D_m is the magnetic diameter. In agreement with the increase of the mean magnetic diameter after annealing in the neutral Co clusters (see table 4.2).

It should be noted that, using XMCD to measure the magnetization curves has some limits as in the absence of applied field ($\mu_0 H = 0$ T) it is impossible to measure a magnetic signal, thus the curves above are extrapolated at 0 T. From the hysteresis loops at 2 K it can be noted that the obtained value for the coercive field of size-selected samples is much smaller than the case of neutral cobalt nanoparticles; with a value of around 100 mT in all the samples (the uncertainty on the experimental values was too high for accurate quantification).

In agreement with the structural results, in the case of the cobalt nanoparticles, annealing promotes an increase in the magnetic moment per atom which from the point of view of EXAFS translates to a demixing of carbon and cobalt atoms.

4.2.1.2 Fe clusters

For the iron nanoparticles, two sizes were studied, $Fe_{3.3}$ and $Fe_{4.4}$. Figures 4.18 and 4.19 show the XMCD signal as-prepared and after annealing for the two sizes, $Fe_{3.3}$ and $Fe_{4.4}$ respectively.

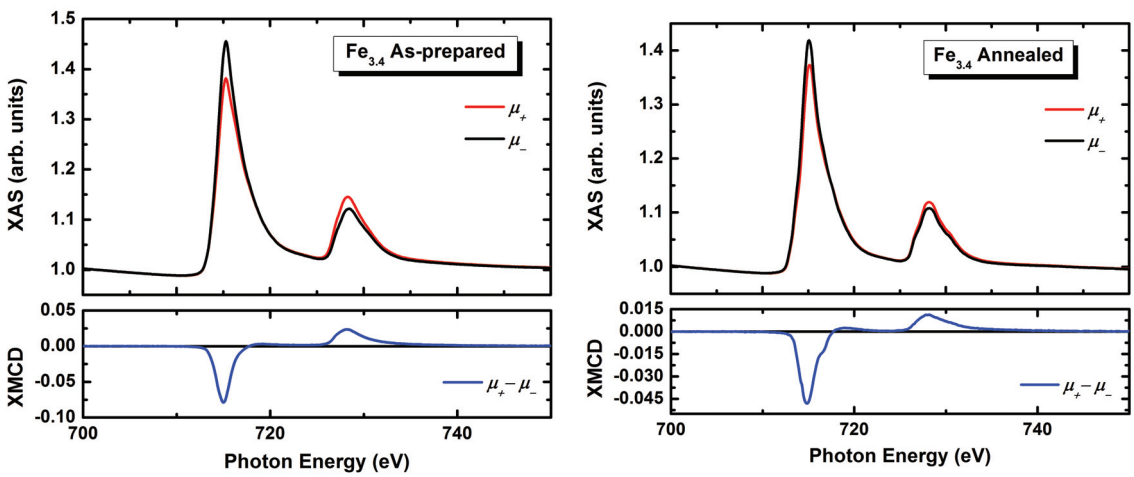

Fig. 4.18 XMCD signal at 2 K at the $L_{2,3}$ Fe edge for the as-prepared (left) and annealed (right) mass-selected $Fe_{3.3}$ nanoparticles.

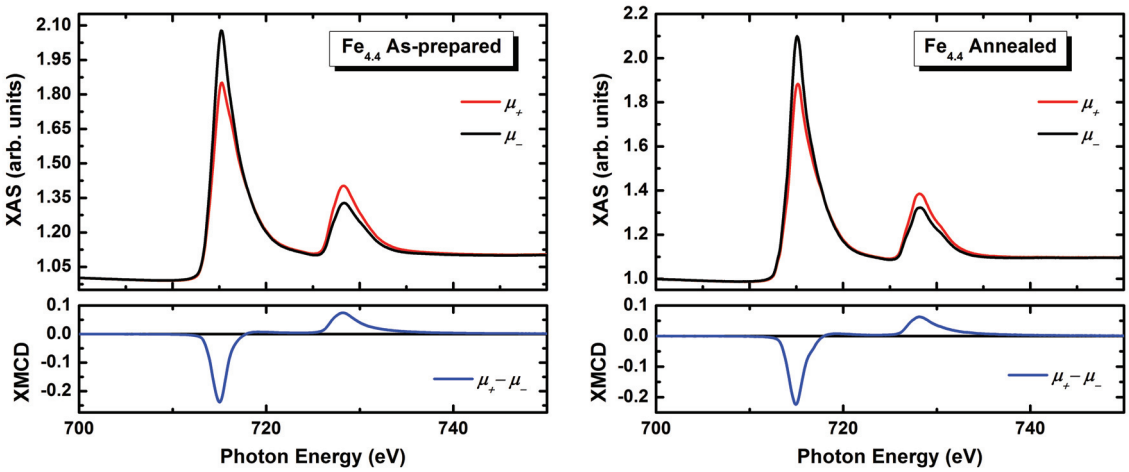

Fig. 4.19 XMCD signal at 2 K at the $L_{2,3}$ Fe edge for the as-prepared (left) and annealed (right) mass-selected $Fe_{4.4}$ nanoparticles.

The spin and orbital moments deduced from the absorption spectra are presented in table 4.7. After annealing, a decrease in the spin magnetic moments is observed while the orbital magnetic moment doubles. In both cases, annealing promotes a decrease of the overall magnetic moment per atom. For the larger size ($Fe_{4.4}$), the average magnetic moment per atom slightly decreases but remains in an uncertainty range. The obtained moments are extremely small compared to the bulk values expected for Fe atoms ($\mu_S = 1.98$ μ_B/at. and $\mu_L = 0.085$ μ_B/at. [88]). This tendency suggests a mixing of the iron and carbon atoms in the samples that is further favoured by the annealing process.

		μ_L (μ_B/at.)	μ_S (μ_B/at.)	$\mu_L+\mu_S$ (μ_B/at.)	μ_L/μ_S
$Fe_{3.3}$	As-prepared	0.02± 0.01	0.60 ± 0.12	**0.62±0.13**	0.03±0.01
	Annealed	0.04± 0.01	0.40 ± 0.08	**0.44±0.09**	0.10±0.02
$Fe_{4.4}$	As-prepared	0.03± 0.01	0.83 ± 0.16	**0.86±0.17**	0.03±0.01
	Annealed	0.05± 0.01	0.79± 0.17	**0.84±0.18**	0.06±0.01

Table 4.7 Orbital and spin moments of the Fe atoms before and after annealing for two nanoparticle sizes, $Fe_{3.3}$ and $Fe_{4.4}$.

Similar to the cobalt, magnetization curves at high temperature ($T = 300$ K) and hysteresis loops at low temperature ($T = 2$ K) were also measured. The spectra were recorded at the L_3 edge for the iron atoms by varying the magnetic field. The resulting hysteresis loops at 2 K and 300 K are presented in figures 4.20 and 4.21 respectively.

For both sizes, annealing shows a reduction of the magnetic moment evidenced by the decrease in saturation of the magnetization curves at high temperature (300 K) and the hysteresis loops at low temperatures (2 K). Nevertheless, after annealing the magnetization does not appear to be saturated at the maximum applied field of 5 T. From the hysteresis loops at 2 K it can be noted that the curves show a very small opening and the experimental error is too high, thus a clear quantification is not possible.

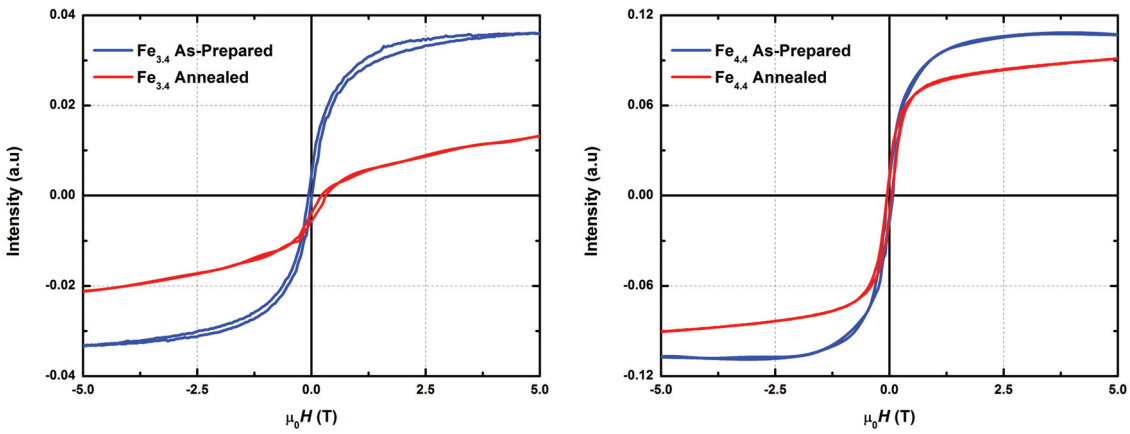

Fig. 4.20 Hysteresis loops of $Fe_{3.3}$ (left) and $Fe_{4.4}$ (right) nanoparticles measured by XMCD at the Fe:L_3-edge at 2 K.

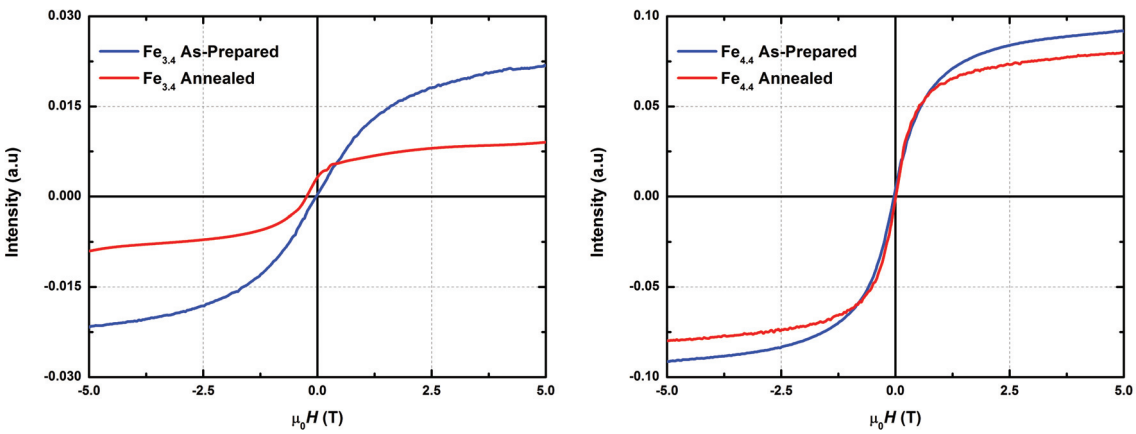

Fig. 4.21 Magnetization curves of $Fe_{3.3}$ (left) and $Fe_{4.4}$ (right) nanoparticles measured by XMCD at the Fe:L_3-edge at 300 K.

In the case of the iron nanoparticles, annealing promotes a decrease in the magnetic moments per atom which from the point of view of EXAFS translates in a bonding of carbon and iron atoms after annealing.

It should be noted that for all the samples prepared for XMCD, the particle density per layer is somewhat high. An equivalent thickness of 2 Å of nanoparticles was deposited per layer which is what we also used for the concentrated samples presented at the beginning of the chapter. Since the XMCD is a surface technique, the chosen particle density was such as to be able to extract a XMCD magnetic signal from the clusters located at the surface of our samples. Depositing a fraction of the actual quantity would mean having a fraction of the signal which would go against a quantitative analysis of the data.

4.2.2 Bimetallic clusters

For the bimetallic FeCo clusters, four voltage deviations were used for each size (see table 4.5). For the cobalt $L_{2,3}$ edge, the polarized XAS signals were measured between $E = 760$ - 860 eV; and for the iron edge $L_{2,3}$ between $E = 690$ - 780 eV.

4.2.2.1 $FeCo_{3.7}$

Figure 4.22 shows the XMCD signals for the $FeCo_{3.7}$ as-prepared and after annealing at both Fe and Co $L_{2,3}$ edges.

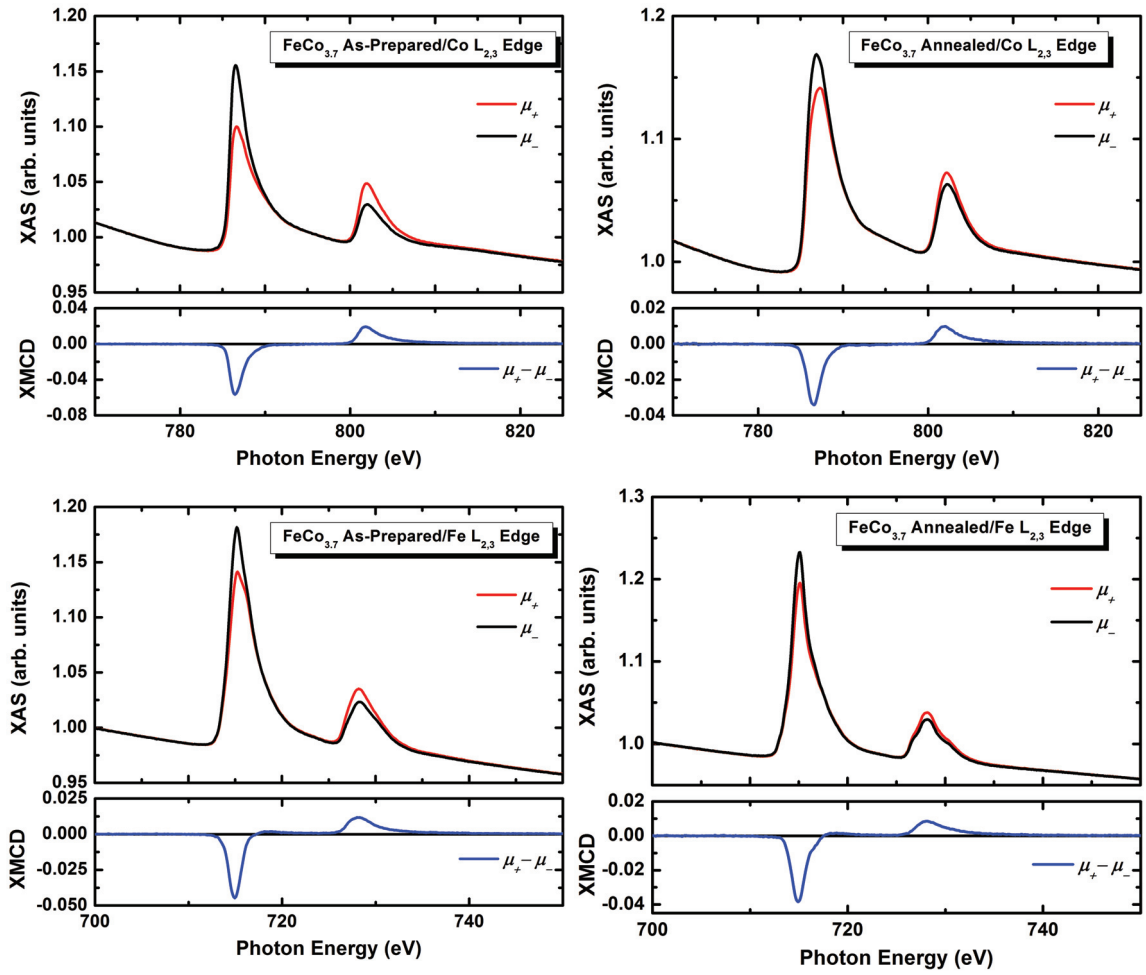

Fig. 4.22 XMCD signal at 2 K at the Co (top) and Fe (bottom) $L_{2,3}$ edges for the as-prepared (left) and annealed (right) mass-selected $FeCo_{3.7}$ nanoparticles.

From the XMCD spectra, it is clear that after annealing the two peaks (L_2 and L_3) decrease in magnitude. Moreover, the shape of the XAS L_3 peak at the Fe edge before

annealing shows a post-edge peak for the μ_+ polarization; after annealing the apparition of both a pre- and post-peak shoulders is more prominent at the L_2 edge, even the L_3 edge shows an evolution of the post edge shoulder probably due to a carbide formation. The same features were observed in pure Fe clusters (see figures 4.18 and 4.19).

4.2.2.2 $FeCo_{4.3}$

Figure 4.23 shows the XMCD signals for the $FeCo_{4.3}$ as-prepared and after annealing at both Fe and Co $L_{2,3}$ edges.

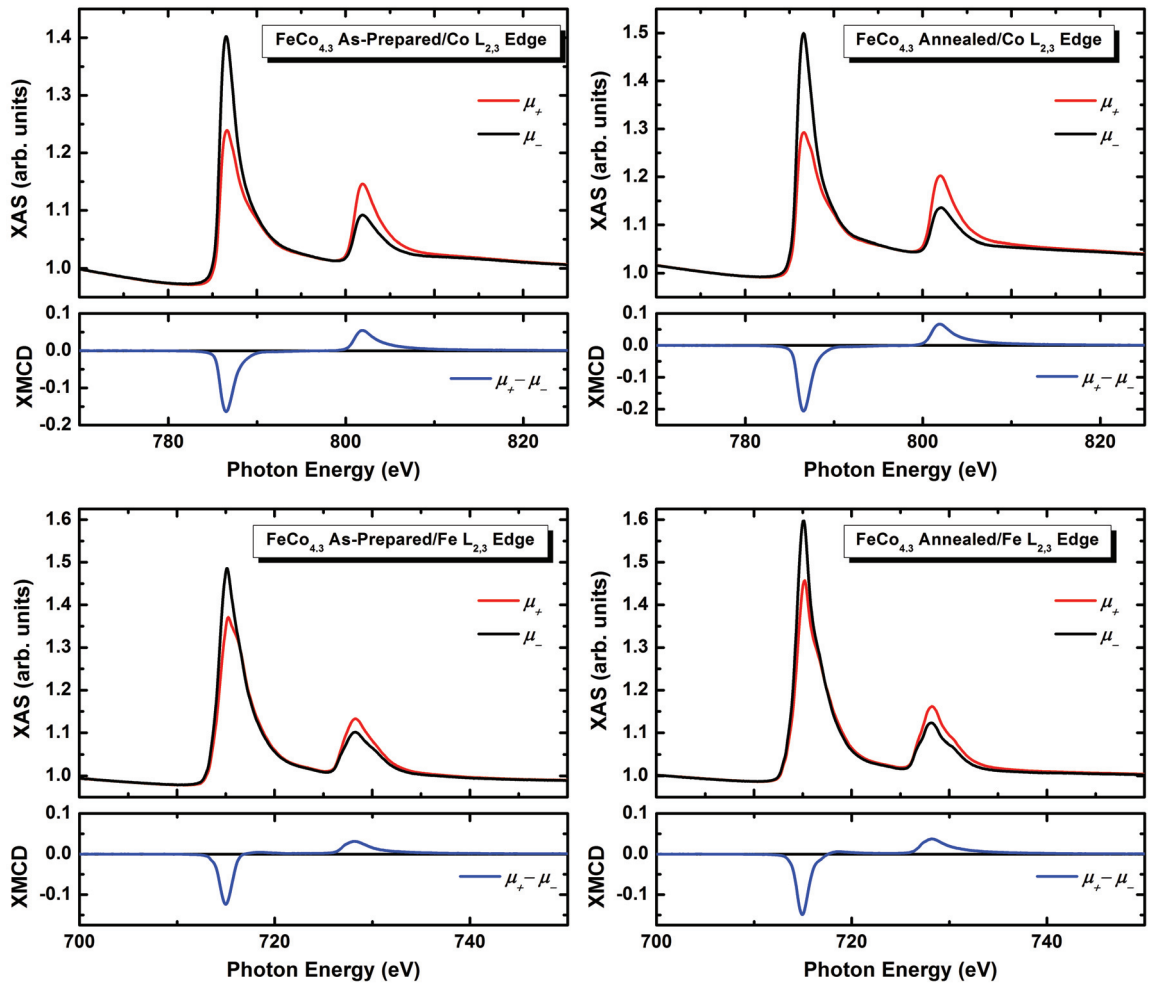

Fig. 4.23 XMCD signal at 2 K at the Co (top) and Fe (bottom) $L_{2,3}$ edges for the as-prepared (left) and annealed (right) mass-selected $FeCo_{4.3}$ nanoparticles.

The XMCD signal shows an enhancement after annealing at the Co edge, while the Fe edge remains almost unchanged. The shape of the XAS signals shows similar features at the Fe edge as for the $FeCo_{3.7}$ nanoparticles.

4.2.2.3 $FeCo_{5.8}$

Figure 4.24 shows the XMCD signals for the $FeCo_{5.8}$ as-prepared and after annealing at both Fe and Co $L_{2,3}$ edges.

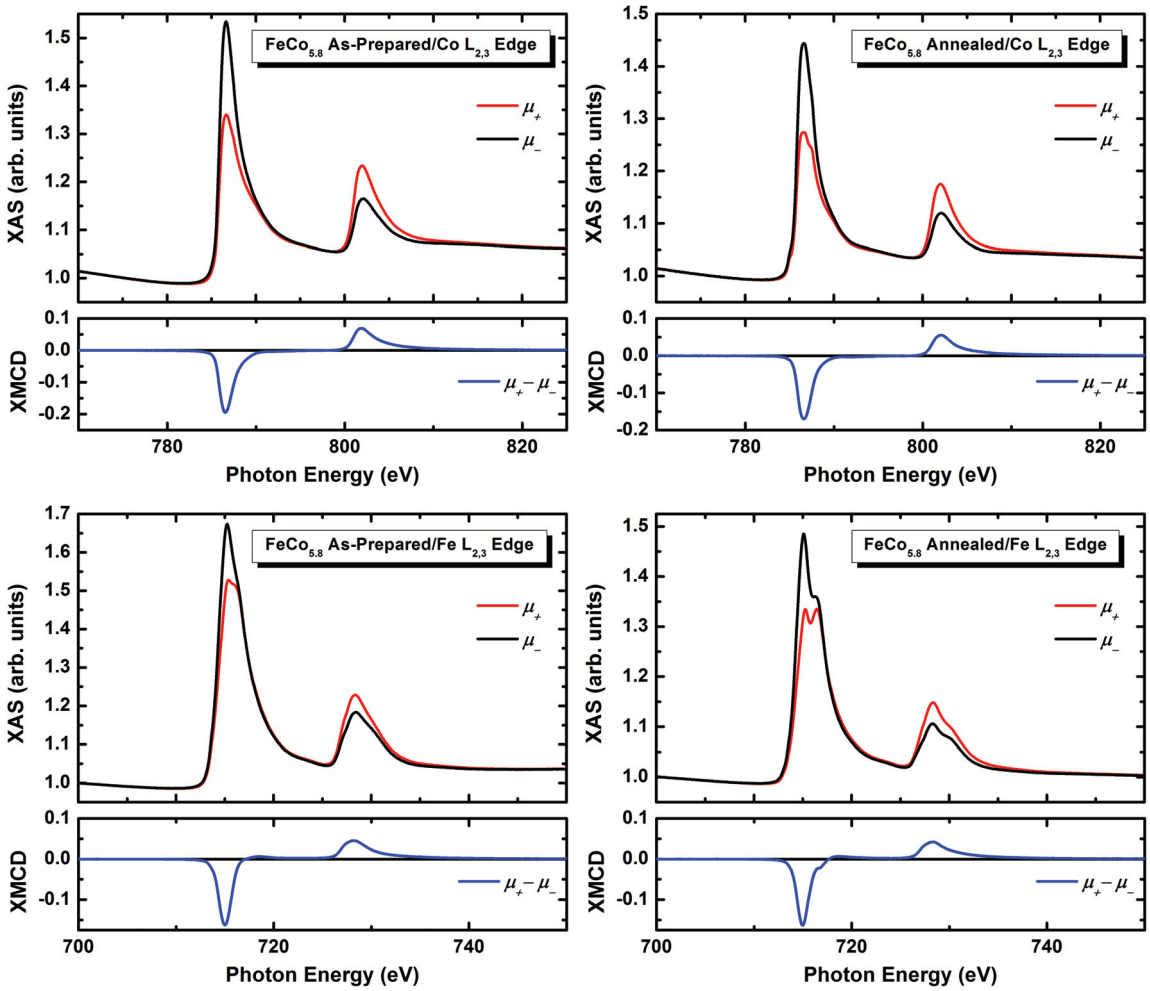

Fig. 4.24 XMCD signal at 2 K at the Co (top) and Fe (bottom) $L_{2,3}$edges for the as-prepared (left) and annealed (right) mass-selected $FeCo_{5.8}$ nanoparticles.

In the case of the larger $FeCo_{5.8}$ nanoparticles, an enhancement of the XMCD signal is observed at the Co edge after annealing, while no significant change is observed at the Fe edge. After annealing the XAS signal at both edges shows some prominent features, double peaks at the Fe:L_3 edge and a post-peak shoulder at the Co:L_3 edge; the Fe:L_2 edge shows the same signature as the previous two sizes ($FeCo_{3.7}$ and $FeCo_{4.3}$). During the beamtime, the annealed sample was broken during the mounting process and a silver paste was used to hold the sample in place for the measurements. The distorted signals measured on this sample maybe caused by the contamination of the sample by the used silver paste.

4.2.2.4 $FeCo_{6.1}$

Figure 4.25 shows the XMCD signals for the $FeCo_{6.1}$ as-prepared and after annealing at both Fe and Co $L_{2,3}$ edges.

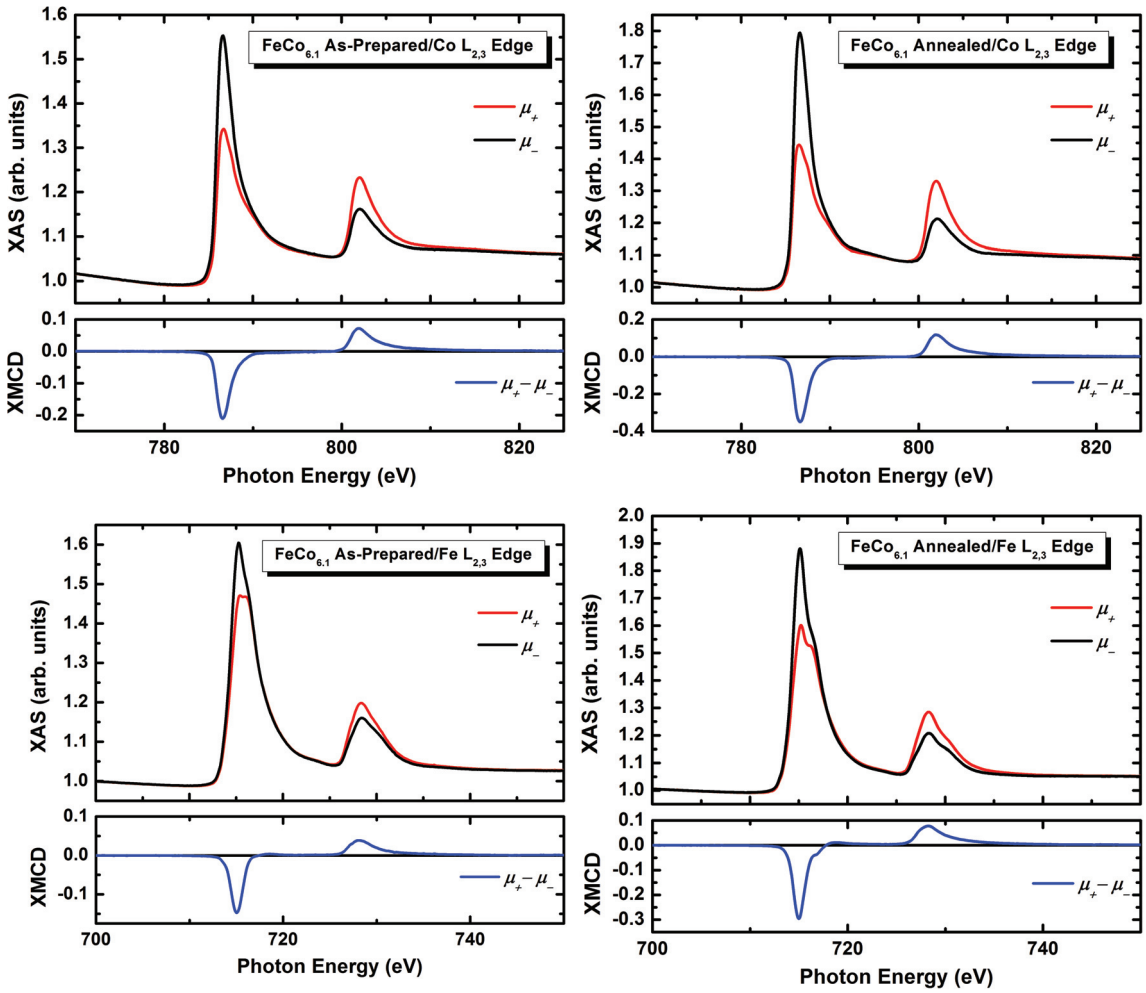

Fig. 4.25 XMCD signal at 2 K at the Co (top) and Fe (bottom) $L_{2,3}$edges for the as-prepared (left) and annealed (right) mass-selected $FeCo_{6.1}$ nanoparticles.

For the $FeCo_{6.1}$ nanoparticles, a prominent enhancement of the XMCD signal is observed at both edges after annealing. The shape of the XAS signals has almost the same features as in smaller samples ($FeCo_{3.7}$ and $FeCo_{4.3}$) but with a stronger post-peak shoulder at the annealed Fe:L_3 edge. It should be noted that the XMCD signal for the as-prepared nanoparticles shows almost the same magnitude for all the samples. Table 4.8 has the quantified values for the spin and angular magnetic moments as well as the average magnetic moment and the μ_L/μ_S ratio for all the samples.

		Fe edge (μ_B/at.)				Co edge (μ_B/at.)				μ_{av} (μ_B/at.)
		μ_L	μ_S	$\mu_L+\mu_S$	μ_L/μ_S	μ_L	μ_S	$\mu_L+\mu_S$	μ_L/μ_S	
$FeCo_{3.7}$	As-prepared	0.01±0.01	0.68±0.14	**0.69±0.15**	0.02±0.01	0.06±0.01	0.75±0.15	**0.81±0.16**	0.08±0.02	**0.75±0.15**
	Annealed	0.04±0.01	0.52±0.10	**0.56±0.11**	0.08±0.02	0.04±0.01	0.33±0.07	**0.37±0.08**	0.13±0.03	**0.46±0.09**
$FeCo_{4.3}$	As-prepared	0.02±0.01	0.71±0.14	**0.73±0.15**	0.03±0.01	0.10±0.02	1.07±0.21	**1.17±0.23**	0.09±0.02	**0.94±0.19**
	Annealed	0.04±0.01	0.81±0.16	**0.85±0.17**	0.05±0.01	0.11±0.02	1.12±0.22	**1.23±0.24**	0.10±0.02	**1.04±0.21**
$FeCo_{5.8}$	As-prepared	0.02±0.01	0.67±0.13	**0.69±0.14**	0.02±0.01	0.07±0.02	1.03±0.21	**1.10±0.23**	0.07±0.02	**0.89±0.18**
	Annealed	0.03±0.01	0.99±0.20	**1.02±0.21**	0.03±0.01	0.10±0.02	1.06±0.21	**1.16±0.23**	0.10±0.02	**1.09±0.22**
$FeCo_{6.1}$	As-prepared	0.04±0.01	0.67±0.13	**0.71±0.14**	0.06±0.01	0.08±0.02	1.12±0.22	**1.20±0.24**	0.07±0.02	**0.95±0.19**
	Annealed	0.02±0.01	1.13±0.23	**1.15±0.23**	0.02±0.01	0.11±0.02	1.33±0.27	**1.44±0.29**	0.08±0.02	**1.29±0.26**

Table 4.8 Orbital and spin moments of the FeCo samples before and after annealing for the four nanoparticle sizes, $FeCo_{3.7}$, $FeCo_{4.3}$, $FeCo_{5.8}$ and $FeCo_{6.1}$.

To better interpret the above data, a plot at each site (Fe and Co) is presented below for the spin and angular moments in figures 4.26 and 4.27 respectively.

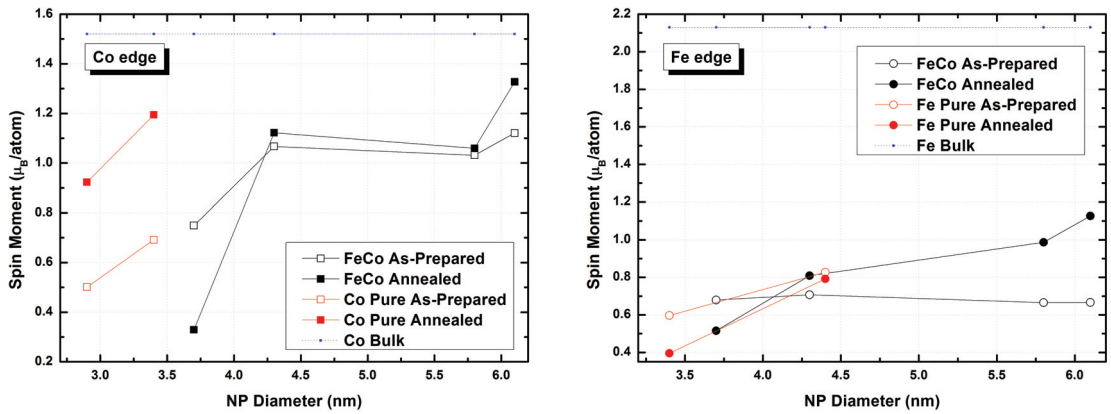

Fig. 4.26 Plot for the evolution of the spin magnetic moment at the Co (left) and Fe (right) edges for the FeCo samples before and after annealing along with the results for the pure samples and the bulk values.

For the small sized $FeCo_{3.7}$ nanoparticles annealing reduced the spin magnetic moment at both the Fe and Co edges. For the other sizes, annealing slightly increased the spin moment at the Co edge. In particular, for the $FeCo_{6.1}$, the annealed spin moment reaches 1.4 μ_B/atom very close to the pure Co clusters. On the other hand, at the Fe edge, for the larger sizes annealing gradually increased the average spin moment per atom to a maximum of around 1.2 μ_B/atom. The as-prepared moments for all sizes at the Fe edge have the same value. The same can be said about the Co edge within the uncertainty, except for the small sized $FeCo_{3.7}$ nanoparticles.

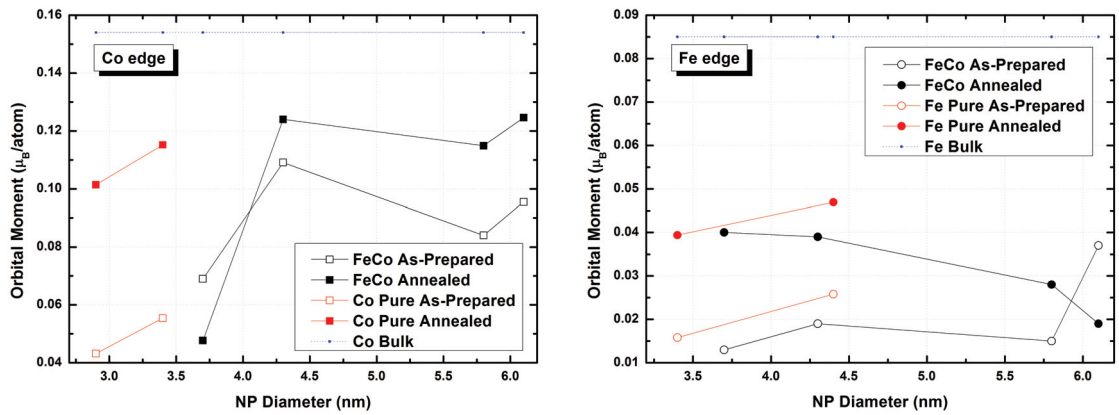

Fig. 4.27 Plot for the evolution of the orbital magnetic moment at the Co (left) and Fe (right) edges for the FeCo samples before and after annealing along with the results for the pure samples and the bulk values.

The average angular moment per atom shows a reduction after annealing for the small sized $FeCo_{3.7}$ nanoparticles at the Co edge followed by an enhancement for the larger nanoparticles; at the Fe edge an enhancement is also observed even for the small $FeCo_{3.7}$ nanoparticles while the largest $FeCo_{6.1}$ showed a reduction after annealing. The average orbital moment at the Co edge reaches values comparable to the bulk values while the values achieved at the Fe edge are quite small relative to the corresponding bulk values.

Analyzing the overall evolution of the average magnetic moments after annealing, two regimes can be identified. For the small sized $FeCo_{3.7}$ nanoparticles, annealing mostly reduced the average moment following the regime for the pure Fe nanoparticles. While for the larger nanoparticles, annealing enhanced the average moment in a manner quite similar to the pure Co nanoparticles. Comparing these findings to the EXAFS results, we can establish two regimes: for the smallest FeCo and the pure Fe nanoparticles, annealing increases carbon diffusion into the nanoparticles thus causing a reduction of the average magnetic moment per atom. While for the larger FeCo and pure Co nanoparticles, annealing helps demix the carbon atoms from the particles thus leading to an increased average magnetic moment per atom. The latter is much more evident as the particle's size increases as seen from both EXAFS and XMCD.

A number of different studies report a reduced magnetic moment due to the presence of carbon impurities in nanoparticles [181, 209, 212]. Sajitha *et al*. reports that iron nanoparticles embedded in a carbon matrix gave values for saturation magnetization equal to the bulk iron carbide values. Briones-Leon *et al*. found an average spin moment of 1.17 μ_B/atom for Fe nanoparticles encapsulated in MWCNT.

In addition to these finding, Aguilera-Granja *et al*. (private comm.) calculated the impact of adding carbon (or oxygen) atoms into FeCo nanoparticles. They found that either adding or substituting impurities into FeCo nanoparticles has a huge impact on the average magnetic moment of both Fe and Co atoms. Fe and Co atoms that are in the vicinity of a carbon atoms showed reduced moments reaching one fifth of the expected moments.

In these calculations, Aguilera-Granja *et al*. (private comm.) studied the effects of having carbon impurities in core-shell like FeCo clusters. The core-shell model presented in this case is having either the surface atoms being Co or Fe. Two cluster sizes were studied, clusters having 56 atoms ($Co_{15}Fe_{41}$ and $Co_{41}Fe_{15}$) and 59 atoms ($Co_{15}Fe_{44}$ and $Co_{44}Fe_{15}$). The 59 atoms cluster is a perfect close bcc geometrical shape, and the 56 atom one is an open shell cluster formed by removing three surface atoms from the 59 atoms cluster.

In the case of the 56 atom clusters, the three removed atoms were substituted by either carbon or oxygen atoms. The magnetic moment per atom is then calculated for the the positions of the substituted atom presented in figure 4.28a for the two configurations, Co core / Fe shell and Fe core / Co shell. For the 59 atom clusters, the impurity (C or O) is added in interstitial positions as shown in figure 4.28b.

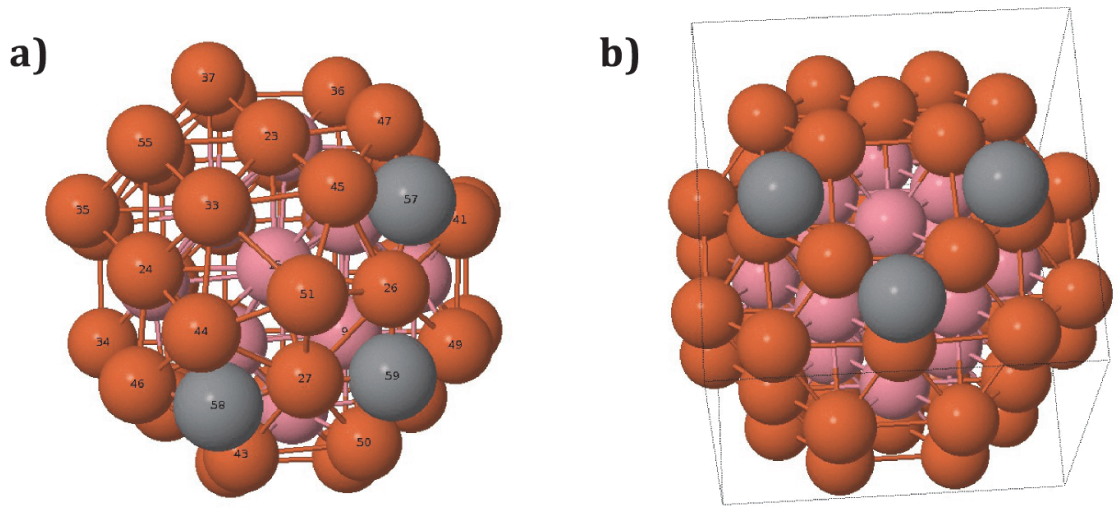

Fig. 4.28 (Left) Surface atom vacancies substituted by impurities (C or O) and (Right) impurities added in interstitial position between surface atoms.

Figures 4.29 and 4.30 show some of the findings of Aguilera-Granja *et al*. (private comm.) for impurities substituted or added in an interstitial position, respectively.

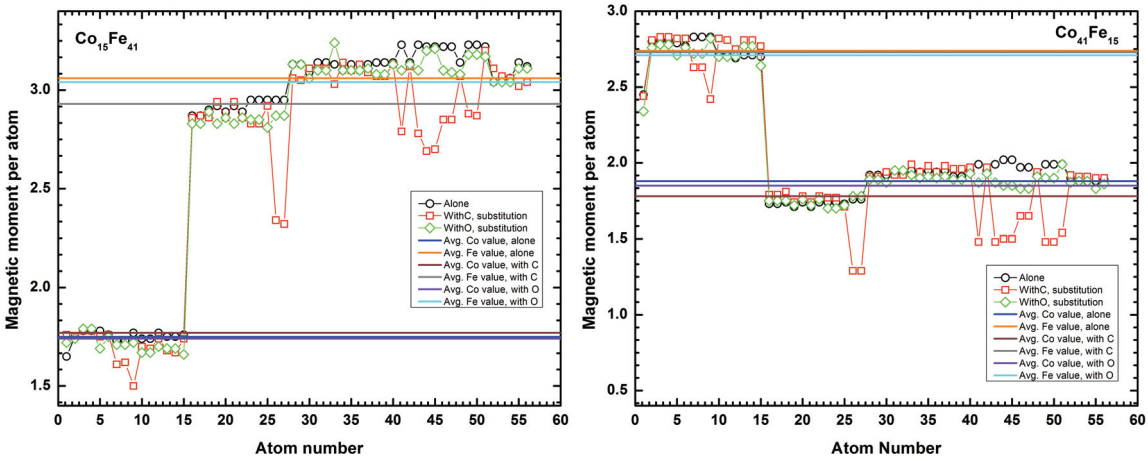

Fig. 4.29 Calculated average moment for Fe and Co atoms with the substitution of three C/O atoms in the vacancy positions for $Co_{15}Fe_{41}$ (Left) and $Co_{41}Fe_{15}$ (right) (in collaboration with Aguilera-Granja *et al*., private comm.).

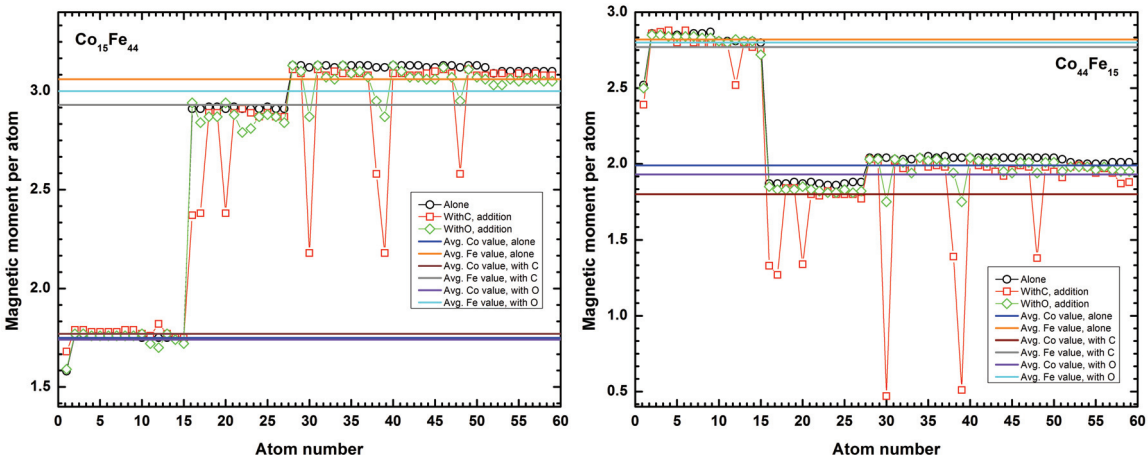

Fig. 4.30 Calculated average moment for Fe and Co atoms with the addition of three C/O atoms in interstitial position for $Co_{15}Fe_{44}$ (Left) and $Co_{44}Fe_{15}$ (right) (in collaboration with Aguilera-Granja *et al*., private comm.).

As seen from the results Aguilera-Granja *et al*. (private comm.), compared to the substitution/addition of oxygen atoms, the carbon atoms have the worst impact on the magnetic moment for atoms located in proximity of the carbon (namely in the NN shell). In addition, comparing the obtained values of the magnetic moment per atom for the presence of carbon in the two cases (substitution and addition) a more steep diminution of the magnetic moment is found in the case of carbon addition. This trend of decreased moment is in agreement with our XMCD findings.

4.2.2.5 Magnetization curves

In addition to the XMCD spectra, hysteresis loops were also recorded at the DEIMOS beamline for the samples at low temperature ($T = 2$ K) as well as high temperature ($T = 300$ K). The spectra were recorded at the Fe and Co L_3 edges by varying the magnetic field. The resulting hysteresis loops at 2 K and 300 K are presented in figures 4.31 and 4.32 respectively.

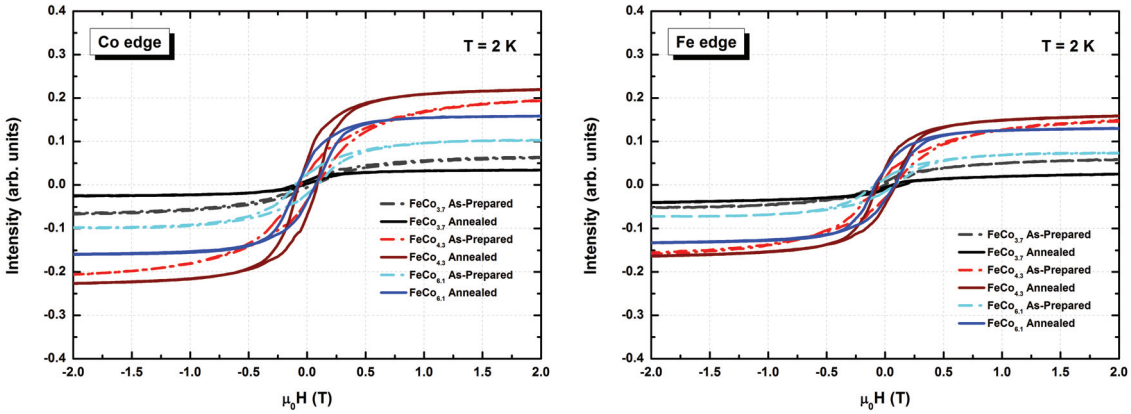

Fig. 4.31 Hysteresis loops of $FeCo_{3.7}$, $FeCo_{4.3}$ and $FeCo_{6.1}$ nanoparticles measured by XMCD at the Co (Left) and Fe (right) L_3-edges at 2 K.

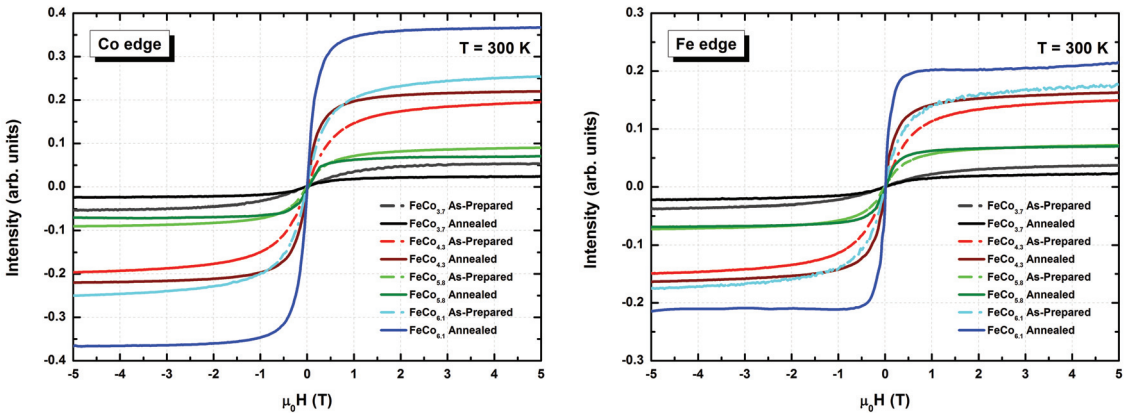

Fig. 4.32 Magnetization curves of $FeCo_{3.7}$, $FeCo_{4.3}$, $FeCo_{5.8}$ and $FeCo_{6.1}$ nanoparticles measured by XMCD at the Co (Left) and Fe (right) L_3-edges at 300 K.

Similar to the XMCD findings, annealing of the small $FeCo_{3.7}$ nanoparticles shows a lower saturation point of the $m(H)$ curves at 2 K and 300 K. For the other sizes annealing always increases the saturation point at both temperatures. Comparing the magnetization curves at high temperature (T = 300 K), shows an increase in the saturation point as the size

increases as well as after annealing for the $FeCo_{4.3}$ and $FeCo_{6.1}$ nanoparticles at both edges. A square shape is observes after annealing of the magnetization curves. The $FeCo_{5.8}$ showed different findings than from the XMCD. The intensity of the measured signal was highly reduced before and after annealing at high temperature and at low temperature the resulting data could not be quantified. The hysteresis loops at low temperature show an increase after annealing for the $FeCo_{4.3}$ and $FeCo_{6.1}$ nanoparticles at both edges. However, no size effect was observed since the intensities from the as-prepared signal of the different nanoparticle sizes was very different. It should be noted, that during the XMCD data acquisition each sample couple was measured at the same run before opening and changing the mounted samples.

4.2.2.6 Saturation magnetization

The saturation magnetization (M_s) for the FeCo samples was extrapolated using the values obtained from XMCD for the average magnetic moment per atom. The values were extrapolated using a simple model by the following equation:

$$M_s = \mu_{av} \times \mu_B \times N \tag{4.1}$$

where μ_{av} is the average magnetic moment obtained from XMCD, μ_B is the Bohr magnetron constant and N is the number of atoms per meter cuber. The latter was estimated using the density and molar mass of bulk FeCo using the following equation:

$$N = \rho \times \frac{N_A}{M} \tag{4.2}$$

where ρ is the density, N_A is Avogadro's number and M is the molar mass. The resulting findings are presented in the tables 4.9 and 4.10 below.

		μ_{av} (μ_B/atom)	M_s (kA.m^{-1})
$Co_{2.9}$	As-prepared	0.54 ± 0.11	460±150
	Annealed	1.12 ± 0.30	860±210
$Co_{3.4}$	As-prepared	0.75 ± 0.15	630±150
	Annealed	1.31 ± 0.26	1100±210
$Fe_{3.3}$	As-prepared	0.62 ± 0.13	480±150
	Annealed	0.44 ± 0.09	340±210
$Fe_{4.4}$	As-prepared	0.86 ± 0.17	670±150
	Annealed	0.84 ± 0.18	660±210

Table 4.9 Saturation magnetization of the Co and Fe samples before and after annealing for all the nanoparticle sizes, $Co_{2.9}$, $Co_{3.4}$, $Fe_{3.3}$ and $Fe_{4.4}$.

		μ_{av} (μ_B/atom)	M_s (kA.m^{-1})
$FeCo_{3.7}$	As-prepared	0.75 ± 0.15	600±120
	Annealed	0.46 ± 0.09	370±75
$FeCo_{4.3}$	As-prepared	0.94 ± 0.19	750±150
	Annealed	1.04 ± 0.21	830±170
$FeCo_{5.8}$	As-prepared	0.89 ± 0.18	710±140
	Annealed	1.09 ± 0.22	870±170
$FeCo_{6.1}$	As-prepared	0.95 ± 0.19	760±150
	Annealed	1.29 ± 0.26	1030±210

Table 4.10 Saturation magnetization of the FeCo samples before and after annealing for the four nanoparticle sizes, $FeCo_{3.7}$, $FeCo_{4.3}$, $FeCo_{5.8}$ and $FeCo_{6.1}$.

The maximum achieved values is estimated at 1028 kA.m^{-1} for the annealed large sized $FeCo_{6.1}$ nanoparticles compared to 1100 kA.m^{-1} and 670 kA.m^{-1} for the annealed $Co_{3.4}$ and as-prepared $Fe_{4.4}$ nanoparticles, respectively. The values for the Fe and FeCo, however, remain significantly small compared to the expected bulk values of 1720 kA.m^{-1} for Fe at less than half and 1912 kA.m^{-1} for FeCo at almost half the value. While the Co value of 1100 kA.m^{-1} is comparable to the bulk Co of 1350 kA.m^{-1}. Nevertheless, these values remain comparable to the values obtained by Edon *et al*. [38] obtained when adding carbon

to FeCo thin films. The latter report values of saturation magnetization ranging between $M_s = 1974$ kA.m^{-1} and $M_s = 414$ kA.m^{-1}.

To sum up, these values will be compared to the values extracted from SQUID magnetometry simulations and will be further discussed in the last section.

4.3 SQUID magnetometry of size-selected clusters

In this section, the cluster samples used are the same as the ones used for the EXAFS study referred to in table 3.13. In addition to these samples, a sample with pure Fe clusters was prepared with a deviation voltage of 600 V. The nanoparticle dilution in all samples was carefully chosen so as to have negligible magnetic interactions between the nanoparticles in the samples. Only the Fe and FeCo nanoparticles are presented below. The results for the pure mass-selected Co particles were previously published from different studies [187, 213–215].

4.3.1 Pure Fe clusters

4.3.1.1 $Fe_{4.4}$ clusters

Figures 4.33 and 4.34 show the complete magnetic characterization of the pure mass-selected $Fe_{4.4}$ samples before and after annealing, respectively.

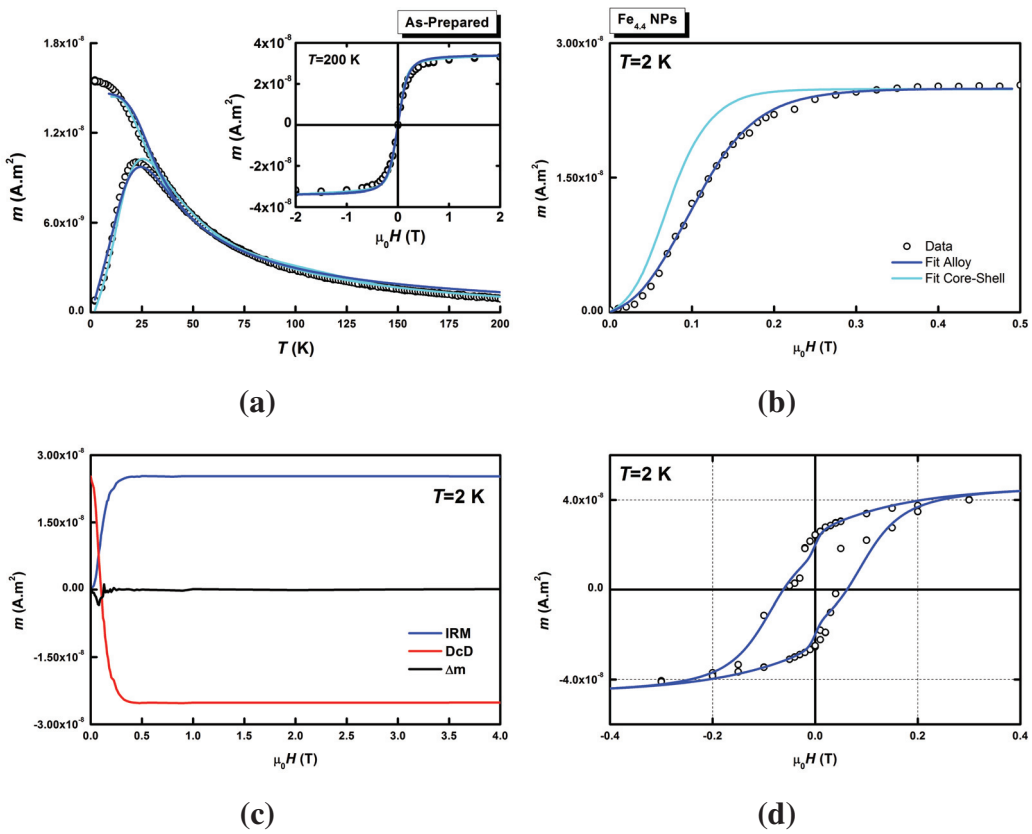

Fig. 4.33 (a) ZFC/FC and $m(H)$ experimental data for mass-selected as-prepared $Fe_{4.4}$ clusters along with their best fits; (b) IRM experimental data with the corresponding biaxial contribution simulation; (c) IRM/DcD curves with the Δm; (d) hysteresis loop at 2 K along with the corresponding simulation.

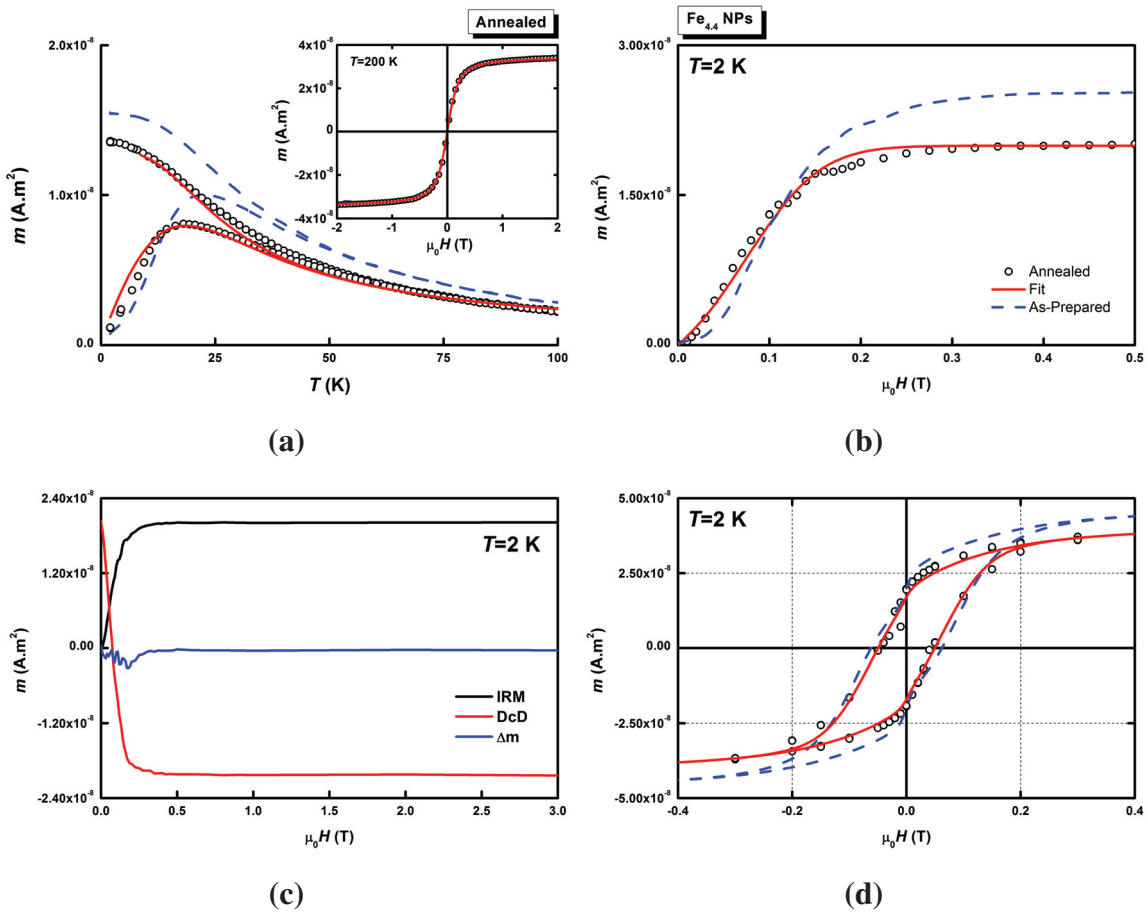

Fig. 4.34 (a) ZFC/FC and $m(H)$ experimental data for mass-selected annealed $Fe_{4.4}$ clusters along with their best fits; (b) IRM experimental data with the corresponding biaxial contribution simulation; (c) IRM/DcD curves with the Δm; (d) hysteresis loop at 2 K along with the corresponding simulation; the dashed line is the as-prepared experimental data.

The corresponding fitting parameters are presented in table 4.11.

		T_{max} (K)	$\mu_0 H_C$ (mT)	D_{mag} (nm)	ω_{mag}	M_s (kA.m^{-1})	K_1 (kJ.m^{-3})	ω_K	K_2/K_1	% SP
Homogeneous	As-prepared	23	53	4.6 ± 0.2	0.11 ± 0.02	1100±100	110 ± 10	0.35 ± 0.05	1.4 ± 0.4	14
	Annealed	19	47	4.25 ± 0.2	0.17 ± 0.02	900±100	90 ± 10	0.45 ± 0.05	0.2 ± 0.4	7
Core-Shell	As-prepared	23	53	4.3 ± 0.2	0.15 ± 0.02	1730	120 ± 10	0.25 ± 0.05	-	-

Table 4.11 Maximums of the ZFC (T_{max}), coercive field ($\mu_0 H_C$) and the deduced parameters from the adjustment of the SQUID measurements for mass-selected $Fe_{4.4}$ nanoparticles embedded in C matrix as-prepared and after annealing in addition to the percentage of SP contribution for the 2 K hysteresis loop.

For both samples, as-prepared and annealed, the Δm (IRM/DcD curves) is at the background noise level indicating that magnetic interactions in the sample are negligible. From a first try, the as-prepared susceptibility curves and the $m(H)$ curve at high temperature were fitted using both previously established models (see figure 4.11). In both cases, the triple-fits were possible giving a magnetic diameter near the expected one from TEM observations with a slightly increased value of anisotropy in the core-shell fit. However, it was impossible to perform a fit of the IRM curves with the core-shell model (see figure 4.33b). Only the homogeneous model with a reduced value of M_s (reduced magnetic moment per atom) allowed the fitting, in qualitative agreement with XMCD results in table 4.9.

For both samples, as-prepared and after annealing, the value of M_s was always found around 1000 ± 100 kA.m^{-1} from the triple-fit. Nevertheless, the initially found value from the triple-fit was found to be smaller after annealing. These same values were used to fit the IRM curves and hysteresis loops at 2 K. In the case of IRM, it should be noted that for a larger value of M_s the simulated curve shifts to the left since the ratio of K_1/M_s, which is proportional to the switching field, decreases. On the other hand, for smaller values of M_s the simulated curve is shifted to the right. However, in this case, the ratio $K_1/M_{s_{as-prepared}} = K_1/M_{s_{annealed}}$. The shift comes from the decrease of the magnetic size because $T = 2$ K instead of $T = 0$ K (see chapter 2).

After annealing, T_{max} decreased and the coercive field slightly decreased too. The complete fit of all the magnetic curves showed a decrease of the mean particle diameter accompanied by an increase in its dispersion. The mean magnetic anisotropy K_1 also decreased after annealing with a widening of the anisotropy dispersion. The observed evolution suggests a decrease in the ordering in the particle causing a decrease of the anisotropy (as was suggested from the EXAFS data on the same sample). To go further, a second iron sample was prepared using a deviation voltage of 600 V. Due to some time limitations with the cluster source, no TEM grid was prepared for this size; the particle diameter and dispersion of $FeCo_{6.1}$ was used.

4.3.1.2 $Fe_{6.1}$ clusters

Figure 4.35 shows the complete magnetic characterization of the as-prepared pure mass-selected $Fe_{6.1}$ samples and the corresponding fitting parameters are presented in table 4.12.

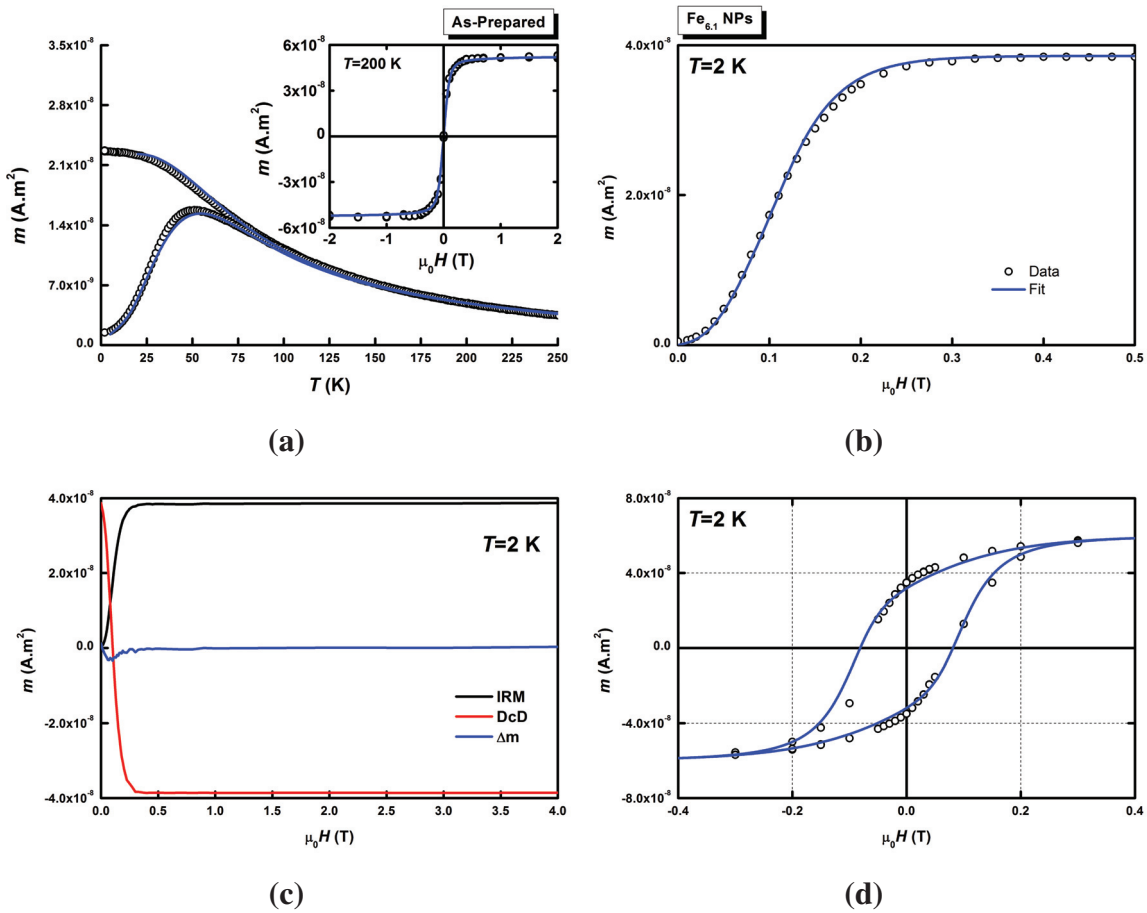

Fig. 4.35 (a) ZFC/FC and $m(H)$ experimental data for mass-selected as-prepared $Fe_{6.1}$ clusters along with their best fits; (b) IRM experimental data with the corresponding biaxial contribution simulation; (c) IRM/DcD curves with the Δm; (d) hysteresis loop at 2 K along with the corresponding simulation.

	T_{max} (K)	$\mu_0 H_C$ (mT)	D_{mag} (nm)	ω_{mag}	M_s (kA.m^{-1})	K_1 (kJ.m^{-3})	ω_K	K_2/K_1	% SP
As-prepared	50	60	6.2 ± 0.2	0.13 ± 0.02	1100±100	100 ± 10	0.30 ± 0.05	1.4 ± 0.4	0

Table 4.12 Maximums of the ZFC (T_{max}), coercive field ($\mu_0 H_C$) and the deduced parameters from the adjustment of the SQUID measurements for as-prepared mass-selected $Fe_{6.1}$ nanoparticles embedded in C matrix in addition to the percentage of SP contribution for the 2 K hysteresis loop.

In the case of $Fe_{6.1}$ pure mass-selected nanoparticles only the as-prepared sample was studied. From the IRM/DcD curves, it can be inferred that the magnetic interactions are negligible. The maximum temperature for these particles is more than the double of that

of smaller $Fe_{4.1}$ nanoparticles while the coercive field is only slightly increased. From the complete fitting of the different magnetic curves, a magnetic diameter of 6.2 nm is found. The saturation magnetization used here is the same as in the case of the smaller particles and also the magnetic anisotropy is 100 kJ.m^{-3}, in the same range as the smaller particles. A biaxial contribution was needed to simulate the IRM curve however for the hysteresis loops at 2 K no superparamagnetic contribution was needed. From these results, it is safe to say that for the largest iron nanoparticles the same magnetic properties are found for both sizes. The blocking temperature is solely increased by the diameter of the nanoparticles.

For the next section, the magnetic response of the bimetallic FeCo mass-selected clusters is studied. We report the magnetic findings for the same samples presented in chapter 3 in the EXAFS section on mass-selected bimetallic FeCo clusters.

4.3.2 Bimetallic clusters

For the bimetallic clusters, each size is presented below in a different section. Figure 4.36 shows the susceptibility curves for all mass-selected FeCo samples as-prepared and after annealing.

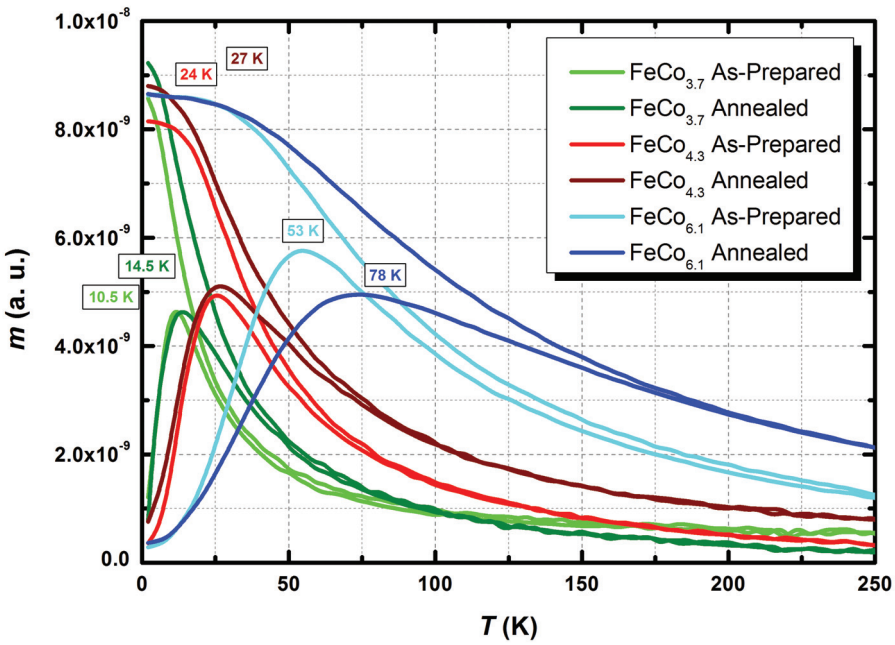

Fig. 4.36 Susceptibility curves for mass-selected $FeCo_{3.7}$, $FeCo_{4.3}$ and $FeCo_{6.1}$ before and after annealing.

From the figure, a size effect as well as an annealing effect can be observed. The maximum temperature increases as the size increases and also after annealing. Since the

maximum temperature is governed by the anisotropy and the volume, the observed increases may simply be due to the increase in the diameter of the particles (from TEM observations); the adjustments presented in the next sections provide a better understanding of this evolution. It should be noted that adjustments presented below were obtained using the homogeneous model with reduced magnetic moment per atom and subsequently a reduced saturation magnetization M_s. The values of M_s obtained from our fits are reported in each case. The data could not be fitted with a core-shell model, *i.e.* with a reduced diameter and the bulk FeCo M_s.

4.3.2.1 $FeCo_{3.7}$ clusters

Figures 4.37 and 4.38 show the complete magnetic characterization of the pure mass-selected $FeCo_{3.7}$ samples before and after annealing, respectively.

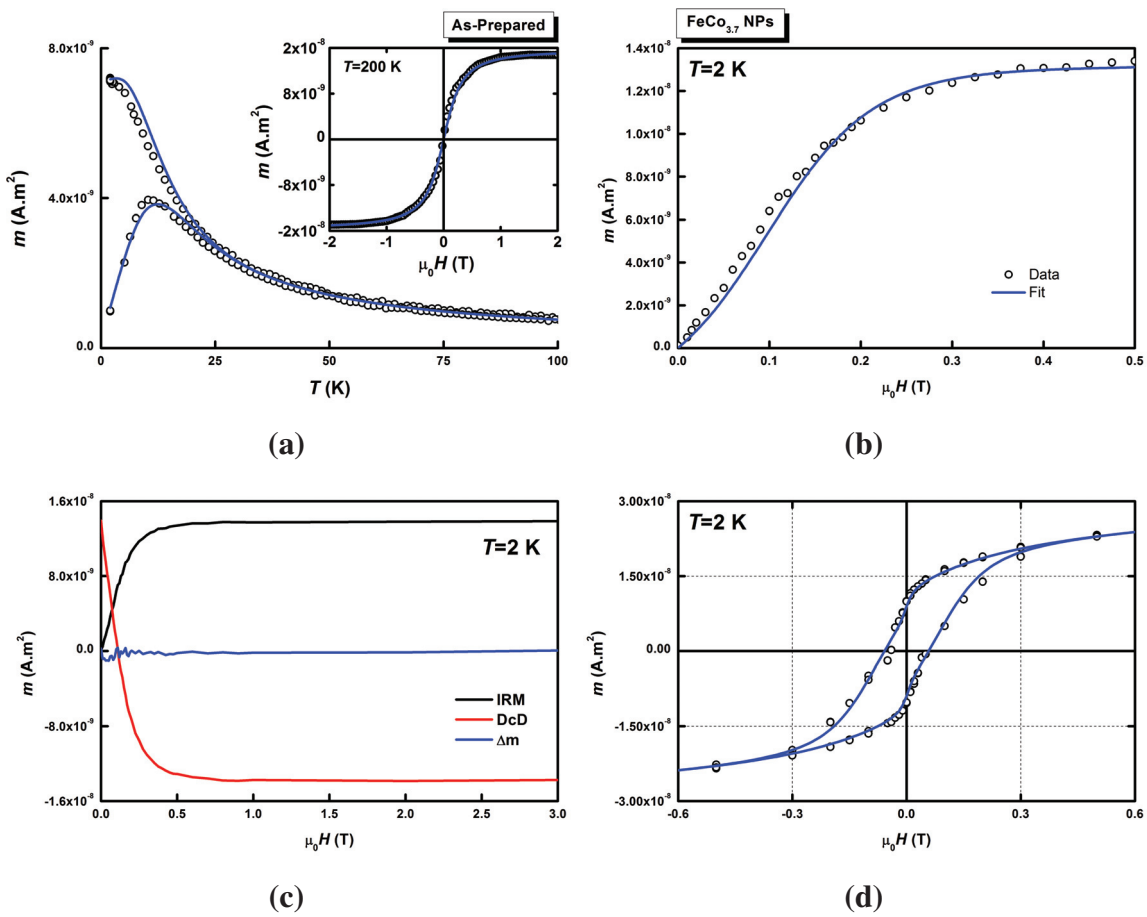

Fig. 4.37 (a) ZFC/FC and $m(H)$ experimental data for mass-selected as-prepared $FeCo_{3.7}$ clusters along with their best fits; (b) IRM experimental data with the corresponding biaxial contribution simulation; (c) IRM/DcD curves with the Δm; (d) hysteresis loop at 2 K along with the corresponding simulation.

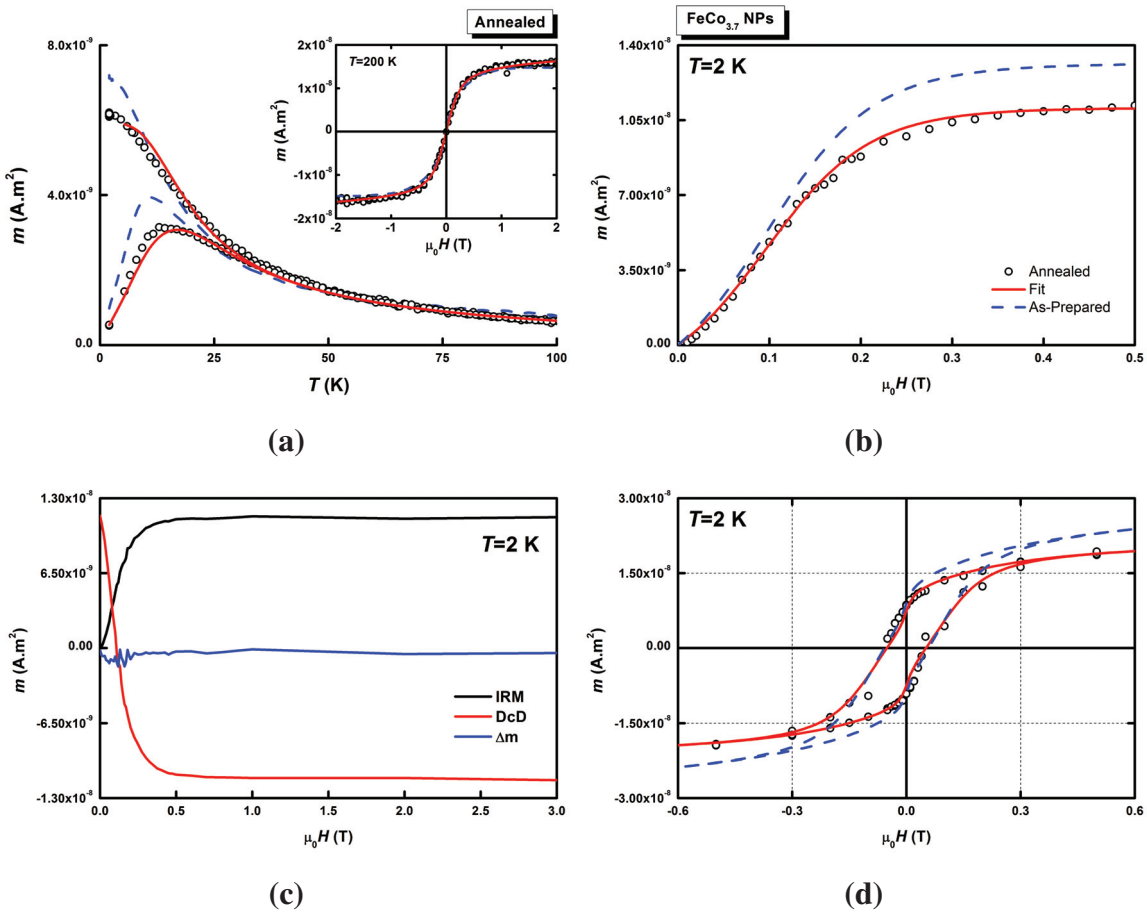

Fig. 4.38 (a) ZFC/FC and $m(H)$ experimental data for mass-selected annealed $FeCo_{3.7}$ clusters along with their best fits; (b) IRM experimental data with the corresponding biaxial contribution simulation; (c) IRM/DcD curves with the Δm; (d) hysteresis loop at 2 K along with the corresponding simulation; the dashed line is the as-prepared experimental data.

The corresponding fitting parameters are presented in table 4.13.

	T_{max} (K)	$\mu_0 H_C$ (mT)	D_{mag} (nm)	ω_{mag}	M_s (kA.m^{-1})	K_1 (kJ.m^{-3})	ω_K	K_2/K_1	% SP
As-prepared	10	40	3.4 ± 0.2	0.15 ± 0.02	950 ± 100	120 ± 10	0.40 ± 0.05	1.4 ± 0.4	17.0
Annealed	14.5	45	3.7 ± 0.2	0.13 ± 0.02	920 ± 100	140 ± 10	0.40 ± 0.05	1.2 ± 0.4	21.4

Table 4.13 Maximums of the ZFC (T_{max}), coercive field ($\mu_0 H_C$) and the deduced parameters from the adjustment of the SQUID measurements for mass-selected $FeCo_{3.7}$ nanoparticles embedded in C matrix as-prepared and after annealing in addition to the percentage of SP contribution for the 2 K hysteresis loop.

For the small mass-selected $FeCo_{3.7}$ nanoparticles, negligible magnetic interactions can be assumed from Δm before and after annealing. A slight increase of both the maximum temperature and the coercive field is observed after annealing. The fits resulted in diameter values in agreement with the TEM observations. Nevertheless, after annealing we observe an increase of the magnetic diameter accompanied by an increase in the anisotropy constant, while its dispersion remains the same. The value of M_s is only slightly reduced after annealing. In both cases, a biaxial contribution was necessary to achieve the simultaneous adjustment of all the magnetic curves. In addition, a SP contribution was needed to simulate the hysteresis loops at 2 K. The M_s value is lower than for all the other sizes, in qualitative agreement with the XMCD results from table 4.10.

4.3.2.2 $FeCo_{4.3}$ clusters

Figures 4.39 and 4.40 show the complete magnetic characterization of the pure mass-selected $FeCo_{4.3}$ samples before and after annealing, respectively.

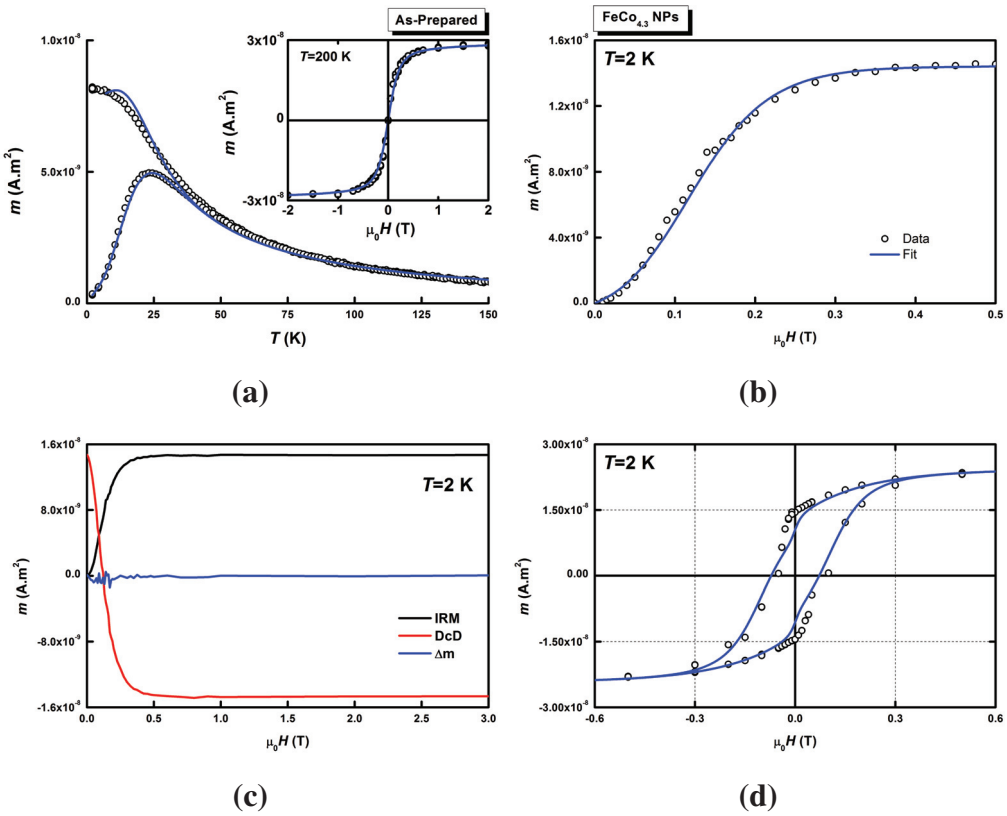

Fig. 4.39 (a) ZFC/FC and $m(H)$ experimental data for mass-selected as-prepared $FeCo_{4.3}$ clusters along with their best fits; (b) IRM experimental data with the corresponding biaxial contribution simulation; (c) IRM/DcD curves with the Δm; (d) hysteresis loop at 2 K along with the corresponding simulation.

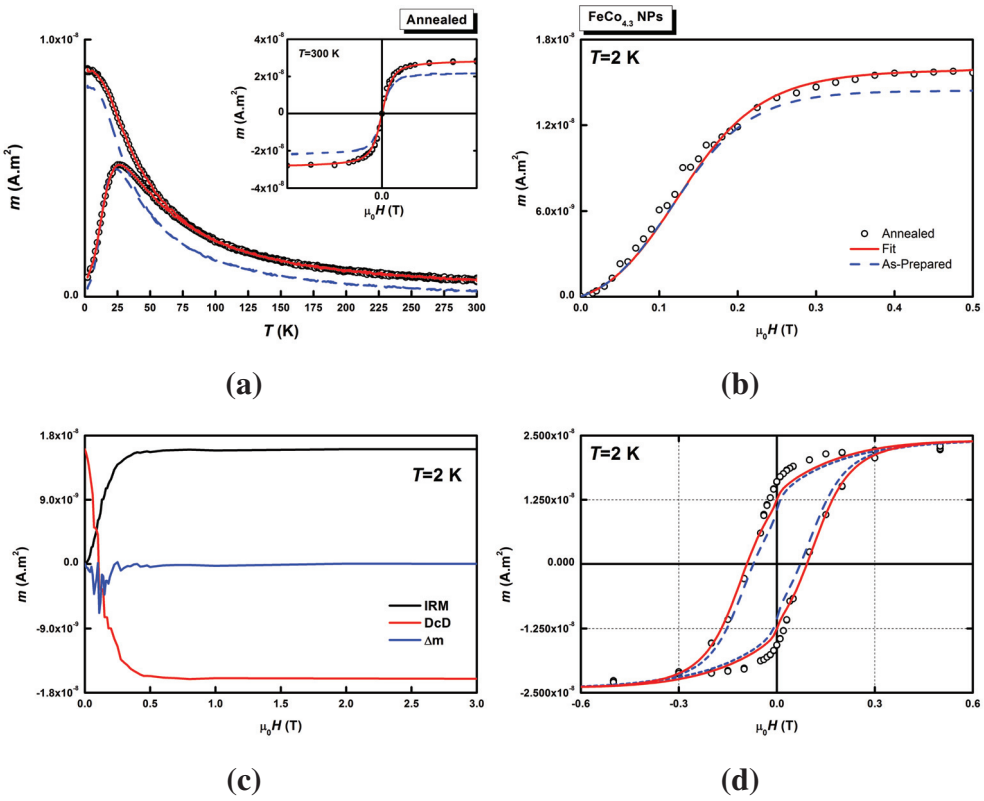

Fig. 4.40 (a) ZFC/FC and $m(H)$ experimental data for mass-selected annealed $FeCo_{4.3}$ clusters along with their best fits; (b) IRM experimental data with the corresponding biaxial contribution simulation; (c) IRM/DcD curves with the Δm; (d) hysteresis loop at 2 K along with the corresponding simulation; the dashed line is the as-prepared experimental data.

The corresponding fitting parameters are presented in table 4.14.

	T_{max} (K)	$\mu_0 H_C$ (mT)	D_{mag} (nm)	ω_{mag}	M_s (kA.m^{-1})	K_1 (kJ.m^{-3})	ω_K	K_2/K_1	% SP
As-prepared	24	75	4.3 ± 0.2	0.1 ± 0.02	1100 ± 100	135 ± 20	0.31 ± 0.05	1.0 ± 0.4	13.1
Annealed	27	93	4.3 ± 0.2	0.15 ± 0.02	1000 ± 100	145 ± 20	0.40 ± 0.05	1.4 ± 0.4	5.9

Table 4.14 Maximums of the ZFC (T_{max}), coercive field ($\mu_0 H_C$) and the deduced parameters from the adjustment of the SQUID measurements for mass-selected $FeCo_{4.3}$ nanoparticles embedded in C matrix as-prepared and after annealing in addition to the percentage of SP contribution for the 2 K hysteresis loop.

In the case of the medium sized ($FeCo_{4.3}$) mass-selected FeCo nanoparticles, the as-prepared sample shows negligible magnetic interactions whereas for the annealed sample a small negative peak is visible. $\Delta m < 0$ indicates the presence of dipolar interactions. Nevertheless, it was possible to simultaneously fit all the magnetic curves for the annealed

sample suggesting that the interactions present in the sample are, in fact, kept to a minimum so as to allow the fit. Qualitatively, an increase of the coercive field is visible along with a slight increase of the maximum temperature. The magnetic diameter remains unchanged after annealing and is indeed in accordance with the TEM observations. M_s shows a small decrease after annealing, while the anisotropy constant slightly increases. However, the anisotropy dispersion shows a noticeable increase after annealing. For both cases, a biaxial contribution was needed for the low temperature curves (IRM curves and hysteresis loops at 2 K). Moreover, a SP contribution was needed for the hysteresis loop simulation. The latter shows a decrease after annealing with possible coalescence in the sample. M_s remains unchanged, the same as from the XMCD results in table 4.10.

4.3.2.3 $FeCo_{6.1}$ clusters

Figures 4.41 and 4.42 show the complete magnetic characterization of the pure mass-selected $FeCo_{6.1}$ samples before and after annealing, respectively.

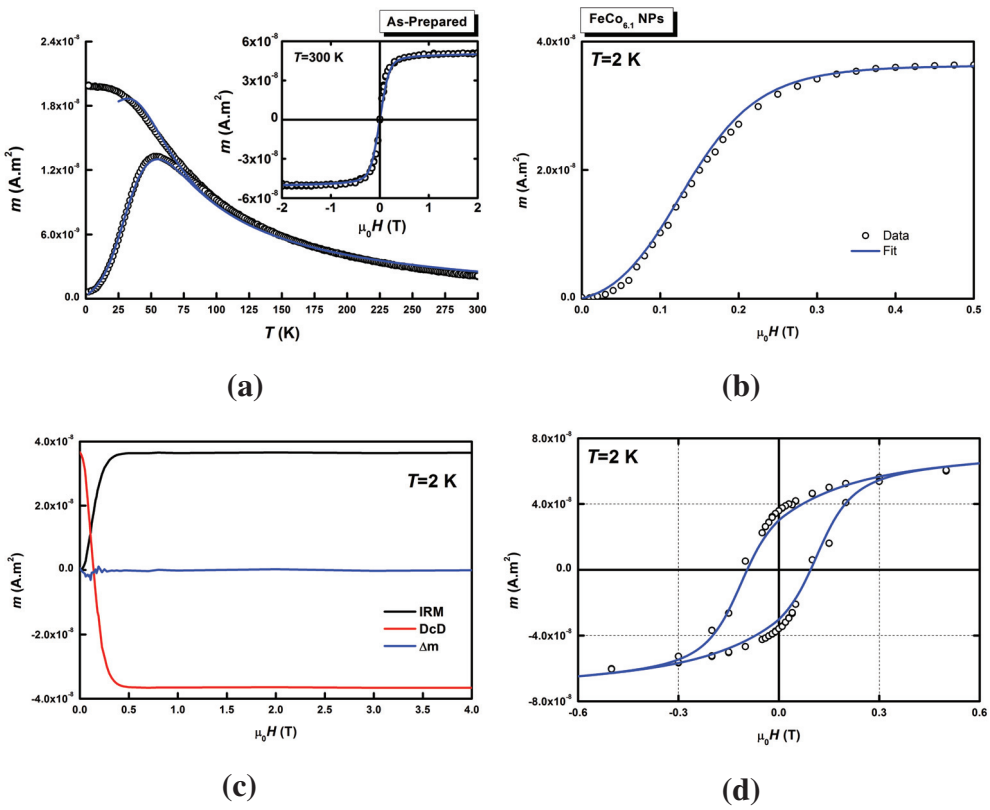

Fig. 4.41 (a) ZFC/FC and $m(H)$ experimental data for mass-selected as-prepared $FeCo_{6.1}$ clusters along with their best fits; (b) IRM experimental data with the corresponding biaxial contribution simulation; (c) IRM/DcD curves with the Δm; (d) hysteresis loop at 2 K along with the corresponding simulation.

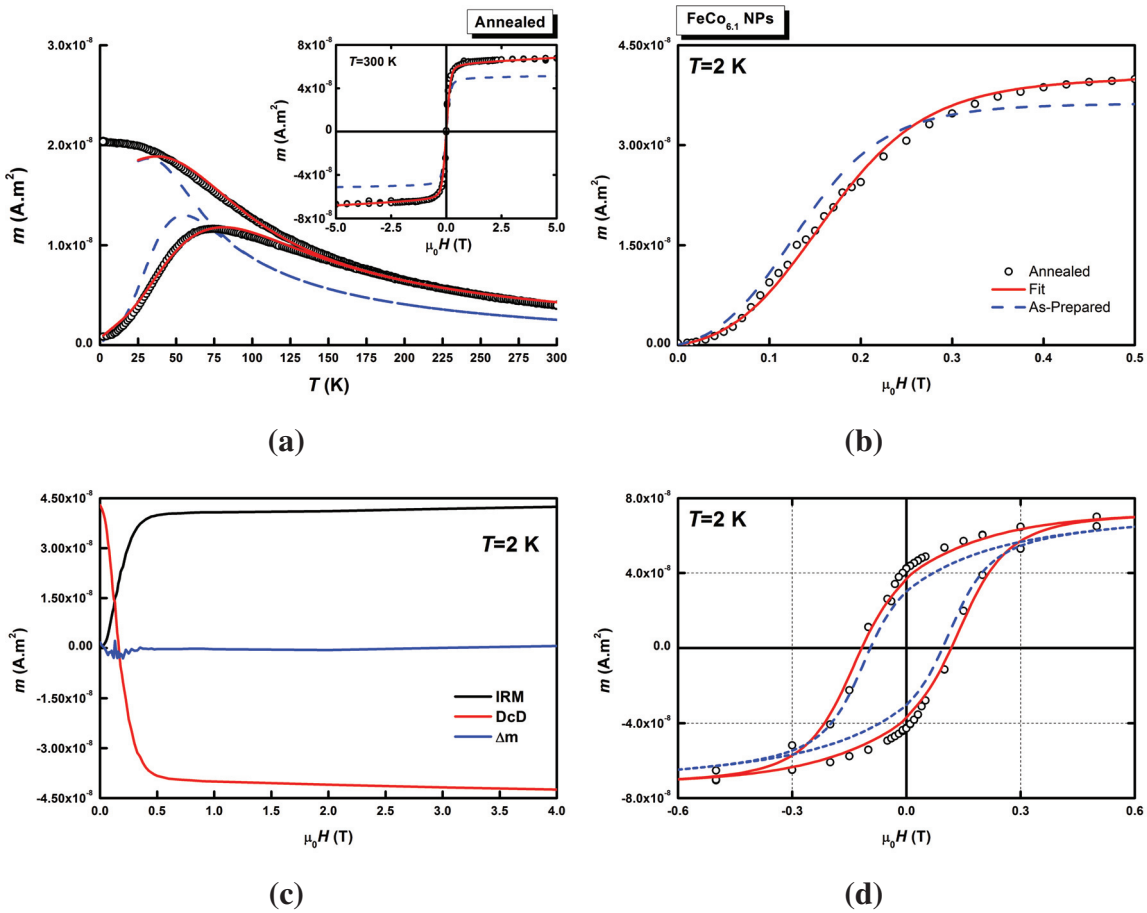

Fig. 4.42 (a) ZFC/FC and $m(H)$ experimental data for mass-selected annealed $FeCo_{6.1}$ clusters along with their best fits; (b) IRM experimental data with the corresponding biaxial contribution simulation; (c) IRM/DcD curves with the Δm; (d) hysteresis loop at 2 K along with the corresponding simulation; the dashed line is the as-prepared experimental data.

The corresponding fitting parameters are presented in table 4.15.

	T_{max} (K)	$\mu_0 H_C$ (mT)	D_{mag} (nm)	ω_{mag}	M_s (kA.m^{-1})	K_1 (kJ.m^{-3})	ω_K	K_2/K_1	% SP
As-prepared	53	101	6.2 ± 0.2	0.08 ± 0.02	1000 ± 100	120 ± 10	0.34 ± 0.05	1.4 ± 0.4	0.0
Annealed	78	121	6.1 ± 0.2	0.12 ± 0.02	1200 ± 100	165 ± 10	0.40 ± 0.05	1.4 ± 0.4	1.0

Table 4.15 Maximums of the ZFC (T_{max}), coercive field ($\mu_0 H_C$) and the deduced parameters from the adjustment of the SQUID measurements for mass-selected $FeCo_{6.1}$ nanoparticles embedded in C matrix as-prepared and after annealing in addition to the percentage of SP contribution for the 2 K hysteresis loop.

Δm in larger ($FeCo_{6.1}$) mass-selected FeCo nanoparticles is at the background noise level both before and after annealing. The curves show a noticeable increase in the maximum temperature as well as in the coercive field. In addition, fitting the experimental curves gives almost the same magnetic diameter as expected from TEM observations with a similarly small size dispersion. Contrary to the other size and in agreement with XMCD results, an increase of the saturation magnetization is observed after annealing. Moreover, the magnetic anisotropy constant shows a prominent increase of 37%. Furthermore, a biaxial contribution was needed to perform the fit. It should be noted that almost no SP contribution was needed to simulate the hysteresis loops at 2 K.

The observed enhancement of the anisotropy constant is in favour of a chemical ordering and an increase of the crystallographic order inside the annealed $FeCo_{6.1}$ nanoparticles. Comparing the results of all the bimetallic FeCo nanoparticles, for all sizes the obtained magnetic diameter and dispersion are in accordance with the TEM observations. The saturation magnetizations undergo only slight variations after annealing, with a slight decrease for the small $FeCo_{3.7}$ and medium $FeCo_{4.3}$ sizes compared to an increase for the large $FeCo_{6.1}$ size. The magnetic anisotropy constant K_1 is almost equal in all the as-prepared nanoparticles within the error range, however, after annealing and for all sizes an enhancement is obtained and most notably for the large $FeCo_{6.1}$ size. This behaviour is indeed expected from the EXAFS results since after annealing, the large $FeCo_{6.1}$ nanoparticles exhibited a substantial enhancement of the number of NN (NN coordination) and a more structured FT up to 6 Å (see figure 3.40). Moreover, since the magnetic measurements were performed on the exact same set of samples, it can be stated and without a doubt that the observed increase in the anisotropy constant value of the $FeCo_{6.1}$ clusters is indeed due to a structural evolution from the disordered A2 phase to a more ordered phase, probably the B2 CsCl phase. The value of M_s increases in a similar fashion to XMCD measurements.

4.3.3 Copper matrix

In addition to the previous samples, two additional samples of mass-selected FeCo nanoparticles embedded in Copper matrix were studied. The samples were fabricated in a co-deposition geometry with the nanoparticles and evaporated matrix arriving on the substrate at 45°. Two voltage deviations were chosen: 300 V and 600 V. The finished samples were capped with a carbon layer to ensure that no contamination of the sample occurred upon transfer into air. Figures 4.43 and 4.44 show the binary phase diagrams of both Fe-Cu [216] and Co-Cu [217], respectively. Both iron and cobalt atoms are immiscible with copper making Cu an excellent candidate as a matrix choice.

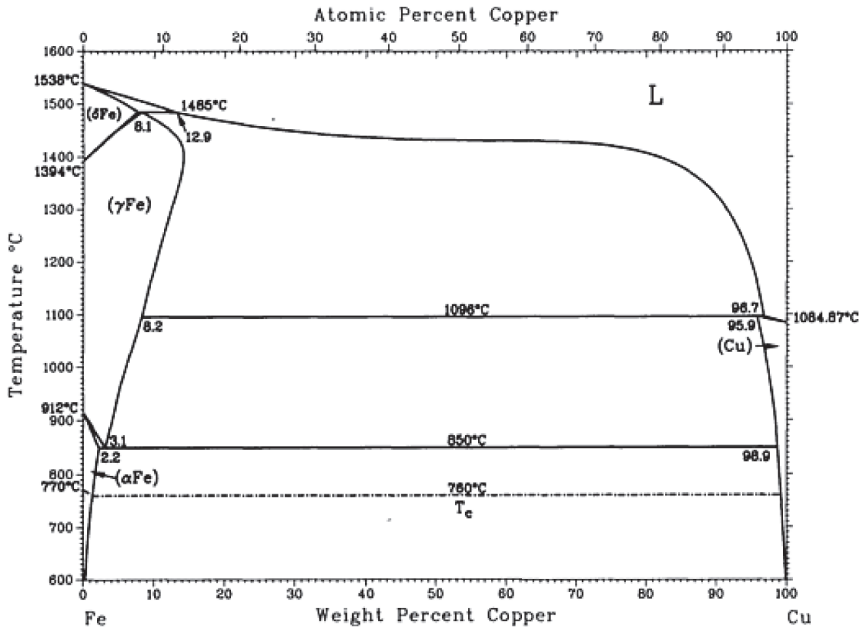

Fig. 4.43 Binary phase diagram of Fe-Cu.

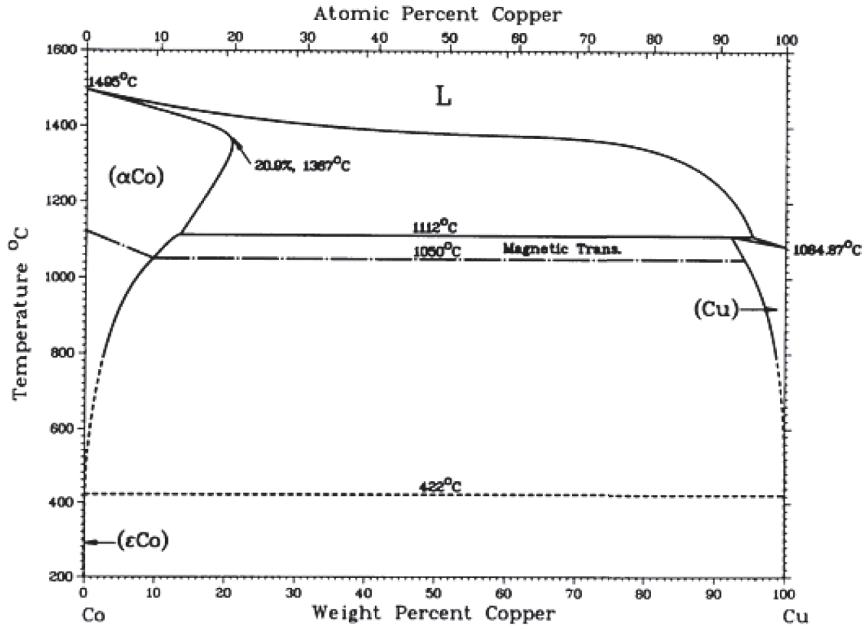

Fig. 4.44 Binary phase diagram of Co-Cu.

The mean diameter size and dispersion of the two samples correspond to the same values obtained in chapter 3 in table 3.5, *i.e.* to that of the $FeCo_{4.3}$ and $FeCo_{6.1}$ samples. The two samples will be referred to from here on out as, $FeCo^{Cu}_{4.3}$ and $FeCo^{Cu}_{6.1}$ for the 300 V and 600 V deviations, respectively.

4.3.3.1 $FeCo^{Cu}{}_{4.3}$ clusters

Figure 4.45 shows the complete magnetic characterization of the as-prepared mass-selected $FeCo^{Cu}{}_{4.3}$ samples and the corresponding fitting parameters are presented in table 4.16.

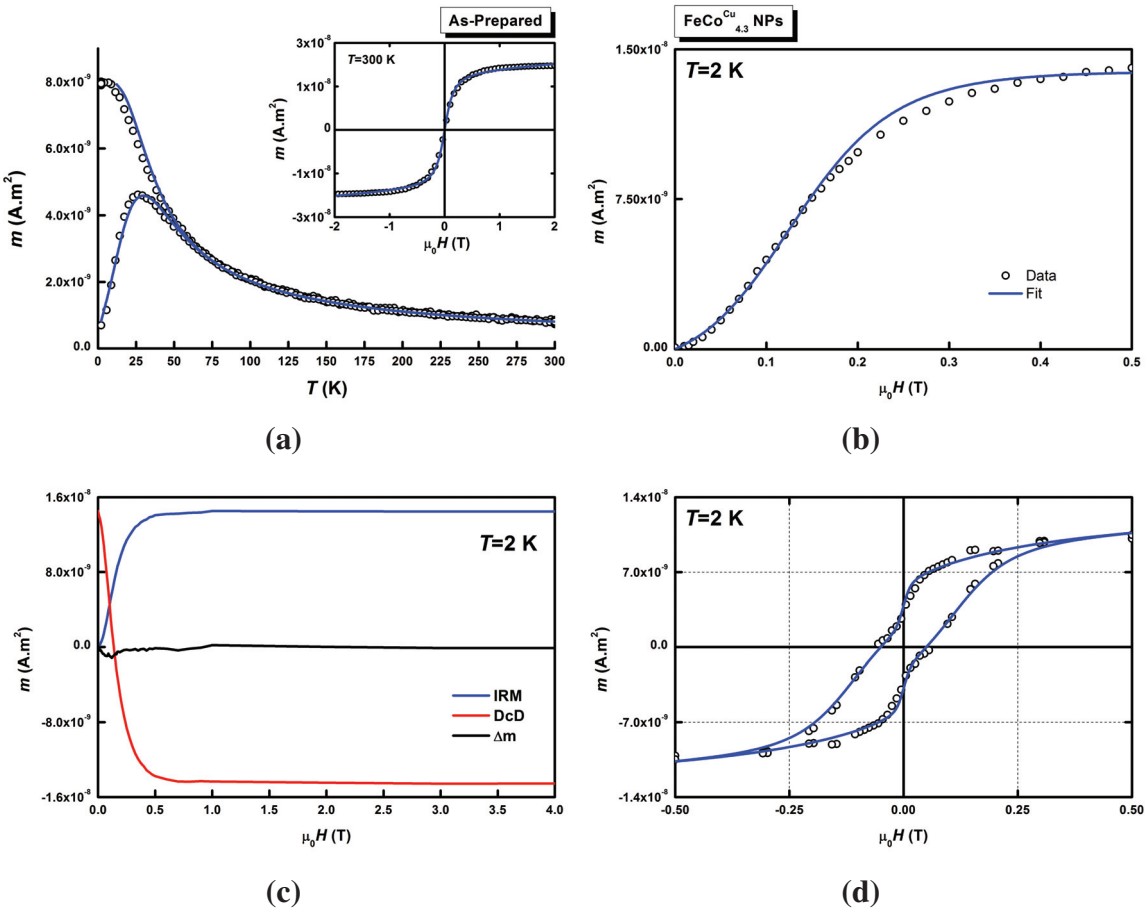

Fig. 4.45 (a) ZFC/FC and $m(H)$ experimental data for mass-selected as-prepared $FeCo^{Cu}{}_{4.3}$ clusters embedded in Cu matrix along with their best fits; (b) IRM experimental data with the corresponding biaxial contribution simulation; (c) IRM/DcD curves with the Δm; (d) hysteresis loop at 2 K along with the corresponding simulation.

	T_{max} (K)	$\mu_0 H_C$ (mT)	D_{mag} (nm)	ω_{mag}	M_s (kA.m^{-1})	K_1 (kJ.m^{-3})	ω_K	K_2/K_1	% SP
As-prepared	30	60	3.9 ± 0.2	0.12 ± 0.02	1650±200	210 ± 20	0.42 ± 0.05	1.4 ± 0.4	24.5

Table 4.16 Maximums of the ZFC (T_{max}), coercive field ($\mu_0 H_C$) and the deduced parameters from the adjustment of the SQUID measurements for as-prepared mass-selected $FeCo^{Cu}{}_{4.3}$ nanoparticles embedded in Cu matrix in addition to the percentage of SP contribution for the 2 K hysteresis loop.

At a first glance, Δm curve shows negligible magnetic interactions. The maximum temperature $T_{max} = 30$ K is slightly higher than for carbon embedded nanoparticles, as-prepared and annealed respectively 24 and 27 K. The coercive field, however, is slightly smaller than in the carbon case. This is due to the high value of M_s in the copper matrix compared to the carbon one. Similar to the switching field, the coercive field is proportional to the ratio K_1/M_s. From the triple-fit, the obtained magnetic diameter is in agreement in both cases as well as with the TEM observations for FeCo nanoparticles (see table 3.6). The complete fit, along with the IRM and hysteresis loop at 2 K, was only possible with a reduced saturation magnetization of $M_s = 1650$ kA.m^{-1} compared to the bulk value of $M_s = 1930$ kA.m^{-1}. M_s was not fixed in this case and the tabulated value allowed fitting all the magnetic curves. This value is larger than those obtained using the carbon matrix, thus further supporting the reduction of the average magnetic moment per atom due to the carbon presence in the other samples. In addition, the magnetic anisotropy in the copper embedded FeCo nanoparticles is larger than that obtained in the carbon embedded ones. In fact, the value obtained for the magnetic anisotropy is even larger than the annealed $FeCo_{4.3}$ nanoparticles embedded in carbon. Moreover, similar to the carbon case, a biaxial contribution was needed to simulate the IRM and hysteresis loops at 2 K. However, compared to the carbon case, here a larger percentage of superparamagnetic contribution was needed to simulate the hysteresis loop at 2 K.

The first magnetic measurements were performed on the $FeCo^{Cu}{}_{6.1}$ which was then annealed and remeasured. The findings for the annealed $FeCo^{Cu}{}_{6.1}$ sample were not expected, so for the $FeCo^{Cu}{}_{4.3}$ sample the annealing was performed at increasing temperatures starting from $T = 250°$C to $500°$C. The evolution of the ZFC/FC curves is presented in figure 4.46.

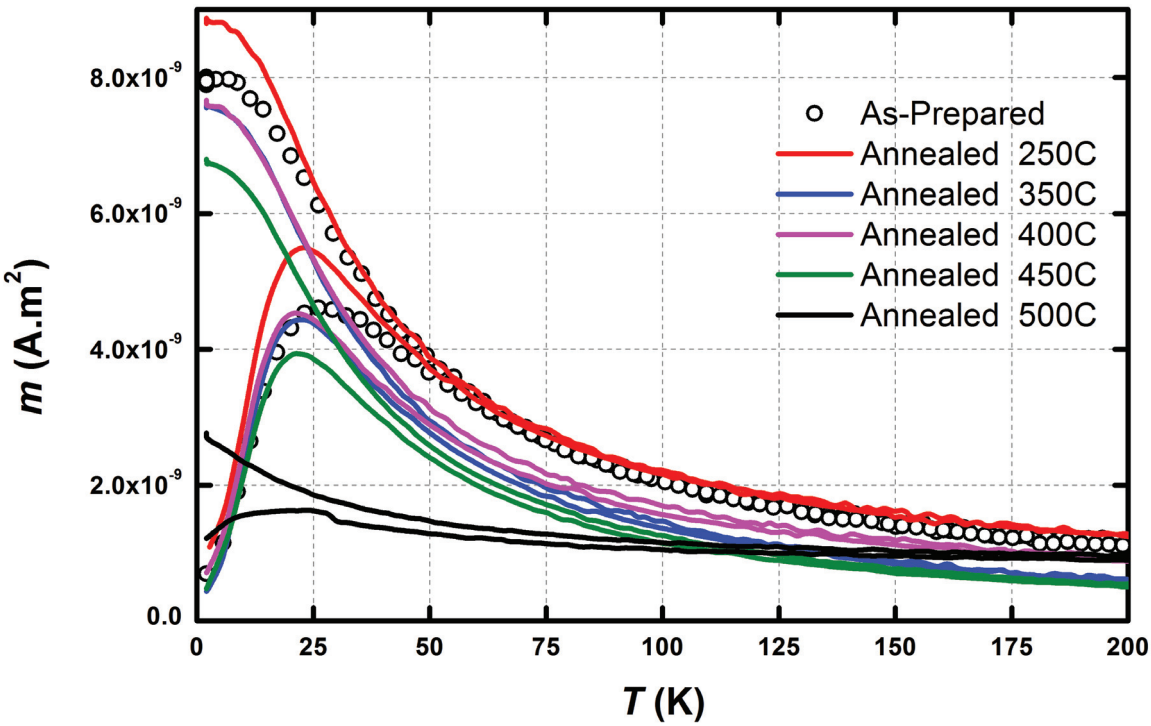

Fig. 4.46 ZFC/FC curves for $FeCo^{Cu}_{4.3}$ nanoparticles embedded in copper matrix and annealed at a range of temperatures from 250°C to 500°C.

From the figure 4.46, comparing the different ZFC/FC curves annealed from 250°C to 450°C, almost no evolution is observed and the difference is due to the centering in the SQUID. In addition, the difference between these curves and the as-prepared one is very small and can be considered the same with a small degree of uncertainty. On the other hand, the ZFC/FC curve for the annealed 500°C shows an almost negligible magnetic signal compared to the other annealing temperatures.

4.3.3.2 $FeCo^{Cu}_{6.1}$ clusters

Figure 4.47 shows the complete magnetic characterization of the as-prepared mass-selected $FeCo^{Cu}_{6.1}$ samples and the corresponding fitting parameters are presented in table 4.17.

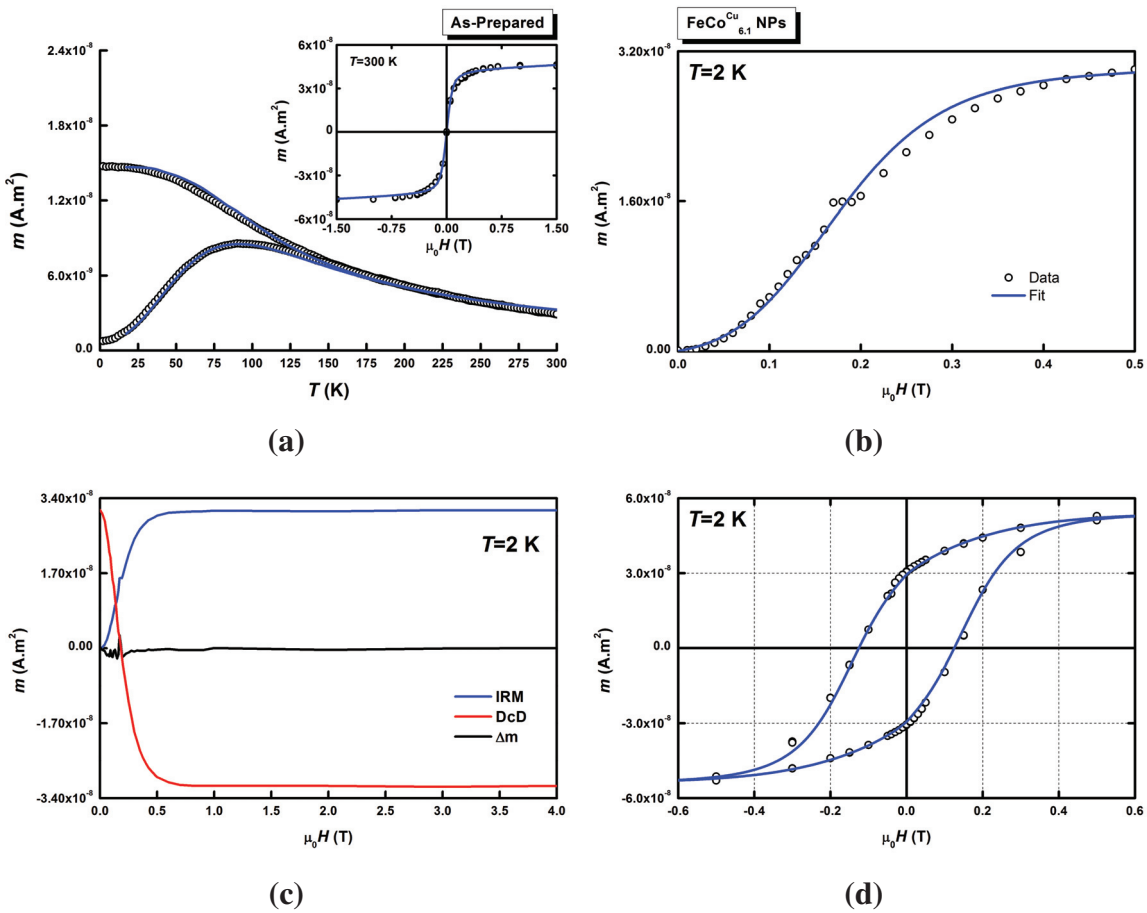

Fig. 4.47 (a) ZFC/FC and $m(H)$ experimental data for mass-selected as-prepared $FeCo^{Cu}{}_{6.1}$ clusters embedded in Cu matrix along with their best fits; (b) IRM experimental data with the corresponding biaxial contribution simulation; (c) IRM/DcD curves with the Δm; (d) hysteresis loop at 2 K along with the corresponding simulation.

	T_{max} (K)	$\mu_0 H_C$ (mT)	D_{mag} (nm)	ω_{mag}	M_s (kA.m^{-1})	K_1 (kJ.m^{-3})	ω_K	K_2/K_1	% SP
As-prepared	95	130	5.7 ± 0.2	0.1 ± 0.02	1700±200	240 ± 20	0.40 ± 0.05	1.4 ± 0.4	0

Table 4.17 Maximums of the ZFC (T_{max}), coercive field ($\mu_0 H_C$) and the deduced parameters from the adjustment of the SQUID measurements for as-prepared mass-selected $FeCo^{Cu}{}_{6.1}$ nanoparticles embedded in Cu matrix in addition to the percentage of SP contribution for the 2 K hysteresis loop.

From a qualitative analysis, the sample shows negligible magnetic interactions as evidenced by the Δm curve (curve is at background noise level). The maximum temperature is obtained around $T_{max} = 95$ K. The latter is larger than the maximum temperature obtained

for the large nanoparticles' sample embedded in a carbon matrix, both before and after annealing. In addition, the coercive field is also larger than the as-prepared and annealed $FeCo_{6.1}$ nanoparticles embedded in carbon matrix.

From a quantitative analysis, the magnetic diameter and dispersion are in agreement with the TEM observations (see table 3.5). Moreover, the value obtained is also in agreement with the carbon matrix case. In addition, similar to the $FeCo^{Cu}{}_{4.3}$ clusters, for the $FeCo^{Cu}{}_{6.1}$ sample the obtained saturation magnetization $M_s = 1700$ kA.m^{-1} is smaller than the bulk value. Moreover, the magnetic anisotropy obtained for these particles was significantly larger than the as-prepared $FeCo_{6.1}$ clusters and even larger than the obtained value after annealing. The addition of a biaxial component was also necessary in this case to simulate the IRM and hysteresis loops at 2 K. However, for the latter, no superparamagnetic contribution was needed to fit the hysteresis loop at 2 K.

After annealing the mass-selected $FeCo^{Cu}{}_{6.1}$ sample gave the ZFC/FC curves shown in figure 4.48 that could not be fitted.

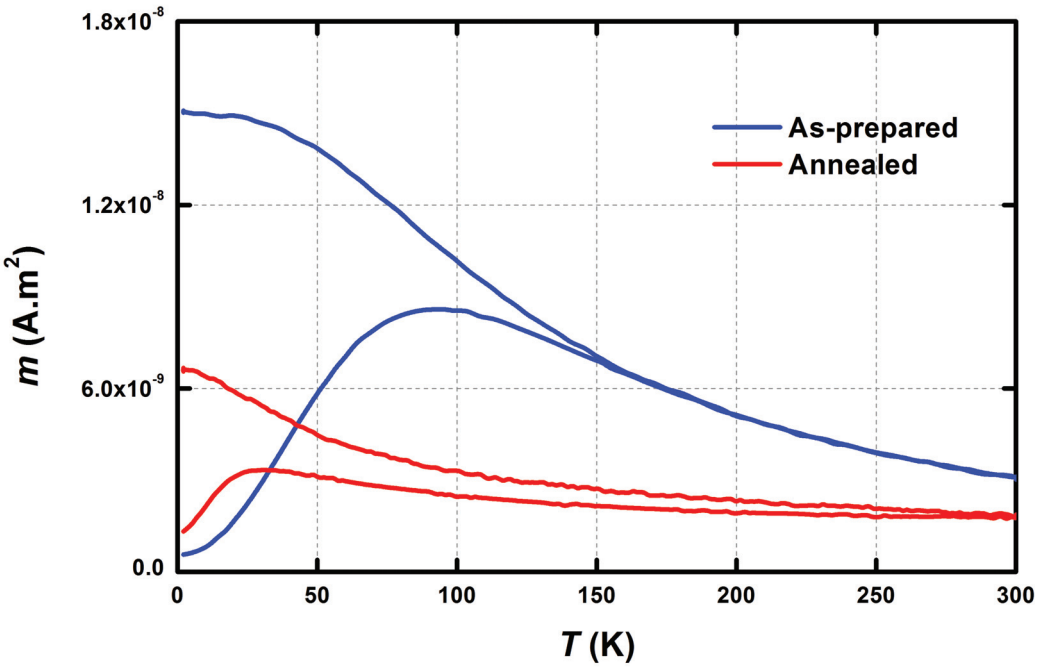

Fig. 4.48 ZFC/FC curves for $FeCo^{Cu}{}_{6.1}$ nanoparticles embedded in copper matrix before and after annealing at 500°C under UHV.

The above evolution after annealing at 500°C under UHV is similar to the $FeCo^{Cu}{}_{4.3}$ sample. The latter suggests a critical limit when annealing at 500°C. Since for the annealing at lower temperatures of the $FeCo^{Cu}{}_{4.3}$ sample, the ZFC/FC curves retained their shape (see

figure 4.46). This evolution can possibly be due to coalescence in the sample after annealing or possibly the formation of a meta-stable alloy. However, in order to clarify the origin of this evolution further study is needed.

4.4 Discussion

The magnetic characterization of all samples was achieved using two complementary techniques, the SQUID and XMCD. The former allows the characterization of the whole sample by measuring the magnetization of the sample (see chapter 2), thus provides raw information of the whole configuration of the sample. While, the latter is a surface sensitive technique that uses the chemical selectivity of X-rays to probe the first few layers of the sample, thus only providing specific moment per iron or cobalt atom from the nanoparticles located at the sample's surface. Combining these two techniques, we were able to provide a thorough analysis of our samples. In this chapter, the following results and points were addressed:

- From preliminary ZFC/FC and $m(H)$ measurements on concentrated neutral FeCo nanoparticles we were able to establish a base line where the magnetic interactions are too prominent, thus inhibiting and even preventing an accurate determination of the intrinsic properties of our nanoparticles. In addition, simulations of the possible modes of coalescence revealed that after annealing, if the nanoparticle concentration is high, a 3D type coalescence occurs in the samples resulting in ambiguities on the intrinsic magnetic properties.

- Diluted neutral reference Fe and Co, as well as bimetallic FeCo samples, provided a thorough look at the magnetic properties of our nanoparticles. The neutral Co nanoparticles provided results that are in agreement with the previous findings on the same system as reported by A. Tamion *et al*. As for the Fe and FeCo neutral nanoparticle samples, from a first glance, a clear indication of evolution is observed after annealing in both samples. However, fitting the samples gave rise to two possible models, a core-shell model made up of a magnetic inner core with a non-magnetic carbide shell, and a homogeneous model where the nanoparticle is made up of a binary (trinary) alloy: of Fe-C (FeCo-C).

- XMCD measurements were performed on mass-selected samples for all three systems (Co, Fe and FeCo). Applying the sum rules to the measured XAS spectra, we were able to extract the magnetic spin and angular moments at each chemical species for all our systems. These extracted values were significantly reduced compared to the expected bulk values thus going in favour of homogeneous nanoparticles with reduced

magnetic moments. After annealing, two regimes were identified: the iron regime, where annealing caused a diminution of the average magnetic moment per atom; and the cobalt regime, where annealing enhanced the average magnetic moment per atom. Comparing these findings to the FeCo system, we obtained for the small $FeCo_{3.7}$ nanoparticles the same trend as the iron regime at both Fe and Co edges, while the larger sizes followed the Co regime. Moreover, from structural results and XMCD measurements, one can correlate the diminution and enhancement of the average magnetic moments to the size, structure and carbon solubility of these nanoparticles. For the smallest FeCo nanoparticles, the carbon solubility is high thus the magnetic moment is low. When the size of the nanoparticles increase, the carbon solubility starts to decrease thus the average moments increase. Nevertheless, it should be noted that the nanoparticles' concentration of the XMCD samples was significantly high per layer, which was necessary to have sufficient material to give a magnetic signal. On the other hand, this increased concentration must have had similar implications as was observed on the neutral concentrated FeCo samples and thus the values obtained from XMCD should be treated as indicative tendencies for the diluted nanocluster assemblies' values.

- The SQUID investigation of the mass-selected Co, Fe and FeCo samples provided additional and conclusive information on the intrinsic properties of our cluster samples. The complete fitting of all the magnetic curves was only possible using the homogeneous model approach. The latter provided, somewhat, precise information on the intrinsic properties of the Fe and FeCo nanoparticles. The values obtained for the saturation magnetization followed a trend similar to those extrapolated from the XMCD measurements. The uncertainty of the XMCD extrapolated values as well as the difference in concentration of the samples in the two techniques makes it difficult to compare the values. As for the fitting values, in the case of FeCo, the small and medium nanoparticle samples ($FeCo_{3.7}$ and $FeCo_{4.3}$) showed similar behaviours before and after annealing with slight variations, whereas the larger $FeCo_{6.1}$ samples showed a clear evolution after annealing that can only be explained as a structural evolution from a disordered A2 phase to the chemically ordered CsCl B2 phase in agreement with EXAFS results.

To go a step further, mass-selected FeCo nanoparticles embedded in a Cu matrix were investigated. The as-prepared samples showed promising results, where in both sizes ($FeCo^{Cu}{}_{4.3}$ and $FeCo^{Cu}{}_{6.1}$) the obtained magnetic properties were enhanced compared to their carbon matrix counterparts. However, after annealing at 500°C the samples showed an unconventional evolution.

In order to understand the magnetic behaviour of the $FeCo^{Cu}{}_{6.1}$, it is necessary to recall the different structural and magnetic results obtained during this study, in order to address several questions:

1. *Why is the saturation magnetization of $FeCo^{Cu}{}_{6.1}$ in the copper matrix smaller than the expected bulk value for FeCo ($M_s = 1700$ kA/m instead of 1930 kA/m)*?

   From the different references mentioned in chapter 1 different studies have been performed on FeCo nanoparticles [40–50]. These studies gave values of saturation magnetization ranging between 1057 kA/m and 1884 kA/m which are in agreement with our obtained values of M_s. In fact, iron and cobalt have an itinerant magnetization, *i.e.* depending on its crystallographic environment it can exhibit different magnetic moment and Curie temperature. As an example, Grinstaff *et al*. studied the magnetic properties of amorphous iron and report that for 30 nm amorphous Fe nanoparticles exhibit a reduced magnetic moment of 1.6 μ_B/atom compared to the iron bulk magnetic moment of 2.2 μ_B/atom [218]. In our case, the as-prepared FeCo nanoparticles, exhibited little to almost no crystallization as found from the TEM observations (see figure 3.11). Thus, the as-prepared nanoparticles could be in a metastable poorly crystallized phase which can explain the reduced saturation magnetization of 1700 kA/m found from the magnetic moments of the $FeCo^{Cu}{}_{6.1}$ nanoparticles. Another explanation for this difference could be surface effects, where the surface atoms (which are not in the FeCo environment) could have not attained the expected increase of magnetic moment per atom of the FeCo bulk alloy.

2. *Why is the saturation magnetization of FeCo small in the nanoparticles embedded in the carbon matrix?*

   From EXAFS results all the as-prepared FeCo samples showed prominent carbon presence, evidenced by the pre-shoulder of the principal peak (see figures 3.31 and 3.32). Thus, not only are the FeCo nanoparticles in a metastable crystallized phase, but carbon diffusion into the nanoparticles further decreases the magnetic moment per atom (notably at the iron edge) and consequently the saturation magnetization which is then lower than in the copper matrix.

3. *What governs the evolution of the saturation magnetization of particles embedded in carbon matrix after annealing?*

   Concerning the evolution after annealing of our FeCo nanoparticles embedded in carbon matrix, we already established two trends. In the iron trend, annealing increases the carbon solubility, decreases the crystal order and decreases the magnetic moment

per atom, whereas in the cobalt case, annealing promotes the demixing of the carbon from the nanoparticles indicating an enhanced crystal coordination and chemical order accompanied by an increase of the magnetic moment per atom. Using these two trends it is possible to correlate the EXAFS and XMCD results. From EXAFS, or the small $FeCo_{3.7}$ nanoparticles, annealing promoted a reduced crystal coordination and order and an increase in the carbon diffusion (see figure 3.36) which can reduce the magnetic moment of the Fe and Co atoms in agreement with XMCD findings at the same size, where the magnetic moment per atom is decreased after annealing (see figure 4.22 and table 4.8). These combined findings show that indeed the $FeCo_{3.7}$ particles follow the iron trend. For the medium $FeCo_{4.3}$ nanoparticles, from EXAFS measurements carbon presence and crystal coordination and order remain almost unchanged after annealing (see figures 3.37, 3.38 and 3.39 and tables 3.16 and 3.17). The consequence on the magnetic moment can be observed from XMCD measurements were the magnetic moment remains almost unchanged after annealing (see figure 4.23 and table 4.8) and from SQUID magnetometry (see table 4.14). The combined results from structure and magnetism, suggest that for the $FeCo_{4.3}$ nanoparticle size, a competition between the iron and cobalt trends is present. As for the larger $FeCo_{6.1}$ nanoparticles, EXAFS measurements show a retraction of the carbon presence after annealing (carbon presence is limited to the vicinity of iron atoms) in addition to a remarkable enhancement of the crystal coordination and ordering (see figures 3.40, 3.41 and 3.42 and table 3.18 and 3.19). The latter is in agreement with XMCD findings of the nanoparticles of the same size, where the magnetic moment per atom (Fe and Co atoms) is enhanced after annealing (see figure 4.25 and table 4.8), following the cobalt tendency. Moreover, the magnetization does not reach the bulk value. This is due to carbon atoms still present in the crystal (see table 3.18). Thus, depending on the crystal ordering (or disordering) and depending on the carbon absence (or presence) the magnetic moment per atom increases (or decreases respectively).

4. *Why is the value of the anisotropy K_1 different in the two cases, $FeCo_{6.1}$ in carbon and $FeCo^{Cu}{}_{6.1}$?*

Finally, if we compare the K_1 anisotropy between the $FeCo_{6.1}$ and $FeCo^{Cu}{}_{6.1}$ as-prepared samples, we find $K_1 = 120 \pm 10$ kJ.m^{-3} in the carbon matrix compared to $K_1 = 240 \pm 20$ kJ.m^{-3} in the copper matrix. On the other hand, the particle's sphericity from TEM observations gave a ratio of $c/a = 1.65$, where c and a are the axis of the ellipsoid used to fit the TEM images (see table 3.5). From equation 2.26 we can

calculate the magnetostatic energy density in the case of an ellipsoid:

$$\begin{aligned} E &= \frac{1}{2}\mu_0 {M_s}^2[N_{zz}-N_{xx}]\cos^2\theta + \frac{1}{2}\mu_0 {M_s}^2[N_{yy}-N_{xx}]\sin^2\theta\sin^2\varphi \\ E &= K_1\cos^2\theta + K_2\sin^2\theta\sin^2\varphi \end{aligned} \tag{4.3}$$

where the N_{ii} are the diagonal terms of the demagnetizing tensor $\mathscr{N}$.

In the case of a spheroid (ellipsoid of revolution) , $N_{yy} = N_{xx}$ and the anisotropy is uniaxial. The calculated values of K_1 given in table 4.18:

	${K_1}^{triplefit}$ (kJ.m^{-3})	${K_1}^{shape}$ (kJ.m^{-3})
$FeCo^{Cu}{}_{6.1}$	240 ± 20	300±30
$FeCo^{C}{}_{6.1}$	120 ± 10	120±20
$FeCo^{Cu}{}_{4.3}$	210 ± 20	230±20
$FeCo^{C}{}_{4.3}$	135 ± 20	105±20

Table 4.18 Anisotropy constants obtained from the magnetic measurements and simulated values from the shape, with a c/a ratio of 1.65 for the $FeCo_{6.1}$ and 1.47 for the $FeCo_{4.3}$ as-prepared nanoparticles samples (see table 3.5).

Figure 4.49 shows the evolution of the shape anisotropy K_1 as a function of the ellipsoid c/a ratio for the two values of saturation magnetization $M_s = 1100$ kA/m and 1650 kA/m. The values obtained for the FeCo nanoparticles embedded in copper matrix are in dashed red, while the those obtained for the carbon case are in dashed back.

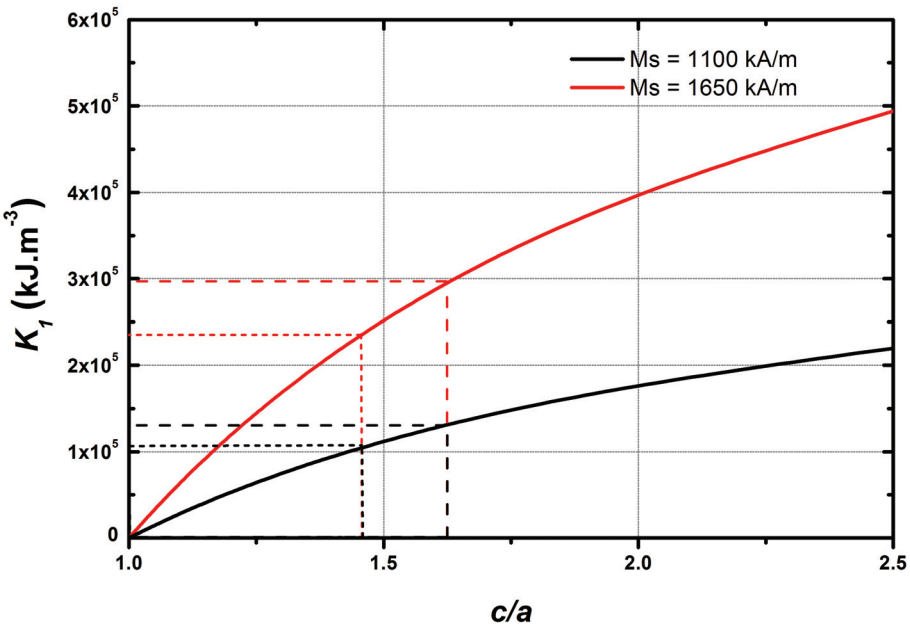

Fig. 4.49 Evolution of the shape anisotropy K_1 as a function of the ellipsoid c/a ratio for the two values of saturation magnetization $M_s = 1100$ kA/m and 1650 kA/m.

The values presented in table 4.18 from the magnetic measurements and simulated values of the shape anisotropy (see table 3.5) are in qualitative agreement. For the large as-prepared FeCo nanoparticles, it is clear that the principal contribution to the magnetic anisotropy comes from the cluster's shape. The difference in the anisotropy values can thus be attributed to a matrix effect, where the carbon matrix diffuses into the FeCo nanoparticles decreasing the magnetization and consequently the anisotropy constant whereas the copper matrix is immiscible (see figure 4.49).

On the other hand, it is not the case for the annealed clusters, where the sphericity is better and the anisotropy constant comes from the shape anisotropy in addition to supplementary facets due to the crystallization of the clusters [128].

As a perspective to this work, further investigation is needed in order to completely unravel and correlate the structural and magnetic properties of our nanoparticles as well as the matrix influence. For the latter, a dedicated study of FeCo nanoparticles embedded in different matrices is needed in order to separate the matrix influence from the nanoparticles' intrinsic properties.

General Conclusion

During this work, we were interested in directly correlating the structural and magnetic properties of our nanoclusters. We have studied the structural and magnetic properties of model systems of assemblies of non mass-selected and mass-selected FeCo nanoparticles embedded in an amorphous carbon matrix. Using the MS-LECBD (Mass Selected Low Energy Custer Beam Deposition) technique coupled to a quadrupole deviator we were able to distinctly study the size effects of our nanoparticles. In addition, thanks to an ultra-high vacuum annealing chamber, the annealing effects were also investigated.

The structural properties were probed using a wide range of complementary techniques in order to shed light on the differences between the size effects and the annealing effects. TEM in normal and high resolution modes were used to investigate the size, size dispersion, morphology and crystallographic structure of our nanoparticles. Using this technique, it was possible to obtain quantitative values for the diameter distribution. To complement the TEM technique, EDX and RBS spectroscopy were used to study the composition of our nanoparticle samples before and after annealing and to verify the equi-stoichiometry of the nanoparticles. In addition, X-ray reflectivity measurements were performed on the amorphous carbon matrix in order to control and quantify the thickness of the carbon layers.

Moreover, density functional $ab-inito$ calculations using the SIESTA code were performed in collaboration with Aguilera-Granja *et al*. where the interatomic distances of small sized FeCo nanocrystals in the B2 CsCl phase were calculated. The latter provided indispensable information in the understanding and quantification of the EXAFS spectroscopy measurements in collaboration with O. Proux. From the EXAFS, the evolution of the crystallographic structure of the different mass-selected FeCo nanoparticles was investigated. For the as-prepared clusters a disordered A2 phase structure was found for all sizes. After annealing, the small nanoparticles showed no enhancement in their structure, however, the larger $FeCo_{6.1}$ nanoparticles exhibited interesting evolution to a bcc like structure accompanied by a strong and prominent enhancement of the crystal coordination as well as evidence of ordering at both site (Fe and Co). The latter was also evidenced from AXD spectroscopy on the same larger nanoparticles. The three Bragg peaks expected for a bcc structure have

been observed. The novelty in this case was the persistence of the ordering and crystal coordination from EXAFS measurements for up to 6 Å which was never observed before for nanoparticles of this size. The same can be said about the anomalous diffraction peaks where for this size range (2-6 nm) only the first Bragg peak is typically observed.

Furthermore, the carbon environment was investigated using the EXAFS measurements and showed the presence of an iron-carbide in the as-prepared nanoparticles that remained after annealing for the smaller nanoparticles. For the large $FeCo_{6.1}$ nanoparticles, annealing inhibited the carbide formation.

Concerning the magnetic properties, SQUID magnetometry and XMCD spectroscopy (in collaboration with P. Ohresser) measurements were used to investigate the intrinsic magnetic properties of our nanoparticle assemblies. The latter was used to determine the evolution of the magnetic moment per atom at both the Fe and Co sites. An interesting evolution was observed where the magnetic moment per atom increased with size and also after annealing. SQUID magnetometry provided conclusive information about the intrinsic properties of our nanoparticles. Most of the samples exhibited negligible magnetic interactions which allow the use of the Stoner-Wohlfarth model to simulate and fit the different obtained magnetization curves. In addition, using the size and size dispersion obtained from TEM observations and the magnetic moments obtained from XMCD spectroscopy it was possible to obtain coherent and consistent results and fits. The magnetic anisotropy constant showed almost no evolution with size in the as-prepared nanoparticles, while the annealed nanoparticles exhibited a slight enhancement of the magnetic properties, except in the case of the $FeCo_{6.1}$ nanoparticles where a prominent enhancement of the anisotropy was observed.

The results of both structure and magnetism are in agreement for almost all sizes. Nevertheless, further investigation is necessary to separate the intrinsic properties of our nanoparticles from the additional matrix effects. Carbon diffusion in the nanoparticle proved to be a challenge to inhibit and lead to unforeseen reduction of the magnetic moments and the particles' crystallographic coordination and order. For the bimetallic FeCo nanoparticles, we identified two trends after annealing: the pure iron trend and the pure cobalt one. After annealing, the iron trend consists of an increase of the carbon diffusion into the nanoparticle's core accompanied by a reduction of the crystal ordering as well as a decrease of the magnetic moment per atom. Whereas, the cobalt trend shows an opposing response due to annealing, where carbon diffusion is inhibited and even a demixing process of carbon and nanoparticle takes place accompanied by an enhancement of the crystal ordering and an increase of the magnetic moment per atom.

Applying these observations to our mass-selected FeCo samples showed that the small sized $FeCo_{3.7}$ nanoparticles followed the iron trend after annealing whereas the largest

$FeCo_{6.1}$ nanoparticles followed the cobalt one. Meanwhile, the medium sized $FeCo_{4.3}$ nanoparticles remained almost unchanged after annealing likely due to a competition between the two trends.

As a perspective, studying the properties of our FeCo nanoparticles embedded in a different matrix than carbon is necessary. Initiative work, concerning the latter, was already underway before the end of this PhD work where the magnetic properties of mass-selected FeCo nanoparticles embedded in a copper matrix were studied using SQUID magnetometry. The nanoparticles embedded in the copper matrix showed enhanced magnetization (M_s) compared to their carbon matrix counterparts and close to the bulk FeCo value.

REFERENCES

[1] D. A. Thompson and J. S. Best, "The future of magnetic data storage techology," *IBM Journal of Research and Development*, vol. 44, no. 3, pp. 311–322, 2000.

[2] B. D. Terris and T. Thomson, "Nanofabricated and self-assembled magnetic structures as data storage media," *Journal of Physics D: Applied Physics*, vol. 38, no. 12, pp. R199–R222, 2005.

[3] "Magnetic nanoparticles: synthesis, functionalization, and applications in bioimaging and magnetic energy storage.," *Chemical Society reviews*, vol. 38, no. 9, pp. 2532–2542, 2009.

[4] A. H. Lu, E. L. Salabas, and F. Schüth, "Magnetic nanoparticles: Synthesis, protection, functionalization, and application," *Angewandte Chemie - International Edition*, vol. 46, no. 8, pp. 1222–1244, 2007.

[5] I. Koh and L. Josephson, "Magnetic Nanoparticle Sensors," *Sensors*, vol. 9, no. 10, pp. 8130–8145, 2009.

[6] M. Colombo, S. Carregal-Romero, M. F. Casula, L. Gutiérrez, M. P. Morales, I. B. Böhm, J. T. Heverhagen, D. Prosperi, and W. J. Parak, "Biological applications of magnetic nanoparticles," *Chemical Society Reviews*, vol. 41, no. 11, p. 4306, 2012.

[7] S. Singamaneni, V. N. Bliznyuk, C. Binek, and E. Y. Tsymbal, "Magnetic nanoparticles: recent advances in synthesis, self-assembly and applications," *Journal of Materials Chemistry*, vol. 21, no. 42, p. 16819, 2011.

[8] M. Arruebo, R. Fernández-Pacheco, M. R. Ibarra, and J. Santamaría, "Magnetic nanoparticles for drug delivery," *Nano Today*, vol. 2, no. 3, pp. 22–32, 2007.

[9] D. Kami, S. Takeda, Y. Itakura, S. Gojo, M. Watanabe, and M. Toyoda, "Application of magnetic nanoparticles to gene delivery," *International Journal of Molecular Sciences*, vol. 12, no. 6, pp. 3705–3722, 2011.

[10] D. Maity, G. Zoppellaro, V. Sedenkova, J. Tucek, K. Safarova, K. Polakova, K. Tomankova, C. Diwoky, R. Stollberger, L. Machala, and R. Zboril, "Surface design of core–shell superparamagnetic iron oxide nanoparticles drives record relaxivity values in functional MRI contrast agents," *Chemical Communications*, vol. 48, no. 93, p. 11398, 2012.

[11] F. Gazeau, M. Lévy, and C. Wilhelm, "Optimizing magnetic nanoparticle design for nanothermotherapy.," *Nanomedicine (London, England)*, vol. 3, no. 6, pp. 831–844, 2008.

[12] A. G. Kolhatkar, A. C. Jamison, D. Litvinov, R. C. Willson, and T. R. Lee, "Tuning the magnetic properties of nanoparticles," *International Journal of Molecular Sciences*, vol. 14, no. 8, pp. 15977–16009, 2013.

[13] C.-W. Chen, *Magnetism and Metallurgy of Soft Magnetic Materials*. Amsterdam: North-Holland Publishing Company, 1977.

[14] R. M. Bozorth, *Ferromagnetism*. D. Van Nostrand Company, Inc., Princeton, New Jersey, 1951.

[15] G. E. Fish, "Soft magnetic materials," *Proceedings of the IEEE*, vol. 78, no. 6, pp. 947–972, 1990.

[16] I. Ohnuma, H. Enoki, O. Ikeda, R. Kainuma, H. Ohtani, B. Sundman, and K. Ishida, "Phase equilibria in the Fe-Co binary system," *Acta Materialia*, vol. 50, pp. 379–393, 2002.

[17] G. V. Raynor and V. G. Rivlin, "10: Critical evaluation of constitution of cobalt-iron-vanadium system," *International Metals Reviews*, vol. 28, no. 1, pp. 211–227, 1983.

[18] S. Kaya and H. Sato, "Superstructuring in the iron–cobalt system and their magnetic properties," *Proc. Phys. Math. Soc. Japan*, vol. 25, p. 261, 1943.

[19] J. M. Cowley, "An approximate theory of order in alloys," *Physical Review*, vol. 77, no. 5, pp. 669–675, 1950.

[20] G. Dienes, "Kinetics of order-disorder transformations," *Acta Metallurgica*, vol. 3, no. 6, pp. 549–557, 1955.

[21] N. Stoloff and R. Davies, "The plastic deformation of ordered FeCo and Fe3 Al alloys," *Acta Metallurgica*, vol. 12, no. 5, pp. 473–485, 1964.

[22] A. W. Smith and R. D. Rawlings, "A neutron diffraction study of ordering in an iron–cobalt–1.8% vanadium alloy," *physica status solidi (a)*, vol. 34, no. 1, pp. 117–123, 1976.

[23] C. E. Johnson, M. S. Ridout, and T. E. Cranshaw, "Nano-Scale Materials Development for Future Magnetic Applications," *Proceedings of the Physical Society*, vol. 81, p. 1079, 1963.

[24] M. F. Collins and J. B. Forsyth, "The Magnetic Moment Distribution in some Transition Metal Alloys," *Philosophical Magazine*, vol. 8, pp. 401–410, 1963.

[25] D. I. Bardos, "Mean Magnetic Moments in bcc *FeCo* Alloys," *Journal of Applied Physics*, vol. 40, p. 1371, 1969.

[26] A. Diaz-Ortiz, R. Drautz, M. F. H., Dosch, and J. Sanchez, "Structure and magnetism in bcc-based iron-cobalt alloys," *Physical Review B*, vol. 73, p. 224208, 2006.

[27] T. Burkert, L. Nordström, O. Eriksson, and O. Heinonen, "Giant magnetic anisotropy in tetragonal FeCo alloys," *Physical Review Letters*, vol. 93, no. 2, p. 027203, 2004.

[28] I. Turek, J. Kudrnovský, and K. Carva, "Magnetic anisotropy energy of disordered tetragonal Fe-Co systems from ab initio alloy theory," *Physical Review B*, vol. 86, p. 174430, 2012.

[29] D. Weller, A. Moser, L. Folks, M. E. Best, W. Lee, M. F. Toney, M. Schwickert, J.-u. Thiele, and M. F. Doerner, "High K u Materials Approach to 100 Gbits / in 2," *IEEE Transactions on Magnetics*, vol. 36, no. 1, pp. 10–15, 2000.

[30] S. Charap, P.-L. L. P.-L. Lu, and Y. H. Y. He, "Thermal stability of recorded information at high densities," *IEEE Transactions on Magnetics*, vol. 33, no. 1, pp. 978–983, 1997.

[31] a. M. Begley, S. K. Kim, F. Jona, and P. M. Marcus, "Growth mode and atomic structure of ultrathin Fe films on Rh{001} determined by quantitative low-energy electron diffraction," *Physical Review B*, vol. 48, no. 3, pp. 1786–1793, 1993.

[32] A. Begley, S. Kim, F. Jona, and P. Marcus, "Low-energy electron diffraction study of the growth of ultrathin films of face-centred cubic Co on Rh(001)," *Journal of Physics: Condensed Matter*, vol. 5, no. 40, pp. 7307–7318, 1993.

[33] J. Quinn, Y. Li, H. Li, D. Tian, F. Jona, and P. Marcus, "Atomic and electronic structure of Fe films grown on Pd {001}," *Physical Review B*, vol. 43, no. 5, pp. 3959–3968, 1991.

[34] H. Giordano, A. Atrei, M. Torrini, U. Bardi, M. Gleeson, and C. Barnes, "Evidence for a strain-stabilized bct phase of cobalt deposited on Pd{100}: An x-ray photoelectron diffraction study," *Physical Review B*, vol. 54, no. 16, pp. 11762–11768, 1996.

[35] N. X. Sun, S. Mehdizadeh, C. Bonhote, Q. F. Xiao, and B. York, "Magnetic annealing of plated high saturation magnetization soft magnetic FeCo alloy films," *Journal of Applied Physics*, vol. 97, pp. 2005–2007, 2005.

[36] E. K. Delczeg-Czirjak, a. Edström, M. Werwiński, J. Rusz, N. V. Skorodumova, L. Vitos, and O. Eriksson, "Stabilization of the tetragonal distortion of Fe_xCo_{1-x} alloys by C impurities: A potential new permanent magnet," *Physical Review B*, vol. 89, p. 144403, 2014.

[37] E. W. Soo, T. J. Zhou, and J. P. Wang, "FeCoC film as the soft magnetic underlayer for perpendicular media," *Journal of Applied Physics*, vol. 91, pp. 8019–8021, 2002.

[38] V. Edon, S. Dubourg, J. Vernières, and J. F. Bobo, "Magnetic properties of FeCoC thin films prepared by various sputtering methods," *Journal of Physics: Conference Series*, vol. 303, p. 012094, 2011.

[39] S. Gautam, S. N. Kane, B. G. Park, J. Y. Kim, L. K. Varga, J. H. Song, and K. H. Chae, "XAS and XMCD studies of amorphous FeCo-based ribbons," *Journal of Non-Crystalline Solids*, vol. 357, no. 11-13, pp. 2228–2231, 2011.

[40] C. W. Kim, Y. H. Kim, H. G. Cha, D. K. Lee, and Y. S. Kang, "Synthesis and characterization of crystalline FeCo nanoparticles.," *Journal of nanoscience and nanotechnology*, vol. 6, no. 11, pp. 3417–3421, 2006.

[41] S. J. Shin, Y. H. Kim, C. W. Kim, H. G. Cha, Y. J. Kim, and Y. S. Kang, "Preparation of magnetic FeCo nanoparticles by coprecipitation route," *Current Applied Physics*, vol. 7, no. 4, pp. 404–408, 2007.

[42] G. S. Chaubey, C. Barcena, N. Poudyal, C. Rong, J. Gao, S. Sun, and J. P. Liu, "Synthesis and stabilization of FeCo nanoparticles," *Journal of the American Chemical Society*, vol. 129, pp. 7214–7215, 2007.

[43] L. M. Lacroix, R. B. Malaki, J. Carrey, S. Lachaize, M. Respaud, G. F. Goya, and B. Chaudret, "Magnetic hyperthermia in single-domain monodisperse FeCo nanoparticles: Evidences for Stoner-Wohlfarth behavior and large losses," *Journal of Applied Physics*, vol. 105, no. 2, 2009.

[44] C. Desvaux, F. Dumestre, C. Amiens, M. Respaud, P. Lecante, E. Snoeck, P. Fejes, P. Renaud, and B. Chaudret, "FeCo nanoparticles from an organometallic approach: synthesis, organisation and physical properties," *Journal of Materials Chemistry*, vol. 19, no. 20, p. 3268, 2009.

[45] S. J. Lee, J.-H. Cho, C. Lee, J. Cho, Y.-R. Kim, and J. K. Park, "Synthesis of highly magnetic graphite-encapsulated FeCo nanoparticles using a hydrothermal process.," *Nanotechnology*, vol. 22, no. 37, p. 375603, 2011.

[46] N. Poudyal, G. S. Chaubey, C.-B. Rong, J. Cui, and J. P. Liu, "Synthesis of monodisperse FeCo nanoparticles by reductive salt-matrix annealing.," *Nanotechnology*, vol. 24, no. 34, p. 345605, 2013.

[47] X. Dong, Z. Zhang, Y. Chuang, and S. Jin, "Characterization of ultrafine Fe-Co particles and Fe-Co(C) nanocapsules," *Physical Review B*, vol. 60, no. 5, pp. 3017–3020, 1999.

[48] Happy, S. R. Mohanty, P. Lee, T. L. Tan, S. V. Springham, A. Patran, R. V. Ramanujan, and R. S. Rawat, "Effect of deposition parameters on morphology and size of FeCo nanoparticles synthesized by pulsed laser ablation deposition," *Applied Surface Science*, vol. 252, no. 8, pp. 2806–2816, 2006.

[49] P. L. Ong, S. Mahmood, T. Zhang, J. J. Lin, R. V. Ramanujan, P. Lee, and R. S. Rawat, "Synthesis of FeCo nanoparticles by pulsed laser deposition in a diffusion cloud chamber," *Applied Surface Science*, vol. 254, no. 7, pp. 1909–1914, 2008.

[50] A. Kleibert, F. Bulut, R. K. Gebhardt, W. Rosellen, D. Sudfeld, J. Passig, J. Bansmann, K. H. Meiwes-Broer, and M. Getzlaff, "Correlation of shape and magnetic anisotropy of supported mass-filtered Fe and FeCo alloy nanoparticles on W(110)," *Journal of Physics: Condensed Matter*, vol. 20, no. 44, p. 445005, 2008.

[51] V. L. Kuznetsov, D. V. Krasnikov, A. N. Schmakov, and K. V. Elumeeva, "In situ and ex situ time resolved study of multi-component Fe-Co oxide catalyst activation during MWNT synthesis," *Physica Status Solidi (B) Basic Research*, vol. 249, no. 12, pp. 2390–2394, 2012.

[52] D. Hardeman, S. Esconjauregui, R. Cartwright, S. Bhardwaj, L. D'Arsié, D. Oakes, J. Clark, C. Cepek, C. Ducati, and J. Robertson, "The synergistic effect in the Fe-Co bimetallic catalyst system for the growth of carbon nanotube forests," *Journal of Applied Physics*, vol. 117, no. 4, p. 044308, 2015.

[53] M. Diarra, a. Zappelli, H. Amara, F. Ducastelle, and C. Bichara, "Importance of carbon solubility and wetting properties of nickel nanoparticles for single wall nanotube growth," *Physical Review Letters*, vol. 109, no. 18, p. 185501, 2012.

[54] M. Diarra, H. Amara, F. Ducastelle, and C. Bichara, "Carbon solubility in nickel nanoparticles: A grand canonical Monte Carlo study," *Physica Status Solidi (B)*, vol. 249, no. 12, pp. 2629–2634, 2012.

[55] Y. Magnin, A. Zappelli, H. Amara, F. Ducastelle, and C. Bichara, "Size dependent phase diagrams of Nickel-Carbon nanoparticles," submitted 2015.

[56] S. Mazzucco, Y. Wang, M. Tanase, M. Picher, K. Li, Z. Wu, S. Irle, and R. Sharma, "Direct evidence of active and inactive phases of Fe catalyst nanoparticles for carbon nanotube formation," *Journal of Catalysis*, vol. 319, pp. 54–60, 2014.

[57] D. E. Powers, S. G. Hansen, M. E. Geusic, A. C. Puiu, J. B. Hopkins, T. G. Dietz, M. A. Duncan, P. R. R. Langridge-Smith, and R. E. Smalley, "Supersonic metal cluster beams: laser photoionization studies of copper cluster (Cu2)," *The Journal of Physical Chemistry*, vol. 86, no. 14, pp. 2556–2560, 1982.

[58] P. Milani and W. A. DeHeer, "Improved pulsed laser vaporization source for production of intense beams of neutral and ionized clusters," *Review of Scientific Instruments*, vol. 61, no. 7, p. 1835, 1990.

[59] M. Pellarin, E. Cottancin, J. Lermé, J. L. Vialle, J. P. Wolf, M. Broyer, V. Paillard, V. Dupuis, A. Perez, J. P. Perez, J. Tuaillon-Combes, and P. Melinon, "High-efficiency cluster laser vaporization sources based on Ti: sapphire lasers," *Chemical Physics Letters*, vol. 224, no. 3, pp. 338–344, 1994.

[60] R. Alayan, L. Arnaud, A. Bourgey, M. Broyer, E. Cottancin, J. R. Huntzinger, J. Lermé, J. L. Vialle, M. Pellarin, and G. Guiraud, "Application of a static quadrupole deviator to the deposition of size-selected cluster ions from a laser vaporization source," *Review of Scientific Instruments*, vol. 75, pp. 2461–2470, 2004.

[61] A. Perez, V. Dupuis, J. Tuaillon-Combes, L. Bardotti, B. Prével, E. Bernstein, P. Mélinon, L. Favre, A. Hannour, and M. Jamet, "Functionalized cluster-assembled magnetic nanostructures for applications to high integration-density devices," *Advanced Engineering Materials*, vol. 7, pp. 475–485, 2005.

[62] R. Alayan, L. Arnaud, M. Broyer, E. Cottancin, J. Lermé, J. Vialle, and M. Pellarin, "Morphology and growth of metal clusters in the gas phase: A transition from spherical to ramified structures," *Physical Review B*, vol. 73, p. 125444, 2006.

[63] C. A. Schneider, W. S. Rasband, and K. W. Eliceiri, "Nih image to imagej: 25 years of image analysis," *Nature Methods*, vol. 9, no. 7, pp. 671–675, 2012.

[64] G. Cliff and G. W. Lorimer, "The quantitative analysis of thin specimens," *Journal of Microscopy*, vol. 103, pp. 203–207, 1975.

[65] M. Mayer, "SimNRA, a simulation program for the analysis of NRA, RBS and ERDA," *AIP Conference Proceedings*, vol. 475, pp. 541–544, 1999.

[66] G. Mülhaupt and R. Rüffer, "Properties of synchrotron radiation," *Hyperfine Interactions*, vol. 123-124, no. 1-4, pp. 13–30, 1999.

[67] B. K. Teo, *EXAFS: basic principles and data analysis*. Inorganic chemistry concepts, Springer-Verlag, 1986.

[68] B. Ravel and M. Newville, "ATHENA, ARTEMIS, HEPHAESTUS: Data analysis for X-ray absorption spectroscopy using IFEFFIT," *Journal of Synchrotron Radiation*, vol. 12, pp. 537–541, 2005.

[69] B. Ravel, "ATOMS: Crystallography for the X-ray absorption spectroscopist," *Journal of Synchrotron Radiation*, vol. 8, pp. 314–316, 2001.

[70] M. Newville, "IFEFFIT: Interactive XAFS analysis and FEFF fitting," *Journal of Synchrotron Radiation*, vol. 8, pp. 322–324, 2001.

[71] B. Ravel, "The athena users' guide." http://bruceravel.github.io/demeter/aug/index.html, 2015.

[72] B. Ravel, "The artemis users' guide." http://bruceravel.github.io/demeter/artug/index.html, 2015.

[73] S. Zabinsky, J. Rehr, A. Ankudinov, R. Albers, and M. Eller, "Multiple-scattering calculations of X-ray absorption spectra," *Physical Review B*, vol. 52, pp. 2995–3009, 1995.

[74] C. R. Natoli, D. K. Misemer, S. Doniach, and F. W. Kutzler, "First-principles calculation of x-ray absorption-edge structure in molecular clusters," *Physical Review A*, vol. 22, pp. 1104–1108, 1980.

[75] D. E. Sayers, E. A. Stern, and F. W. Lytle, "New technique for investigating noncrystalline structures: Fourier analysis of the extended x-ray-absorption fine structure," *Physical Review Letters*, vol. 27, pp. 1204–1207, 1971.

[76] A. Ankudinov, C. Bouldin, J. Rehr, J. Sims, and H. Hung, "Parallel calculation of electron multiple scattering using Lanczos algorithms," *Physical Review B*, vol. 65, 2002.

[77] A. Hillion, A. Cavallin, S. Vlaic, A. Tamion, F. Tournus, G. Khadra, J. Dreiser, C. Piamonteze, F. Nolting, S. Rusponi, K. Sato, T. J. Konno, O. Proux, V. Dupuis, and H. Brune, "Low temperature ferromagnetism in chemically ordered FeRh nanocrystals," *Physical Review Letters*, vol. 110, no. February, p. 087207, 2013.

[78] K. V. Klementev, "Extraction of the fine structure from x-ray absorption spectra," *Journal of Physics D: Applied Physics*, vol. 34, pp. 209–217, 2000.

[79] J. Stöhr, "Exploring the microscopic origin of magnetic anisotropies with X-ray magnetic circular dichroism (XMCD) spectroscopy," *Journal of Magnetism and Magnetic Materials*, vol. 200, no. 1–3, pp. 470–497, 1999.

[80] M. Sacchi and J. Vogel, *Magnetism and Synchrotron Radiation, Lecture Notes in Physics*, vol. 565. Springer Verlag, 2001.

[81] H. Wende, "Recent advances in x-ray absorption spectroscopy," *Reports on Progress in Physics*, vol. 67, no. 12, pp. 2105–2181, 2004.

[82] W. Kuch, "X-ray Magnetic Circular Dichroism for Quantitative Element-Resolved Magnetic Microscopy," *Physica Scripta*, vol. T109, p. 89, 2004.

[83] C. M. Schneider and G. Schönhense, "Investigating surface magnetism by means of photoexcitation electron emission microscopy," *Reports on Progress in Physics*, vol. 65, no. 12, pp. 1785–1839, 2002.

[84] G. Schtz, W. Wagner, W. Wilhelm, P. Kienle, R. Zeller, R. Frahm, and G. Materlik, "Absorption of circularly polarized x rays in iron," *Physical Review Letters*, vol. 58, pp. 737–740, 1987.

[85] P. Carra, B. Thole, M. Altarelli, and X. Wang, "X-ray circular dichroism and local magnetic fields," *Physical Review Letters*, vol. 70, pp. 694–697, 1993.

[86] B. Thole, P. Carra, F. Sette, and G. Van der Laan, "X-Ray Circular-Dichroism as a Probe of Orbital Magnetization," *Physical Review Letters*, vol. 68, pp. 1943–1946, 1992.

[87] Y. Wu, J. Stöhr, B. D. Hermsmeier, M. G. Samant, and D. Weller, "Enhanced orbital magnetic moment on Co atoms in Co/Pd multilayers: A magnetic circular x-ray dichroism study," *Physical Review Letters*, vol. 69, pp. 2307–2310, 1992.

[88] C. Chen, Y. Idzerda, H.-J. Lin, N. Smith, G. Meigs, E. Chaban, G. Ho, E. Pellegrin, and F. Sette, "Experimental confirmation of the X-ray magnetic circular dichroism sum rules for iron and cobalt.," *Physical review letters*, vol. 75, no. 1, pp. 152–155, 1995.

[89] G. Friedel, "Anisotropy in FeCo nanoparticles , a first step," *Comptes Rendus*, vol. 157, pp. 1533–1536, 1913.

[90] D. Coster, K. Knol, and J. Prins *Zeitschrift für Physik*, vol. 63, no. 5-6, pp. 345–369, 1930.

[91] P. Debye, "Zerstreuung von Röntgenstrahlen," *Annalen der Physik*, vol. 351, no. 6, pp. 809–823, 1915.

[92] N. Blanc, *Caractérisation structurale et magnétique de nanoparticules de CoPt : mise en évidence de la transition de phase A_1 vers $L1_0$*. PhD thesis, 2009.

[93] QD, "MPMS XL Specifications." http://www.qdusa.com/sitedocs/productBrochures/1014-003.pdf, 2014.

[94] J. Gallop, "SQUIDs, the Josephson effects and measurement," *Measurement Science and Technology*, vol. 2, pp. 485–496, 1999.

[95] O. Lounasmaa, *Experimental Principles and Methods Below 1K*. London: Academic Press, 1974.

[96] D. A. Allwood, G. Xiong, C. C. Faulkner, D. Atkinson, D. Petit, and R. P. Cowburn, "Magnetic domain-wall logic," *Science*, vol. 309, no. 5741, pp. 1688–1692, 2005.

[97] R. Vajtai, *Springer Handbook of Nanomaterials*. Springer Science & Business Media, 2013.

[98] R. Skomski and J. M. D. Coey, *Permanent magnetism*. Institute of Physics Pub., 1999.

[99] E. Stoner and E. Wohlfarth, "A mechanism of magnetic hysteresis in heteresis in heterogeneous alloys," *Phil. Trans. Roy. Soc.*, vol. A-240, pp. 599–642, 1948.

[100] C. Tannous and J. Gieraltowski, "The Stoner-Wohlfarth model of ferromagnetism," *European Journal of Physics*, vol. 29, no. 3, p. 475, 2008.

[101] L. Néel, "Influence des fluctuations thermiques sur laimantation de grains ferromagnetiques tres fins," *Comptes Rendus Hebdomadaires Des Seances De L Academie Des Sciences*, vol. 228, no. 8, pp. 664–666, 1949.

[102] W. F. Brown, "Thermal fluctuations of a single-domain particle," *Physical Review*, vol. 130, pp. 1677–1686, 1963.

[103] J. L. Dormann, "Le phénoméne de superparamagnétisme," *Revue de Physique Appliquee*, vol. 16, no. 6, pp. 275–301, 1981.

[104] W. Wernsdorfer, E. Orozco, K. Hasselbach, A. Benoit, B. Barbara, N. Demoncy, A. Loiseau, H. Pascard, and D. Mailly, "Experimental Evidence of the Néel-Brown Model of Magnetization Reversal," *Physical Review Letters*, vol. 78, no. 2, pp. 1791–1794, 1997.

[105] F. Tournus and A. Tamion, "Magnetic susceptibility curves of a nanoparticle assembly II. Simulation and analysis of ZFC/FC curves in the case of a magnetic anisotropy energy distribution," *Journal of Magnetism and Magnetic Materials*, vol. 323, pp. 1118–1127, 2011.

[106] P. Bruno and C. Chappert, "Ruderman-Kittel theory of oscillatory interlayer exchange coupling," *Physical Review B*, vol. 46, pp. 261–270, 1992.

[107] S. S. P. Parkin, N. More, and K. P. Roche, "Oscillations in exchange coupling and magnetoresistance in metallic superlattice structures: Co/Ru, Co/Cr, and Fe/Cr," *Physical Review Letters*, vol. 64, pp. 2304–2307, 1990.

[108] H. Kramers, "L'interaction Entre les Atomes Magnétogènes dans un Cristal Paramagnétique," *Physica*, vol. 1, no. 1-6, pp. 182–192, 1934.

[109] R. Chantrell, J. Popplewell, and S. Charles, "Measurements of particle size distribution parameters in ferrofluids," *IEEE Transactions on Magnetics*, vol. 14, 1978.

[110] C. Binns, K. N. Trohidou, J. Bansmann, S. H. Baker, J. A. Blackman, J.-P. Bucher, D. Kechrakos, A. Kleibert, S. Louch, K.-H. Meiwes-Broer, G. M. Pastor, A. Perez, and Y. Xie, "The behaviour of nanostructured magnetic materials produced by depositing gas-phase nanoparticles," *Journal of Physics D: Applied Physics*, vol. 38, no. 22, p. R357, 2005.

[111] D. Babonneau, G. Abadias, J. Toudert, T. Girardeau, E. Fonda, J. S. Micha, and F. Petroff, "Effects of thermal annealing on C/FePt granular multilayers: in situ and ex situ studies," *Journal of Physics: Condensed Matter*, vol. 20, no. 3, p. 35218, 2008.

[112] A. Tamion, M. Hillenkamp, F. Tournus, E. Bonet, and V. Dupuis, "Accurate determination of the magnetic anisotropy in cluster-assembled nanostructures," *Applied Physics Letters*, vol. 95, p. 062503, 2009.

[113] F. Tournus and A. Tamion, "Comment on "Determining magnetic nanoparticle size distributions from thermomagnetic measurements" [Appl. Phys. Lett. 96, 222506 (2010)]," *Applied Physics Letters*, vol. 98, no. 21, p. 216102, 2011.

[114] R. W. Chantrell and E. P. Wohlfarth, "Rate Dependence of the Field-Cooled Magnetisation of a Fine Particle System," *Physica Status Solidi (A)*, vol. 91, no. 2, pp. 619–626, 1985.

[115] J.-O. Andersson, C. Djurberg, T. Jonsson, P. Svedlindh, and P. Nordblad, "Monte Carlo studies of the dynamics of an interacting monodispersive magnetic-particle system," *Physical Review B*, vol. 56, pp. 13983–13988, 1997.

[116] R. W. Chantrell, N. Walmsley, J. Gore, and M. Maylin, "Calculations of the susceptibility of interacting superparamagnetic particles," *Physical Review B*, vol. 63, no. 2, p. 24410, 2000.

[117] M. A. Chuev, "Generalized Stoner-Wohlfarth model and the non-langevin magnetism of single-domain particles," *Jounal of Experimental and Theoretical Physics Letters*, vol. 85, no. 12, pp. 611–616, 2007.

[118] Z. Mao, D. Chen, and Z. He, "Equilibrium magnetic properties of dipolar interacting ferromagnetic nanoparticles," *Journal of Magnetism and Magnetic Materials*, vol. 320, pp. 2335–2338, 2008.

[119] A. A. Timopheev, V. M. Kalita, and S. M. Ryabchenko, "Simulation of the magnetization reversal of an ensemble of single-domain particles in measurements with a continuous sweep of the magnetic field or temperature," *Low Temperature Physics*, vol. 34, pp. 446–457, 2008.

[120] Y. L. Raikher and V. I. Stepanov, "Magnetization of a superparamagnet measured under temperature-sweep in zero and field cooled states," *Journal of Magnetism and Magnetic Materials*, vol. 316, pp. 348–350, 2007.

[121] F. Tournus and E. Bonet, "Magnetic susceptibility curves of a nanoparticle assembly, I: Theoretical model and analytical expressions for a single magnetic anisotropy energy," *Journal of Magnetism and Magnetic Materials*, vol. 323, pp. 1109–1117, 2011.

[122] R. W. Chantrell, M. El-Hilo, and K. O'Grady, "Spin-glass behavior in a fine particle system," *IEEE Transactions on Magnetics*, vol. 27, pp. 3570–3578, 1991.

[123] C. Antoniak, J. Lindner, and M. Farle, "Magnetic anisotropy and its temperature dependence in iron-rich Fe_xPt_{1-x} nanoparticles," *EuroPhysics Letters*, vol. 70, pp. 250–256, 2005.

[124] H. T. Yang, D. Hasegawa, M. Takahashi, and T. Ogawa, "Achieving a noninteracting magnetic nanoparticle system through direct control of interparticle spacing," *Applied Physics Letters*, vol. 94, no. 1, pp. –, 2009.

[125] H. Pfeiffer and R. Chantrell, "Zero-field-cooled magnetization and initial susceptibility of magnetic particle systems," *Journal of Magnetism and Magnetic Materials*, vol. 120, pp. 203–205, 1993.

[126] M. Respaud, J. M. Broto, H. Rakoto, A. R. Fert, L. Thomas, B. Barbara, M. Verelst, E. Snoeck, P. Lecante, A. Mosset, J. Osuna, T. O. Ely, C. Amiens, and B. Chaudret, "Surface effects on the magnetic properties of ultrafine cobalt particles," *Physical Review B*, vol. 57, no. 5, pp. 2925–2935, 1998.

[127] S. Rohart, C. Raufast, L. Favre, E. Bernstein, E. Bonet, and V. Dupuis, "Magnetic anisotropy of Cox Pt1-x clusters embedded in a matrix: Influences of the cluster chemical composition and the matrix nature," *Physical Review B*, vol. 74, p. 104408, 2006.

[128] M. Jamet, W. Wernsdorfer, C. Thirion, D. Mailly, V. Dupuis, P. Mélinon, and A. Pérez, "Magnetic anisotropy of a single cobalt nanocluster," *Physical Review Letters*, vol. 86, no. 111, pp. 4676–4679, 2001.

[129] V. Franco and A. Conde, "Thermal effects in a Stoner-Wohlfarth model and their influence on magnetic anisotropy determination," *Journal of Magnetism and Magnetic Materials*, vol. 278, pp. 28–38, 2004.

[130] J. García-Otero, A. García-Bastida, and J. Rivas, "Influence of temperature on the coercive field of non-interacting fine magnetic particles," *Journal of Magnetism and Magnetic Materials*, vol. 189, pp. 377–383, 1998.

[131] H. Pfeiffer, "Determination of anisotropy field distribution in particles assemblies taking into account thermal fluctuations," *Physica Status Solidi (a)*, vol. 118, pp. 295–306, 1990.

[132] R. W. Chantrell, D. Weller, T. J. Klemmer, S. Sun, and E. E. Fullerton, "Model of the magnetic properties of FePt granular media," *Journal of Applied Physics*, vol. 91, pp. 6866–6868, 2002.

[133] C. E. Johnson and W. F. Brown, "Theoretical Magnetization Curves for Particles with Cubic Anisotropy," *Journal of Applied Physics*, vol. 32, no. 3, 1961.

[134] A. Thiaville, "Extensions of the geometric solution of the two dimensional coherent magnetization rotation model," *Journal of Magnetism and Magnetic Materials*, vol. 182, no. 1-2, pp. 5–18, 1998.

[135] A. Thiaville, "Coherent rotation of magnetization in three dimensions: A geometrical approach," *Physical Review B*, vol. 61, no. 18, pp. 12221–12232, 2000.

[136] R. H. Victoria, "Predicted time dependence of the switching field for magnetic materials," *Physical Review Letters*, vol. 63, no. 4, pp. 457–460, 1989.

[137] J. García-Otero, M. Porto, J. Rivas, and A. Bundle, "Influence of dipolar interaction on magnetic properties of ultrafine ferromagnetic particles," *Physical Review Letters*, vol. 84, pp. 167–170, 2000.

[138] N. A. Usov and Y. B. Grebenshchikov, "Hysteresis loops of an assembly of superparamagnetic nanoparticles with uniaxial anisotropy," *Journal of Applied Physics*, vol. 106, no. 2, p. 023917, 2009.

[139] J. Garcia-Otero, M. Porto, and J. Rivas, "Henkel plots of single-domain ferromagnetic nanoparticles," *Journal of Applied Physics*, vol. 87, no. 10, p. 7376, 2000.

[140] O. Hellwig, A. Berger, T. Thomson, E. Dobisz, Z. Z. Bandic, H. Yang, D. S. Kercher, and E. E. Fullerton, "Separating dipolar broadening from the intrinsic switching field distribution in perpendicular patterned media," *Applied Physics Letters*, vol. 90, no. 16, 2007.

[141] S. A. Majetich and M. Sachan, "Magnetostatic interactions in magnetic nanoparticle assemblies: energy, time and length scales," *Journal of Physics D: Applied Physics*, vol. 39, no. 21, pp. R407–R422, 2006.

[142] P. I. Mayo, K. O'Grady, P. E. Kelly, J. Cambridge, I. L. Sanders, T. Yogi, and R. W. Chantrell, "A magnetic evaluation of interaction and noise characteristics of CoNiCr thin films," *Journal of Applied Physics*, vol. 69, no. 8, pp. 4733–4735, 1991.

[143] X. Batlle, M. García del Muro, and A. Labarta, "Interaction effects and energy barrier distribution on the magnetic relaxation of nanocrystalline hexagonal ferrites," *Physical Review B*, vol. 55, pp. 6440–6445, 1997.

[144] J. Rivas, A. Kazadi Mukenga Bantu, G. Zaragoza, M. C. Blanco, and M. A. López-Quintela, "Preparation and magnetic behavior of arrays of electrodeposited Co nanowires," *Journal of Magnetism and Magnetic Materials*, vol. 249, no. 1-2, pp. 220–227, 2002.

[145] A. D. C. Viegas, J. Geshev, L. S. Dorneles, J. E. Schmidt, and M. Knobel, "Correlation between magnetic interactions and giant magnetoresistance in melt-spun Co[sub 10]Cu[sub 90] granular alloys," *Journal of Applied Physics*, vol. 82, no. 6, p. 3047, 1997.

[146] J. M. Martínez Huerta, J. De La Torre Medina, L. Piraux, and A. Encinas, "Self consistent measurement and removal of the dipolar interaction field in magnetic particle assemblies and the determination of their intrinsic switching field distribution," *Journal of Applied Physics*, vol. 111, no. 8, 2012.

[147] S. Laureti, G. Varvaro, A. M. Testa, D. Fiorani, E. Agostinelli, G. Piccaluga, A. Musinu, A. Ardu, and D. Peddis, "Magnetic interactions in silica coated nanoporous assemblies of CoFe2O4 nanoparticles with cubic magnetic anisotropy.," *Nanotechnology*, vol. 21, no. 31, p. 315701, 2010.

[148] O. Henkel, "Remanenzverhalten und Wechselwirkungen in hartmagnetischen Teilchenkollektiven," *Physica Status Solidi B*, vol. 7, no. 3, pp. 919–929, 1964.

[149] G. Apai, J. F. Hamilton, J. Stohr, and a. Thompson, "Extended x-ray absorption fine structure of small Cu and Ni clusters: Binding-energy and bond-length changes with cluster size," *Physical Review Letters*, vol. 43, no. 2, pp. 165–169, 1979.

[150] P. a. Montano, G. K. Shenoy, E. E. Alp, W. Schulze, and J. Urban, "Structure of copper microclusters isolated in solid argon," *Physical Review Letters*, vol. 56, no. 19, pp. 2076–2079, 1986.

[151] A. Balerna, E. Bernieri, P. Picozzi, A. Reale, S. Santucci, E. Burattini, and S. Mobilio, "A structural investigation on small gold clusters by exafs," *Surface Science Letters*, vol. 156, p. A307, 1985.

[152] G. M. Pastor, J. Dorantes-Dvila, and K. H. Bennemann, "Size and structural dependence of the magnetic properties of small 3d-transition-metal clusters," *Physical Review B*, vol. 40, no. 11, pp. 7642–7654, 1989.

[153] P. Ballone and R. Jones, "Structure and spin in small iron clusters," *Chemical Physics Letters*, vol. 233, no. 5-6, pp. 632–638, 1995.

[154] M. Castro, C. Jamorski, and D. R. Salahub, "Structure, bonding, and magnetism of small Fe_n, Co_n, and Ni_n clusters, n<=5," *Chemical Physics Letters*, vol. 271, no. 1-3, pp. 133–142, 1997.

[155] D. P. Dinega and M. G. Bawendi, "A solution-phase chemical approach to a new crystal structure of cobalt," *Angewandte Chemie - International Edition*, vol. 38, no. 12, pp. 1788–1791, 1999.

[156] S. Laurent, D. Forge, M. Port, A. Roch, C. Robic, L. Vander Elst, and R. N. Muller, "Magnetic iron oxide nanoparticles: Synthesis, stabilization, vectorization, physicochemical characterizations and biological applications," *Chemical Reviews*, vol. 108, no. 6, pp. 2064–2110, 2008.

[157] V. Dureuil, C. Ricolleau, M. Gandais, and C. Grigis, "Phase transitions in Co nanoclusters grown by pulsed laser deposition," *The European Physical Journal D*, vol. 14, no. 1, pp. 83–88, 2001.

[158] J. P. Chen, C. M. Sorensen, K. J. Klabunde, and G. C. Hadjipanayis, "Magnetic properties of nanophase cobalt particles synthesized in inversed micelles," *Journal of Applied Physics*, vol. 76, no. 10, 1994.

[159] L. T. Kuhn, *Studies of isolated single crystalline nanoparticles by a ballistic Hall micro-magnetometer*. University of Copenhagen. Niels Bohr Institute for Astronomy, Physics and Geophysics, 1998.

[160] J. Shen, P. Ohresser, C. Mohan, M. Klaua, J. Barthel, and J. Kirschner, "Magnetic Moment of fcc Fe(111) Ultrathin Films by Ultrafast Deposition on Cu(111)," *Physical Review Letters*, vol. 80, no. 9, pp. 1980–1983, 1998.

[161] I. M. Billas, A. Châtelain, and W. A. de Heer, "Magnetism of Fe, Co and Ni clusters in molecular beams," *Journal of Magnetism and Magnetic Materials*, vol. 168, no. 1-2, pp. 64–84, 1997.

[162] G. Wulff, "On the question of speed of growth and dissolution of crystal surfaces," *Z. Kristallogr*, vol. 34, pp. 449–530, 1901.

[163] J. Buttet and J. P. Borel, "STRUCTURAL AND ELECTRONIC-PROPERTIES OF SMALL METAL AGGREGATES," *Helvetica Physica acta*, vol. 56, no. 1-3, pp. 541–550, 1983.

[164] M. Aldén, H. Skriver, S. Mirbt, and B. Johansson, "Surface energy and magnetism of the 3d metals," *Surface Science*, vol. 315, no. 1-2, pp. 157–172, 1994.

[165] K. Zehani, R. Bez, a. Boutahar, E. Hlil, H. Lassri, J. Moscovici, N. Mliki, and L. Bessais, "Structural, magnetic, and electronic properties of high moment FeCo nanoparticles," *Journal of Alloys and Compounds*, vol. 591, pp. 58–64, 2014.

[166] J. M. Soler, E. Artacho, J. D. Gale, A. Garcia, J. Junquera, P. Ordejon, and D. Sanchez-Portal, "The SIESTA method for ab initio order-N materials simulation," vol. 2745, p. 22, 2001.

[167] G. Khadra, A. Tamion, F. Tournus, B. Canut, and V. Dupuis, "Anisotropy in FeCo nanoparticles , a first step," *Solid State Phenomena*, vol. 233–234, pp. 550–553, 2015.

[168] P. Zaumseil, "RCRefSimW: Rocking curve and reflectivity curve simulation and fitting (Version 1.09)." http://www.ihp-microelectronics.com/en/services/xrr-hrxrd-simulation.

[169] K. W. Andrews, "The structure of cementite and its relation to ferrite," *Acta Metallurgica*, vol. 11, no. 8, pp. 939–946, 1963.

[170] S. Brennan and P. L. Cowan, "A suite of programs for calculating x-ray absorption, reflection and diffraction performance for a variety of materials at arbitrary wavelengths," *Review of Scientific Instruments*, vol. 63, pp. 850–853, 1992.

[171] P. Bayliss, "University of calgary," *Alberta, Canadian, ICDD Grant-in-Aid*, 1990.

[172] I. Baker, "Thayer school of engineering," *Dartmouth College, NH, USA. ICDD Grant-in-Aid*, 1997.

[173] M. A. Willard, D. E. Laughlin, M. E. McHenry, D. Thoma, K. Sickafus, J. O. Cross, and V. G. Harris, "Structure and magnetic properties of (Fe0.5Co0.5)88Zr7B4Cu1 nanocrystalline alloys," *Journal of Applied Physics*, vol. 84, no. 12, pp. 6773–6777, 1998.

[174] M. A. Willard, M. Gingras, M. J. Lee, V. G. Harris, D. E. Laughlin, and M. E. McHenry, "Magnetic Properties of *HITPERM* $(Fe,Co)_{88}Zr_7B_4Cu_1$ Nanocrystalline Magnets (Invited)," *MRS Proceedings*, vol. 577, pp. 469–479, 1999.

[175] M. A. Willard, *Structural and Magnetic Properties of HITPERM Soft Magnetic Materials for High Temperature Applications.* PhD thesis, 2000.

[176] P. Scherrer, "Bestimmung der Grösse und der inneren Struktur von Kolloidteilchen mittels Röntgenstrahlen," *Nachrichten von der Gesellschaft der Wissenschaften zu Göttingen, Mathematisch-Physikalische Klasse*, vol. 2, pp. 98–100, 1918.

[177] A. L. Patterson, "The scherrer formula for X-ray particle size determination," *Physical Review*, vol. 56, no. 10, pp. 978–982, 1939.

[178] A. Tamion, M. Hillenkamp, A. Hillion, F. Tournus, J. Tuaillon-Combes, O. Boisron, S. Zafeiratos, and V. Dupuis, "Demixing in cobalt clusters embedded in a carbon matrix evidenced by magnetic measurements," *Journal of Applied Physics*, vol. 110, p. 063904, 2011.

[179] K. Ishida and T. Nishizawa, "The C-Co(Carbon-Cobalt) system," *Journal of Phase Equilibria*, vol. 12, pp. 417–424, 1991.

[180] H. Okamoto, "The C-Co(Carbon-Cobalt) system," *Journal of Phase Equilibria*, vol. 13, pp. 543–565, 1992.

[181] H. I. Faraoun, Y. D. Zhang, C. Esling, and H. Aourag, "Crystalline, electronic, and magnetic structures of θ-Fe[sub 3]C, χ-Fe[sub 5]C[sub 2], and η-Fe[sub 2]C from first principle calculation," *Journal of Applied Physics*, vol. 99, p. 093508, 2006.

[182] S. Nagakura, "Study of Metallic Carbides by Electron Diffraction Part III. Iron Carbides," *Journal of the Physical Society of Japan*, vol. 14, pp. 186–195, 1959.

[183] G. Hägg *Zeitschrift für Physikalische Chemie (B)*, vol. 12, pp. 33–56, 1931.

[184] B. H. Davis and M. L. Occelli, "Advances in Fischer-Tropsch Synthesis, Catalysts, and Catalysis," *Focus on Catalysts*, vol. 2010, no. 3, p. 8, 2010.

[185] A. Bianconi, "SURFACE X-RAY ABSORPTION SPECTROSCOPY: SURFACE EXAFS AND SURFACE XANES.," vol. 6, no. 3 - 4, pp. 392–418, 1980.

[186] N. Blanc, L. E. Díaz-Sánchez, a. Y. Ramos, F. Tournus, H. C. N. Tolentino, M. De Santis, O. Proux, a. Tamion, J. Tuaillon-Combes, L. Bardotti, O. Boisron, G. M. Pastor, and V. Dupuis, "Element-specific quantitative determination of the local atomic order in CoPt alloy nanoparticles: Experiment and theory," *Physical Review B - Condensed Matter and Materials Physics*, vol. 87, no. 15, p. 155412, 2013.

[187] A. HILLION, *Étude des propriétés magnétiques d'assemblées de nanoparticules de Co , FeRh et FeAu.* PhD thesis, 2012.

[188] B. K. Teo, P. A. Lee, A. L. Simons, P. Eisenberger, and B. M. Kincaid, "EXAFS: a New Parameterization of Phase Shifts," *Journal of the American Chemical Society*, vol. 99, no. 11, pp. 3854–3856, 1977.

[189] B. K. Teo and P. A. Lee, "Ab initio calculations of amplitude and phase functions for extended x-ray absorption fine structure spectroscopy," *Journal of the American Chemical Society*, vol. 101, no. 11, pp. 2815–2832, 1979.

[190] M. G. Del Muro, X. Batlle, and a. Labarta, "Glassy behavior in magnetic fine particles," *Journal of Magnetism and Magnetic Materials*, vol. 221, no. 1-2, pp. 26–31, 2000.

[191] F. Luis, F. Petroff, J. M. Torres, L. M. García, J. Bartolomé, J. Carrey, and a. Vaurès, "Magnetic relaxation of interacting co clusters: crossover from two- to three-dimensional lattices.," *Physical review letters*, vol. 88, no. 21, p. 217205, 2002.

[192] P. Poddar, T. Telem-Shafir, T. Fried, and G. Markovich, "Dipolar interactions in two- and three-dimensional magnetic nanoparticle arrays," *Physical Review B*, vol. 66, no. 6, p. 060403, 2002.

[193] G. F. Goya, T. S. Berquó, F. C. Fonseca, and M. P. Morales, "Static and dynamic magnetic properties of spherical magnetite nanoparticles," *Journal of Applied Physics*, vol. 94, no. 5, pp. 3520–3528, 2003.

[194] X. X. Zhang, G. H. Wen, G. Xiao, and S. Sun, "Magnetic relaxation of diluted and self-assembled cobalt nanocrystals," *Journal of Magnetism and Magnetic Materials*, vol. 261, no. 1-2, pp. 21–28, 2003.

[195] J. M. Vargas, W. C. Nunes, L. M. Socolovsky, M. Knobel, and D. Zanchet, "Effect of dipolar interaction observed in iron-based nanoparticles," *Physical Review B - Condensed Matter and Materials Physics*, vol. 72, no. 18, pp. 2–7, 2005.

[196] M. Georgescu, M. Klokkenburg, B. H. Erné, P. Liljeroth, D. Vanmaekelbergh, and P. a. Zeijlmans Van Emmichoven, "Flux closure in two-dimensional magnetite nanoparticle assemblies," *Physical Review B - Condensed Matter and Materials Physics*, vol. 73, no. 18, p. 184415, 2006.

[197] C. J. Bae, S. Angappane, J. G. Park, Y. Lee, J. Lee, K. An, and T. Hyeon, "Experimental studies of strong dipolar interparticle interaction in monodisperse Fe3 O4 nanoparticles," *Applied Physics Letters*, vol. 91, no. 10, pp. 2005–2008, 2007.

[198] M. Georgescu, J. L. Viota, M. Klokkenburg, B. H. Erné, D. Vanmaekelbergh, and P. a. Zeijlmans Van Emmichoven, "Short-range magnetic order in two-dimensional cobalt-ferrite nanoparticle assemblies," *Physical Review B - Condensed Matter and Materials Physics*, vol. 77, no. 2, p. 024423, 2008.

[199] S. H. Masunaga, R. F. Jardim, P. F. P. Fichtner, and J. Rivas, "Role of dipolar interactions in a system of Ni nanoparticles studied by magnetic susceptibility measurements," *Physical Review B - Condensed Matter and Materials Physics*, vol. 80, no. 18, p. 184428, 2009.

[200] V. B. Barbeta, R. F. Jardim, P. K. Kiyohara, F. B. Effenberger, and L. M. Rossi, "Magnetic properties of Fe3O4 nanoparticles coated with oleic and dodecanoic acids," *Journal of Applied Physics*, vol. 107, no. May 2015, p. 073913, 2010.

[201] J. Chen, A. Dong, J. Cai, X. Ye, Y. Kang, J. M. Kikkawa, and C. B. Murray, "Collective dipolar interactions in self-assembled magnetic binary nanocrystal superlattice membranes," *Nano Letters*, vol. 10, no. 12, pp. 5103–5108, 2010.

[202] P. J. Cregg, K. Murphy, A. Mardinoglu, and A. Prina-Mello, "Many particle magnetic dipole-dipole and hydrodynamic interactions in magnetizable stent assisted magnetic drug targeting," *Journal of Magnetism and Magnetic Materials*, vol. 322, no. 15, pp. 2087–2094, 2010.

[203] D. Serantes, D. Baldomir, M. Pereiro, C. E. Hoppe, F. Rivadulla, and J. Rivas, "Non-monotonic evolution of the blocking temperature in dispersions of superparamagnetic nanoparticles," *Physical Review B - Condensed Matter and Materials Physics*, vol. 82, no. 13, p. 134433, 2010.

[204] S. H. Masunaga, R. F. Jardim, R. S. Freitas, and J. Rivas, "Increase in the magnitude of the energy barrier distribution in Ni nanoparticles due to dipolar interactions," *Applied Physics Letters*, vol. 98, no. 1, pp. 11–13, 2011.

[205] S. K. Mishra and V. Subrahmanyam, "Slow dynamics of interacting antiferromagnetic nanoparticles," *Physical Review B - Condensed Matter and Materials Physics*, vol. 84, no. 2, p. 024429, 2011.

[206] J. a. De Toro, J. a. González, P. S. Normile, P. Muñiz, J. P. Andrés, R. López Antón, J. Canales-Vázquez, and J. M. Riveiro, "Energy barrier enhancement by weak magnetic interactions in Co/Nb granular films assembled by inert gas condensation," *Physical Review B - Condensed Matter and Materials Physics*, vol. 85, no. 5, p. 054429, 2012.

[207] C. Albin, A. Tamion, and F. Tournus, "Sublimation head and implementation method." http://www.freepatentsonline.com/WO2014191688.html, December 2014.

[208] Z. Lv, W. Fu, S. Sun, Z. Wang, W. Fan, and M. Qv, "Structural, electronic and magnetic properties of cementite-type Fe3X (X=B, C, N) by first-principles calculations," *Solid State Sciences*, vol. 12, no. 3, pp. 404–408, 2010.

[209] A. Briones-Leon, P. Ayala, X. Liu, K. Yanagi, E. Weschke, M. Eisterer, H. Jiang, H. Kataura, T. Pichler, and H. Shiozawa, "Orbital and spin magnetic moments of transforming one-dimensional iron inside metallic and semiconducting carbon nanotubes," *Physical Review B - Condensed Matter and Materials Physics*, vol. 87, no. 19, 2013.

[210] F. Calvo, "Thermodynamics of nanoalloys," *Physical Chemistry Chemical Physics*, 2015.

[211] R. Nakajima, J. Stöhr, and Y. Idzerda, "Electron-yield saturation effects in L-edge x-ray magnetic circular dichroism spectra of Fe, Co, and Ni," *Physical Review B*, vol. 59, no. 9, pp. 6421–6429, 1999.

[212] E. P. Sajitha, V. Prasad, S. V. Subramanyam, S. Eto, K. Takai, and T. Enoki, "Synthesis and characteristics of iron nanoparticles in a carbon matrix along with the catalytic graphitization of amorphous carbon," *Carbon*, vol. 42, pp. 2815–2820, 2004.

[213] C. Raufast, A. Tamion, E. Bernstein, V. Dupuis, T. Tournier, T. Crozes, E. Bonet, and W. Wernsdorfer, "Microwave-assisted magnetization reversal in individual isolated clusters of cobalt," *IEEE Transactions on Magnetics*, vol. 44, pp. 2812–2815, 2008.

[214] F. Tournus, N. Blanc, a. Tamion, M. Hillenkamp, and V. Dupuis, "Dispersion of magnetic anisotropy in size-selected CoPt clusters," *Physical Review B - Condensed Matter and Materials Physics*, vol. 81, no. 22, p. 220405, 2010.

[215] S. O. Medina, *SPINTRONICS IN CLUSTER-ASSEMBLED NANOSTRUCTURES*. PhD thesis, 2013.

[216] L. J. Swartzendruber, *Cu-Fe (Copper-Iron)*. ASM International, 1993.

[217] T. Nishizawa and K. Ishida, "The Co-Cu (Cobalt-Copper) system," *Bulletin of Alloy Phase Diagrams*, vol. 5, no. 2, pp. 161–165, 1984.

[218] M. Grinstaff, M. Salamon, and K. Suslick, "Magnetic properties of amorphous iron.," *Physical review. B, Condensed matter*, vol. 48, no. 1, pp. 269–273, 1993.

Thèse de l'Université Claude Bernard-Lyon 1
Discipline : physique

Nom : **Ghassan KHADRA**	Numéro d'ordre : 145-2015
Directrice de thèse : **Véronique DUPUIS**	Date de soutenance : 25/09/2015

Titre : Propriétés magnétiques et structurales d'assemblées de nanoparticules de FeCo triées en taille.

Résumé : La recherche sur les nanostructures n'a cessé de croître au cours de ces dernières années. En particulier, de grands espoirs sont basés sur l'utilisation possible de nanoparticules, objets situés à la frontière entre les agrégats moléculaires et l'état massif, dans les différents domaines des nanosciences. Mais à cette échelle, les phénomènes physiques ne sont pas encore bien compris. Les nanoparticules magnétiques sont mises en avant pour leurs applications potentielles dans les dispositifs d'enregistrement denses, plus récemment dans le domaine médical, mais aussi comme catalyseur de nombreuses réactions chimiques.
Dans ce travail, nous nous sommes intéressés aux propriétés magnétiques intrinsèques (moments et anisotropie magnétiques) de nanoparticules bimétalliques fer-cobalt. Pour cela, des agrégats FeCo dans la gamme de taille 2-6 nm ont été préparés en utilisant la technique MS-LECBD (Mass Selected Low Energy Cluster Beam Deposition) et enrobés en matrice $in-situ$ afin de les séparer, d'éviter leur coalescence pendant les recuits et de les protéger à leur sortie à l'air. Dans un premier temps, les propriétés structurales (dispersion de taille, morphologie, composition, structure cristallographique) ont été étudiées en vue de corréler directement les modifications des caractéristiques magnétiques des nanoparticules, à leur structure et à l'ordre chimique obtenu après traitement thermique haute température. D'autre part, pour mettre en évidence les effets d'alliages à cette échelle, des références d'agrégats purs de fer et de cobalt ont été fabriquées et étudiées en utilisant les mêmes techniques. Par microscopie électronique en transmission à haute résolution, diffraction anomale et absorption de rayons X (high resolution transmission electron microscopy (HRTEM), anomalous x-ray diffraction (AXD) and extended x-ray absorption fine structure (EXAFS), nous avons mis en évidence un changement structural depuis une phase A2 chimiquement désordonnée vers une phase B2 type CsCl chimiquement ordonnée. Cette transition a été validée par nos résultats obtenus par magnétomètrie SQUID et dichroïsme magnétique circulaire (x-ray magnetic circular dichroism (XMCD)).

Mots-clés : nanoparticules, anisotropie magnétique, ordre chimique, fer-cobalt, METHR, AXD, EXAFS, SQUID, XMCD.

Title : Magnetic and structural properties of size-selected FeCo nanoparticle assemblies.

Abstract : Over the past few decades, use of nanostructures has become widely popular in the different field of science. Nanoparticles, in particular, are situated between the molecular level and bulk matter size. This size range gave rise to a wide variety physical phenomena that are still not quite understood. Magnetic nanoparticles are at their hype due to their applications in medical field, as a catalyst in a wide number of chemical reactions, in addition to their use for information storage devices and spintronics.
In this work, we are interested in studying the intrinsic magnetic properties (magnetic moments and anisotropy) of FeCo nanoparticles. Thus, in order to completely understand their properties, mass-selected FeCo nanoparticles were prepared using the MS-LECBD (Mass Selected Low Energy Cluster Beam Deposition) technique in the sizes range of 2-6 nm and $in-situ$ embedded in a matrix in order to separate them, to avoid coalescence during the annealing and to protect during transfer in air. From a first time, the structural properties (size, morphology, composition, crystallographic structure) of these nanoparticles were investigated in order to directly correlate the modification of the magnetic properties to the structure and chemical ordering of the nanoparticles after high temperature treatment. In addition to the bimetallic FeCo nanoparticles, reference Fe and Co systems were also fabricated and studied using the same techniques. The structural properties were investigated using high resolution transmission electron microscopy (HRTEM), anomalous x-ray diffraction (AXD) and extended x-ray absorption fine structure (EXAFS) where a phase transition from a disordered A2 phase to a chemically ordered CsCl B2 phase was observed and further validated from the magnetic findings using SQUID magnetometry and x-ray magnetic circular dichroism (XMCD).

Keywords : nanoparticle, magnetic anisotropy, ordering, iron-cobalt, HRTEM, AXD, EXAFS, SQUID. XMCD.

Institute Lumière Matière
UMR 5306 Université Lyon 1-CNRS
F-69622 Villeurbanne Cedex